"The Structure and Properties of Autogenous Laser Beam Welds in Aluminium Alloys"

by Iain R. Whitaker, BEng(Hons)

Thesis submitted to the University of Nottingham for the degree of Doctor of Philosophy, May 1994

Acknowledgements

I am indebted to my supervisor, Dr. Graham McCartney, who was and always will be a willing listener, for his patience, advice and encouragement. Thanks to my colleague, Neil Calder, without whom there would have been no welds, and to Prof. W.M. Steen for the use of facilities in the Laser Division, Department of Mechanical Engineering, Liverpool. In addition, I am grateful to the staff both in the Department of Materials Engineering and Materials Design, Nottingham and the Department of Materials Science and Engineering, Liverpool.

Special thanks go to my parents whose love knows no limits, to Pam for nurturing me back from reciprocal space and to fellow solidifiers, Louise and Cathy, who guaranteed a bustling day.

Finally, thanks are also due to the Science and Engineering Research Council and British Aerospace for their support through a Co-operative Research Grant and CASE award research studentship.

Table of Contents

THE STRUCTURE AND PROPERTIES OF AUTOGENOUS LASER BEAM WELDS IN ALUMINIUM ALLOYS

Abstract

Autogenous laser beam welds were made in sheets of the aluminium alloys 8090, 8009 and 6061. The Al-Li based alloy 8090 was subjected to both continuous wave CO_2 and pulsed Nd:YAG thermal cycles with average powers of 1.5-3.8 kW and 0.8-0.9 kW respectively. The two techniques were compared for their influence on the 8090 solidified weld pool shape, the fusion zone microstructure and microhardness, the HAZ and the susceptibility of the fusion zone to post-weld heat treatment. It was found that CO_2 keyhole welding is preferable to Nd:YAG welding, under the welding conditions investigated, as essential elements such as Li and Mg were lost by evaporation during Nd:YAG processing.

Microscopy of the 8090 CO_2 weld fusion zone revealed that the solidification mode was sensitive both to the temperature gradient and growth rate during solidification, with a transformation from cellular to equiaxed dendritic growth occurring from the weld pool edge to the weld centre. The secondary dendrite arm spacing was found to be 2-5μm and the metastable phase δ' (Al_3Li) was present after welding with a very fine homogeneous distribution of ~5nm diameter spheres. Porosity was identified as a major welding defect and was attributed to two distinct formation mechanisms. Firstly, the release of hydrogen gas during welding caused spherical gas bubbles throughout the weld pool. Secondly, the delicate balance of forces within the keyhole resulted in larger irregular shaped pores at the weld centre-line towards the weld root. This second type of pore was virtually absent in full penetration welds.

The influence of heating rate to the solution treatment temperature on 8090 CO_2 weld metal was assessed and the weld metal grain size was found to be most uniformly small after a heating rate of 1 K/min. A TEM investigation confirmed that the grain boundary pinning dispersoid β' (Al_3Zr) was responsible for inhibiting grain growth. However, the microhardness and notch-tensile strength of the CO_2 weld metal did not depend on the weld metal grain size. Instead, it was suggested that the residual cast structure was responsible for determining the mode of failure and fracture strength.

Microstructural studies of CO_2 laser welds in RS/PM 8009 and wrought 6061 confirmed the cooling rate of 10^2-10^3 K/s predicted for CO_2 welds in 8090. However, the 8009 CO_2 weld metal did not solidify by epitaxial growth from the fusion boundary, which was the case for CO_2 welds in 8090 and 6061. Instead, solidification in 8009 weld pools occurred via many isolated events on primary intermetallic particles. The intermetallic particles had the stoichiometry $Al_{4.5}(Fe,V,Si)$ with the Al_mFe tetragonal lattice parameters. It was qualitatively shown that the 8009 weld microhardness had an inverse relationship with the volume fraction of intermetallic particles. Chemical analysis of the 6061 weld metal confirmed that even when aluminium is alloyed with volatile elements such as Mg it is mostly retained within the weld pool during CO_2 keyhole laser welding. It was found that a much higher power was required to obtain a deep penetration weld in 6061 than in either of the other alloys.

Chapter 1. Introduction

The development of aluminium alloys containing Li has progressed during the twentieth century to the present day[1]. In the early days, Li was added to Al alloys to help improve the strength of the age-hardening Al-Zn-Cu alloys. However, the twin benefits of lower density and increased modulus with Li addition were only realised more recently and current aerospace design utilises the reduction in density afforded by Li additions to Al. The density of aluminium is reduced by about 3% for each weight percent addition of Li, while the Young's modulus is increased by about 6%[2]. The binary alloys, however, have very poor fracture toughness properties, especially in the short-transverse direction. Improvements have been made by alloying element additions, together with thermomechanical treatments. Furthermore, additions of Cu, Mg and Zr can enhance the strength, modulus of elasticity, fatigue, corrosion, and stress corrosion cracking resistance. Where aircraft applications are concerned, then, Li alloying presents the possibility of weight saving and therefore reduced fuel usage. Thus, Al-Li alloy development has been focused towards replacing other conventional aircraft alloys such as the 2XXX and 7XXX series Al alloys. These types of alloys used in airframe structures are mechanically fastened which requires several operations with a consequently reduced production rate and an upper limit to the thickness of the sheet being fastened. Hence there is a strong desire to introduce welding as part of the manufacturing route.

Recent work by Pickens[3][4], Lippold[5], Edwards et al.[6], Pickens et al.[7] and Yunjia et al.[8] indicated that difficulties such as hot cracking and weld porosity were encountered when filler alloys were employed in either gas-metal or gas-tungsten-arc welding of Al-Li based alloys. However, welding with high energy density heat sources, such as electron beams or laser, at high welding speeds can eliminate the need for a filler alloy, reduce the heat input to the workpiece, give a fine scale, rapidly solidified weld pool microstructure and minimize weld cracking. Indeed, there have been several reports[9][10][11][12][13][14] for laser and electron beam welding of Al-Li based alloys which have indicated that autogenous keyhole type welding

(typical of a high energy density beam) leads to a reduction in both porosity and hot cracking.

In this thesis the main aim was to assess the weldability of the Al-Li based alloy 8090 (Al-2.4wt%Li-1.1wt%Cu-0.6wt%Mg-0.1wt%Zr) using both CO_2 and Nd:YAG lasers. A material can be said to be weldable if the 'properties' of the weld metal match to a reasonable degree those of the unwelded base metal. Thus the procedure adopted to gain this assessment falls into three parts. Firstly, a detailed characterisation of the solidified weld pool structure was undertaken. This included an analysis of the weld pool shape and HAZ, the solidified grain structure, dendritic structure, interdendritic segregation and sub-micron precipitation, as well as porosity formation. Secondly, the susceptibility of the weld microstructure to post-weld heat treatments was evaluated. Special regard was given to the development of the fusion zone grain structure and sub-micron precipitate reactions occurring during solution treatment and/or ageing. Thirdly, the microhardness and tensile properties of the base and weld metal were compared to determine the weldability.

In addition, supporting work was also undertaken on CO_2 laser welds on two other aluminium alloys. A conventional medium strength age hardenable alloy 6061 (Al-0.9wt%Mg-0.6wt%Si-0.5wt%Fe-0.3wt%Cu-0.1wt%Ti) was investigated to evaluate the ease with which this material could be power beam welded. The alloy 8009 (Al-8.5wt%Fe-1.7wt%Si-1.3wt%V), which is of potential interest because of its high strength at elevated temperatures, was also examined to provide basic information on the feasibility of laser welding it during airframe assembly.

Chapter 2. Literature Review

2.1 Introduction to Laser Welding

2.1.1 Historical Development of Welding

Metal joining technology has been developing from an early age. Brazing and soldering techniques were adopted for jewellery and domestic articles during the Bronze Age (7000 - 1000 BC) but welding did not become technically important until the blacksmiths managed to attain yellow or white heat in iron (500 - 300 BC). So it is necessary to distinguish between simple joins and welds; the latter can be defined as a coalescence of metals by heating to a suitable temperature with or without the application of pressure or filler material.

In more modern times with the introduction of cast iron, welding was restricted to the blacksmiths and the jeweller, with most structural and non-structural joints performing satisfactorily with bolts or rivets. But by the end of the 19th Century rivetting was struggling to cope with the pressures of industrialization and proved distinctly inadequate in the manufacture of enclosed containers such as boilers. Gas welding, arc welding and resistance welding all appeared as rudimentary processes on the crest of modernization.

Wide scale adoption of the new welding processes was unhurried until the outbreak of World War I, and by 1916 the oxy-acetylene process was well developed. Similarly arc welding was not universally used until World War II when the urgent need for more rapid means of construction for shipping, powerplants, transportation and structures spurred the necessary development work.

Inert gases were used for the first time in 1941 as a protective atmosphere for tungsten inert gas (TIG) welding of light alloys in the American Aeronautic Industry and metal inert gas (MIG) welding appeared in 1948 enabling the semi-automatic welding of aluminium alloys. More recently, electron beam welding in the 1950's and laser beam welding in the 1970's saw the advancement towards high power density welding with

narrow fusion zones, minimum heat distortion and minimum overheating.

The development of multikilowatt continuous wave CO_2 lasers during the 1970's offered high technology industries a new and exciting degree of freedom. But the rate of advance has been slow due to widespread scepticism and worryingly high initial capital investment required.

2.1.2 The CO_2 Laser[15]

C.K.N. Patel was first able to cause lasing with a CO_2 laser in 1964 with a meagre 1mW of power. Later additions of nitrogen and then helium were made to the lasing medium which saw the power output boosted to 100W. Modern CO_2 lasers typically have a power output of 5kW and the radiation wavelength is 10.6μm.

Since the early 1970's the use and application of CO_2 lasers has steadily increased and welds have been made in many alloy systems. During the early days stainless steels were found to be readily weldable and Willgoss et al.[16] obtained acceptable welds in austenitic and ferritic steels. The metallurgy of laser welded Ti alloys has been investigated by various authors[17][18] and recently aluminium alloys such as Al-Mg-Si[19][20], Al-Mg-Mn[20][21][22], Al-Cu-Li[9][10][22], Al-Mg-Zn[22] and Al-Li-Cu[11][12][13] have been satisfactorily joined.

2.1.3 The Nd:YAG Laser[15]

The power output of Nd:YAG lasers can be boosted by beam oscillation which gives a non-continuous, pulsed output. The laser is solid state with a lasing medium of neodymium in a Yttrium Aluminium Garnet crystal rod. A considerable amount of energy is required to lase which causes serious heating problems. 400W/rod is recognised as the power limit, after which heating causes beam degradation through distortion of the laser optics. The output radiation is shorter in wavelength than the CO_2 laser at 1.06μm and provides the advantage of optical fibre transmission[15][24].

The application of the Nd:YAG laser to welding technology has not advanced at the same pace as the CO_2 laser. This is principally due to the lower average power output

and slightly higher operating costs. Various studies have been made into the weldability of Al alloys[23][24][25][26][27] and a Ni-Cr alloy[24].

2.1.4 Laser-Material Interactions

As the laser beam is a form of electromagnetic radiation it undergoes the normal interactions of absorption, transmission and reflection when it impinges on a metal surface. Absorption occurs as the photons interfere with metal electrons and is known as the Inverse Bremsstrahlung Effect. This interference appears as electron vibrations caused by the electric force from the electric field component of the radiation. The vibrating electrons thus have a higher energy and are able to reradiate in all directions, or even heat the metal by doing work on the molecular bonds. If enough energy is supplied to cause large electron vibrations, melting and eventually vaporization can occur.

However, the absorption of energy from the photons is quite low in metals because only the free electrons are initially interfered with which are able to oscillate free of molecular constraints, thus most of the photon energy is reradiated. The absorption can be increased significantly by reducing the wavelength of the incident radiation or by increasing the temperature of the target[15][28].

2.1.5 Laser Welding Mechanisms

Laser beam welding relies on the generation of very high power densities[15], typically 10^{10}-10^{12} W/m^2, which are sufficiently high to cause vaporization of the substrate due to the absorption mechanisms described above. Although most of the radiation is at first reflected, the substrate does warm up with radiation time and absorptivity gradually increases. When the material begins to vaporize a depression is created on the substrate surface which is surrounded by a thin layer of molten metal. With more radiation time, the hole deepens to form a 'keyhole', Fig 2.1[31]. There exists a complicated distribution of forces within this keyhole but in simple terms the pressure created by the formation of vapour tends to open and maintain the keyhole whereas the surface tension supplied by the liquid layer tends to close the keyhole[29][30]. Once created, the keyhole is believed to act as an optical black body where nearly all

the incident radiation is absorbed due to multiple reflections[15][29]. Consequently, energy is deposited deep within the bulk of the material and energy transfer is not reliant on conventional conduction modes of heating.

The forces created during keyhole formation therefore control its overall stability. If the keyhole is to remain stable during welding then the vapour pressure force within the keyhole should be of sufficient magnitude to overpower the surface tension forces in the liquid layer[31], Fig 2.2. The effective surface pressure of the photons in the keyhole will be negligibly small, P_b, and the primary force supporting the cavity is that provided by the pressure of the metal vapour, P_v. This force is opposed by hydrostatic, $h\rho g$, and surface tension forces, γ/r. Both the vapour pressure force and the force due to surface tension have a significant dependence on temperature so the force distribution within the keyhole is clearly complex[32]. Any instability during welding could upset the fragile equilibrium and render the weld pool susceptible to perturbations[32]. The bottom of the keyhole experiences the highest temperature so at this point the vapour pressure force is maximum and the force due to surface tension is small (assuming that $d\gamma/dT$ is positive). However, as the opening of the keyhole is approached the temperature decreases causing a drop in the vapour pressure force and an increase in the force due to the surface tension. Thus there is a point, possibly within the keyhole, where the dominant force changes from vapour pressure controlled to surface tension controlled and constrictions might form causing keyhole instability.

The molten pool has been shown to display turbulent flow[33] with the formation of twin vortices in some deep keyholes in the molten wake which could present sources of instability.

Instability may also arise due to plasma formation at the point where the high intensity beam impinges on the metal surface[34][35]. The metal vapour inside the keyhole still contains electrons and is therefore susceptible to absorption of radiation and capable of becoming hotter. As the kinetic energy of the free electrons increases the metal vapour ionizes. Since welding takes place within an inert atmosphere the hot

metal vapour or plasma can cause ionization of the shielding gas if its ionization potential is low enough[35]. Thus ionization increases with increasing temperature and the electron density within the plasma can increase to the point where the plasma causes beam blocking. The continuous formation of metal vapour ceases and welding is interrupted. Everything begins to cool at this stage causing the plasma to subside. With the absence of plasma blocking, the beam can re-impinge on the metal surface enabling renewed vaporization and the whole process of plasma formation resumes.

The threshold intensity required to produce a laser induced plasma is dependent on the wavelength of the radiation and the ionization potential of the shielding gas[35]. Table 2.1 lists the ionization potential of some common metals[34]. At shorter radiation wavelengths the threshold intensity is higher and a more intense laser beam is required. If the shielding gas has a high ionization potential then more energy, or a higher temperature, is required before it will become a plasma.

Plasmas with low electron densities, perhaps formed with shielding gases whose ionization potentials are high, remain relatively transparent to the laser radiation but have a high temperature due to some absorption. It has been noted that in this case the plasma might actually encourage laser coupling into the metal[34]. These optically transparent plasmas are also thought to be the main cause of the characteristic 'wine-glass' or 'nail-head' weld bead profiles due to reradiation at the weld surface.

2.1.6 Laser Welding Parameters

There are many parameters which can be used to define a laser welding process and the intention here is not to show an exhaustive list but to describe only the main process variables as listed elsewhere[15][36];

1. Laser beam power, W
2. Welding traverse speed, v
3. Incident spot size radius, r
4. Absorption
5. Focus position

6. Radiation wavelength, λ
7. Shielding gas.

The power, speed and incident spot size have been assessed by Swift-Hook and Gick[29] for their influence on weld bead shape. They have shown that by treating the welding process as a line heat source moving through the metal a single curve can be drawn which relates the power and speed to the weld bead width and depth of penetration, Fig 2.3[29][31]. The normalized power input, X, and the normalized weld width, Y, where

$$X = \frac{W}{k_c T d} \qquad Y = \frac{vw}{\alpha} \tag{2.1}$$

(k_c is the thermal conductivity, T is the temperature, d is the weld penetration depth, w is the weld width and α is the thermal diffusivity) are plotted on a logarithmic scale. At high speeds X varies linearly with Y and

$$\frac{vw}{\alpha} = \left(\frac{W}{k_c T d}\right)^{0.483} \tag{2.2}$$

At these high speeds, input power can be reduced by altering the welding speed or beam power without any loss in the melting ratio, or equivalently the welding efficiency. The melting ratio is defined as the percentage of the beam power which is used to melt the metal and has been shown to reach a theoretical maximum of 0.48. At low speeds, Y falls off very rapidly with X and

$$\frac{vw}{\alpha} = \exp\left(\frac{-k_c T d}{W}\right) \tag{2.3}$$

In principle it is possible to achieve a given penetration with a lower welding speed and less power if a narrow molten pool or beam size is produced, hence making the normalized power input, X, smaller. But at these low speeds a power reduction of 20% would require a reduction in weld bead width of at least 5 times. In reality, if the input power is reduced, the melting ratio plummets.

Banas[34] developed this further and showed that published data for power, speed and incident spot size, i.e. the main process variables, can be correlated according to the following equation,

$$\frac{2vr}{\alpha} = 0.15^2\left(\frac{k_c T d}{W}\right)^{-2} \qquad 2.4$$

The variation in the weld bead shape with laser parameters, i.e. power and speed, has been monitored by various authors[16][28]. This has shown that the depth of penetration is nearly inversely proportional to the traverse speed but increases almost linearly with the laser beam power.

The way in which absorption of the laser beam by the metal can influence the processing, and how the metal absorption characteristics can be altered has been discussed in Section 2.1.4.

The influence of the focal position has been assessed by Willgoss et al.[16] using CO_2 lasers on steels, Fig 2.4. When the focus point was positioned deep inside the workpiece a V-shaped weld resulted. When focusing was well above the workpiece a large 'nail-head' was formed with consequent loss of penetration. The optimum focus was found to be 1mm below the surface of the workpiece which produced little or no 'nail-head' and near parallel sided fusion zones. Work by Engel[28] showed that penetration could be maximised with minimum weld bead width by focusing the beam 1.2 - 2.5mm below the material surface. It was also noted that short focal length lenses gave deeper penetration but were less tolerant to vibrations in the focusing position.

The focus point tolerance in Nd:YAG welds was investigated by Nakajima et al.[24]. Their work has shown that the focus can be varied between ±0.5mm of the surface without any significant deterioration in depth of penetration.

The choice of shorter wavelength of the radiation once a keyhole has been formed is

considered to have little effect during operation due to the high absorbtivity within the keyhole. However, prior to keyhole formation, surface reflectivity will be reduced when using shorter wavelength radiation[15][28], as illustrated in Fig 2.5. Banas[34] cites several possible processing advantages for moving onto shorter wavelengths e.g. (1) lower metal reflectivity, (2) higher threshold limit for plasma formation, (3) the ability to use less expensive and more durable optical materials for beam formation, transmission and focusing and (4) the potential for beam transmission through fibre optics.

The influence of the shielding gas during welding has been summarized by Bharti[36]. He points to three functions in laser processing. Its basic function is to protect the keyhole from the outside atmosphere. Other functions are forming or removing laser induced plasma and protecting the lenses from welding debris. It has been noted[15] that the composition of the shielding gas can affect the absorption of the beam by the material probably because of plasma formation. Since the plasma formation occurs by ionization of the gas, it follows that gases with high ionization potentials are least likely to form a plasma. Helium and argon are commonly used gases, and helium, though more expensive than argon, has a higher ionization potential[35]. The formation of the plasma during welding has been discussed in Section 2.1.5 and can be summarized as follows[15]; if the plasma is near the workpiece surface or even in the keyhole it may be beneficial for weld penetration but if the plasma is thick or becomes detached from the surface it may absorb the beam power and interrupt the welding process.

Behler et al.[37] have studied the influence of the shielding gas composition and flow rate on the properties of laser welds in an Al-Mg-Si alloy. It was demonstrated that a minimum nitrogen flow rate of 30 l/min was required to prevent plasma shielding and to get a high rate of energy coupling with the laser operating at 3.8kW. A homogeneous black layer of Al-N-O was observed on the bead surface which was also evident as thin flakes within the weld bead on transverse sections. With increasing gas flow rate the energy coupling was enhanced and the depth of penetration increased accordingly. Welding with different shielding gases at otherwise constant conditions

showed that helium caused very little penetration. Nitrogen, on the other hand, gave deep penetration, and oxygen deeper still.

Nd:YAG laser welds[24] in Ni-Cr heat exchangers were made with and without shielding gas. When welds were made with argon a large vapour plume was created with very little penetration. In the nitrogen and helium shielding atmospheres similar weld bead shapes were obtained but the helium welds were irregular in penetration with large pores at the weld root. In the unshielded, atmospheric welds the weld bead was deep and narrow but covered in an oxide film.

2.2 Weld Pool Solidification[38]

2.2.1 Weld Pool Solidification Structures

The mechanism of weld pool solidification is similar in principle to that of a small scale ingot but with some basic differences such as:

(a) castings begin to solidify with the nucleation of a characteristic chill zone whereas with the weld pool partially melted grains in the base metal are readily wetted and solid growth proceeds epitaxially.

(b) solidification rates are generally higher in weld pool solidification than in ingot solidification.

(c) the shape of the macroscopic solid/liquid interface remains approximately constant throughout the weld length whereas in the ingot the solid/liquid interface changes with time.

(d) the fluid flow within the weld pool is driven by extra forces and can be more turbulent than in an ingot.

In contrast to ingot solidification, weld pool solidification occurs in the absence of a typical nucleation event via a mechanism of 'epitaxial' growth from grains in the base metal. The molten pool has a similar composition to the base metal and thus readily wets partially melted grains at the fusion boundary in the base metal providing a nearly ideal case of heterogeneous nucleation at low contact angle. Savage et al.[39][40] have demonstrated the continuity of grain boundaries across the fusion line and recognised that the process of grain growth is influenced by the size and

orientation of the grains in the base metal at the solid/liquid interface. The crystallographic orientations of grains on both sides of the fusion boundary were compared using the X-ray Laue back reflection technique and identical orientations were found for continuous grains[40][41].

These epitaxially nucleated grains grow via the addition of atoms onto the solid surface at the solid/liquid interface. The macroscopic form of the interface, either planar, cellular or dendritic has been shown by Tiller and Rutter[42] to be dependent on:

(1) the crystallographic features of the growing crystal
(2) the temperature distribution in the metal
(3) the solute distribution in the metal.

A solute rich layer of liquid exists ahead of the advancing interface and under certain conditions this liquid layer can be constitutionally supercooled below its equilibrium liquidus temperature[42], Fig 2.6. This layer is unstable and will be able to alter its shape in an attempt to eliminate the instability. The development of constitutional supercooling is thus enhanced by factors which alter the equilibrium temperature and solute distributions at the solid/liquid interface, such as[42]:

(1) low temperature gradients in the liquid
(2) fast growth rates
(3) a large freezing range in the alloy
(4) high alloy contents.

Some of these are illustrated in Fig 2.6. This diagram shows that as solid forms, solute is ejected into the liquid ahead of the solid/liquid interface. The composition of the liquid at the solid/liquid interface is given by C_0/k where C_0 is the alloy bulk composition and k is the partition coefficient, the ratio of the composition of the solid to the composition of the liquid. Due to solute diffusion in the liquid the composition of the liquid decreases exponentially from the interface to the value C_0 at large distances from the interface. The concentration profile has a characterisitc width D/R which determines the critical temperature gradient for constitutional supercooling;

$$\frac{(T_1 - T_3)}{(D/R)} \qquad 2.5$$

where (T_1-T_3) is the equilibrium freezing range of the alloy, D is the diffusivity of the solute and R is the growth rate. The equilibrium liquidus temperature, T_e, varies according to the liquid composition gradient, C_l, and planar interfaces are stable if the critical temperature gradient is greater than the equilibrium liquidus temperature. However, if the temperature gradient ahead of the interface, G, is less than the critical temperature gradient then the liquid is below its equilibrium freezing temperature and is therefore constitutionally supercooled. Thus if a protrusion forms on the planar interface it can grow into a region of liquid which is at a low enough temperature for the protrusion to remain stable[43].

Growth structures in weld metal have been described by Calvo et al.[44] and were observed to be dependent on the degree of constitutional supercooling. During welding, grains nucleate and grow at the fusion boundary and a very high temperature gradient initially exists. This soon decreases as the centre of the weld is reached, thus a range of solidification structures exists within the weld metal. Initially cells form at the edge of the weld pool which rapidly become columnar-dendritic as the centre of the weld is approached. With decreasing temperature gradient the columnar dendrites transform to dendrites with various orientations at the centre of the weld pool.

The weld grain structures develop in preferred easy growth directions. The preferred growth direction in both fcc and bcc metals is parallel to the edge of the unit cube in three mutually perpendicular <100> directions[45]. After epitaxial growth has taken place, those grains which happen to have their <100> directions nearly parallel to the maximum thermal gradient will tend to grow into the liquid more rapidly, expanding in cross-section at the expense of their less favourably oriented neighbours. This is known as a competitive growth process. In the weld pool, however, the direction of the maximum thermal gradient is not necessarily constant. In fact the direction of the maximum thermal gradient can continually change from normal to the

welding direction at the edge of the weld pool to parallel to the welding direction at the weld centre-line. Thus the maximum thermal gradient and grain growth direction try to follow a direction which is normal to the solid/liquid interface at any point[39].

The characteristics of competitive growth are therefore dependent on the weld pool shape, which is controlled by the welding parameters. This is illustrated in Fig 2.7[46]. At fast welding speeds a tear-drop shaped weld pool is formed which has, at the surface, a nearly constant maximum thermal gradient direction from the weld pool edge to the weld centre[40]. Thus any grain at the fusion boundary which is favourably oriented for growth grows quickly and widens to dominate a large area up to the centre-line and other less favourably oriented grains are inhibited. Thus relatively few grains survive to reach the weld centre-line. In contrast, at slower welding speeds an elliptically shaped weld pool is formed and the direction of the maximum thermal gradient continually changes from the pool edge to the weld centre. Therefore no single grain is in a favourable growth situation long before one of its neighbours becomes more favourably oriented and many more grains survive to reach the weld centre. Columnar grains in elliptical weld pools can display considerable curvature due to the changing thermal gradient direction. The curvature is thought to be caused by repeated side-branching of the solidification substructure, with the crystallographic orientation of the curved grain remaining constant[38].

The shape of the weld pool, governed by the welding parameters, is a nearly constant entity bounded by a progressing solid-liquid interface. From the imposed geometrical constraints, the interface at the centre of the weld pool must travel a greater distance than the growing interface at any other point on the pool boundary, as illustrated in Fig 2.8[47]. As stated earlier, the favoured growth direction is along those <100> directions which are most nearly aligned with the maximum thermal gradient. Thus for a welding speed of v and a growth rate of R, if the maximum thermal gradient is oriented at an angle θ from the welding direction then the maximum growth rate is given by

$$R = v\cos\theta \qquad 2.6$$

However, if the favoured growth direction is inclined at an angle θ' to the welding direction then the growth rate along the favoured direction, R_f is given by

$$R = R_f \cos(\theta' - \theta) \qquad 2.7$$

When these two equations are combined the actual growth rate is given by

$$R_f = \frac{v\cos\theta}{\cos(\theta' - \theta)} \qquad 2.8$$

This means that the solidification rate is greatest at the weld pool centre-line where the temperature gradients are most shallow due to the proximity of the welding heat source. The lowest growth rates are found at the weld pool edge where the temperature gradients are steepest. This further exemplifies the progressive change in solidification structure across the weld bead[44] as constitutional supercooling is promoted by low thermal gradients and high solidification velocities[42].

Relationships have been found between the scale of the solidified microstructure and the local solidification time. It has been shown that the secondary dendrite arm spacing, λ_2, is proportional to the cube root of the local solidification time, t_f[48];

$$\lambda_2 \propto (t_f)^{\frac{1}{3}} \qquad 2.9$$

where the local solidification time is given by

$$t_f = \frac{(T_l - T_s)}{G.R} \quad \text{where} \quad \frac{dT}{dt} = \frac{dT}{dx} \cdot \frac{dx}{dt} = G.R \qquad 2.10$$

G is the temperature gradient, R is the growth rate and $(T_l - T_s)$ is the solidification range. Thus for a particular alloy, G and R are the main parameters which need to be varied for the control of microstructure; morphology and scale. The plot of G vs. R in Fig. 2.9[104] shows that for specific values of G/R the microstructure can be broadly defined as planar, cellular or dendritic, with the scale of the microstructure

becoming finer with increasing values of G.R.

2.2.2 Microstructure of Al-Li alloys

The technologically important features of the Al-Li alloy systems, such as high elastic modulus and low density, have stimulated intensive research into the microstructure and properties of binary, ternary and quaternary alloys which have been reviewed by Quist et al.[1], Miller et al.[49], Flower et al.[50] and Enrique et al.[51]. All the Al-Li alloys rely on the classical age hardening phenomenon for the sought after strength, and the binary phase diagram[52] illustrated in Figs. 2.10 and 2.11[53][54][55] shows that Li can dissolve in Al up to ≈1.5 wt% at room temperature. Thus an alloy containing more than this amount can be solution treated at temperatures greater than 500°C and aged at lower temperatures whereupon the supersaturated solid solution will decompose. For alloys containing more than ≈2 wt% Li the decomposition begins during the quench from solution treatment[53][54][55][56].

Indeed, the nature of the decomposition has been the focus of attention for decades. In a detailed study on the structural ageing characteristics of Al-Li alloys containing Cu, Silcock[57] showed that the supersaturated solid solution of a binary Al-Li alloy decomposes as follows:

$$\alpha\text{-}Al \rightarrow \delta'(Al_3Li) \rightarrow \delta(AlLi) \qquad 2.11$$

The intermediate δ′ phase is a metastable superlattice of the type $L1_2(Cu_3Au)$ which can nucleate homogeneously as spherical precipitates and causes considerable hardening of the matrix. The equilibrium δ phase precipitated during ageing at higher temperatures and the X-ray diffraction patterns suggested it was cubic with a $\{111\}_{Al}$ habit plane and an orientation relationship with the matrix of:

$$(100)_{AlLi} \parallel (110)_{Al} \qquad (0\bar{1}1)_{AlLi} \parallel (1\bar{1}2)_{Al} \qquad (011)_{AlLi} \parallel (\bar{1}11)_{Al} \qquad 2.12$$

δ had no observable hardening effect on the matrix. The equilibrium δ is richer in Li than the metastable δ′ and δ′ precipitate zones form around the δ precipitates.

Thus, the non-equilibrium precipitation reactions, which dictate the mechanical properties, were in need of closer scrutiny before the alloy characteristics could be rationalized. Noble et al.[53] used TEM and resistivity measurements to determine the non-equilibrium solvus temperature for 2 and 4 wt% Li alloys, which is plotted in Fig 2.11 together with data from Williams et al.[54] and Nozato et al.[55].

Noble et al.[58] investigated the yield characteristics of binary Al-Li alloys and considerable increases in strength were obtained via the precipitation of δ'. However δ' was found to be sheared by dislocation pairs resulting in heterogeneous planar slip and consequently brittle grain boundary failure.

Small amounts of Zr are added to commercial Al-Li alloys as an essential alloying element for the control of grain structure during thermomechanical processing. The influence of particles precipitated in a binary Al-Zr alloy was studied by Ryum[59] and Rystad et al.[60] They used TEM to confirm the following decomposition mode from supersaturated Al-Zr solid solution.

$$\alpha\text{-}Al \rightarrow \text{cubic rods/spheres } Al_3Zr \rightarrow \text{tetragonal } Al_3Zr \qquad 2.13$$

Electron diffraction patterns from the metastable Al_3Zr (β') rods and spheres showed that the latter were ordered, coherent dispersoids iso-structural with Al_3Li (i.e. Ll_2) and caused a +1% misfit with the matrix. After longer annealing times the equilibrium precipitate formed whose electron diffraction pattern was indexed according to the tetragonal Al_3Zr given by Fink et al.[61] with a DO_{23} space lattice where a=0.401nm and c=1.73nm[62]. The metastable precipitates had only a moderate effect on hardness but raised the recrystallisation temperature quite considerably after cold working. The precipitates were observed to pin on low and high angle grain boundaries of the deformed structure.

Zr also has a pronounced effect on the size, distribution and coarsening kinetics of δ'. Novel microstructures were reported by Gayle et al.[63] and Gregson et al.[64] where a fine distribution of Al_3Zr dispersoids served as preferred nucleation/growth

sites for δ′. These 'composite' precipitates can co-exist with the fine homogeneous δ′ creating a bi-modal δ′ precipitate distribution[65].

The age hardening of Al-Li alloys was found by Silcock[57] to be much improved when Cu was added to make a ternary alloy. It was shown that Cu decreases the maximum solid solubility of Li in Al at all temperatures and the Al rich phase diagram sections attributed to Hardy et al.[66] are shown in Fig 2.12. The equilibrium structures obtained at 350°C were dependent on the Cu:Li ratio and the phases were identified by X-ray diffraction as θ(Al_2Cu), δ(AlLi), T_B, T_1 and T_2 where

T_B = Al_7Cu_4Li, cubic CaF_2 structure (a=0.583nm)

T_1 = Al_2CuLi, hcp (a=0.497nm and c=0.934nm)

T_2 = Al_6CuLi_3, structure was not determined.

The ternary alloys were aged at 165°C and the observed precipitates were superimposed on the 350°C phase section. For the concentrations of interest, i.e. up to 2.5 wt% Li and 5 wt% Cu, precipitation of θ″, θ′, θ, T_1 and δ′ occurred[57] as illustrated in Fig 2.13.

Hardy et al.[66] determined that T_1 formed thin hexagonal platelets on $\{111\}_{Al}$ planes with an orientation relationship with the matrix of

$$(0001)T_1 \parallel (111)_{Al} \qquad [10\bar{1}0] \parallel [\bar{1}10]_{Al} \qquad 2.14$$

and an ideal crystal structure of P6/mmm has been proposed by Huang et al.[67]

Cassada et al.[68][69] studied T_1 precipitation in an Al-Li-Cu-Zr alloy and have shown that T_1 phase nucleates and grows by the dissociation of matrix dislocations into Shockley Partials (1/6 <112>) and nucleation is favoured at jogs and kinks. Thus a pre-age stretch, which increases the number of dislocations, was observed to increase nucleation sites for T_1. The resulting aged microstructures showed increased volume fractions of precipitates with increased number densities, since the T_1 plates became thinner and shorter. The peak yield stress was found to be a maximum for samples which had been aged for ~ 4 hours at 190°C with (a) a 6% stretch and (b) a pre-age

followed by a 6% stretch. T_1 has been shown to grow at the expense of δ' and θ' by Tosten et al.[70] as δ' precipitate free zones (PFZ) were observed adjacent to the T_1 plates.

The equilibrium phase T_2 with a stoichiometry of Al_6CuLi_3 determined by Hardy et al.[66] has been investigated by several workers[71][72][73]. Ball et al.[74] first reported the existence of particles exhibiting icosahedral, five-fold symmetry in an Al-Li-Cu-Mg alloy. Marcus et al.[72] re-examined the X-ray diffraction data from Hardy et al.[66] and showed that their T_2 phase could be indexed to an icosahedral structure with a lattice parameter of 0.52nm. Bartges et al.[73] used high purity Al-Li-Cu alloys to demonstrate that the T_2 phase displays icosahedral symmetry which can be attributed to quasi-crystallinity, a solid matter which is neither amorphous nor crystalline. Quasi-crystallinity has been reviewed by Levine et al.[75] and Socolar[76].

Investigations into rapidly solidified Al-Cu-Li-Mg-Zr alloys by Crookes et al.[77] and Kim et al.[78] have revealed electron diffraction patterns from intermetallic Al-Cu-Li phases which display five fold symmetry.

Apart from the precipitation of δ' and T_1 in Al-Li-Cu alloys, additional strengthening can be obtained by alloying with Mg to form the quaternary Al-Li-Cu-Mg alloy. Matrix precipitation of S′ (Al_2CuMg) occurs and this phase was shown by Perlitz et al.[79] to have an orthorhombic crystal structure (a=0.400nm, b=0.923nm and c=0.714nm). Silcock[80] monitored the decomposition of Al-Cu-Mg alloys using X-ray diffraction to show that

$$\alpha - Al \rightarrow GPB\ zones \rightarrow S' \rightarrow S \qquad 2.15$$

The distinction between the metastable S′ and equilibrium S phases was thought to be 'slight and somewhat arbitrary', but the individual morphologies have recently been identified by Yan[81].

Silcock[80] showed that considerable matrix hardening was effected by the GPB zones, and the formation of S′ caused additional hardening in the presence of GPB zones. X-ray diffraction determined that the S phase (or equivalently, S′ phase) has an orientation relationship with the matrix as follows[80]

$$[100]_S \parallel [100]_\alpha \qquad [010]_S \parallel [0\bar{2}1]_\alpha \qquad [001]_S \parallel [012]_\alpha \qquad 2.16$$

The morphology of the S′ precipitation has been studied by Wilson et al.[82] using TEM. Small, partially coherent, rod shaped precipitates formed during the ageing of a ternary Al-2.5wt.% Cu-1.2wt.% Mg alloy at 190°C. These formed on dislocation loops and helices, grew in $<100>_{Al}$ directions and widened to form laths on $\{120\}_{Al}$ planes. Thus, a pre-age stretch performed by Gregson et al.[83] on an Al-Li-Cu-Mg-Zr increased the number of nucleation sites and hence caused widespread S′ phase precipitation. It was shown that copious precipitation of S′ phase reduced the slip coplanarity of Al-Li alloys as substantial amounts of ductile tearing were observed on fractured samples after a pre-age stretch. In comparison, enhanced T_1 precipitation in an Al-Li-Cu alloy was not observed to inhibit coplanar slip[83].

2.2.3 Thermal Analysis of Precipitation in Al-Li Alloys

The age hardening and precipitation sequences outlined in the preceding section were determined by isothermal transformations. Clearly, the precise temperature at which the transformation occurs is difficult to determine in this way, and an alternative possibly more accurate method is to measure the enthalpy of the material during continuous heating or cooling.

Thermal analysis of the pertinent precipitation reactions has been carried out in binary Al-Li alloys[55][84][85], ternary Al-Cu-Mg alloys[86][87] and quaternary Al-Li-Cu-Mg alloys[88][89][90][91][92][93][94]. Trowsdale has studied the precipitation in binary Al-Li and ternary Al-Li-Mg alloys containing Zr[95].

Specific heat measurements made by Nozato et al.[55] indicate that precipitation in the Al-Li alloys is a five stage process as follows:

$$\alpha\text{-}Al \rightarrow GP1 \rightarrow GP2 \rightarrow \delta'' \rightarrow \delta' \rightarrow \delta \qquad 2.17$$

for ageing at temperatures below about 90°C.

The existence of a phase which is metastable with respect to δ′ has also been demonstrated by Papazian et al.[84]. It was not present immediately after quenching but formed during room temperature ageing. A Cluster Variation Model was developed by the authors and used to calculate the stable and metastable phase boundaries, which showed good agreement with experiment for the δ′ solvus. The model also predicted a metastable miscibility gap below ≈130°C inside the α-δ′ two phase field. Thus, the explanation of a low temperature endotherm is favoured in terms of a metastable GP zone dissolution reaction, rather than the reversion of fine δ′ precipitates as proposed by Balmuth[85].

The ternary Al-Cu-Mg alloys investigated by Howe[86] and Jena et al.[87] decomposed according to Silcock[80] though there is no distinction made between S′ and S phases. Jena et al.[87] monitored the influence of heating rate on the reaction kinetics. It is suggested that GPB zones form by quenched-in vacancy aided diffusion of solutes whereas S′ phase grows by diffusion controlled radial growth.

From the work on the quaternary alloys, Gregson et al.[90] and Mukhopadhyay[88] showed that the inclusion of Li slowed down the precipitation of S′ phase during ageing.

The equilibrium phase T_2 has been recorded using thermal analysis by deMacedo et al.[91] and Gomiero et al.[92] in 2091 alloys.

The interpretation of heat flow in 8090 has been difficult due to the overlapping temperatures of precipitation reactions[88] but more recently Luo et al.[94] have presented thermograms for 8090 in the as-quenched and T4 heat treatment conditions which are described in terms of heat flow for GPB zone, δ′, S′ and δ phase

precipitation and dissolution reactions, Fig 2.14[94].

2.4 The Weldability of Al-Li Based Alloys

The weldability of Al-Li alloys has been reviewed by Pickens[3][4] and an in-depth review will not be presented here. Instead, a few of the more relevant works will be introduced with reference to gas tungsten arc (GTA), electron beam (EB) and laser welds in 8090, 2090 and 2091 alloys.

Firstly, though, with reference to Al-Li alloys, Cross et al.[96] found that high purity Al-Li binary alloys were readily weldable using autogenous GTA techniques, with no loss of Li occurring. The depth of penetration increased with heat input and Li concentration, probably because of the decrease in thermal conductivity associated with the addition of Li. The weld solidification microstructure was cellular or cellular-dendritic. When the Li content was low, cellular dendrites grew perpendicular to the welding direction with well defined grain boundaries. At high Li concentrations, however, the grains grew parallel to the welding direction. This again is probably due to a change in weld pool geometry associated with the thermal conductivity. Some of the individual cells contained a eutectic constituent at the centre which was observed optically but not analyzed in detail. The alloy with 2.6 wt% Li was found to be most susceptible to hot cracking.

2.4.1 Welds in 8090

GTA welds made in 8090 by Edwards et al.[6] and Ravindra et al.[97] showed that the microstructures which formed when 8090 was used as a filler consisted of large equiaxed grains with unidentified precipitation within the grains[6]. The grains at the weld fusion boundary were small in comparison to the weld centre and were more equiaxed[97]. Porosity was present but was reduced if a surface layer was removed prior to welding[6] and hot cracking could be avoided if the thermal gradients were not too severe.

The joint efficiency, defined as the weld strength divided by the base metal strength, was improved if a post-weld heat treatment was applied. After a T6 thermal treatment

the grain boundary ductility and strength were enhanced[6][97]. During tensile testing, failure occurred in a brittle inter-granular manner even after solutionizing and ageing[6] or with dimple features and extensive multiple cracking[97].

EB welds were also made by Edwards et al.[6]. These displayed similar features to the GTA weld but with much finer grains. Close to the fusion line there was an area of still finer grains in which recrystallisation and grain growth occurred during solution treatment and ageing. Welds failed in a brittle inter-granular manner in the fine grained region, even after heat treatment, but more grain boundary ductility was observed in the heat treated condition. A study into the mechanical properties of EB welds in 8090 by Le Poac et al.[98] revealed that post-weld ageing alone increased weld metal hardness but reduced tensile strength.

Laser welding has been attempted by Gittos[11], Biermann et al.[12] and Gnanamuthu et al.[13] using a CO_2 laser with He[11][13] or He:Ar[12] shielding gases. Successful welds were made on 2mm thick sheet[11] but when 4mm thick sheet was used welds were mostly porous with rounded pores near the centre-line. The amount of porosity increased with penetration but was not affected by surface preparation. This is contrary to the work by Gnanamuthu et al.[13] who showed that a six fold reduction in porosity in 2.7mm thick sheet was effected by a chemical milling procedure which removed $\approx$150μm from both sides of the sheet. Biermann et al.[12] showed that in butt welds strings of porosity formed at both sides of the weld bead. Erjing et al.[99] eliminated porosity in GTA welds by chemical milling prior to welding. After a full heat treatment of solutionizing and ageing the weld achieved 75%[11], 80%[12] and $\geq$90%[13][99] of the parent metal strength.

The microstructure was one of fine dendrites[11] which were cellular at the weld edge and equiaxed at the weld centre[13]. A eutectic phase was distributed non-uniformly along the interdendritic regions and also trapped within the dendrites[13]. After solution treatment the weld consisted of large columnar grains originating near the weld/substrate interface which were oriented nearly perpendicular to the interface. The prior cast structure could be seen within these large grains and was similar to those

reported by Edwards et al.[6]. Coarse and fine equiaxed grains were observed around the weld zone[13].

The HAZ width was dependent on the heat input[13] and was typically ≈165μm[13] and 200-300μm[12] identified by a region in the base metal which had undergone liquation[11].

Gittos[11] did not identify hot cracking as being a problem during welding.

Biermann et al.[12] used plasma spectroscopy to analyze the composition of the plasma during welding. They found that the relative intensity of the peaks in the spectrum varied with the composition of the base metal and consisted, in proportion, of Mg,Li,Al and Cu.

2.4.2 Welds in 2090, 2091

The welding efficiency (weld strength compared to base metal strength) of 2090 has been shown by several workers to be improved by the application of post-weld heat treatments[9][14][100][101], and Sunwoo et al.[101] have shown that both GTA and EB weld fusion zones lack the strength and ductility of the base metal because of a low volume fraction and inhomogeneous distribution of strengthening precipitates. In the peak aged condition the joint efficiencies were ≈75% and 50% for EB and GTA welding respectively. In another study by Lin[9] joint efficiencies of ≈100% were recorded after solution treating and ageing CO_2 laser welds.

The composition of the weld relative to the base metal has been measured by atomic absorption spectroscopy[22][100] and is essentially unchanged, even though in most cases full parent metal strength cannot be achieved after post-weld heat treatments.

The morphologies of the microstructures in GTA[8][100][101], EB[14][100][101] and laser[9][10][22][102][103] weldments have been described. Sunwoo et al.[100][101] have shown for both GTA and EB weldments that dendrites grow epitaxially from grains in the base metal. In the EB weld dendrites were equiaxed with little solute

segregation but in the GTA weld pronounced solute segregation existed within a cellular-dendritic structure.

Fine equiaxed grains (2-4μm) were observed at the fusion boundary in GTA welds[8] and laser welds[9][10][22][102][103] and cellular-dendrites grow out of these and into the weld. In the GTA welds[8] a transition from fine equiaxed grains, through cellular dendrites, columnar-dendrites, quasi-equiaxed dendrites to equiaxed dendrites was seen to take place as the weld centre was approached from the fusion line. Yunjia et al.[8] has proposed that a dispersion of unmelted tiny $ZrAl_3$ and $TiAl_3$ from the partially melted base metal at the fusion line may exist and cause heterogeneous nucleation of fine equiaxed grains rather than epitaxial growth during the initial freezing of the weld pool.

Porosity has been quantified in EB[14] and laser[10][102][103] welds as 2-5% and 2.3% of the weld bead area at the centre-line. This was unaffected by mechanical cleaning of the surface prior to welding[14]. Molian et al.[10][102][103] on the other hand showed that porosity could be reduced by mechanical surface cleaning prior to welding, but this could be interpreted in terms of the influence of weld bead shape on porosity.

Investigations by Yunjia et al.[8] and Zacharia et al.[14] have shown that 2090 is susceptible to fusion zone cracking.

2.5 Rapid Solidification/Powder Metallurgy Alloys

2.5.1 Introduction to Rapid Solidification

Lavernia et al.[104] have reviewed the current status with regard to the recent developments and applications of rapidly solidified aluminium alloys.

The most widely used approach used to achieve rapid solidification is to impose a high rate of heat extraction during solidification, which effects a rapid cooling rate. This effectively removes the total enthalpy released before, during and after solidification. Thus the alloy is exposed to extreme non-equilibrium conditions which result in microstructural modifications such as

(a) constitutional changes, especially extension of solid solubility

(b) size refinements, especially grain size and solidification structure

(c) metastable phase formation.

The nucleation of the solid during processing takes place via heterogeneous mechanisms, and the subsequent growth and morphology of the microstructure is determined primarily by the growth rate of the solid (R) and the thermal gradient across the liquid phase (G).

The progression from a planar to a dendritic microstructure with increasing growth rate has been discussed in a previous section during normal modes of solidification (2.2.1). However, during rapid solidification, where faster rates of growth are attainable, the morphology continues to develop, becoming microcellular and finally planar. Thus plane front solidification becomes increasingly stable with increasing interface velocity, and the melt can solidify devoid of features as the solute remains trapped in an 'extended solid solubility'.

The refinement of grain size and solidification structure is closely linked to the velocity of the interface during solidification[48][104][105]. The classical theory of constitutional supercooling was introduced in section 2.2.1 and was used to show that an unstable solid/liquid interface can develop at a critical value of G/R where G is the temperature gradient and R the growth rate. As shown in Fig. 2.9 planar, cellular and dendritic interfaces can develop with variations in G and R. Thus, as G.R increases t_f must decrease resulting in fine scale microstructures illustrated by the arrow in Fig. 2.9 since secondary dendrite arm spacings are proportional to $(t_f)^{1/3}$. The cooling rates in rapid solidification processing are usually high enough to prevent the formation of equilibrium phases and extend solid solubility, but complete solid solubility is difficult to achieve. Thus metastable, non-equilibrium phases can form whose free energies are higher than those of the equilibrium phases[104][105][106].

2.5.2 Solidification of Al-Fe Alloys

The RS/PM alloy 8009 has a nominal composition of Al-8.5wt.% Fe-1.7wt.% Si-

1.3wt.% V and it is with reference to this alloy that the equilibrium and non-equilibrium freezing of Al-Fe alloys will be introduced.

The binary Al-Fe equilibrium phase diagram[52] is illustrated in Fig. 2.15 which shows a maximum solid solubility of Fe in Al of ≈0.04 wt.% at 655°C, the eutectic temperature. The structure of the Al-Al_3Fe eutectic consists of plates of Al_3Fe in an aluminium matrix[107]. The plates are highly branched with low G/R and relatively straight and parallel at higher G/R. At higher G/R conditions it was shown[108] that the plates grew with an orientation relationship with the matrix and growth direction as follows:

$$[010]_{Al_3Fe} \parallel [100]_{Al} \parallel \text{growth direction} \qquad 2.18$$

2.5.3 Metastable Al-Fe Phases

Hollingsworth et al.[109] found that deviations from the Al_3Fe eutectic in a Al-2wt.% Fe alloy could be obtained by a rapid chilling technique. The new intermetallic constituent was determined to be Al_6Fe and suggested to be orthorhombic with lattice parameters a=0.6492, b=0.7437nm and c=0.8788nm. The phase was metastable and converted to Al_3Fe during annealing up to ≈649°C. Hughes et al.[110] showed that the coupled eutectic Al-Al_6Fe with 2.6 to 5.3 wt.% Fe was selected in preference to Al-Al_3Fe eutectic for growth velocities of ≈5mm/s.

The transformation during solidification of hypoeutectic alloys from stable Al_3Fe to metastable Al_6Fe has been demonstrated by Young et al.[111] to take place via an intermediate constituent. The equilibrium lamellar eutectic between Al and Al_3Fe transformed to the fibrous, metastable Al-Al_6Fe structure via an intermediate Al_xFe phase which had an approximate stoichiometry of Al_5Fe.

As the cooling rate is increased further the metastable phases Al_mFe[112][113] (where m is between 4.0 and 4.4) and Al_9Fe_2[114] can form, Fig. 2.16[111]. Al_mFe is body centred tetragonal with a=0.884nm and c=2.16nm[112] and the electron diffraction characteristics have been given by Skjerpe[113]. Al_9Fe_2 is monoclinic with a=0.869nm,

b=0.635nm, c=0.632nm and ß=93.4°.

2.5.4 Microstructure of the Al alloy 8009

The Al alloy 8009 has a nominal composition of Al-8.5wt.% Fe-1.7wt.% Si-1.3wt.% V and is rapidly solidified into ribbons by melt spinning[115][116]. The ribbons are comminuted into powder, vacuum hot pressed into billets and extruded to achieve full densification.

The extruded microstructure consists of a homogeneous distribution of very fine, spherical (or polygonal) dispersoids which are 0.05μm in diameter within a 0.5μm size α-Al grain structure[115][116]. They have a nominal composition of $Al_{12}(Fe,V)_3Si$ and are body centred cubic with a=1.256nm[115][116][117]. This is close to 3 times the aluminium lattice parameter (a=0.40496nm) so a low interfacial energy provides little driving force for dispersoid coarsening[118], coupled with the fact that Fe and V have low diffusivities in Al[119] such as 1.12×10^{-15} cm²/s and 3.94×10^{-15} cm²/s at 427°C respectively, compared to Li for example where $D \approx 6.67 \times 10^{-15}$ cm²/s at 190°C[56].

Thus the dispersion strengthened alloys have enhanced high temperature properties over conventional precipitation strengthened alloys, illustrated by the graph in Fig. 2.17 from Lee et al.[120]

2.5.5 Welding of RS/PM Alloys

Baeslack[121] and Krishnaswamy et al.[122] have welded RS/PM Al-8wt.% Fe based alloys using high power density techniques which can be optimized to simultaneously produce steep temperature gradients, high solidification velocities and rapid fusion zone cooling rates.

In a study on RS/PM Al-8 wt.% Fe-1.7 wt.% Ni, Baeslack[121] used an electron beam to produce autogenous bead-on-plate welds. Using light, SEM and TEM microscopy techniques he was able to determine a range of solidification structures throughout the

fusion zone. At the base of the fusion zone columnar grains grew epitaxially from a partially melted region with a fine, coupled eutectic substructure. As the centre of the fusion zone was approached, equiaxed α-Al grains nucleated on primary intermetallics and coupled eutectic growth ended solidification.

Microhardness testing suggested that the regions in which the structure was fine coupled eutectic the highest strength would be afforded.

In a similar study on RS/PM Al-8wt.% Fe-2wt.% Mo, Krishnaswamy et al.[122] used a Nd:YAG laser to produce autogenous pulsed welds. Light microscopy revealed 'light' and 'dark' etching regions within the fusion zone which were characterized using SEM and TEM techniques. Equiaxed, spherical and irregular particle morphologies were observed with a size variation depending on the local thermal conditions. The 'light' etching regions contained fine spherical particles in a fine dendritic α-Al matrix, whereas the 'dark' etching regions consisted of irregular particles in a coarse α-Al matrix.

The microstructural analysis was confirmed by microhardness measurements which showed that the hardness of the 'light' etching regions always far exceeded that of the 'dark' etching regions.

2.6 Microstructure of Alloy 6061

Alloy 6061 is a commercial wrought aluminium alloy which has Mg and Si as its principle alloying elements with a nominal composition shown in table 3.2. A ratio of Mg:Si of 1.73 is adopted since the compound Mg_2Si is in equilibrium with Al under these conditions, and the solid solubility of Mg_2Si in Al is reduced for excesses of Mg and Si[52], as shown in the liquidus projection in Fig. 2.18.

Equilibrium Mg_2Si is cubic with a lattice parameter a = 0.635 - 0.640 nm. It precipitates from the solid solution as plates with the following orientation relationship[52]

$$(100)_{Mg_2Si} \parallel (100)_{Al} \; ; \; [011]_{Mg_2Si} \parallel [001]_{Al} \qquad 2.19$$

During precipitation hardening of the Al-Mg_2Si system a sequence of metastable phases have been observed and the general decomposition from the supersaturated solid solution is

$$\alpha - Al \rightarrow GP\,zones \rightarrow \beta'' \rightarrow \beta' \rightarrow \beta \qquad 2.20$$

and peak hardness is reached just before the platelets of equilibrium β (Mg_2Si) form.

2.6.1 Laser Welding of 6061

Sonti[123] has studied the influence of process parameters on the characteristics of laser welds in annealed 2219, 5XXX and T6 6061 using a 15 kW CO_2 laser. The weld penetration and top bead width were both observed to increase with increasing laser beam power and decreasing welding speed. All surfaces were mechanically cleaned prior to welding and only the high Mg containing 5XXX alloys contained serious porosity. The 2219 and 6061 alloys contained non-spherical shrinkage cavities in the middle of the weld which measured up to 0.3 - 0.4 cm across. Subsequent EPMA on as-welded material confirmed that some 5XXX alloys could loose ~ 25 % of the total Mg concentration of the base metal during welding.

Microstructural analysis of the base metal, HAZ and fusion zone was carried out. For alloy 6061, the base metal contained fine grey particles of the intermetallic $(Fe,Mn,Cr)_3SiAl_{12}$ as well as dark particles of Mg_2Si distributed throughout a matrix of elongated α-Al grains. The HAZ was identified by the Mg_2Si distribution. In the overaged region Mg_2Si had coarsened but towards the fusion boundary liquation of the Al-Mg_2Si eutectic had occurred at grain boundaries. The weld fusion zone consisted of a network of the Al-Si eutectic with an α-Al columnar-dendritic structure existing at the edge of the weld pool. Further towards the weld centre the α-Al was equiaxed-dendritic and the primary dendrite arm spacing progressively decreased from the edge of the weld to the weld centre.

Cieslak et al.[124] have monitored the influence of pulsed and continuous Nd:YAG

laser welding on T6 6061 and two 5XXX series alloys. Pulsed welding resulted in the formation of cracks which radiated parallel to the grain growth direction. Subsequent EPMA on the continuously welded material showed that Mg loss was dependent on the welding speed, as illustrated in the graph of Fig. 2.19 for 6061. The 6061 welds were given a post-weld solution treatment and age. Hardness measurements showed that when Mg loss had been high (~ 50%) the hardness of the fusion zone was reduced, whereas when Mg loss was low (~ 3%) there was no apparent difference between the base metal and fusion zone hardness.

Table 2.1. First ionization potential of some common gases taken from Banas[34].

Material	First ionization potential, eV
Argon	15.68
Helium	24.46
Oxygen (O_2)	12.50
Neon	15.54
Carbon Dioxide	14.41
Water Vapour	12.56

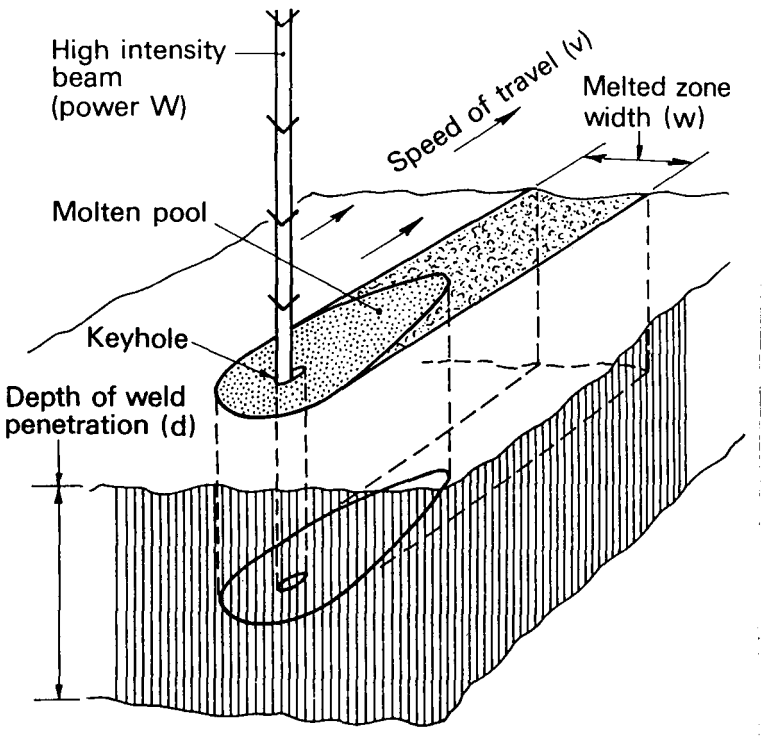

Figure 2.1. Schematic diagram of the keyhole welding process for beam power, W, welding speed, v, weld bead width, w and depth of penetration, d. The welding direction is that of the workpiece relative to the laser[31].

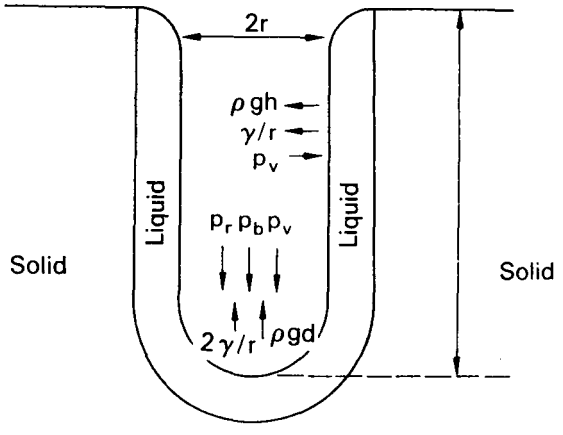

Figure 2.2. Schematic diagram of the forces which exist within the keyhole of radius r. γ is the surface tension, p_v is the vapour pressure, p_r is the beam recoil pressure and p_b is the beam pressure. The hydrostatic force is represented by $h\rho g$[31].

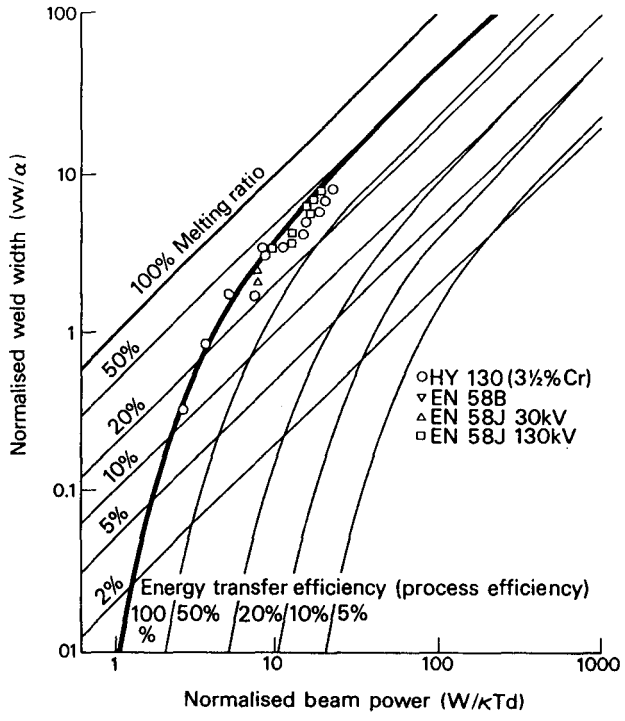

Figure 2.3. Graph of normalised beam power, X, vs. normalised weld width, Y, for electron beam welding. The influence of weld parameters on the melting ratio and process efficiency is illustrated[31].

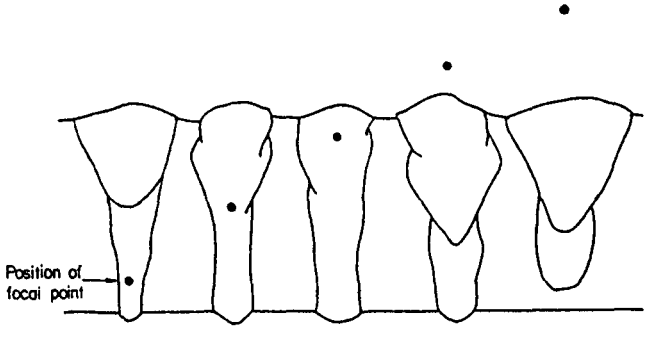

Figure 2.4. Schematic diagram of the influence of focal position on weld bead shape for CO_2 laser welding of stainless steels. Power = 5 kW and speed = 16 mm/s. For welds made in 6 mm thick sheet, the optimum focus was ~ 1 mm below the surface[16].

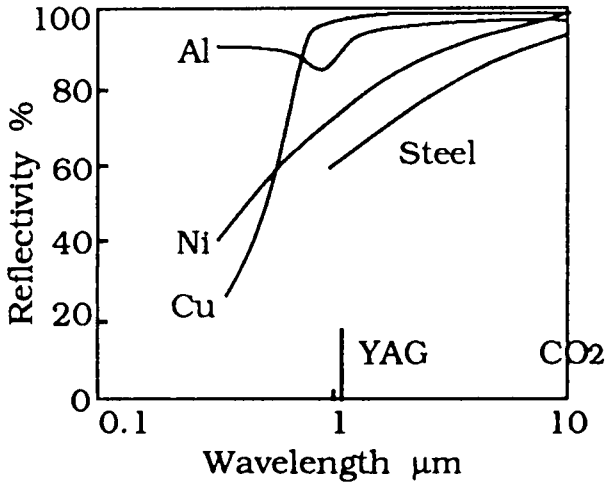

Figure 2.5. Graph illustrating the influence of wavelength on the reflectivity of Al, Ni and Cu. Notice Al is most absorptive at approximately the Nd:YAG wavelength[15].

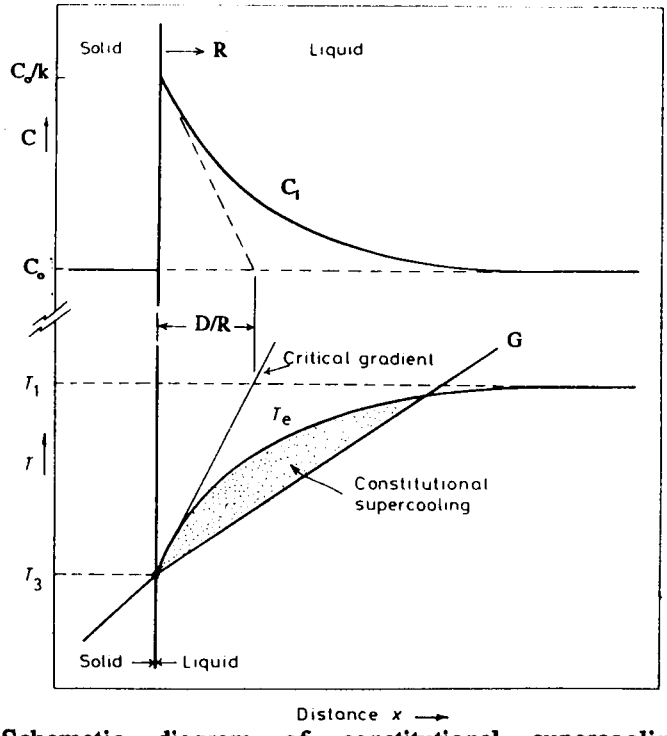

Figure 2.6. Schematic diagram of constitutional supercooling showing solute distribution in the liquid ahead of the interface with the liquidus temperature and temperature gradient below[43].

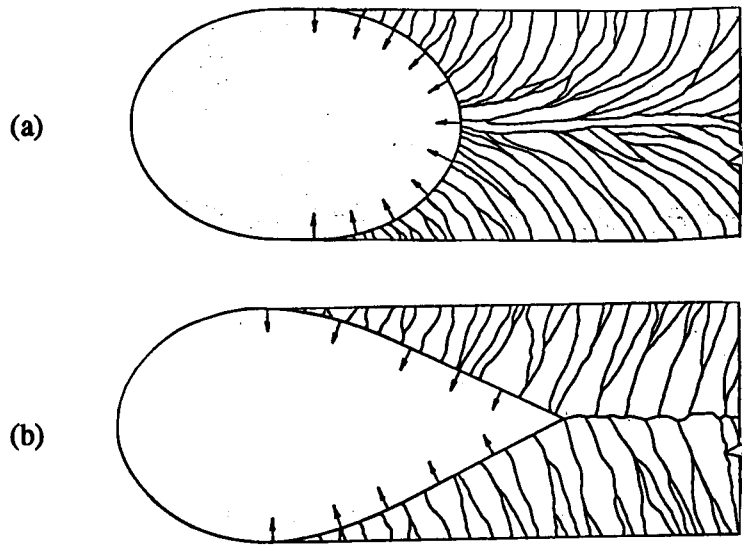

Figure 2.7. Schematic diagram illustrating the influence of welding speed on weld pool shape and grain growth. At low welding speeds in (a) the pool is elliptical whereas at higher welding speeds in (b) the pool becomes tear-drop in shape[46].

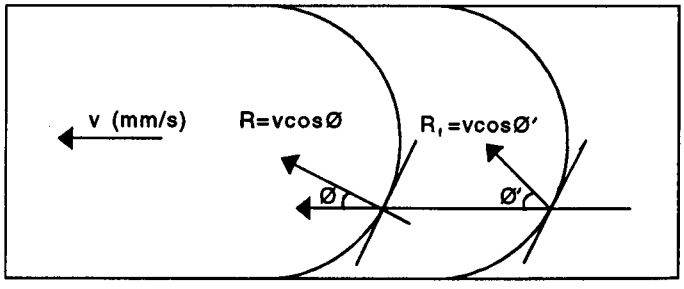

Figure 2.8. Relationship between welding speed, v, and growth rate, R_f, for grains growing in most favourably oriented <100> directions nearest to the maximum thermal gradient[47].

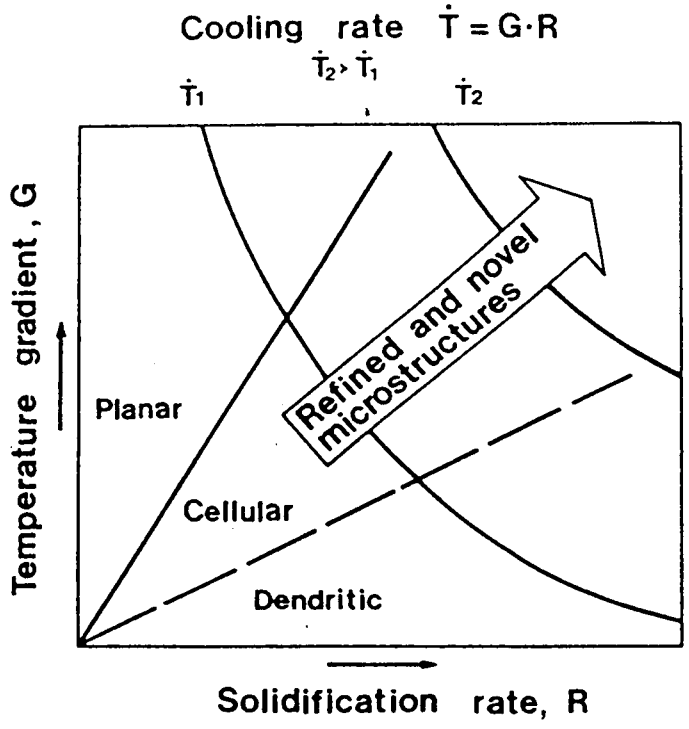

Figure 2.9. A plot of temperature gradient, G, vs. growth rate, R, illustrating planar, cellular and dendritic growth regimes[104].

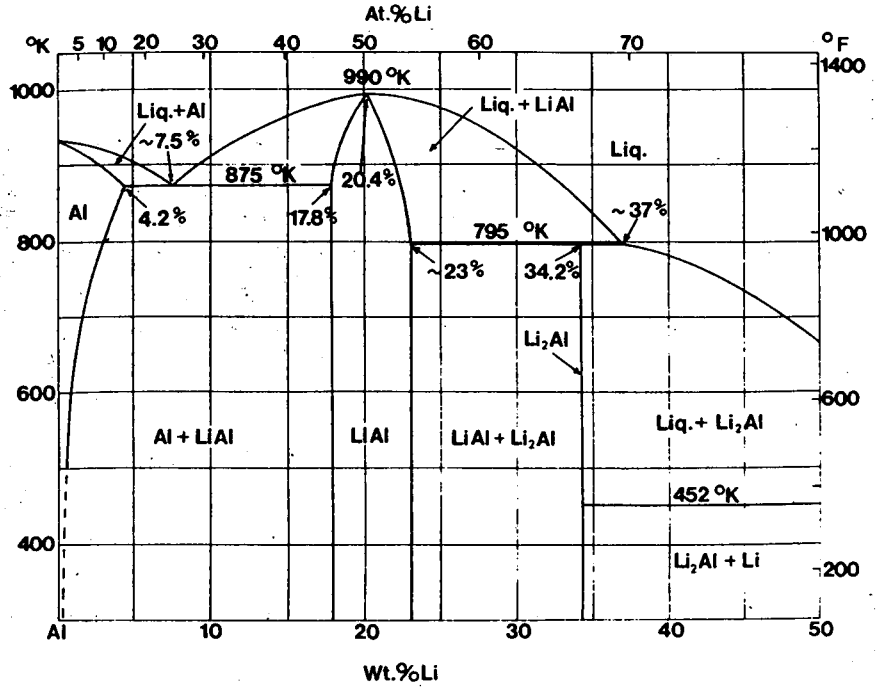

Figure 2.10. The aluminium end of the Al-Li binary equilibrium diagram[52].

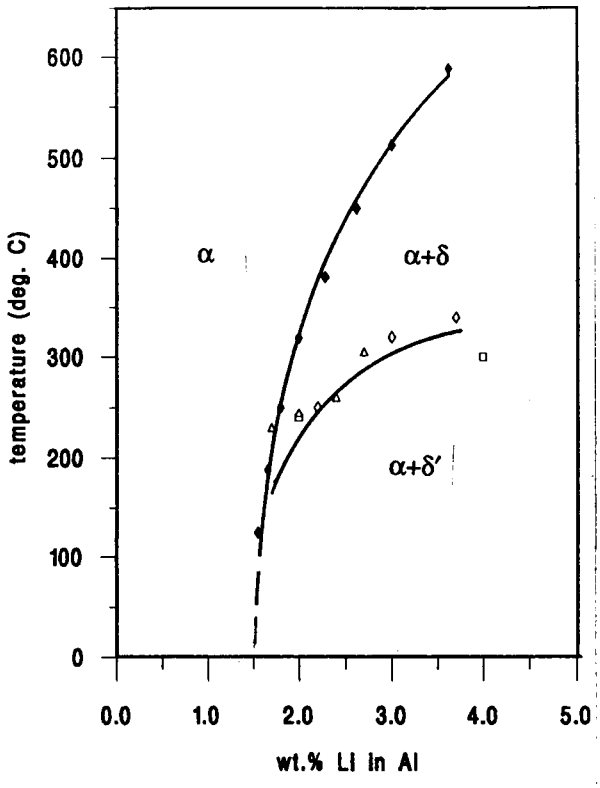

Figure 2.11. The phase diagram for dilute Al-Li alloys showing the non-equilibrium δ′ solvus as predicted by Noble et al.[53], Williams et al.[54] and Nozato et al.[55].

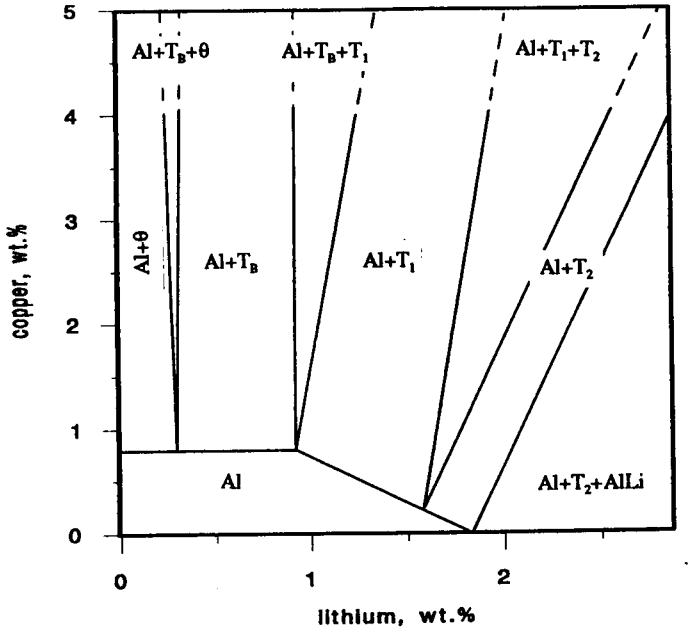

Figure 2.12. Corner of the phase diagram for Al-Cu-Li alloys heat treated at 350°C[66].

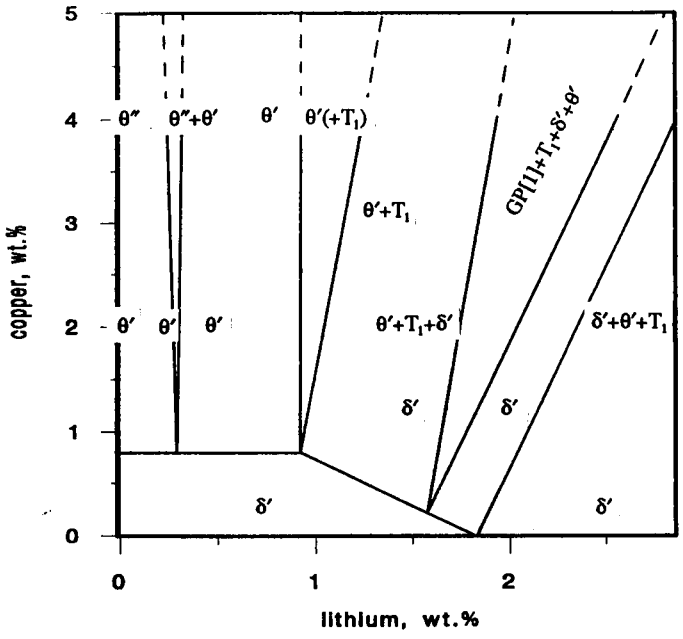

Figure 2.13. Diagram showing the precipitates formed in Al-Cu-Li alloys during ageing at 165°C[57].

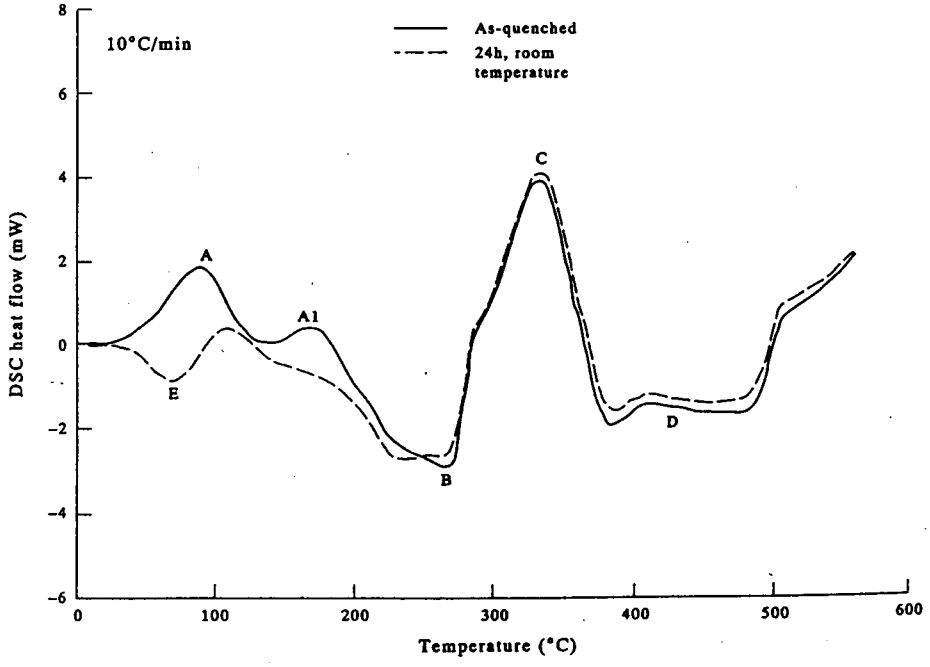

Figure 2.14. DSC thermograms for the as quenched and room temperature aged 8090 alloy[94].

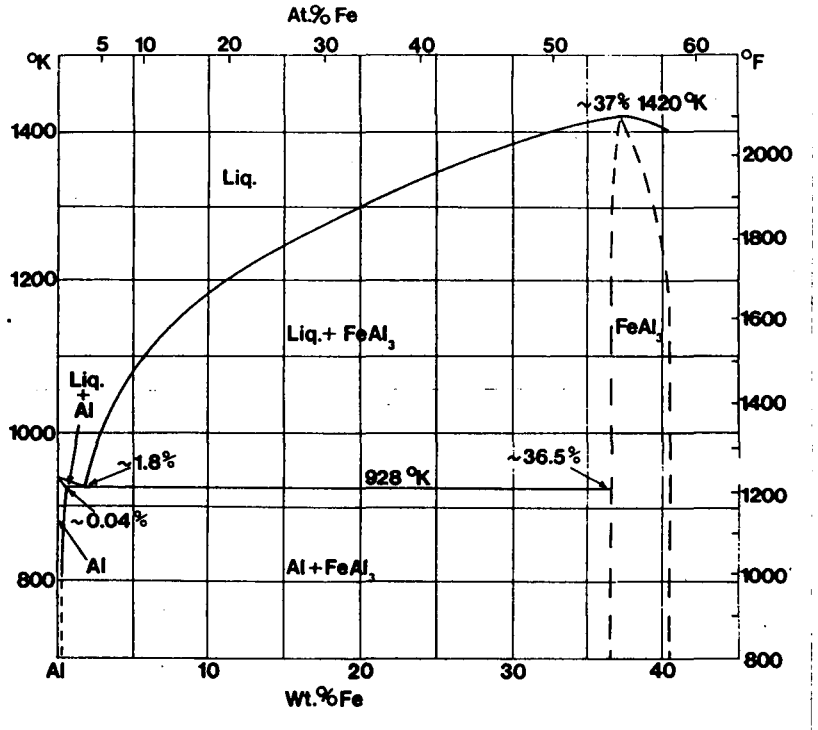

Figure 2.15. The aluminium end of the Al-Fe equilibrium diagram[52].

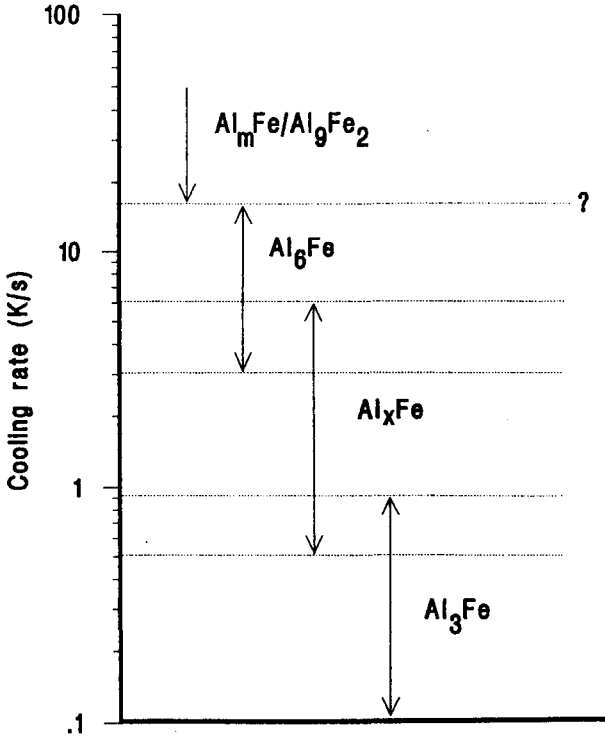

Figure 2.16. Approximate cooling rate regimes for the formation of different intermetallic precipitates in hypoeutectic Al-Fe alloys[111].

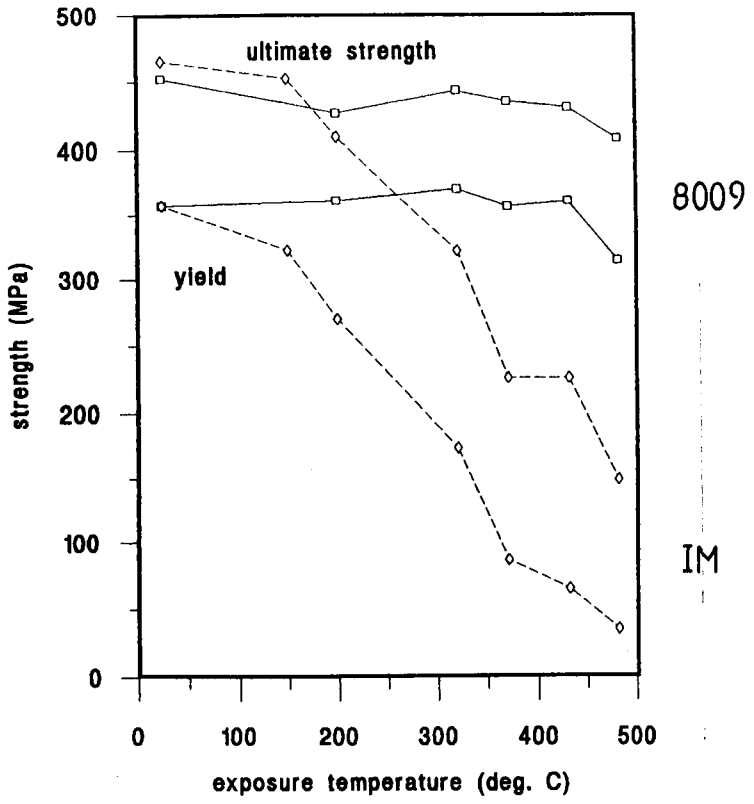

Figure 2.17. Plot of room temperature strength vs. exposure temperature for 8009 and a conventional IM Al-Cu (2219) alloy[120].

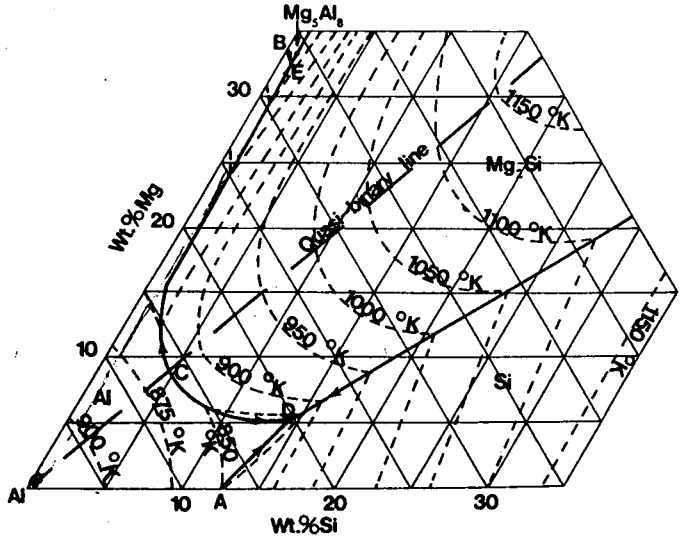

Figure 2.18. The liquidus projection of the Al-Mg_2Si phase equilibria illustrating the quasi-binary line[52].

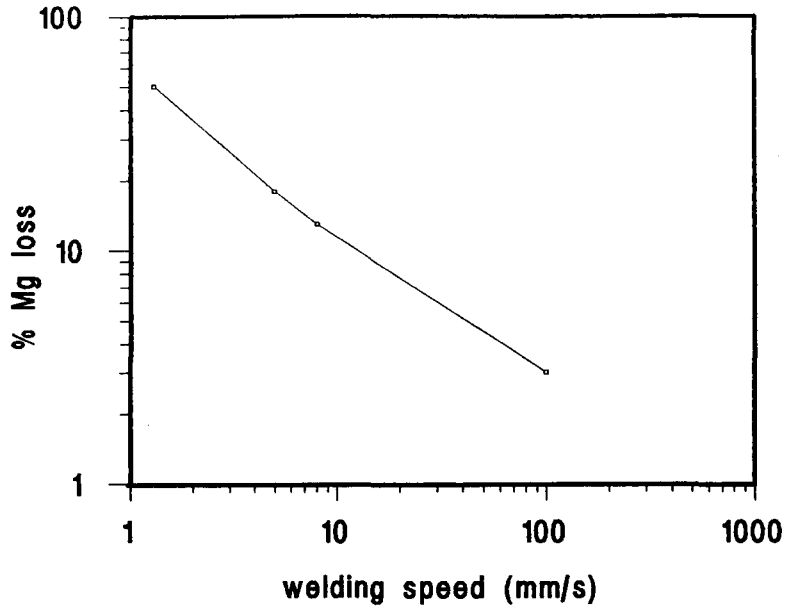

Figure 2.19. Plot of % Mg loss vs. welding speed for continuous Nd:YAG welding of 6061 at 675 W[124].

Chapter 3. Experimental Techniques

3.1 Laser Welding

3.1.1 Laser Equipment

Autogenous bead-on-plate laser welding was performed with either CO_2 or Nd:YAG lasers enabling a maximum nominal power delivery of 5kW. The most powerful laser was the 5kW Ferranti AF5 fast axial flow CO_2 laser, illustrated in Fig 3.1 (a). This has twenty discharge tubes and produces laser radiation at 10.6μm wavelength. The Electrox 1500W CO_2 laser is also a fast axial flow laser but has only four discharge tubes. Processing environments were created using a co-axial jet of helium, nitrogen or argon with a flow rate of 10 - 40 l/min. Both CO_2 lasers were operated with continuous wave output and the laser beam was focused using potassium chloride lenses with focal lengths between 75 and 125mm. The output beam was circular in cross section with an approximately Gaussian energy distribution.

Pulsed laser welding was carried out with the solid state Lumonics 1kW Nd:YAG laser, illustrated in Fig. 3.1 (b). This produces pulsed laser radiation with a wavelength of 1.06μm. The pulse shape was varied by introducing pre- and post-pulses and the total pulse length was ≈1.5ms with a typical pulse frequency between 80 and 100Hz. The shape of the output pulse was monitored on an oscilloscope. A processing environment was created in the chamber which could be evacuated and back filled with inert gas. The output beam was circular in cross-section with an approximately Gaussian energy distribution and was transmitted through glass optics with a nominal focal length of 160mm. The welding process was watched via a camera which was coaxial with the laser beam and coupled to a T.V. monitor.

3.1.2 Determination of Process Variables

The processing variables which were systematically varied were the focal point of the laser beam, the beam power and the substrate velocity. The following section explains how measurements were made, together with the technique used for the measurement of the beam diameter.

(i) *Focal Point of Laser Beam*

A reproducible focus position was obtained by moving the helium/argon shrouded target in a vertical direction until single bursts of laser power produced a brilliant blue plasma plume. Alternatively, a sloping target of known slope was traversed with a bead-on-plate weld. The position along the weld length at which the quality of the weld was visually superior was ascertained and the height of the target was calculated using similar triangles. This point was taken to be the zero focus position and adjustments could be made above or below this point.

(ii) *Laser Beam Power and Traverse Speed*

The actual laser beam power incident on the target was not determined, but the nominal power delivery was displayed on each laser. This figure is quoted as the beam power in each case. On the Nd:YAG laser this figure corresponds to the average power supplied during the pulse duration, not the peak power which was dependent on the pulse shape. Welding speeds were set via a computer numerically controlled (CNC) X-Y table which had rapid acceleration and deceleration rates.

(iii) *Laser Beam Diameter*

The Nd:YAG laser beam diameter was measured off burn prints made on ceramic targets. The beam was fired instantaneously at the required focal position and the diameter of the beam imprint was determined to be ~ 0.8mm. However, the diameter of the CO_2 laser beam was measured using a Laser Beam Analyser (LBA)[125] to be ~ 0.4mm.

Table 3.1 lists the ranges of variables used for each material and laser.

3.2 Materials and Preparation

The majority of the work in the present research involved the superplastically formable aluminium-lithium based alloy 8090 which has the nominal composition listed in table 3.2. The major alloying elements are Li-Cu-Mg-Zr. Sheets were supplied with thicknesses varying from 1 to 4mm and all had undergone a proprietary thermomechanical treatment to create an unrecrystallised, micron sized grain structure

suitable for superplastic forming. This is termed the SPF condition.

Other alloys which have been investigated are the aluminium alloys 8009 and 6061. Alloy 8009 is a rapidly solidified, powder metallurgy (RS/PM) Al-Fe-V-Si alloy which has a useful service temperature up to 400°C. It was supplied with a sheet thickness of 2mm, and had the nominal composition listed in Table 3.2. Alloy 6061 is a conventionally weldable, medium strength age hardening Al-Mg-Si alloy. It was supplied with sheet thicknesses of 1.6 and 3mm and was received in the solution treated and naturally aged (T4) heat treatment condition. The nominal compositions of 1.6 and 3mm sheet are also listed in table 3.2.

All sheets were degreased prior to welding and in some cases 8090 was chemically etched to remove surface oxide. The latter process was carried out by immersing the sheet in 30 vol% NaOH solution and rinsing in dilute HNO_3, followed by water and alcohol before hot air drying. Approximately 100μm was removed from both sides of the sheet.

3.3 Radiographic Examination

X-ray radiography of all welds was carried out by British Aerospace X-ray laboratories at Samlesbury, performed to standard GTA welding specification R05-0521. The minimum measurable pore size was ≈0.1mm diameter.

3.4 Microstructural and Chemical Characterisation

This section describes the techniques used for optical and electron microscopy and includes the quantitative assessment of grain sizes and weld porosity.

3.4.1 Optical Microscopy

Optical microscopy of welds was performed on planes perpendicular and parallel to the welding direction, and the three mutually perpendicular planes are defined in Fig. 3.2. Specimens were mechanically ground and polished via SiC papers to 1 or 0.25μm diamond paste and a final polish was obtained with Struers OP-s Colloidal

Silica on a soft cloth. All three alloys were etched with either Keller's reagent, or 10 vol% NaOH solution followed by rinsing in dilute HNO_3. After etching samples were rinsed in water and alcohol before drying. In addition, 8090 and 6061 were anodized in Barker's reagent (5ml HBF_4 in 200ml H_2O). The sample was made the anode in an electrolytic cell with a stainless steel cathode and a D.C. voltage of 20V was applied. The sample was immersed for ≈10 seconds and rinsed in water. This procedure was repeated several times until the grain structure was revealed under crossed-polars in the optical microscope.

3.4.2 Scanning Electron Microscopy (SEM)

Samples which were polished for SEM were gold coated to prevent sample charging. Fractured samples were mounted on an aluminium disc with sticky carbon pads. SEM was carried out using either a Philips EM501 fitted with a LINK EDX analysis system, or a JEOL 6400 fitted with a NORAN EDX analysis system and WINSEM computer software. Both microscopes were operated at 15 - 20kV.

Secondary electron intensity (SEI) images were used to observe polished, etched or fractured surfaces and EDX analysis was either performed on areas or spots. Quantitative analyses were obtained from the JEOL 6400 EDX software with ZAF correction.

3.4.3 Transmission Electron Microscopy (TEM)

Thin foils for TEM were taken from sections parallel to the rolling plane and close to the surface of the CO_2 / Nd:YAG, 8090 and 8009 weld/base metal. Where possible, ie in sheet ≥3mm thick, samples were taken from the longitudinal centre-line section of the deep penetration CO_2 weld. The foil preparation procedure is illustrated in Fig. 3.3. To prepare the foil, a section was hacksawed out of the bulk sample with a width ≥2mm and carefully ground on SiC papers from both sides to ≈500μm. Discs which were 3mm in diameter were punched, or more accurately, carefully diamond drilled from the bulk sample and further ground using a grinding block to a thickness of ≥100μm. Electron transparency was obtained through twin jet electropolishing with a Struers TENUPOL using a solution of 25 vol% HNO_3 and 75 vol% CH_3OH at a

temperature between -20 and -30°C. 8090 and 8009 base metal samples were successfully thinned using a voltage of 12 - 15V which produced a current of ≈100mA. The flow rate was 3 - 4. Weld metal for both 8090 and 8009 was very fragile due to porosity, cracking or inclusion of large intermetallic phases. In this case successful thinning was achieved by reducing the voltage to 8 - 10V after an initial short period at 12 - 15V, and the flow rate was similarly reduced from 3 to 1. Alternatively, where porosity or cracking comprised a significant area of sample, preferential thinning was effected at the pore/crack edges using 12V and a flow rate of 1. The sample was repeatedly re-polished if after TEM observation insufficient thin area had been produced. Samples were gently washed for 30 seconds in three cooled alcohol baths and dried in air.

TEM was carried out on Philips EM301, EM400T and JEOL 2000 FX2 microscopes operating at 100kV, 120kV and 200kV respectively. The latter two were equipped with LINK and NORAN EDX analysis systems respectively.

3.4.4 Electron Probe Microanalysis (EPMA)

EPMA was undertaken on a 6061 CO_2 weld. 3mm thick sheet was welded at 20mm/s with a power of 1.8kW. A near surface section was polished and immediately positioned for analysis. An area of 50 x 50μm was analyzed for Mg concentration at 250μm intervals from one side of the weld to the other. In total, 20 readings from the base metal and 8 from the weld metal were obtained. The test was performed twice. A JEOL electron microprobe was used at 20kV with a wavelength dispersive spectrometer.

3.4.5 Grain Size Measurements

Grain size measurements were made according to the linear intercept procedure (ASTM E112 - 60T). The grain size was estimated by drawing five parallel lines each 100mm long separated by 25mm on a photograph magnified sufficiently to yield at least 50 grain boundary intercepts. In this way, the grain size was obtained as the reciprocal of the average number of grain boundary intercepts per mm on the sample.

3.4.6 Assessment of Weld Porosity

In order to quantify the porosity in 8090 CO_2 laser welds a technique was developed for sectioning accurately through successive longitudinal planes. A section of bead-on-plate weld was mounted in bakelite so that the longitudinal plane was parallel to the grinding surface. The process is illustrated in Fig. 3.4. A jig was designed to hold the sample and a fine screw thread enabled weld sections to be polished every 50μm through the weld width. At each interval a 9mm long section was enlarged 32X using a Leitz MM3 optical microscope equipped with a viewing screen. A trace of the weld section including porosity was made onto acetate sheet and the area fraction of porosity was subsequently calculated using computerised area analysis. By examining a sufficient number of closely spaced longitudinal planes (up to 25) it was possible to determine the total volume fraction of porosity in each length of weld examined. In addition, the nature and morphology of the pores were investigated using SEM.

3.4.7 Bulk Chemical Analysis

Bulk, wet chemical analysis of 8090 weld and base metal was undertaken by Anglo Blackwells Ltd. with ≈1.8g of material. A sample of base metal weighing 8.25g was analyzed for comparative purposes to assess the effect of sample weight on compositional result.

3.5 Heat Treatment Procedures

Solutionising and ageing treatments were carried out in fan ovens equipped with temperature controllers allowing variations in heating rate. Samples heated for subsequent metallography were of the order of 2 x 3cm in size whereas samples for tensile testing were 10 x 16cm in size. The accuracy of the heating rate set by the oven controller was tested by using a computer controlled data acquisition system. A thermocouple was prepared and inserted via the oven gas outlet pipe into a 0.5mm drilled hole in a ≈ 2 x 3cm sized piece of material. The sample and thermocouple were then lagged with insulating fibre. Typical traces for the oven heating rates of 1 and 10K/min are shown in Fig. 3.5 (a) and (b) respectively. The measured gradients were (a) 0.86 K/min and (b) 10.8 K/min. When the sample was placed straight into

a hot oven (530°C) the heating rate was estimated to be ≈100K/min.

3.6 Differential Thermal Analysis (DTA)

Differential thermal analysis was employed to investigate the possibility of low melting point phases being present in 8090 weld metal. A DUPONT 990 Thermal Analyser was used and the set up is shown schematically in Fig. 3.6 (a). The sample and super pure (SP) Al reference sample both weighed ~ 30 mg and were contained in alumina crucibles. With the reference sample placed on the back thermocouple in the heating head, a cover was placed over the samples and Ar gas was set to flow through at a rate of 15 l/min. The furnace heating rate was set to 1, 10 or 50 K/min on these experiments and the temperature output data was amplified and collected using a computer controlled Thermal Analysis Program supplied by MC Squared Thermal Systems. Eight heating runs were performed in total; 3, SP Al vs. SP Al runs at 1, 10 and 50 K/min up to 550°C; 3, weld vs. SP Al at 1, 10 and 50 K/min up to 550°C; and to final runs were performed at 10 K/min up to 670° to observe melting peaks for weld vs. SP Al and SP Al vs. SP Al.

The Data Management option in the software allowed data files to be subtracted from each other and the base-line data i.e. the SP Al vs. SP Al data was subtracted from the weld vs. SP Al data at each heating rate and the result was plotted on an X-Y plotter. A typical trace is shown in Fig. 3.6 (b) which illustrates the melting of SP Al vs. SP Al. Melting occurred at 655°C and this figure can be taken as an accurate calibration of the equipment according the real melting point of Al; 660°C[52].

3.7 Mechanical Testing

The hardness test was used as a convenient method of assessing the weldability of the alloys. Vicker's microhardness was preferred and a load of 25g was generally used. Fig. 3.7 illustrates how measurements were made across the fusion zone and around the HAZ.

Alloy 8090 was inspected for its deformation behaviour. Base and weld metal were

assessed in various heat treatment conditions using the tensile test. A standard test specimen is illustrated in Fig. 3.8 (a). A strain gauge was connected to this specimen to accurately record the yield point of the material. The strain gauge was a dual averaging strain gauge extensometer connected to an AC carrier amplifier. A chart recorder plotted the variation in voltage with applied load.

Notched tensile specimens were also used primarily to ensure that welded samples failed in the weld region. The geometry of a notched specimen is illustrated in Fig. 3.8 (b). The notch was placed in the weld as illustrated in the shaded section of the gauge length, and the notch geometry is shown enlarged in diagram A. Gregson[126] has reviewed some of the literature on notch tensile tests in aluminium alloys and has shown that the notch tensile strength to yield strength ratio serves as a reasonable measure of toughness for some Al-Li based alloys.

A MAYES DM4 tensile testing machine was used operating at a cross-head speed of 15mm/min and the load vs. cross-head displacement was continuously recorded on an X-Y plotter. Fractography was carried out on the SEM.

Table 3.1 A table showing the ranges of variables employed for each material and laser.

Material	Laser Used	Thickness Range (mm)	Power Range (kW)	Speed Range (mm/s)	Focus Range (mm)	Shield Gas
8090	CO_2 Nd:YAG	1-4 1-3	1.5-3.8 0.8-0.9	20-100 2.5-20	-2 to+4 -2 to+4	He Ar/He
8009	CO_2	2	2-3	50-150	0	He
6061	CO_2	1.6-3	1.7-3	10-100	0	He + N_2

Table 3.2. Nominal compositions (wt.%) of the alloys used in this study.

8090						
Element	Li	Cu	Mg	Zr		Al
%	2.4	1.1	0.6	0.1		rem
6061 (3 mm thick, top, 1.6 mm thick, below)						
Element	Mg	Si	Fe	Cu	Ti	Al
	0.88	0.57	0.46	0.31	0.17	rem
%	0.95	0.56	0.42	0.27	0.13	rem
8009						
Element	Fe	Si	V			Al
%	8.5	1.7	1.3			rem

(a)

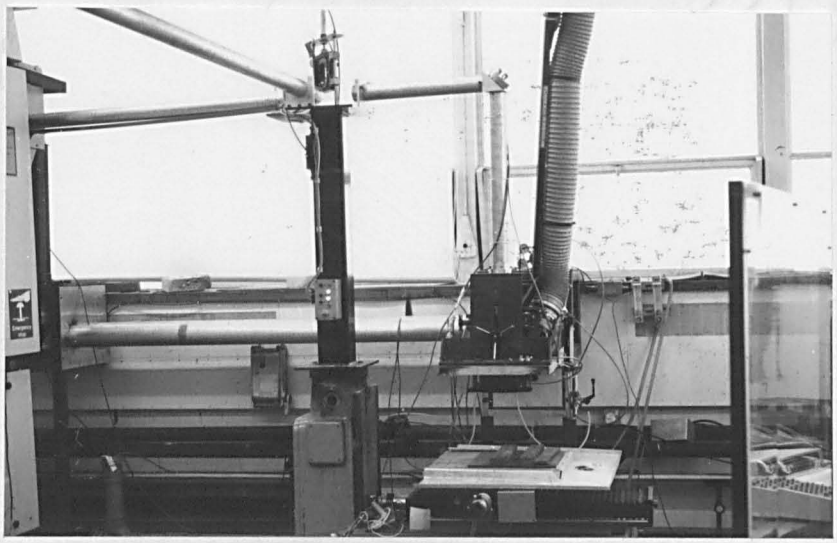

(b)

Figure 3.1. Photographs of the two types of laser equipment used in this work. (a) is the 5 kW Ferranti AF5 fast axial flow CO_2 laser, and (b) is the 1 kW Lumonics Nd:YAG laser.

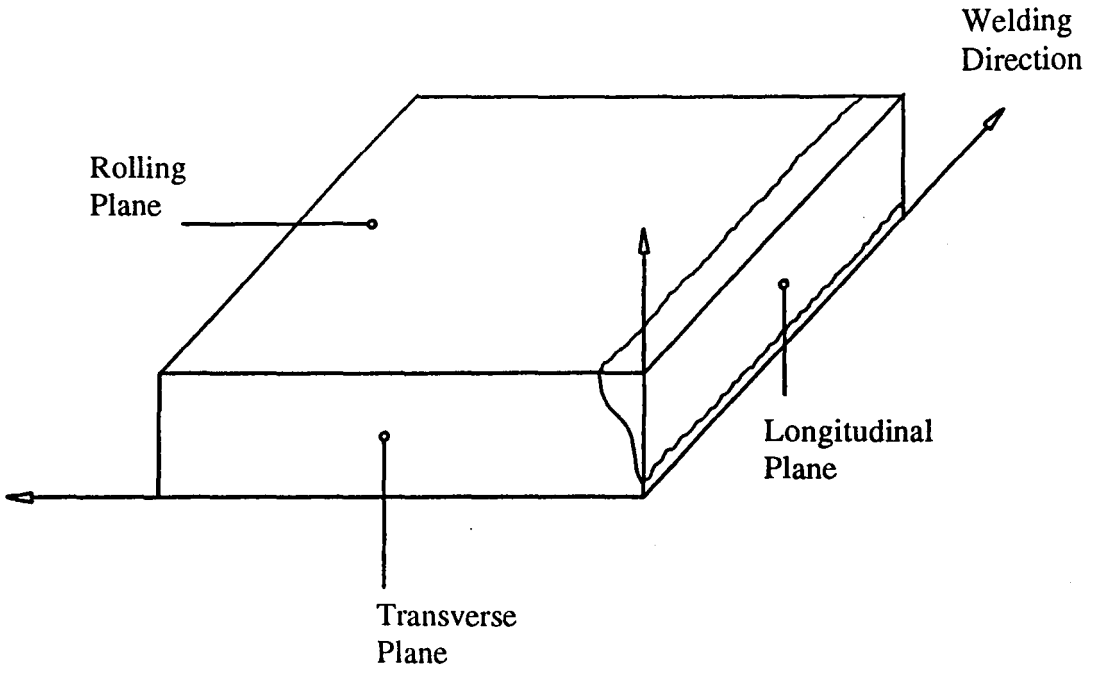

Figure 3.2. Definition of Specimen Planes

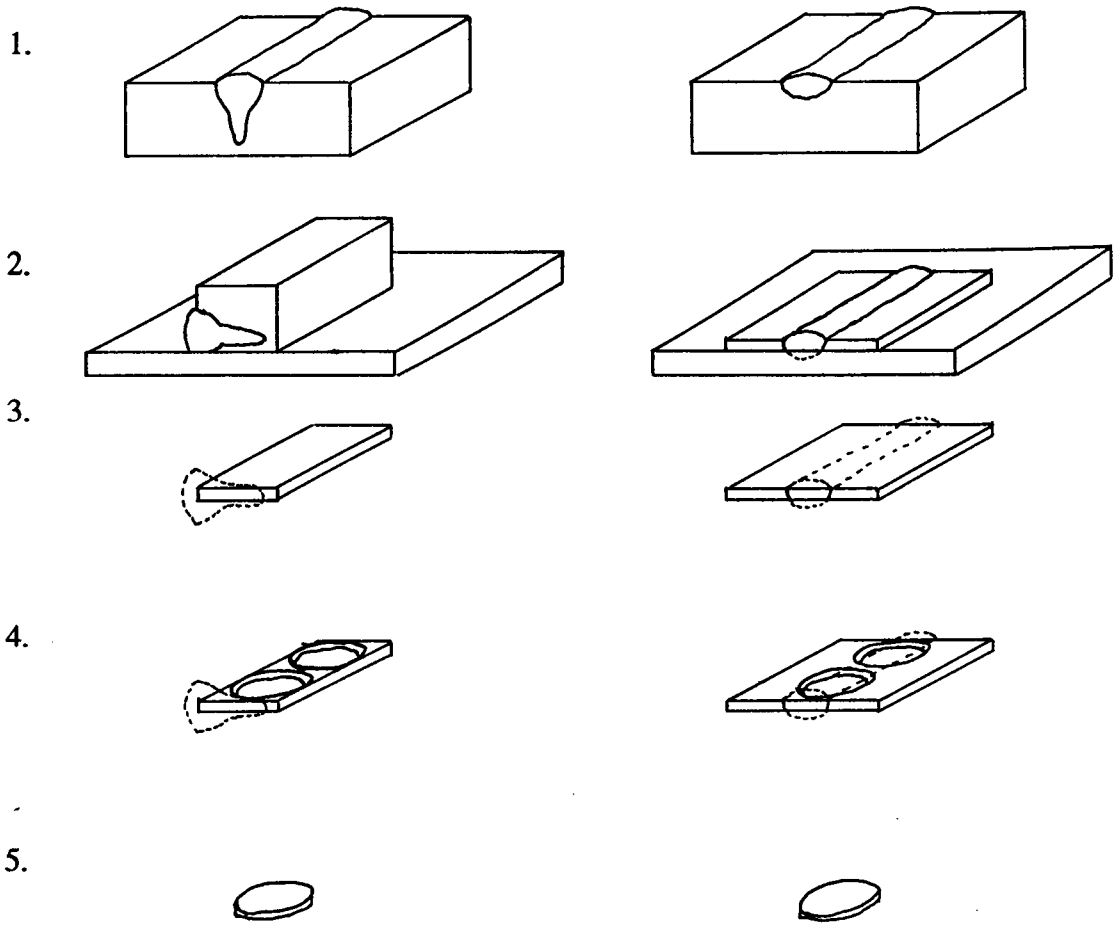

Figure 3.3. TEM Foil Preparation Procedure

1. Hacksaw the weld out of the bulk sample.
2. Grind the sample on SiC paper from one side.
3. Grind the sample on SiC paper from the other side until the section is 500 μm thick.
4. Punch or diamond drill 3 mm discs from the thin section.
5. Grind further on SiC paper until the disc is 100 μm thick.

Create electron transparency using twin jet electropolishing.

1.

2.

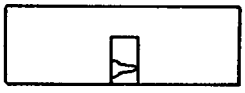

3.

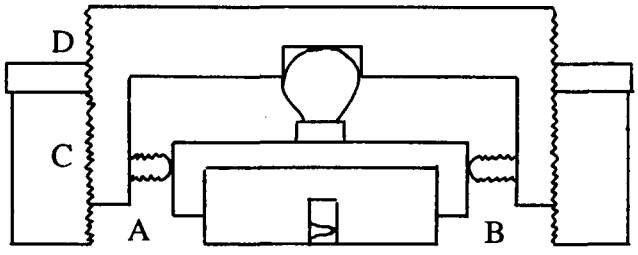

Figure 3.4. Weld Sectioning Procedure for Porosity Measurements

1. Hacksaw the weld out of the bulk sample.
2. Mount the sample in bakelite so that the longitudinal plane is parallel to the grinding surface.
3. Position the sample in the jig using the grub screws (e.g. A & B) to keep the bakelite grinding surface parallel to the jig grinding surface (C).

Grind, polish, etch and trace the section onto acetate sheet. Unscrew the locking ring (D) and screw the jig grinding surface in 50 μm. Re-lock the locking ring and repeat the procedure until the weld width has been traversed.

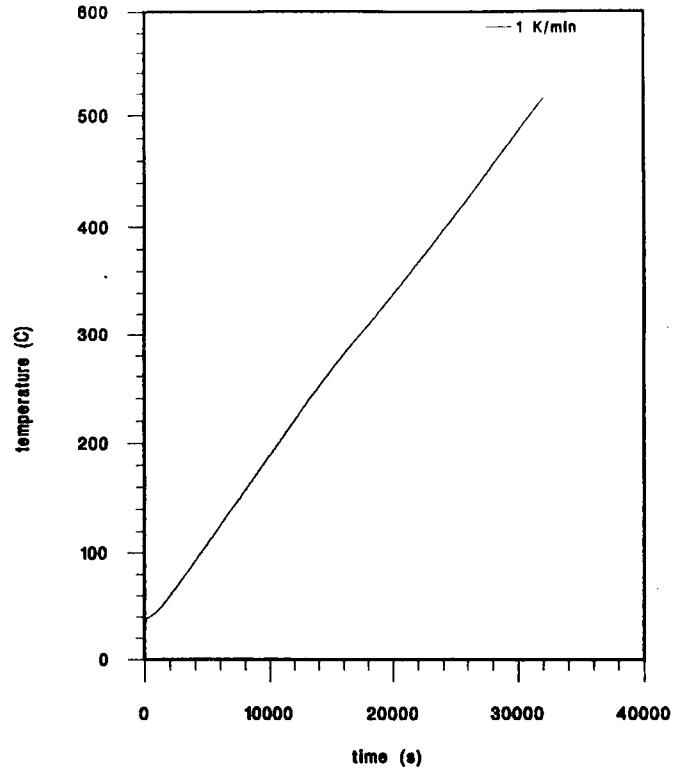

(a)

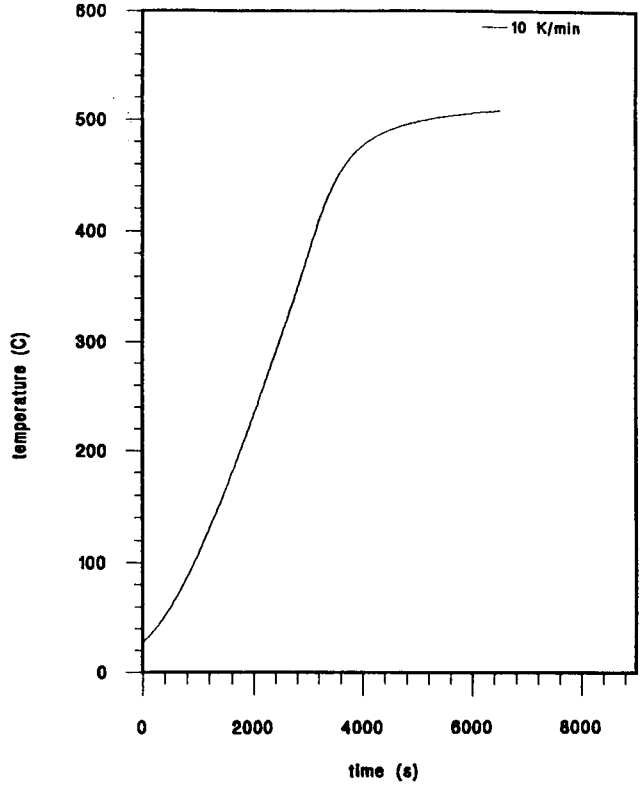

(b)

Figure 3.5. Traces of the measured heating rates obtained for oven heating rates of (a) 1 K/min and (b) 10 K/min. The calculated gradients were (a) 0.86 K/min and (b) 10.8 K/min.

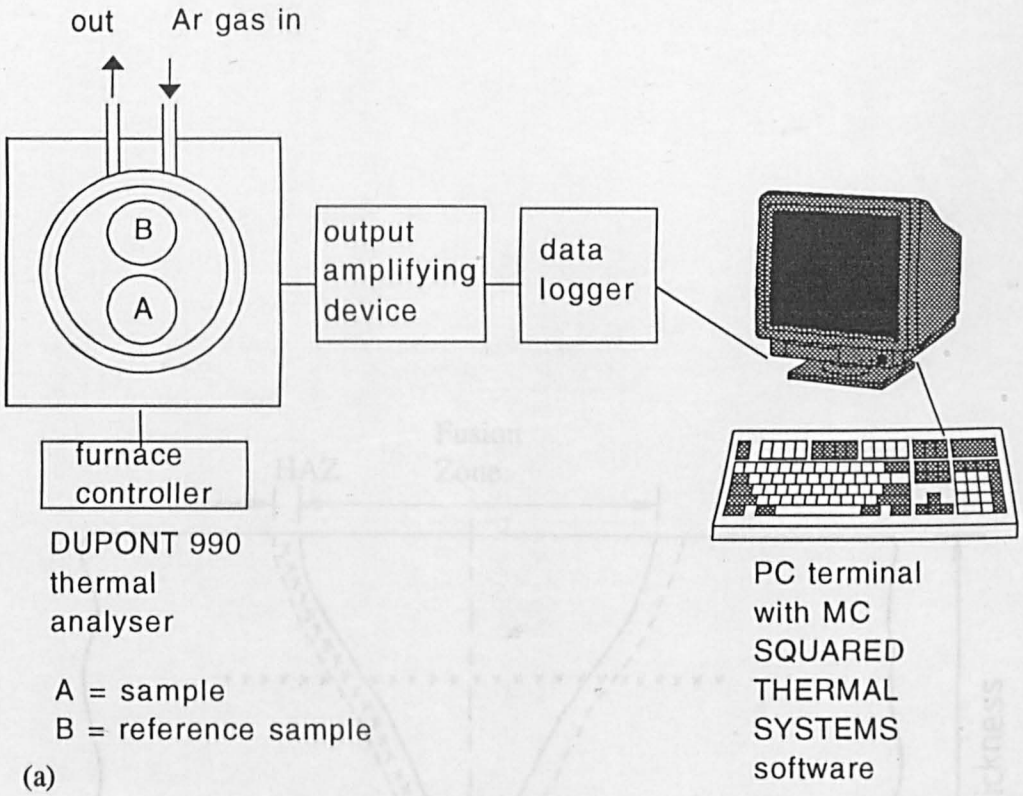

(a)

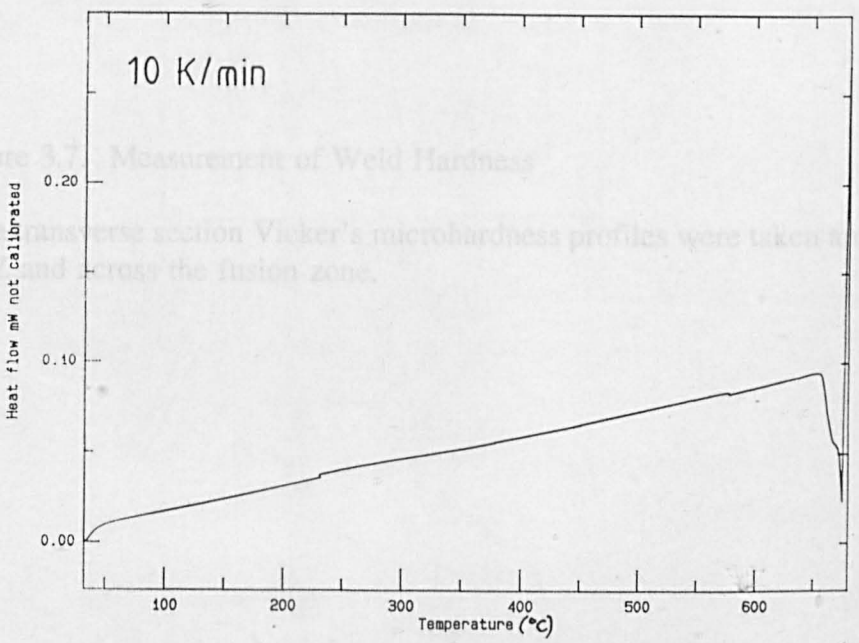

(b)

Figure 3.6. The experimental set up of the DTA equipment is shown in (a) and a typical trace for the melting of super purity Al is shown in (b).

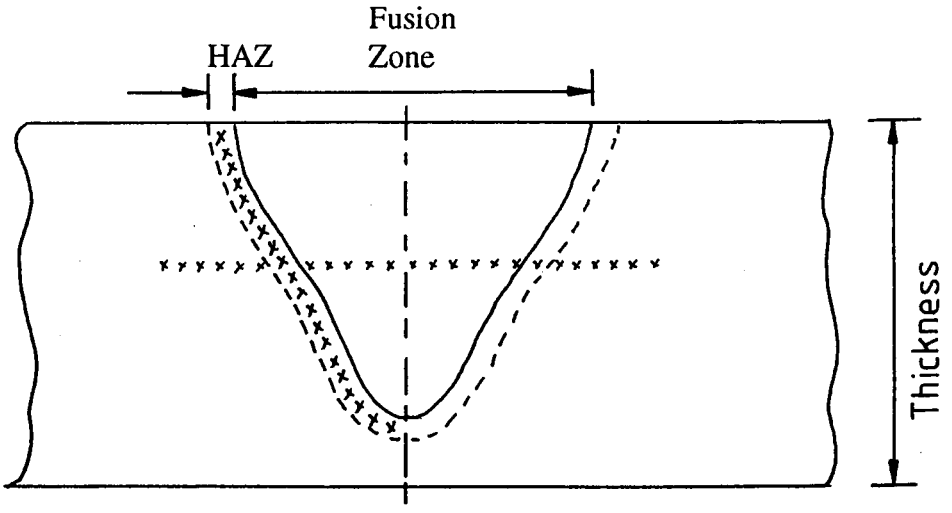

Figure 3.7. Measurement of Weld Hardness

On a transverse section Vicker's microhardness profiles were taken around the HAZ and across the fusion zone.

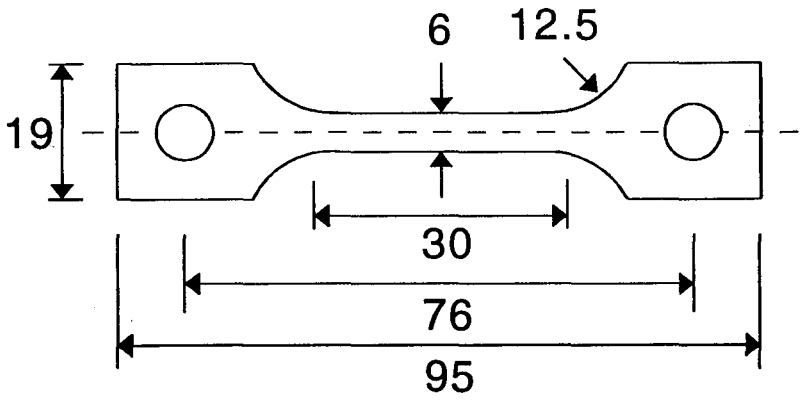

(a)

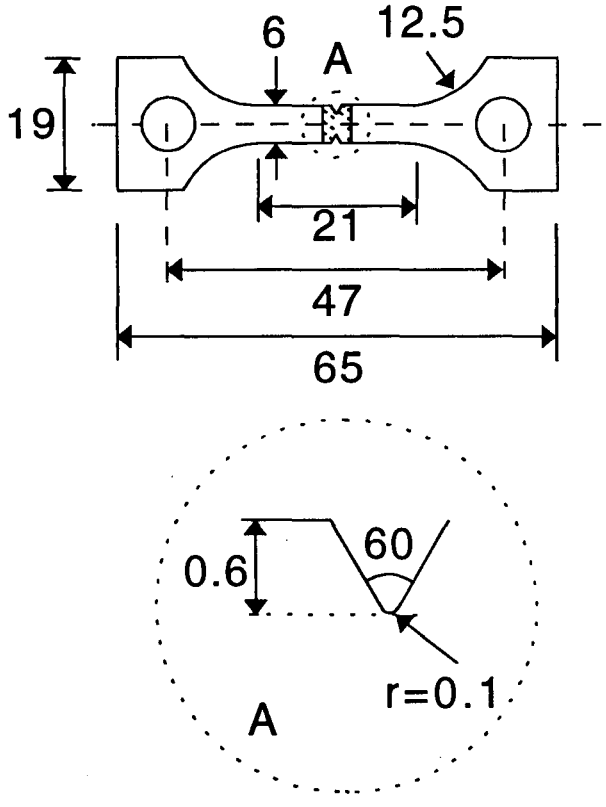

(b)

Figure 3.8. Tensile test piece geometry. (a) shows a standard test peice which was large enough to hold the extensometer. (b) is a notch tensile test piece[126] with the weld at the centre of the gauge length, and the notch geometry is enlarged in A. All dimensions are in mm.

Chapter 4. 8090 Results

The results pertaining to the laser welding of 8090 are presented in this chapter in several sections which describe the following features:

(i) on a macroscale, the weld dimensions and grain structure - section 4.1,

(ii) the microstructure and hardness of base and as-welded metal - section 4.2,

(iii) an assessment of porosity in CO_2 laser welds - section 4.3,

(iv) the microstructure and hardness of heat treated weld and base metal after a variation in the solution treatment temperature - section 4.4,

(v) the microstructure and hardness of heat treated weld and base metal after a variation in the heating rate to the solution treatment temperature - section 4.5,

(vi) the microstructure and hardness of heat treated base and weld metal after ageing - section 4.6,

(vii) thermal analysis of CO_2 weld metal - section 4.7,

(viii) the fracture characteristics of base and CO_2 weld metal after tensile testing, - section 4.8.

4.1 Weld Dimensions and Grain Structure

4.1.1 CO_2 Weld Metal

In these experiments the weld bead size has been determined by its top bead width, w, and depth of penetration, d. The graphs in Fig. 4.1 (a) and (b) summarize the effect of laser beam power and welding speed on the weld bead size. Fig. 4.1 (a) is for a fixed speed of 100 mm/s whilst Fig 4.1 (b) was obtained at a constant nominal beam power of 2.1 kW. As the welding speed is decreased, or as the laser beam power is increased, the width and depth both increase. The weld bead shape was found to be largely unaffected by the flow rate of the shielding gas.

The position of the workpiece relative to the focus of the laser beam was examined as a possible variable in the welding process. Two laser powers were used on 4 mm thick sheet at a welding speed of 60 mm/s. In the first case the nominal beam power was 2.25 kW and bead-on-plate welds were made with the focus at 0, -1, -2, +1, +2

mm, where '0' indicates a focus on the workpiece surface, '-' indicates a focus below the surface and '+' indicates a focus above the surface. The diagrams of weld transverse sections in Fig. 4.1 (c) (i) shows that at '0' focus the weld was fully penetrating and the bead profile was quite narrow with a small amount of drop out. As the focus is moved into the workpiece (ii and iii) penetration decreases and the bead adopts a more pronounced 'wine-glass' profile. On the other hand, as the focus is moved above the workpiece (iv and v) the weld bead maintains full penetration and barely changes in bead profile. In the second case the nominal beam power was 2 kW. Bead-on-plate welds were made with the focus at 0, -1, -2, +1, +2, +3, +4 mm and the schematic diagrams in Fig. 4.1 (c) (vi-xii) show that full penetration was not achieved in any case. The weld bead width appeared to be independent of the focus position. The weld bead profile did change slightly, however, when the focus was moved above the workpiece. The change is apparent as a sharpening of the weld root. The weld made at +2 mm was significantly lower in penetration when compared to the other welds and the weld root in this case was more rounded.

The shape of the weld transverse section with a 'wine-glass' profile is characteristic of high power density, deep penetration keyhole welding. In the micrograph of Fig. 4.2 (a) the solidified grain structure in the transverse section is revealed in a sample which has been anodized and viewed under polarized light. In the lower section of the weld fine columnar grains have grown in from the fusion boundary, but towards the centre an approximately equiaxed structure has formed. This is confirmed by Fig. 4.2 (c) which is taken form a longitudinal plane along the weld centre-line. In the upper region of the weld pool the columnar grains growing from the fusion boundary are clearly significantly coarser and again transform to a more equiaxed structure in the central region of the weld. Fig. 4.2 (b) which was taken from a plane parallel with the surface and Fig. 4.2 (c) from a longitudinal plane confirm that the grains in the central region were indeed equiaxed. Porosity is observable in the lower part of the weld (see Figs. 4.2 (a) and (c)) and this will be discussed in greater detail in section 4.3. Another feature of note is the irregular depth of penetration and grain structure banding which is apparent in Fig. 4.2 (c). This is presumably attributable to fluctuations in the processing conditions.

Weld cracking is a common problem in certain Al alloys and in this study weld cracks were observed predominantly in the upper region of the weld pool. The optical micrograph in Fig. 4.3 was taken from a near surface section and it demonstrates that cracks run across the weld width and that the cracks are intergranular.

4.1.2 Nd:YAG weld metal

The Nd:YAG weld macrostructure was quite different from that of the CO_2 weld: optical micrographs of the Nd:YAG weld transverse sections are presented in Fig. 4.4 (a-d). In particular the weld bead shape is not characteristic of a deep penetration keyhole weld owing to its high width to depth ratio. Pores and cracks are evident in the micrographs with in some cases vertical cracks running deeply into the weld. Numerous spherical pores were present within all the welds shown and were typically about 150 μm in diameter.

The position of the workpiece was varied with respect to the focus of the laser beam and the laser was set to pulse at 100 Hz with 7.85 J per pulse (average power = 785 W). The welding speed was 5 mm/s, and Figs. 4.4 (a-d) demonstrate the effect of focus position on weld bead shape. The micrographs represent focus positions of +4, +2, 0, -2 mm respectively where '+' indicates a focus above the surface, '0' indicates a focus on the surface and '-' indicates a focus below the surface. The micrographs illustrate that for focus positions above the surface, Figs. 4.4 (a) and (b), the weld bead shape is very wide with little penetration. As the focus is moved closer to the surface the weld top bead width decreases and penetration fractionally increases. At the surface focus position penetration had slightly increased, Fig. 4.4 (c) and the top bead width was further reduced. But for a focus of -2 mm the weld bead showed enhanced penetration as well as a dished surface, Fig. 4.4 (d). The variation in weld bead shape with focus position was greater than for CO_2 laser welding.

It was found that for a laser set to pulse at 86 Hz with 9.55 J per pulse (average power = 821 W), increasing the welding speed from 5 to 20 mm/s had little effect on the weld bead shapes.

4.2 Microstructure and Hardness of Base and Weld Metal

4.2.1 Base Metal

Bulk chemical analysis of the base metal was performed by an outside laboratory using atomic absorption spectrophotometry. For 8.25 g of material the composition was Al-2.29 wt.% Li-1.11 wt.% Cu-0.59 wt.% Mg-0.12 wt.% Zr, whereas for 1.8 g of material the composition was Al-2.34wt.% Li-1.14 wt.% Cu-0.60 wt.% Mg-0.13 wt.% Zr. There is little difference between the two sets of results, which are comparable to the nominal composition given in the Experimental Techniques.

An optical micrograph of the unetched base metal is shown in Fig. 4.5 which reveals that the as-received SPF condition base metal consists of an α-Al matrix together with a number of intermetallic phases. Using EDX analysis on the SEM the following types of intermetallic phase were identified, (i) a widespread flaky phase measuring ~ 2 μm by 10 μm containing Al-Mg-Cu, (ii) a dispersion of a globular phase around 2 μm in diameter and containing Al-Mg-Fe-Cu and (iii) an occasional 20 μm size phase containing Al-Zr-Ti-Cu. These phases might also contain Li which cannot be detected by EDX analysis. After anodizing and when viewed under polarized light the grain structure was found to be unrecrystallized. Furthermore, TEM showed that 1 - 2 μm sized sub-grains were present within the grains. Fig. 4.6 shows the sub-grains and sub-micron precipitates were also present within them which can be seen from this bright field micrograph. TEM centred dark field imaging from the δ′ (Al_3Li) reciprocal lattice spots (described in Appendix A1) revealed that the δ′ phase had a bi-modal size distribution as shown in Fig. 4.7 (a). The selected area diffraction pattern is shown in Fig. 4.7 (b) and the spot used for imaging is marked. A precipitate free zone (PFZ) is obvious on this micrograph around the larger precipitates. There is a distribution of fine scale ~ 15 nm diameter precipitates together with larger precipitates e.g. labelled 'D' measuring up to 100 nm in diameter. The latter were found to exhibit a core of reduced contrast under the centred dark field imaging conditions of Fig. 4.7. This core was found to be enriched in Zr, 20 - 50 nm in diameter and hence presumably the coherent, metastable form of β′ (Al_3Zr). In addition to the δ′ and β′ phases which can be seen as the rather grey, haloed images again labelled 'D' in Fig. 4.8, a further blocky precipitate ~ 100 nm in size labelled

'Z' can be seen in the matrix under the bright field conditions. EDX analysis showed that this phase contains principally Al and Zr with lesser amounts of Cu and Ti. Further analysis using SADP techniques enabled this phase to be identified as the equilibrium tetragonal form of Al_3Zr. The measured lattice parameters are a = 0.438 nm and c = 1.714 nm, which agree closely with those of Rystad et al[60].

The average microhardness of the base metal in the SPF condition taken from a transverse section was measured as ~ 71 ± 6 kgf/mm^2.

4.2.2 CO_2 Weld Metal

Bulk chemical analysis of 1.8 g of weld metal revealed that it had a composition of Al-2.35 wt.% Li-1.11 wt.% Cu-0.60 wt.% Mg- 0.12 wt.% Zr. This is similar to that of the base metal reported in the previous section. Therefore there was essentially no loss of Mg, Li or Cu during welding and so various solid state precipitation reactions can be expected.

The features of the weld metal microstructure are related to position within the fusion zone since the temperature gradient and growth rate are not constant during welding. Fig. 4.9 (a) illustrates the fusion zone, fusion boundary and HAZ regions and demonstrates the microstructural variations which take place within the weld metal. Higher magnification micrographs in Figs. 4.9 (b) and (c) show that the HAZ is ≤ 150 μm wide and consists of intergranular regions with a star-shaped morphology typical of grain boundary melting. As the fusion boundary is approached this star-shaped morphology is more pronounced until at the fusion boundary complete melting of intermetallic material has occurred and a narrow band of almost globular, non-dendritic grains has formed. Cellular dendrites then form which grow a short way into the centre of the weld, but soon become more equiaxed. Fig. 4.9 (c) is taken from the central region of the weld pool and illustrates that this region consists of cellular or dendritic equiaxed grains of various sizes with a fine interdendritic structure.

The interdendritic phases which formed were examined in greater detail using TEM,

and the micrograph in Fig. 4.10 (a) shows cells or dendrite arms of the α-Al together with interdendritic phases. This micrograph was taken from a near surface section parallel with the rolling plane. Semi-quantitative EDX analysis revealed that the α-Al was depleted in Cu and Mg at the cell/dendrite arm centre but enriched in these elements at the edges. This is typical of non-equilibrium solidification which is observed in cast structures. The EDX spectrum shown in Fig. 4.10 (d) was taken from the interdendritic material and showed that it was enriched in Mg-Si-Cu when compared to the spectrum obtained from the α-Al shown in Fig. 4.10 (e). A secondary dendrite arm spacing of 2 - 5 μm was measured from a TEM sample taken from the near surface plane parallel with the rolling direction. The interdendritic material was crystalline but the structure has not been determined.

The δ′ phase was also present in the as-solidified weld as a very fine precipitate ≤ 5 nm in diameter within the α-Al cells, as shown in Fig. 4.10 (c). The δ′ reciprocal lattice spots illustrated in the SADP of Fig. 4.10 (b) are quite large and diffuse when compared to the α-Al matrix spots which suggests that the δ′ precipitates are indeed very small spheres. The small scale of the precipitates indicates that they formed during cooling after solidification and that the cooling rate of the weld was insufficient to keep the Li in solid solution. The β′ phase did not appear to form in the as-solidified structure.

A microhardness profile was taken across a weld transverse section and is illustrated in Fig. 4.11. Approximately ten indents were made in the fusion zone and the average weld microhardness was measured as ~ 80 ± 4 kgf/mm^2, compared to the HAZ hardness of ~ 100 kgf/mm^2 and base metal hardness of ~ 71 ± 6 kgf/mm^2.

4.2.3 Nd:YAG Weld Metal

Compared to the CO_2 weld metal the structure of the Nd:YAG weld metal is much finer in scale, although the basic features are very similar. It is clear from Fig. 4.12 that the fusion boundary can again be identified as a narrow region of globular, non-dendritic grains which separate the weld metal from the HAZ. The HAZ width has

been measured from etched samples and the dark etching band surrounding the weld metal is only ~ 50 μm wide. Star-shaped intermetallic regions typical of localized grain boundary melting can be observed very close to the fusion boundary.

The fusion boundary can be identified as a narrow region of small, globular non-dendritic grains. The transverse section in Fig. 4.13 (a) shows that this region of globular grains is very narrow at the bottom of the weld bead, but appears to increase in width up the weld pool edges. There is quite a large region in the base metal which has been affected by the welding thermal cycle, which appears quite different from that on the near surface section in Fig. 4.12. Copious melting of intermetallic has taken place and coarse grains have formed adjacent to the fusion boundary. Cells appear to grow out of the globular grains comprising the fusion boundary and into the weld metal, along the direction of the maximum thermal gradient. Long stringers of intermetallic material weave upwards through the weld, enclosing grains which themselves contain fine rounded precipitates. Periodic bands are also observed within the weld metal which are illustrated in the near surface section in Fig. 4.13 (b). The banding is regular with a separation which was observed to decrease with decreasing welding speed and might be attributed to the distance travelled by the workpiece between successive laser pulses. The nature of the band microstructure has not been thoroughly investigated but optical microscopy has shown that each band constitutes a coarsened interdendritic phase, which is evident in Fig. 4.13 (b) with a secondary dendrite arm spacing of ~ 0.5 μm. Grains can be seen to grow unaltered through the bands as shown in Fig. 4.13 (b) for example at 'y'. This probably means that the solidification process has not actually been interrupted, as in the CO_2 weld banding, but only slowed down due to the thermal cycle within the pulsed volume.

Samples were prepared for the TEM as shown in Fig. 3.3 for shallow welds. TEM micrographs of the fine solidification structure in Fig. 4.14 (a) show that the microstructure consists of small, almost spherical intermetallic particles which are less than ~ 250 nm in diameter dispersed within the α-Al solid solution. Analysis of the phase was attempted using SADP's in the TEM which showed that the particles were polycrystalline and probably clusters of smaller particles. EDX analysis from this

intermetallic material showed that it was composed of Al-Cu-Fe as shown in the spectrum of Fig. 4.14 (b). When compared to the spectrum for the α-Al, Fig. 4.14 (c), the intermetallic is obviously enriched in Cu and Fe. Semi-quantitative EDX profiles across grain boundaries showed enrichment of Cu at the boundary compared to the grain interior.

The microstructure of the solidified weld was also studied in detail for δ′ precipitation. TEM discs were taken from two different weld tracks. Both samples revealed, on SADP's, that the $L1_2$ reciprocal lattice spots (see Appendix A1) characteristic of the δ′ and β′ phases were absent. One of these SADP's is illustrated in Fig. 4.15 (a) and only reciprocal lattice spots for aluminium and Al_2O_3[67] could be indexed. This SADP can be compared to other δ′ containing structures discussed later (for example in Fig. 4.25 (b)).

The average microhardness of the weld metal has been measured as ~ 59 ± 7 kgf/mm^2 from a near surface profile, Fig. 4.15 (b). This is lower than the CO_2 weld value of ~ 80 ± 4 kgf/mm^2 and the base metal value of ~ 71 ± 6 kgf/mm^2. The microhardness of the HAZ was not measured owing to its small scale.

4.3 Assessment of Porosity in CO_2 Welds

Radiographs of autogenous bead-on-plate welds confirmed that large pores were situated predominantly along the weld centre-line, i.e. the region which would have been traversed by the vaporized region known as the keyhole.

In partial penetration welds two different types of pores could be clearly identified as shown in Fig. 4.16 (a) and (c). The near-spherical pore of Fig. 4.16 (a), in which the dendritic solidification structure is visible on pore walls will be termed type I porosity. Fig. 4.16 (b) is a higher magnification SEM micrograph illustrating the dendritic morphology at the pore wall with a secondary dendrite arm spacing of ~ 2 μm. This latter micrograph was taken from the fracture surface of a tensile test specimen. The irregular shaped pores, one of which is shown in Fig. 4.16 (c) will be termed type II

porosity. These did not reveal the solidification structure on the pore walls, but instead appeared to possess a complex, folded type of structure characteristic of cold-shuts in conventional castings. In full penetration welds the type II porosity was virtually absent, indicating a different balance of forces between vapour pressure and surface tension. This will be discussed more fully in section 5.2.

Using the technique described in the Experimental Techniques chapter, measurements were made at 50 - 100 μm intervals of the area fraction of porosity on longitudinal plane sections. Macrophotographs of four successive longitudinal plane sections from a partial penetration weld made in 4 mm thick sheet are illustrated in Fig. 4.17. Large spheroidal gas pores can be seen, for example at the point marked 'A' on each section, which illustrate the connectivity of the porosity. The 'bubbles' appear to be inclined towards the welding direction. It can be seen in Fig. 4.17 (a) that the majority of the smaller porosity is concentrated in the lower part of the weld. This is non-spherical and is typical of cold shut type porosity. Careful inspection of the micrographs shows that the area fraction of the total porosity decreases quite rapidly with distance from the centre-line when the weld root depth and shape is compared on each section. The graph in Fig. 4.18 (a) displays the results for welding speeds of 60 and 100 mm/s which both gave partial penetration welds at 2 kW beam power. The 60 mm/s weld is in fact illustrated in Fig. 4.17. A peak in area fraction of porosity is observed on a plane which is assumed to be the weld centre-line and falls very steeply with distance on either side as was observed on the micrographs in Fig. 4.17. Similar plots in Fig. 4.18 (b) and (c) also show the same trend, but it must be emphasised that these welds were made on different days and a reproducible level of porosity cannot be expected. In fact, the results shown in Fig. 4.18 (a) demonstrate higher levels of porosity than subsequently found in other weld sections, which are attributed to the large gas pores, for example labelled 'A' in Fig. 4.17. Fig. 4.18 (b) and (c) represent welds which were made at 2 kW beam power but in 4 and 3 mm thick sheet respectively. Fig. 4.18 (b) shows small peaks either side of the centre-line which tend to increase in size with increasing welding speed, i.e. opposite to the trend of the central peak. Inspection of the traced plane sections from the welds described by this graph shows that the secondary peaks are caused by small spherical gas pores.

These are located in the upper, broader part of the weld bead but towards the weld bead edge. On these sections, the area of weld metal is small hence the area fraction of porosity can become quite large. However, as the weld centre-line is approached the weld metal area increases dramatically and the area fraction of porosity decreases until very close to the centre-line where the majority of the porosity is located. Comparison of the weld transverse sections for the welds used for Figs. 4.18 (a) and (b), which were essentially produced under similar conditions, revealed only that the penetration was slightly increased in the case of Fig. 4.18 (b), i.e. the weld bead still displayed a generally 'wine-glass' profile.

From data of this type the total volume fraction of porosity in ~ 9 mm long sections of weld was calculated and table 4.1 summarizes the results obtained. Generally, the volume fraction of porosity decreases with increasing welding speed for a fixed power input. The transition from partial to full penetration (FP) for a given speed and power but different sheet thickness can lead to a reduction in porosity, as shown by comparing the values for 4 mm and 3 mm thick sheet welds made at 60 mm/s (3 vol.% cf. 0.78 vol. %). The interpretation of these results is difficult due to the limited length of weld studied in each case and several sections from each weld would need to be investigated in order to fully quantify the volume fraction of porosity. In all these experiments the beam power and focus position were unchanged.

Samples which underwent a chemical etch which removed ~ 100 μm from both sides of the sheet prior to welding appeared to contain similar levels of porosity, according to X-ray radiographs, as the unetched samples.

4.4 Microstructure and Hardness of Heat Treated Base and CO_2 Weld Metal after a Variation in the Solution Treatment Temperature

The solution treatment temperature was varied from 460°C to 530°C for fixed solutionizing times of ~ 40 minutes. Samples were placed into a hot fan oven which produced an uncontrolled heating rate of ~ 100 K/min and finally cooled in air. This

heating and cooling rate was adopted in an attempt to try and simulate a SPF thermal cycle.

4.4.1 Base Metal

After solution treatment at 530°C optical microscopy showed that the coarse intermetallic phases which were present in the as-received SPF microstructure had largely disappeared. Furthermore, optical microscopy revealed that the solution treated microstructure was extensively recrystallized with grains which were elongated in the rolling direction with sizes of the order of 3 - 10 μm, Fig. 4.19 (a). This transverse section also illustrates a light etching region at the surface with few grain boundaries due to Li depletion during heat treatment. Some low angle grain boundaries were however seen in the TEM. Furthermore, centred dark field microscopy from $L1_2$ reciprocal lattice spots showed that the δ′ precipitates had grown with a bi-modal size distribution. As well as the fine homogeneous precipitates there was an appreciable amount of larger precipitates. The latter had a core of reduced contrast and were situated within grains and at grain boundaries. These were presumably due to favoured nucleation and growth of δ′ on β′ dispersoids.

After solution treatment at lower temperatures optical microscopy showed that there was less extensive homogenization of the coarse intermetallic phases. A TEM investigation of the 460°C solution treated sample showed that the microstructure was essentially unrecrystallized with a sub-grain size of ~ 1μm.

Microhardness measurements were made at all solution treatment temperatures. Errors in the microhardness values were calculated as two standard deviations from the mean value, and these are shown as error bars in the graph of Fig. 4.19 (b). The graph demonstrates that the microhardness increases with solution treatment temperature from ~ 73 kgf/mm^2 at 460°C to ~ 94 kgf/mm^2 at 530°C. Thus solution treatment effectively increases the base metal hardness to a degree dependent on the solution treatment temperature.

4.4.2 CO_2 Weld Metal

Optical microscopy of CO_2 weld metal has shown that homogenization of the cast structure and the development of the grain structure begins during solution treatment at ~ 470°C, although homogenization is not complete after 40 minutes at this temperature. As the solution treatment temperature is increased the grain size increases and elimination of the weld structure is more complete and new, well defined grains are formed. Optical micrographs of the weld fusion zone which was solution treated at 530°C are illustrated in Fig. 4.20 which show the nature of the grain structure. The average grain size across the lower half of the fusion zone, or keyhole, was measured to be ~ 22 ± 12 μm, but massive grains measuring up to ~ 200 μm can also be seen. These are observed predominantly around the fusion boundary in Fig. 4.20 (a) but can also be seen randomly within the middle of the keyhole. Those large grains which are typically found at the fusion boundary can extend part way into the base metal/HAZ region. At higher magnifications the residual cast structure is clearly visible within the massive grains as shown in Fig. 4.20 (b). Small precipitates remain at the prior cell boundaries which did not completely solutionize. TEM showed that δ′, which presumably formed during air cooling, is present with a uni-modal size distribution, which is illustrated in the centred dark field micrograph of Fig. 4.21. The width of the elongated grains in the upper region of the weld pool was measured to be ~ 30 μm.

Microhardness measurements were made at all solution treatment temperatures and the results have shown that microhardness increases with increasing solution treatment temperature. The graphs in Fig. 4.22 illustrate that by raising the temperature from 460°C to 530°C the microhardness can be increased from ~ 73 ± 5 kgf/mm^2 to ~ 95 ± 10 kgf/mm^2. By comparing this graph with that in Fig. 4.19 (b) for the base metal hardness it is clear that both weld and base metal microhardness show the same dependence on solution treatment temperature, with a close match in average values.

4.5 Microstructure and Hardness of Heat Treated Base and CO_2 Weld Metal after a Variation of Heating Rate

In order to try and elucidate the mechanisms underlying the growth of massive grains in the weld metal during solution treatment at 530°C it was decided to examine other heating rates with a view to achieving a smaller grain size and improved homogenization. Heating rates of ~ 100, 10 and 1 K/min were thus investigated prior to solution treatment at 530°C for ~ 40 minutes. All samples were air cooled.

4.5.1 Base Metal

The final microstructure of the base metal was found to be essentially independent of the solution treatment route in these experiments. Optical microscopy showed that all three solution treated microstructures were recrystallized with the typical microstructure shown in Fig. 4.19 (a). A solute depleted surface layer of ~ 50-60 μm had formed presumably due to Li and Mg migration to the free surface[127][128]. TEM also showed that the distribution of the δ′ phase, formed during air cooling, was bi-modal in all cases; fine homogeneous precipitates were seen along side larger precipitates which contained reduced contrast cores. These results have already been presented in a previous section for the 100 K/min heating rate.

Microhardness measurements showed that the average hardness was apparently highest for the slow heating rate of 1 K/min. The graph in Fig. 4.23 summarizes the influence of heating rate on microhardness and shows that average hardnesses of ~ 94, 87 and 109 kgf/mm^2 were obtained with heating rates of 100, 10 and 1 K/min respectively. Given the scatter in the data (revealed by the size of the error bars) it is reasonable to conclude that 10 and 100 K/min heating rates gave similar hardnesses but that a 1 K/min heating rate gave a significantly higher hardness.

4.5.2 CO_2 Weld Metal

In contrast to the base metal results, the microstructure of the CO_2 weld fusion zone was found to be strongly dependent on the heating rate to the solution treatment temperature. The results after heating at a rate of 100 K/min have been presented in

section 4.4.2 but it is useful to summarize them at this point. The average keyhole grain size was ~ 22 ± 12 μm with massive grains measuring up to ~ 200 μm forming within the keyhole but especially at the fusion boundary. TEM showed that δ′ was present with a uni-modal size distribution of fine scale precipitates and β′ was not identified. The keyhole microhardness was measured as ~ 95 ± 10 kgf/mm^2.

Grain sizes were measured across the keyholes of the 10 and 1 K/min samples which showed that the average size and the scatter decreased with decreasing heating rate. At 10 and 1 K/min the grain sizes were respectively ~ 11 ± 4 μm and ~ 10 ± 1 μm. It is obvious, however, that the exact value will depend on the section of the keyhole selected and will undoubtedly vary on each section. However, the optical micrographs shown in Fig. 4.24 illustrate clearly the influence of heating rate on weld metal grain size. The grain size is clearly most uniformly small for the 1 K/min heating rate, though some larger grains are still evident at the fusion boundary which can extend into the HAZ. This microstructure can be contrasted to that of the 100 K/min heating rate microstructure in Fig. 4.20.

TEM was performed on all samples. Fig. 4.25 (a) is a bright field TEM micrograph from part of a massive grain in the 100 K/min sample. The small rod-like intermetallic phases, examples of which are arrowed, were analysed using EDX and contained Al, Fe and Cu. They are generally ~ 250 nm long and ~ 80 nm wide. EDX spectra from various particles are shown in Figs. 4.25 (b) and (c). Subsequent analysis of the SADP of Fig. 4.25 (d), using the techniques outlined in Appendix A1, showed that the reciprocal lattice spots additional to those from the α-Al matrix and δ′, e.g. marked with an arrow could be indexed as Al_2O_3. Huang et al.[67] have also observed Al_2O_3 reflections in Al-Cu-Li alloys. The precipitates appeared to be arranged in a cellular network with boundaries of the order of 2 - 5 μm spacing. This is consistent with the boundaries of the cellular-dendritic cast structure observed in the as-welded condition which is illustrated in Fig. 4.10 (a). TEM microscopy for the 10 and 1 K/min heating rate samples confirmed that this network structure was most apparent in the 100 K/min sample of Fig. 4.25 (a). Larger micron sized intermetallic phases which were shown to consist of Al-Si-Cu using EDX in the TEM were also

present at grain boundaries and triple points.

The δ′ distribution was analysed for the 10 and 1 K/min samples and centred dark field images from $L1_2$ reciprocal lattice spots showed that δ′ had precipitated with a bi-modal size distribution in both samples. In the 10 K/min heating rate sample, which is illustrated in the dark field δ′ micrograph in Fig. 4.26 (a), fine homogeneous δ′ precipitates can be seen together with some larger round precipitates with reduced contrast cores. Similar observations can be made for Fig. 4.26 (b) which represents the 1 K/min heating rate although the size of the larger precipitates appears to be somewhat larger in the latter. The observation of these 'duplex' precipitates presumably indicates that β′ has had time to form during the slow heating rate, Fig. 4.26, but not during the fast heating rate, Fig. 4.21.

Microhardness measurements were made across the keyhole in each case. The graphs in Fig. 4.27 summarize the influence of heating rate on the average weld metal hardness. For heating at rates of 100, 10 and 1 K/min microhardness values were respectively ~ 95 ± 10 kgf/mm^2, ~ 93 ± 11 kgf/mm^2 and ~ 118 ± 10 kgf/mm^2. Thus a significant increase in hardness occurs after heating at a rate of 1 K/min followed by air cooling.

4.6 Microstructure and Hardness of Heat Treated Base and Weld Metal after Ageing Treatments

Ageing treatments were conducted on the as-received base metal, the CO_2 weld metal and the Nd:YAG weld metal. Two treatments were applied and these were (a) a simple post-weld age and (b) a full solution treatment and age. The purpose of these experiments was two fold. Firstly, to better observe the distribution of Li and Zr bearing phases using centred dark field imaging techniques in the TEM. The second reason was to investigate the production of matching properties between base metal and weld metal through appropriate heat treatment.

4.6.1 Base Metal

The microhardness of the as-received base metal which had been overaged for 16 hours at 190°C has been measured as ~ 88 ± 3 kgf/mm^2 which can be compared to the as-received hardness of ~ 71 ± 6 kgf/mm^2. The microhardness of the solution treated base metal which was aged for 16 hours at 190°C was measured after two different heating rates to the solution treatment temperature. The results are as follows; for a heating rate of 1 K/min the microhardness was ~ 137 ± 4 kgf/mm^2 whereas for a heating rate of 100 K/min the microhardness was ~ 139 ± 8 kgf/mm^2. Clearly, the heating rate to the solution treatment temperature has little if any influence on the final aged microhardness.

4.6.2 CO_2 Weld Metal

TEM was performed on CO_2 weld metal which had been (a) post-weld aged for 16 hours at 190°C and (b) solution treated with heating rates of 100 and 1 K/min and aged for 16 hours at 190°C. The TEM micrograph in Fig. 4.28 (a) is a centred dark field δ′ image of the aged welded structure. This illustrates that the δ′ phase has precipitated with an essentially uni-modal size distribution and the spheres have grown to ~ 30 nm in diameter. Enhanced precipitation appears to have occurred at α-Al cell boundaries compared to the quite sparse cell centres. This was presumably due to solute segregation during solidification. The large black circles are holes where weak triple points have been etched away during sample thinning. Fig. 4.28 (b) is a SADP which clearly shows the δ′ reciprocal lattice spots and faint streaking due to S′ can also be seen in $<120>_{Al}$ directions. The bright field micrograph in Fig. 4.28 (c) was taken from the cell boundary region and S′ rods are visible within a background of spherical δ′ precipitates.

The heating rate to the solution treatment temperature has been shown to influence the size distribution of δ′ precipitates in the weld metal. Fig. 4.29 (a) is the centred dark field δ′ image of a sample which was heated at a rate of 100 K/min, solution treated and aged for 16 hours at 190°C. δ′ has precipitated with a uni-modal size distribution and has grown to ~ 25 nm in diameter. S′ rods can also be seen due to the overlapping of the objective aperture onto bright S′ streaks. Fig. 4.29 (b) is the SADP

from this region and the δ′ reciprocal lattice spots are clearly visible as are the streaks in $<120>_{Al}$ directions due to S′ phase.

After heating at a rate of 1 K/min to the solution treatment temperature and ageing for 16 hours at 190°C, the sub-micron structure consisted of a bi-modal δ′ distribution. Fig. 4.30 (a) is a centred dark field δ′ image which shows that as well as the small spherical precipitates which have coarsened to a diameter of 20 - 30 nm, larger precipitates with diameters of ~ 90 nm have formed. The latter have reduced contrast cores and are presumably due to preferred nucleation and growth of δ′ on β′. This dark field micrograph clearly shows a grain boundary as marked by arrows at its limits and the 'duplex' precipitates can be seen within the oriented grain and at several positions along this short length of grain boundary. Thus it is reasonable to conclude that the 1 K/min heating rate has provided favourable conditions for β′ growth and due to its location on the grain boundaries has probably assisted in preventing grain growth during solution treatment. Fig. 4.30 (b) is the SADP which shows the δ′ reciprocal lattice spots and streaks in $<120>_{Al}$ directions due to S′ phase.

Microhardness measurements of the weld metal in these heat treatment conditions were made and are summarized in the graph of Fig. 4.31. For completeness the as-welded graph of Fig. 4.11 is included. After post-weld ageing the microhardness was ~ 130 ± 7 kgf/mm^2. After solution treatment and ageing the microhardness proved to be quite insensitive to the heating rate used; a 100 K/min heating rate gave an aged hardness of ~ 140 ± 9 kgf/mm^2 whereas a 1 K/min heating rate gave a hardness ~ 138 ± 6 kgf/mm^2.

4.6.3 Nd:YAG Weld Metal

TEM was performed on Nd:YAG weld metal after post weld ageing for 16 hours at 190°C. Samples were taken from the near surface plane as illustrated in Fig. 3.3 for shallow welds. However, an extra precaution was made to remove ~ 200 μm of surface layer since Li would have diffused out of the surface during heat treatment. The SADP in Fig. 4.32 (a) shows that $L1_2$ reciprocal lattice spots are absent when compared with the SADP's in Figs. 4.28 (b) and 4.29 (b), but streaks for S′ phase and

T_1 phase are present in $<120>_{Al}$ and $<111>_{Al}$ directions respectively. The bright field micrograph in Fig. 4.32 (b) was taken in this orientation and is from a region close to a cell boundary. S′ rods can be seen in the three $<100>_{Al}$ directions and T_1 plates can be seen on $<111>_{Al}$ planes.

The microhardness profile in Fig. 4.33 for the aged weld also includes the profile for the as-received weld of Fig. 4.15. These profiles demonstrate that ageing has had relatively little effect on the weld metal microhardness. The average aged hardness was ~ 62 ± 4 kgf/mm^2 whereas the as welded hardness was ~ 59 ± 7 kgf/mm^2. There is, however, a noticeable difference between the profiles at the fusion boundary and HAZ. For the aged sample there is a significant increase in hardness at the HAZ up to ~ 116 kgf/mm^2. Note also that the base metal has increased in hardness.

It is clear from these results that there has been no observable precipitation of δ′ during ageing, but that S′ and T_1 have formed near the cell boundaries.

In summary, the results have shown that for the CO_2 laser welds, the massive grain growth observed during solution treatment with a fast heating rate (~ 100 K/min) can be controlled by imposing reduced heating rates of 10 and 1 K/min. Analysis of the weld microstructure was completed by solution treating with 100 and 1 K/min heating rates followed by an ageing treatment in order to precipitate homogeneous and heterogeneous δ′. This had the desired effect of 'outlining' the larger β′ precipitates with heterogeneous δ′ and these were only observed in the 1 K/min heating rate sample. (The sample heated at 10 K/min was not aged). Thus, a small weld grain size of the order of 10 μm was manufactured together with a reasonable match in hardness between the weld and base metal. In comparison the Nd:YAG weld results demonstrate, that for weld metal treated in a similar manner to the CO_2 weld metal, a favourable match in hardness between the weld and base metal cannot be obtained, and TEM showed that there was a distinct absence of the precipitate δ′ in the as-welded and as-welded and aged heat treatment conditions.

4.7 Thermal Analysis of CO_2 Weld Metal

Differential thermal analysis (DTA) of the 8090 CO_2 weld metal was carried out with heating rates of 1, 10 and 50 K/min up to 550°C. These heating rates were selected to correspond closely to those used in previous sections for control of fusion zone grain size. Samples weighed ~ 30 mg, as did the Super Purity aluminium reference samples which were also used to obtain base-line data. The traces from welds for the 1, 10 and 50 K/min heating rates are illustrated in Fig. 4.34 (a), (b) and (c) respectively and base line plots are shown in Fig. 4.35 (a), (b) and (c) for the same heating rates.

The main point to note is that there is no endothermic melting peak below 550°C in any of the traces in Fig. 4.34. The melting peak of the reheated 10 K/min sample shown in Fig. 4.34 (d) is that of the bulk weld metal at ~ 593°C. The trace in Fig. 4.34 (b) gives the clearest picture of the reactions which take place during heating. The 1 and 50 K/min heating rates of Fig. 4.34 (a) and (c) respectively are more difficult to interpret due to the thermodynamic relationships between heat flow and heating rate,

$$\frac{dH}{dt} = MC_p \frac{dT}{dt} \qquad 4.1$$

where dH/dt is the heat flow in mW, M is the sample mass in g, C_p is the specific heat capacity of the sample in J/kg.K and dT/dt is the heating rate in K/s. At high heating rates the heat flow is proportionally high and the peaks become less well defined. Conversely, at low heating rates insufficient heat flow results in ill defined peaks. There is also a tendency for the peaks to be shifted to higher temperatures with increasing heating rate.

The major peaks A, A1, B, C and D can be interpreted according to recent work by Luo et al.[94], Papazian et al[84]. and de Macedo et al[91]. Without explanation, the peaks are identified as follows,

the small exotherm A is due to S phase GPB zone precipitation,

the exotherm A1 is due to δ′ precipitation,

the endotherm B is due to S phase GPB zone and δ′ dissolution,

the exotherm C is due to S′ or S phase and δ precipitation,
the endotherm D is due to dissolution of S′ or S phase and δ.
The remaining peaks at Y and Z are as yet unidentified.

The base-line curves in Fig. 4.35 demonstrate that base-line drift from the zero position increases with increasing heating rate.

4.8 Fracture Characteristics of Base and CO_2 Weld Metal

4.8.1 Tensile Properties

Tensile tests were performed on base and CO_2 weld metal with the following conditions, where 'S.T.' defines solution treatment at 530°C for ~ 40 minutes, with a heating rate control of 1 or 100 K/min for the weld samples followed by air cooling and 'A' defines ageing for 16 hours at 190°C.

1. unnotched base metal, S.T. + A,
2. notched base metal, S.T. + A,
3. notched weld metal,
4. notched weld metal, heated at 1 K/min to the S.T. temperature,
5. notched weld metal, heated at 100 K/min to the S.T. temperature,
6. notched weld metal, heated at 1 K/min to the S.T. temperature + A,

Microhardness measurements have already demonstrated in section 4.6.2 that a close match in hardness can be achieved between base and weld metal after the application of a suitable post-weld heat treatment namely heating at a rate of 1 K/min to the solution treatment temperature of 530°C, annealing for ~ 40 minutes and ageing for 16 hours at 190°C. Tensile tests were therefore undertaken in order to investigate further the properties of base and weld metal. The notch tensile test was selected as a convenient method for ensuring that failure would occur within the fusion zone; the geometry of the test piece is illustrated in Fig. 3.8 (b).

The suitability of the test was first confirmed by performing unnotched and notched tensile tests on base metal samples, as the ratio of notch tensile strength to unnotched yield strength has been shown to provide a good measure of toughness in Al-Li based

alloys[126].

Five tests were performed in each of the above heat treatment conditions and table 4.2 shows the results for unnotched and notched tensile strength, unnotched elongation to failure and unnotched 0.2 % proof stress. The results presented in this table demonstrate that for the base metal the ratio of the notch tensile strength to the unnotched yield strength is ~ 1.19 which is comparable to results given by Gregson.

Considering the weld metal, the results have shown that the notched weld metal strength is lowest in the as-welded condition, with a value of 235 ± 5 MPa. However, solution treatment and air cooling can increase this to ~ 312 ± 38 Mpa and ~ 323 ± 28 MPa for heating rates of 1 and 100 K/min to the solution treatment temperature respectively. Maximum strength was achieved after solution treating and ageing which resulted in a tensile strength of ~ 415 ± 19 MPa. This value is comparable to the notched base metal strength in the same heat treatment condition; ~ 426 ± 5 MPa.

4.8.2 Fractography

The SEM micrographs from the fracture surface of an unnotched base metal tensile specimen which was tested after solution treating and ageing are shown in Fig. 4.36. Fig. 4.36 (a) is taken at a low magnification and shows that large steps exist on the fracture surface together with secondary cracks, for example at the position marked 'S'. The secondary cracks are oriented perpendicular to the short transverse direction of the sheet. At higher magnifications in Fig. 4.36 (b) and (c) the mode of failure is revealed. The crack has propagated intergranularly along high angle grain boundaries to produce relatively large grain faces, e.g. marked 'I', due to the pancake structure of the base metal grains in the rolling direction. Smaller grains can be seen where the crack has followed lower angle grain boundaries. Furthermore, shallow dimples can be seen such as at 'D'. These are probably caused by void formation around particles such as S′ (Al_2CuMg) or T_1 (Al_2CuLi) which form at the grain boundaries during ageing.

The failure mode of the notched as-welded sample is shown in Fig. 4.37. At a low magnification in Fig. 4.37 (a) two very different regions can be seen on the fracture

surface. On the left, large rupture steps are present with cracks which run the entire length of the step, e.g. marked 'S'. This region represents the coarse columnar structure in the upper region of the weld and failure has occurred along cell boundaries. Fig. 4.37 (b) reveals that the steps were caused by a mixed mode of failure. The crack has followed the cell boundaries but some transgranular failure has occurred as shown by the large ductile dimples separating the rupture steps, marked 'DD'. What appear to be slip bands, marked 'SB', can also be seen on the surfaces of the elongated grains. The fracture surface of the lower region of the weld is shown in Figs. 4.37 (c) and (d) and the fine equiaxed grains are clearly visible. Individual grains e.g. marked 'C' can be seen which suggests that failure occurred intergranularly and the dendritic morphology is visible on the grain surfaces, marked 'I'. However, some regions of ductility can be seen. At positions marked 'T' there are obvious ductile dimples due to transgranular failure and in Fig. 4.37 (d) very shallow dimples can be seen on the grain surfaces due to grain boundary precipitates. Again, secondary cracks e.g. marked 'S' in Fig. 4.37 (d) are present.

The fracture surfaces of the welds which were solution treated with heating rates of 1 and 100 K/min are very similar in appearance. Fig. 4.38 (a) from the 1 K/min sample shows that the fracture surface of the upper region of the weld is much smoother when compared to Fig. 4.37 (a) from the as-welded sample. Ductile dimples which were observed in Fig. 4.37 (b) are not apparent in Fig. 4.38 (b) and failure has occurred predominantly intergranularly along prior cell boundaries. The dendritic structure is still visible on the grain surfaces as in Fig. 4.38 (a). This can be compared to the micrograph in Fig. 4.39 (a) for the 100 K/min weld also taken from the upper region of the weld. The dendritic structure is clearly visible on the grain faces marked 'I'. Furthermore, ductile dimples can be seen at 'T' where a grain has failed transgranularly. The major differences, then, between the heating rates appear in the lower region of the weld. It has already been shown in table 4.2 that there is negligible difference in fracture strength between the heating rates and this can be explained as follows. Figs. 4.38 (b) and 4.39 (b) are comparable in that failure has occurred predominantly along grain boundaries and individual grains are visible in both Fig. 4.38 (b) and Fig. 4.39 (b). However, Fig. 4.39 (b) shows generally larger

grains and the region ringed 'A' appears to consist of a larger, single grain with an internal dendritic sub-structure. It is likely that the crack has propagated along the spatial distribution of undissolved intermetallic particles within the grain. Shallow dimples can be seen on grain surfaces in Fig. 4.39 (b) which is characteristic of low ductility intergranular failure. Regions of deeper dimples associated with some more ductile, transgranular failure are also present, marked 'T'.

After solution treating and ageing failure is intergranular predominantly at high angle grain boundaries, though transgranular regions are visible marked 'T' which contain large ductile dimples in Figs. 4.40 (a), (b) and (c). Secondary cracks are also present marked 'S'. On the intergranular region marked 'I' in Fig. 4.40 (c) the dendritic structure is present together with shallow dimples.

In summary, solution treating and ageing can produce comparable fracture strengths in notched tensile specimens of base and weld metal. However, there seems to be no observed difference in fracture strength between weld samples heat treated to contain either large or small grains. This can be explained by considering the failure mode of the samples. Failure occurs intergranularly in the small grain sample, where the grain size is essentially that of the cast structure. However, when large grains are present, for example after a heating rate of 100 K/min to the solution treatment temperature, cracks can propagate transgranularly across the large grains. This can be interpreted as an intersubgranular mode of failure, as indicated in Fig. 4.41. This is because the residual cast structure illustrated in Fig. 4.25 (a) is present within the large grains and low angle or sub-grain boundaries are formed during solution treatment. Thus there is an easy, transgranular path for crack propagation. The fact that shallow dimples are formed on the transgranular surfaces suggests that the actual failure mechanism is one of intersubgranular in the large grains. Thus, it would appear that the failure mode in both small grain and large grain welds is controlled by the presence of the undissolved intermetallic particles both at grain boundaries and within the grains. This is because the spatial distribution of the intermetallic particles is essentially the same after both heat treatments. After solution treating and ageing the micrographs suggest that there is an increase in ductility, both transgranular and

intergranular, though this can only be estimated qualitatively.

Table 4.1 Table showing vol.% porosity in 8090 CO_2 laser welds for different sheet thicknesses and welding speeds, with a laser power of 2 kW.

Sheet Thickness	Volume percent porosity for various welding speeds				
	60 mm/s	80 mm/s	100 mm/s	120 mm/s	140 mm/s
4 mm	1.50	0.98	0.94	0.67	-
4 mm	3.00	-	2.30	-	-
3 mm	-	1.56 (FP)	0.68 (FP)	0.30	0.10
3 mm	0.78 (FP)	-	1.10	-	-

FP = fully penetrating welds. The remainder are partially penetrating.

Table 4.2 Table of 8090 base and CO_2 weld metal strengths in various heat treatment conditions.

Sample	Tensile strength (MPa)	Strain to failure	0.2% Proof stress (MPa)
Unnotched B.M. S.T. + A	452 ± 5	0.061	357 ± 7
Notched B.M. S.T. + A	426 ± 5	-	-
Notched W.M.	235 ± 18	-	-
Notched W.M. S.T. at 1 K/min	312 ± 38	-	-
Notched W.M. S.T. at 100 K/min	323 ± 28	-	-
Notched W.M. S.T. at 1 K/min + A	415 ± 19	-	-

The error indicated is two standard deviations about the mean.

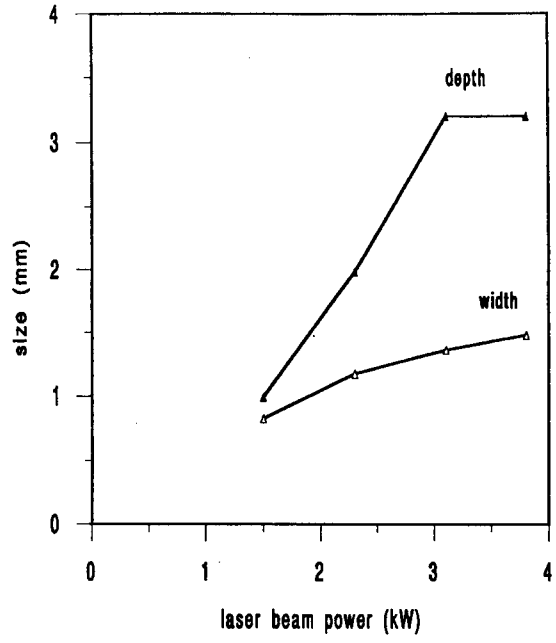

(a)

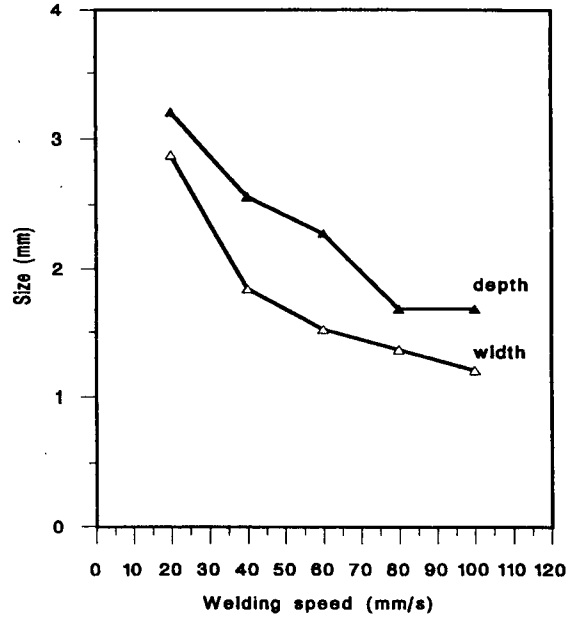

(b)

Figure 4.1. The effect of welding parameters on 8090 CO_2 weld top bead width, w, depth of penetration, d, and weld bead shape for 3.2 mm thick sheet. (a) shows the variation in w and d with incident laser beam power at 100 mm/s welding speed, (b) illustrates the variation of w and d with welding speed at 2.1 kW laser beam power and (c) illustrates the influence of beam focus position on weld bead shape.

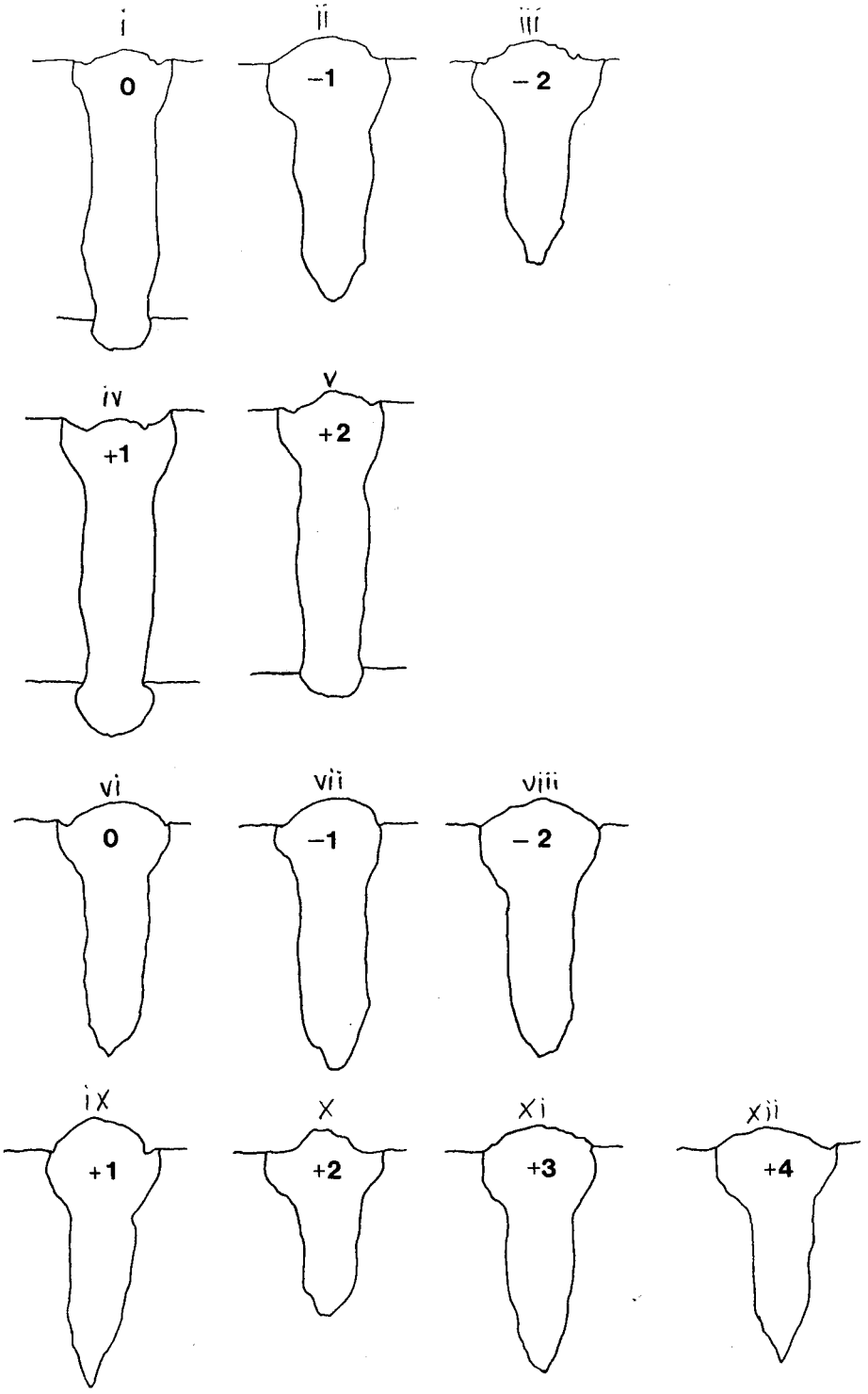

(c)

Figure 4.1. The effect of welding parameters on 8090 CO_2 weld top bead width, w, depth of penetration, d, and weld bead shape for 3.2 mm thick sheet. (a) shows the variation in w and d with incident laser beam power at 100 mm/s welding speed, (b) illustrates the variation of w and d with welding speed at 2.1 kW laser beam power and (c) illustrates the influence of beam focus position on weld bead shape.

(a)

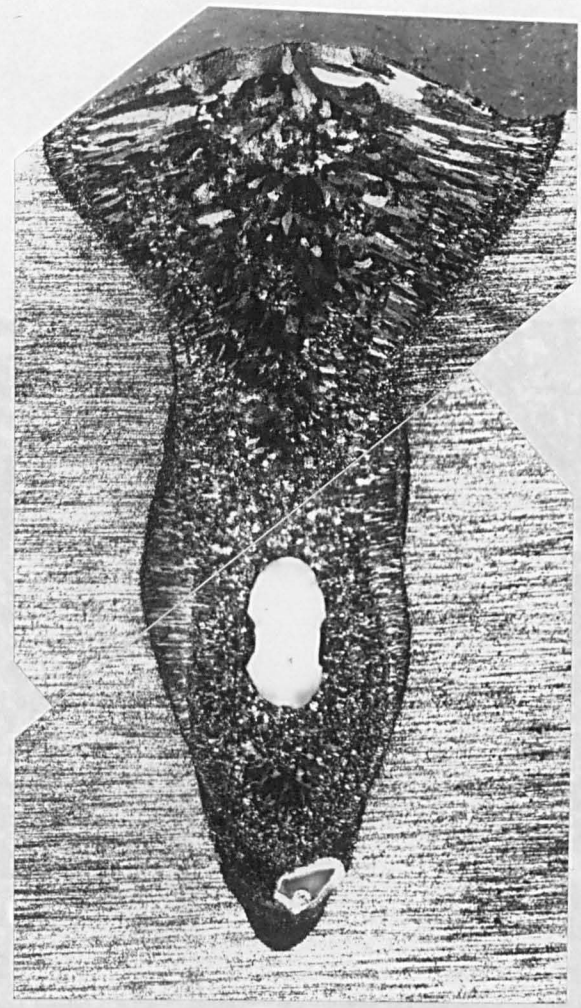

(b)

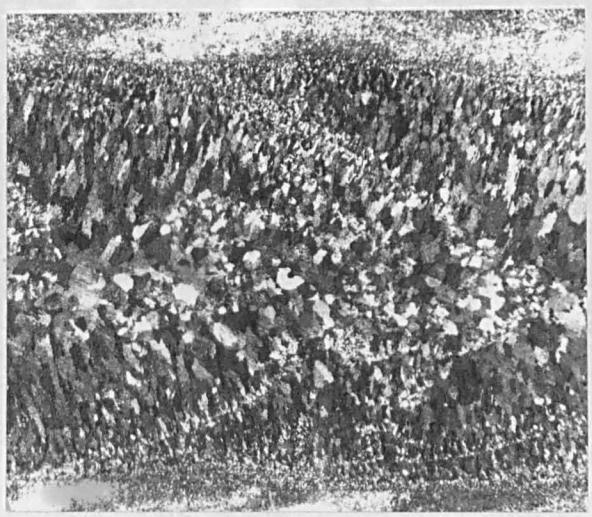

250μm

Figure 4.2. Optical micrographs showing the grain structure of a partial penetration CO_2 weld in 3.2 mm thick 8090 sheet (3.1 kW, 100 mm/s). Anodized structures viewed under polarized light. (a) shows a transverse plane, (b) shows a rolling plane close to the top surface and (c) is a longitudinal plane along the weld centre-line.

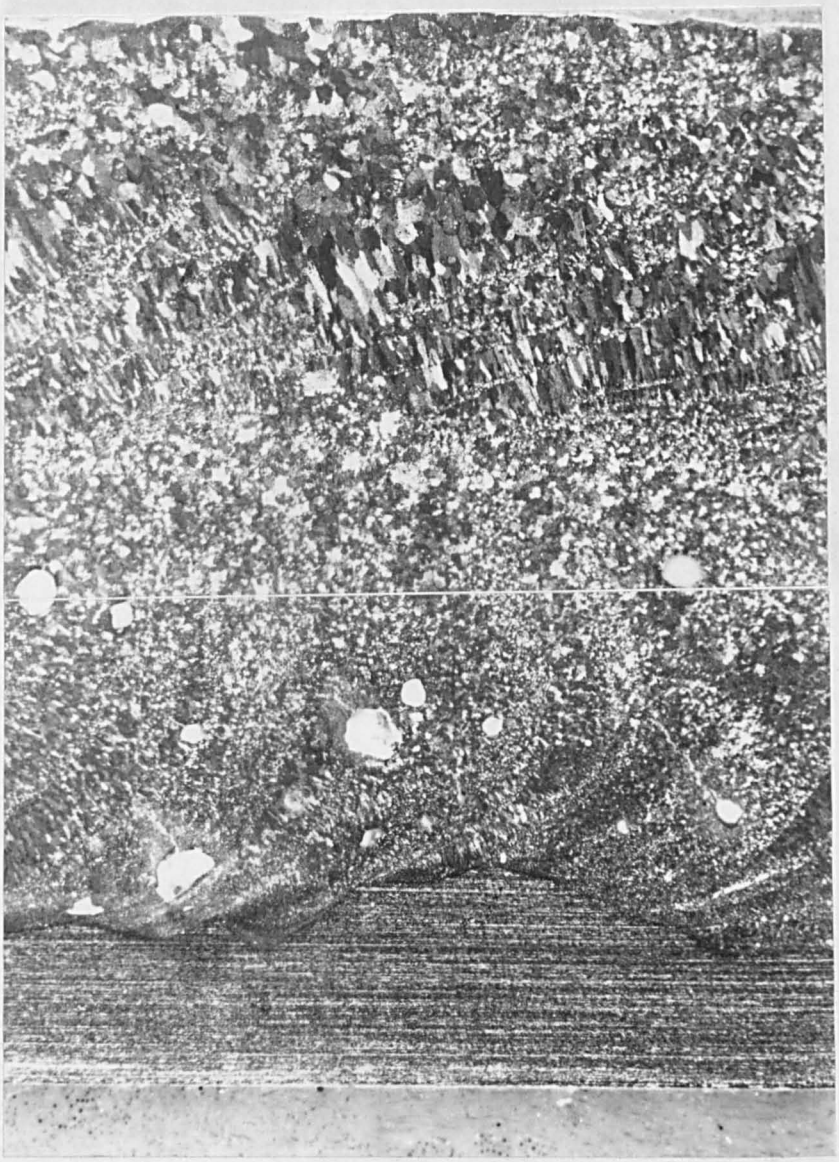

(c) 250μm

Figure 4.2. Optical micrographs showing the grain structure of a partial penetration CO_2 weld in 3.2 mm thick 8090 sheet (3.1 kW, 100 mm/s). Anodized structures viewed under polarized light. (a) shows a transverse plane, (b) shows a rolling plane close to the top surface and (c) is a longitudinal plane along the weld centre-line.

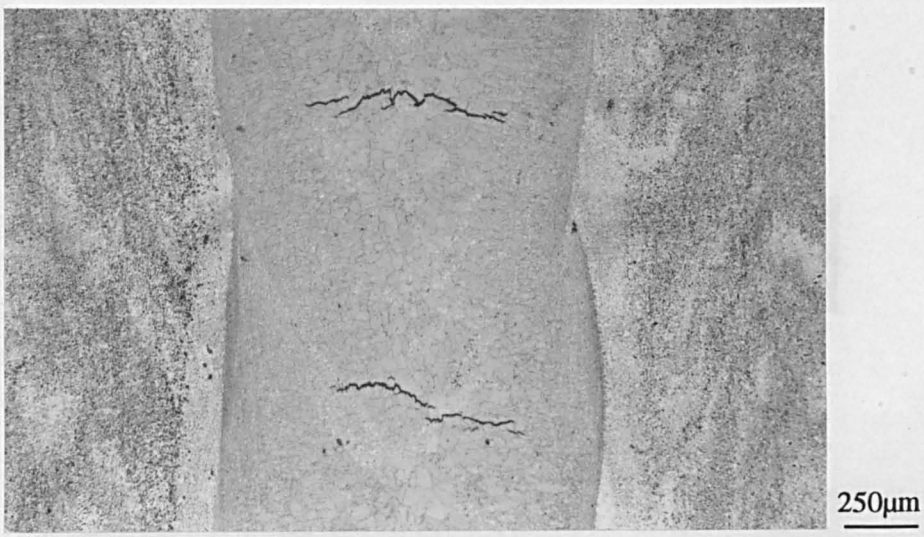

Figure 4.3. Optical micrograph illustrating the nature of 8090 CO_2 weld cracking. On a near surface plane cracks run across the weld width.

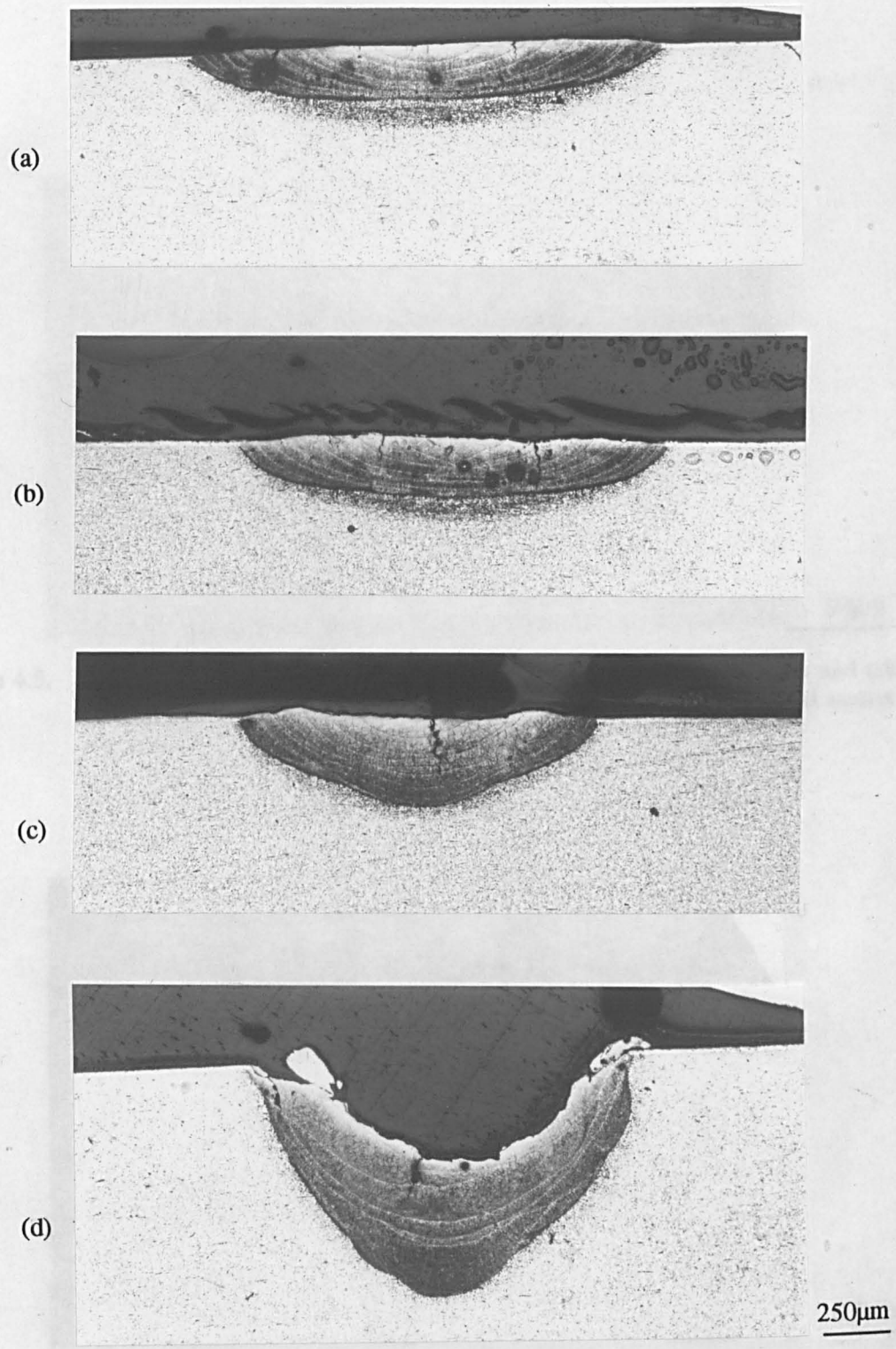

Figure 4.4. Optical micrographs of 8090 Nd:YAG welds illustrating macrostructure and the variation in weld bead shape with laser beam focus. (a) represents +4 mm focus, (b) represents +2 mm focus, (c) represents surface focus and (d) represents -2 mm focus. (speed=5mm/s, ave. power=785W)

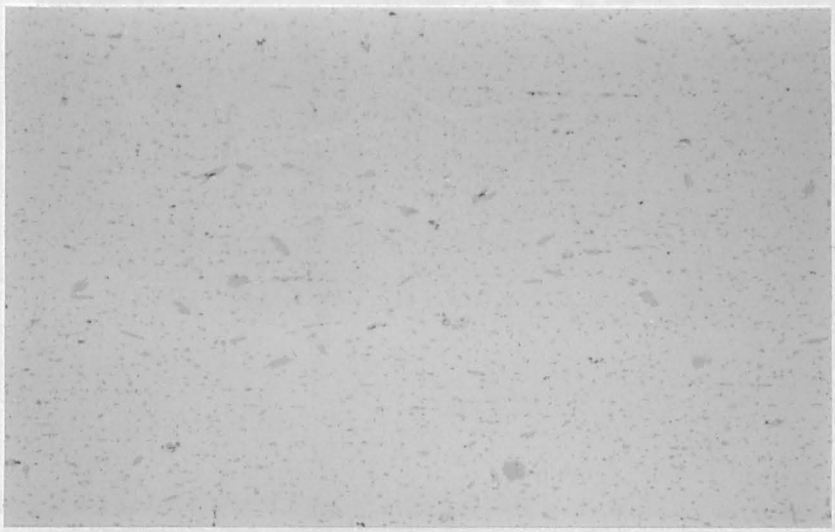

Figure 4.5. Optical micrograph of 8090 base metal in the unetched condition and taken from a transverse plane. Intermetallic phases are seen in the α-Al matrix.

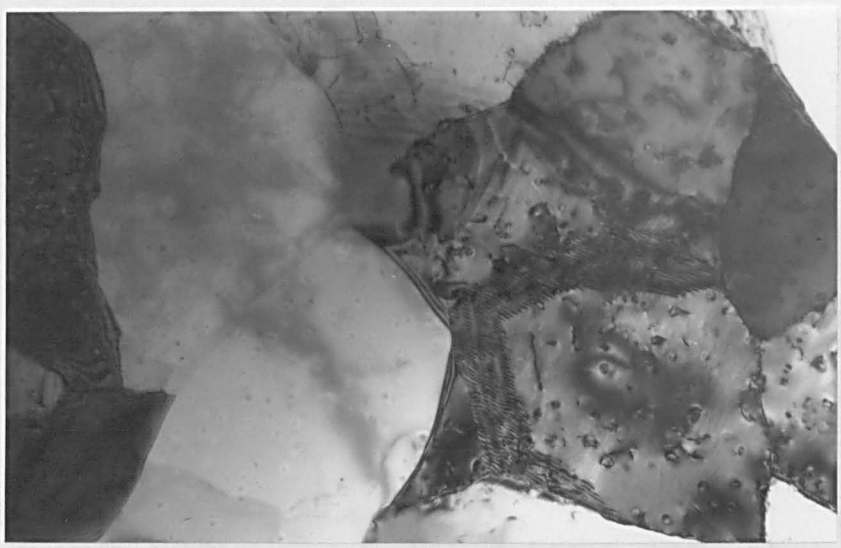

Figure 4.6. A transmission electron micrograph of 8090 base metal in the as-received condition showing the sub-grain structure.

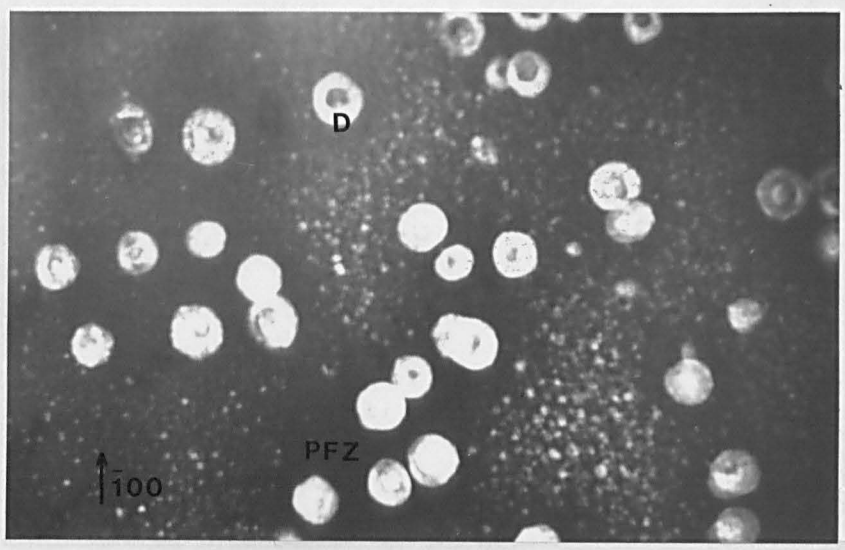

(a)

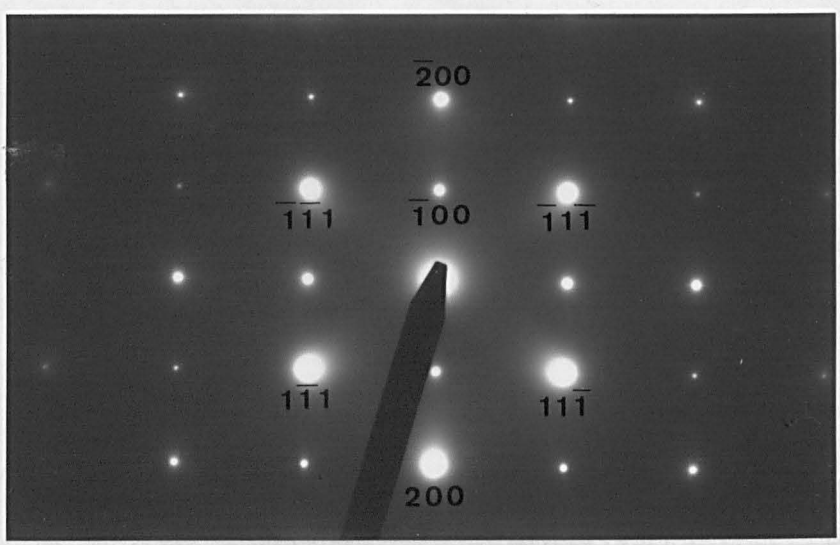

(b)

Figure 4.7. As-received 8090 base metal. Dark field transmission electron micrograph is shown in (a) using a δ′ superlattice reflection from a [011] zone axis orientation. Homogeneous δ′ and composite δ′/β′ precipitates are visible. (b) shows the corresponding selected area diffraction pattern.

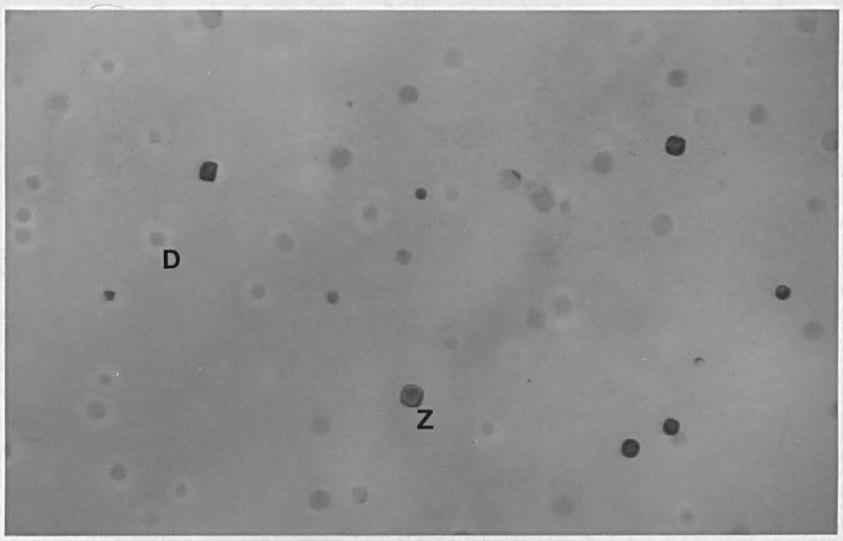

Figure 4.8. Transmission electron micrograph of 8090 sheet in the as-received condition. Bright field image close to a [001] zone axis. Faint contrast from δ′ and β′ can be seen with strong contrast from blocky precipitates such as Z, identified as tetragonal Al_3Zr.

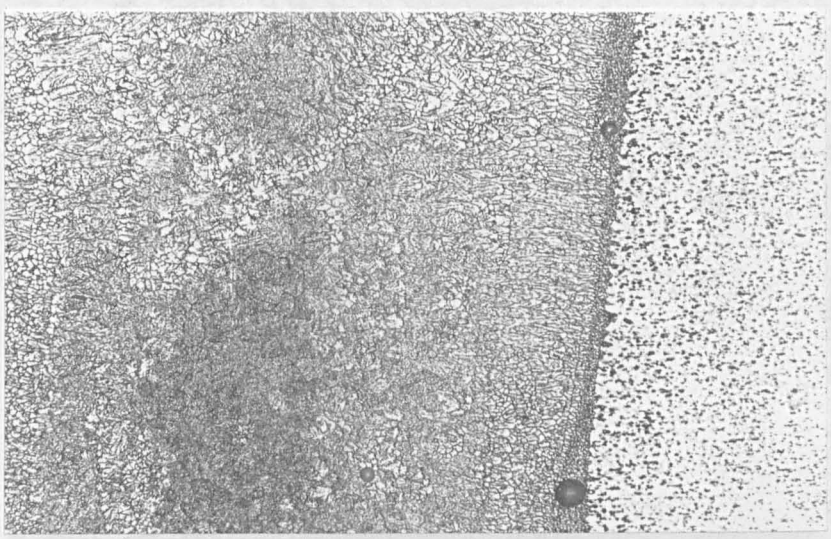

Figure 4.9. Optical micrographs of an etched 8090 CO_2 weld transverse section. (a) illustrates small globular grains at the fusion boundary with columnar grains growing into the weld. (b) shows that the HAZ consists of star-shaped intergranular regions. (c) is taken from the weld centre and shows the equiaxed nature of the grains

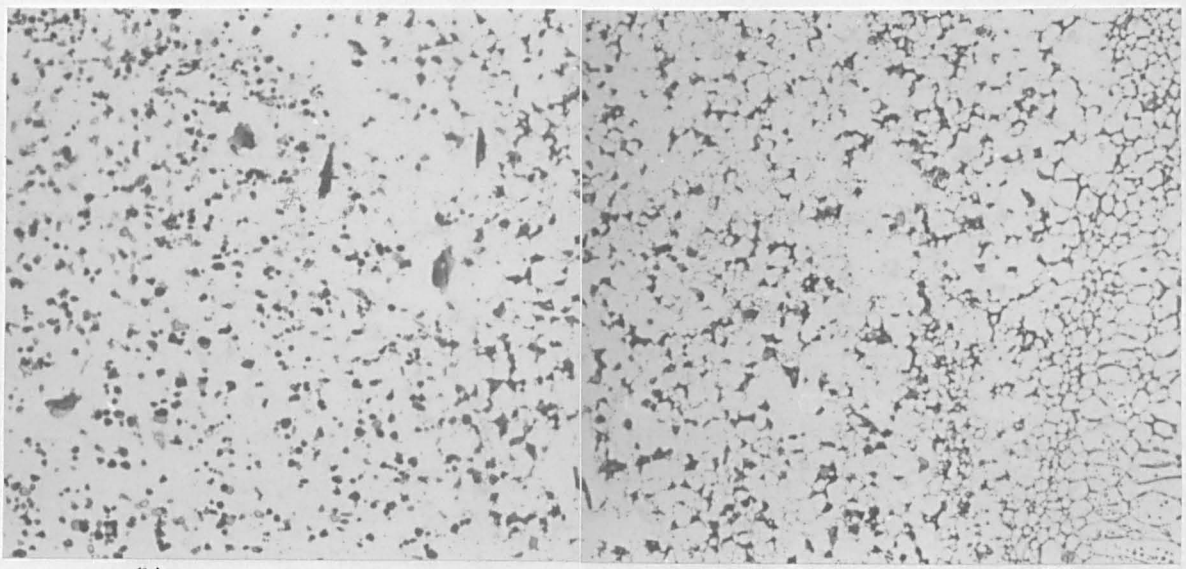

(b) 25μm

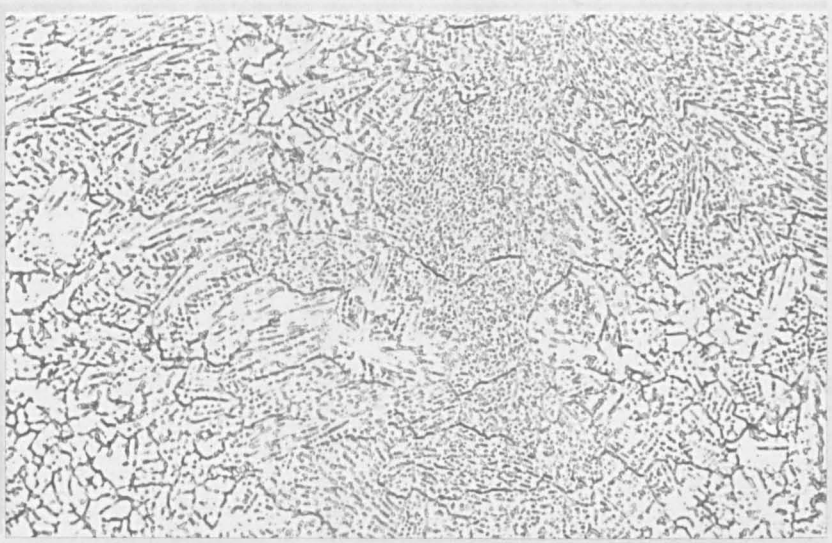

(c) 25μm

Figure 4.9. Optical micrographs of an etched 8090 CO_2 weld transverse section. (a) illustrates small globular grains at the fusion boundary with columnar grains growing into the weld. (b) shows that the HAZ consists of star-shaped intergranular regions. (c) is taken from the weld centre and shows the equiaxed nature of the grains.

(a)

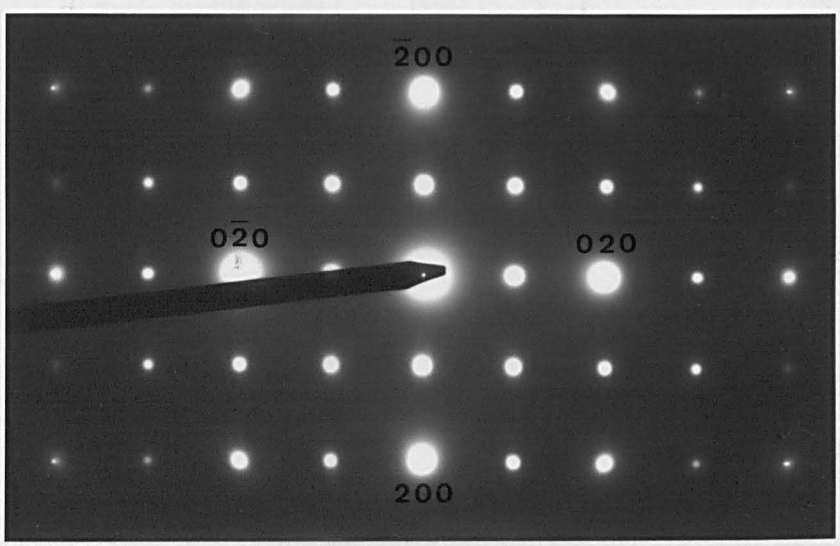

(b)

Figure 4.10. Transmission electron micrograph of the 8090 CO_2 weld solidification structure is shown in (a), the SADP shown in (b) and a bright field micrograph illustrating δ′ is shown in (c). EDX spectra from the intercellular region and α-Al cells are shown in (d) and (e) respectively.

(c)

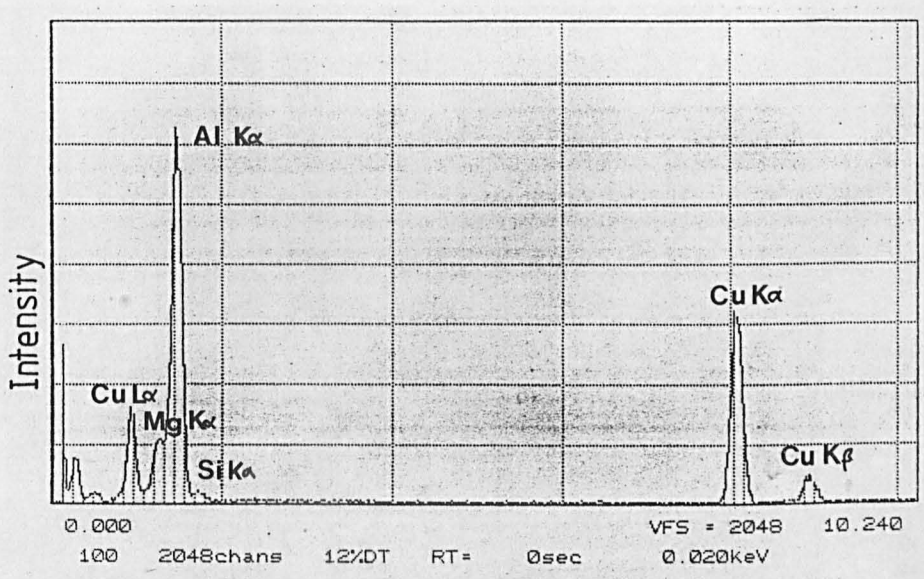

(d)

Figure 4.10. Transmission electron micrograph of the 8090 CO_2 weld solidification structure is shown in (a), the SADP shown in (b) and a bright field micrograph illustrating δ′ is shown in (c). EDX spectra from the intercellular region and α-Al cells are shown in (d) and (e) respectively.

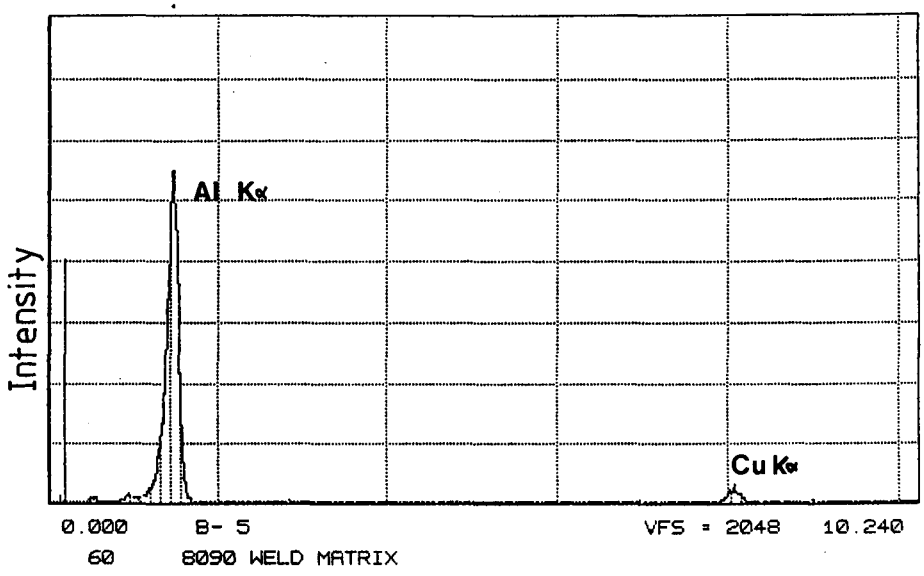

(e)

Figure 4.10. Transmission electron micrograph of the 8090 CO_2 weld solidification structure is shown in (a), the SADP shown in (b) and a bright field micrograph illustrating δ' is shown in (c). EDX spectra from the intercellular region and α-Al cells are shown in (d) and (e) respectively.

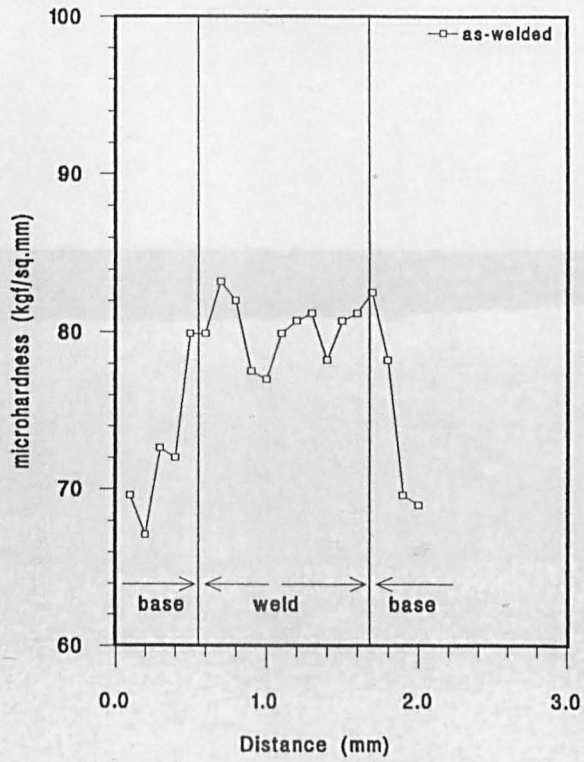

Figure 4.11. A microhardness profile taken across a 8090 CO_2 weld transverse section.

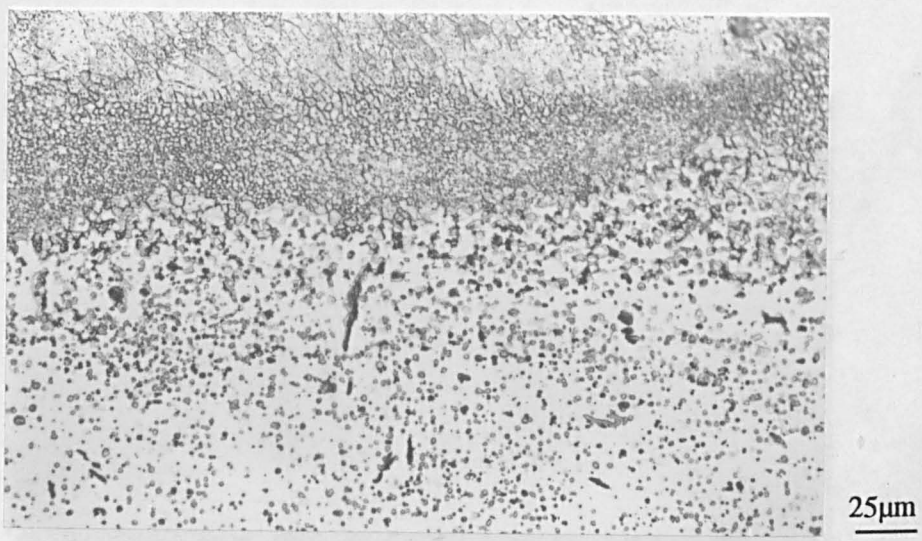

Figure 4.12. Optical micrograph illustrating the nature of the 8090 Nd:YAG weld fusion boundary and HAZ. Taken from a near surface section, small globular grains can be seen at the fusion boundary and star-shaped intermetallics are present very close to the fusion boundary.

(a)

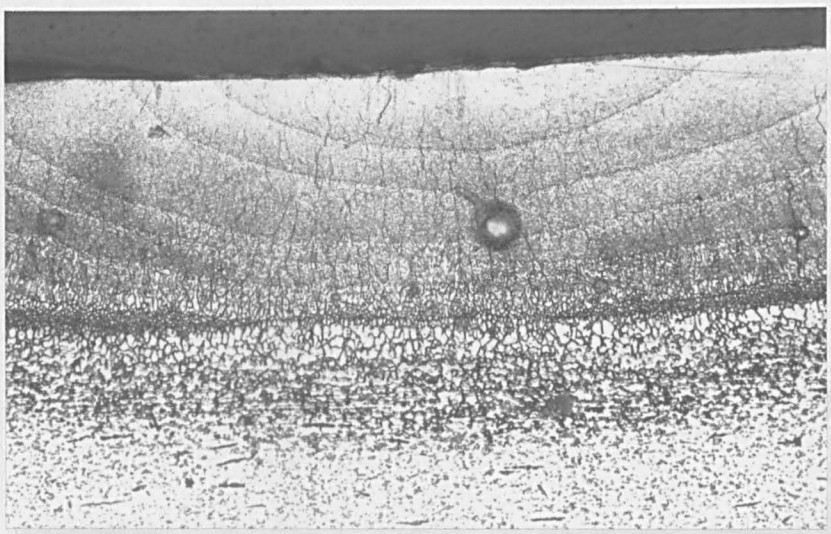

50μm

(b)

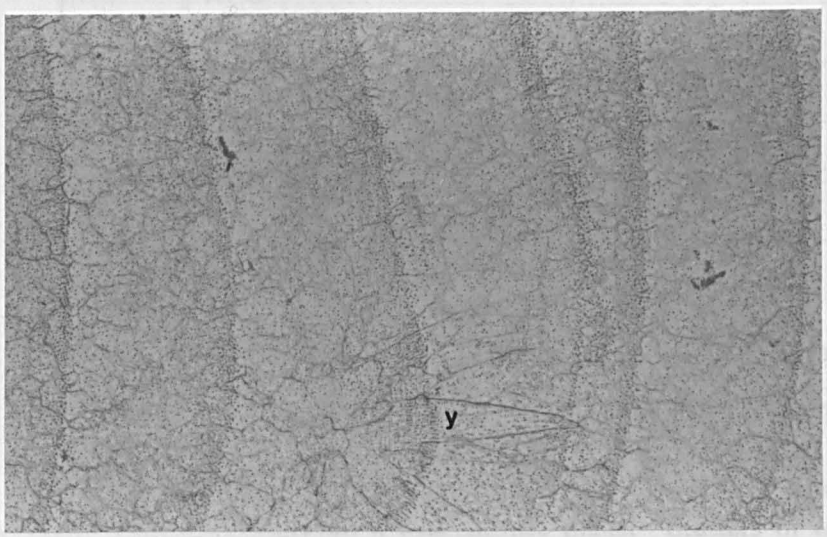

25μm

Figure 4.13. Optical micrographs of etched 8090 Nd:YAG transverse (a), and near surface section, (b).

(a)

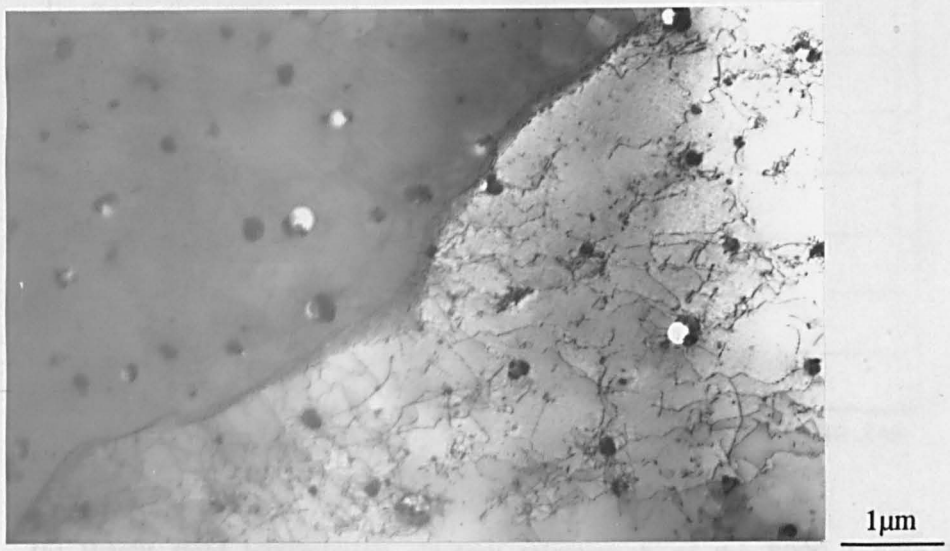

(b)

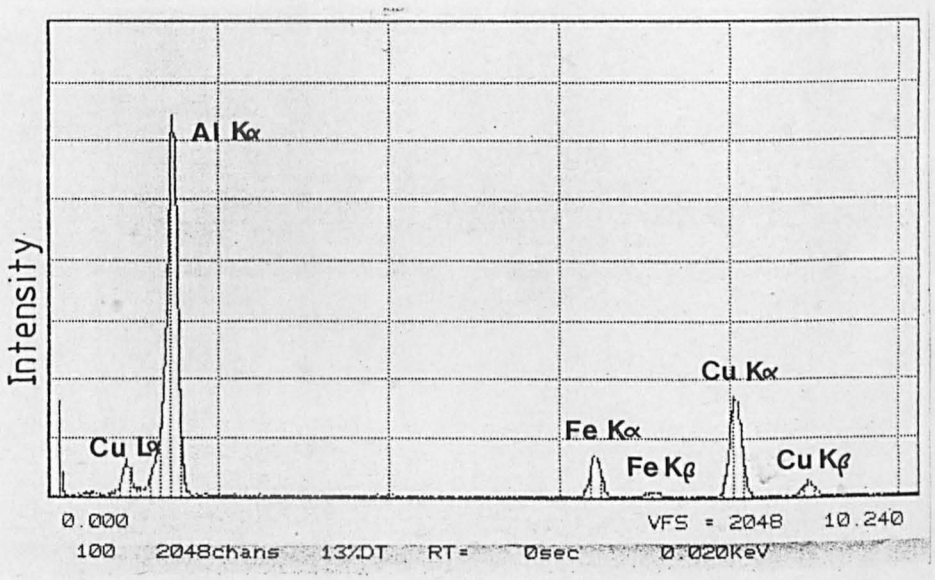

Figure 4.14. (a) Bright field transmission electron micrograph of the 8090 Nd:YAG solidification structure on a near surface plane. Clusters of intermetallic particles can be observed together with EDAX spectra from (b) the particles and (c) the α-Al cells.

(c)

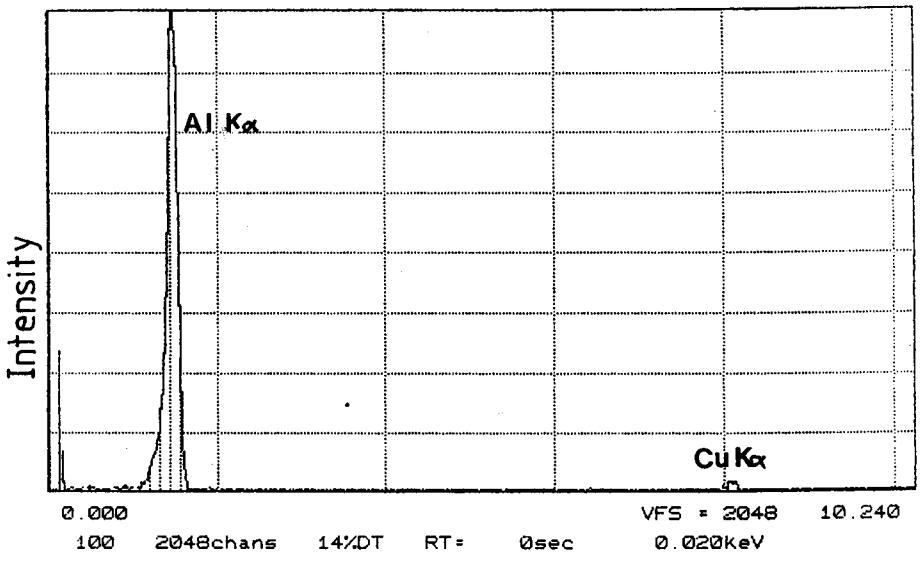

Figure 4.14. (a) Bright field transmission electron micrograph of the 8090 Nd:YAG solidification structure on a near surface plane. Clusters of intermetallic particles can be observed together with EDAX spectra from (b) the particles and (c) the α-Al cells.

(a)

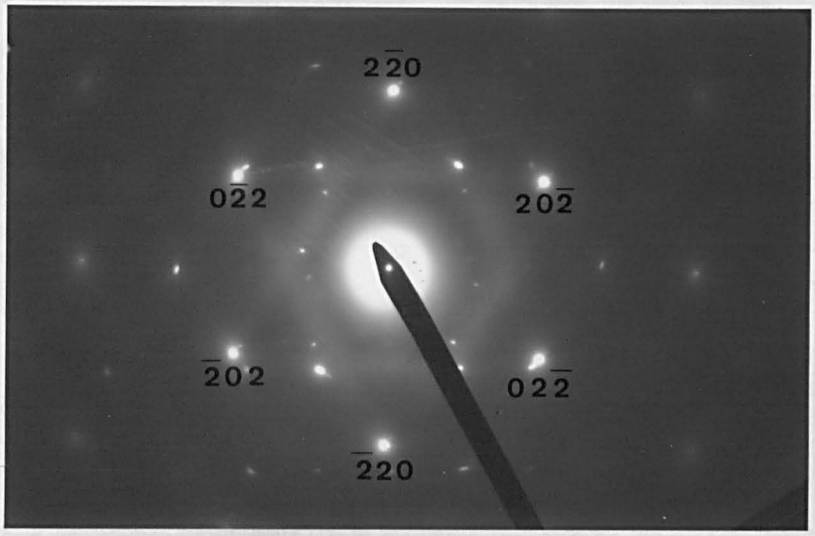

(b)

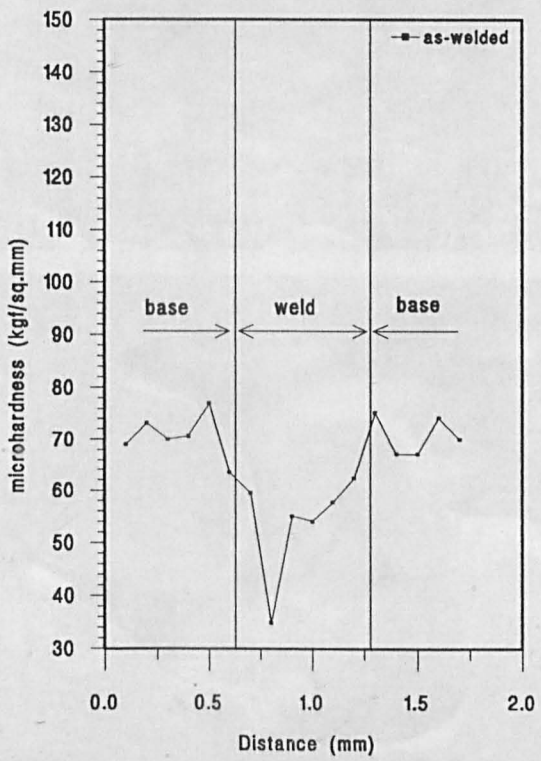

Figure 4.15. (a) A selected area diffraction pattern taken from a Nd:YAG 8090 weld with a [111] zone axis. $L1_2$ reciprocal lattice spots are absent, the non Al spots are due to Al_2O_3. (b) shows the hardness profile across a near surface section of the weld.

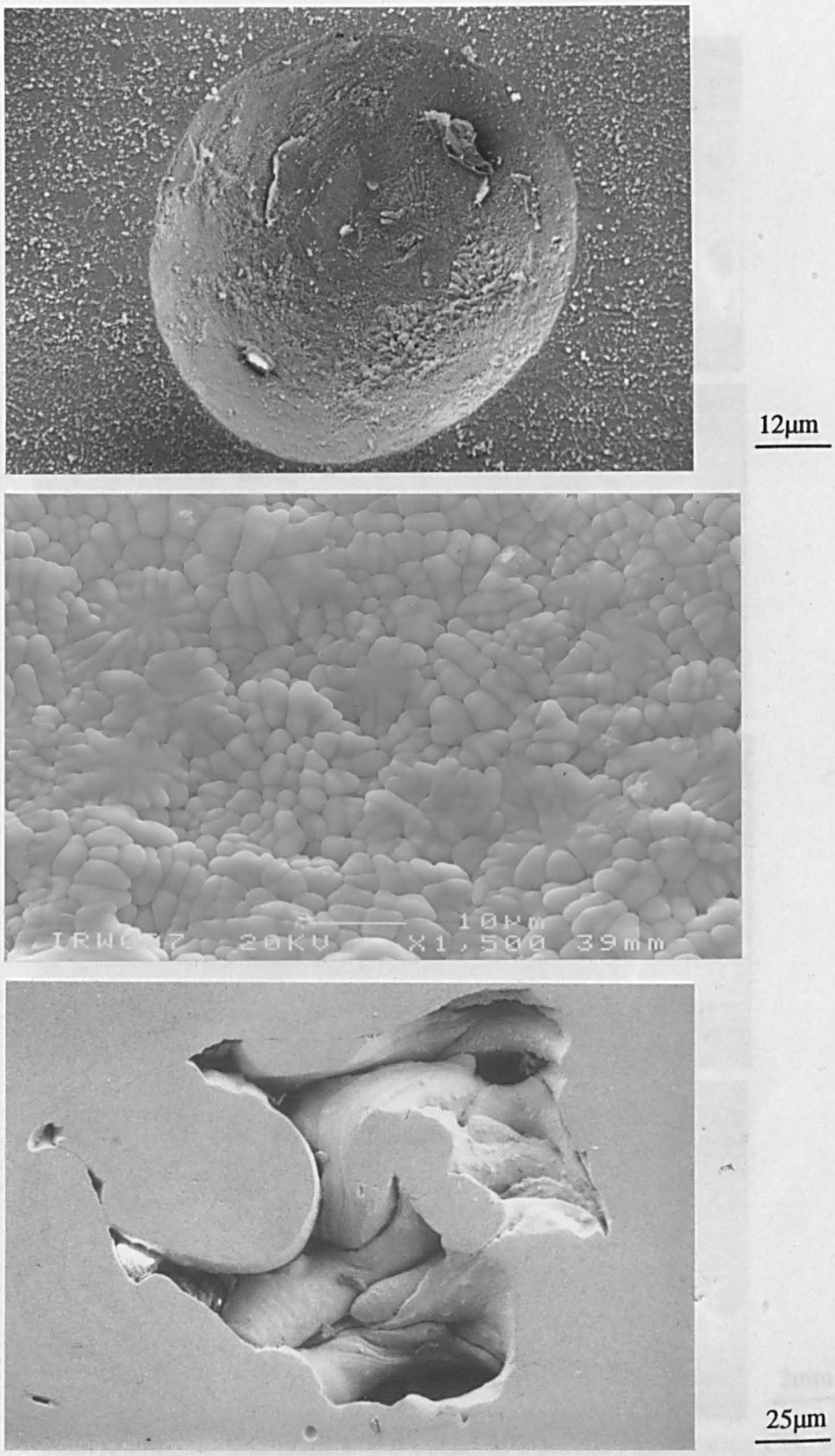

Figure 4.16. Scanning electron micrographs illustrating the different forms of porosity in a partially penetrating 8090 CO_2 weld. A regular spherical pore is shown in (a) with the pore wall structure in (b) and (c) shows a typical example of an irregular pore with folds of metal.

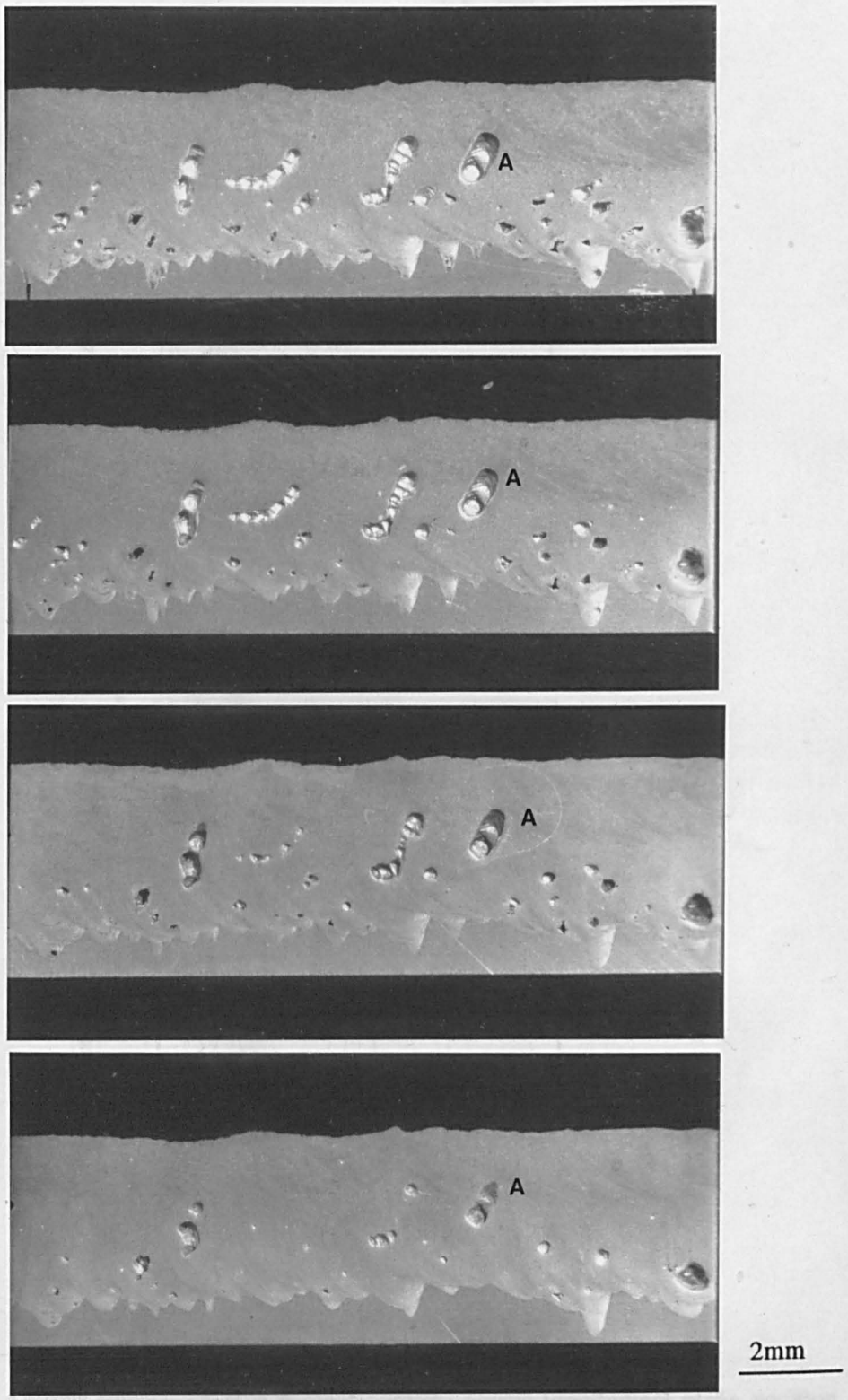

Figure 4.17. Macrophotographs of longitudinal planes in a partially penetrating CO_2 weld in 4 mm thick 8090 sheet. The plane shown in (a) was very close to the weld centre-line whilst (b), (c), and (d) were from planes 50, 100 and 150 μm from (a) respectively.

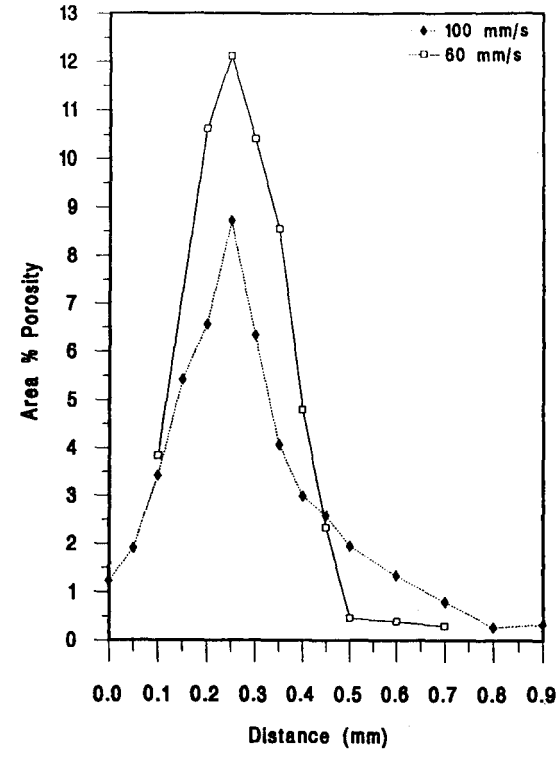

(a)

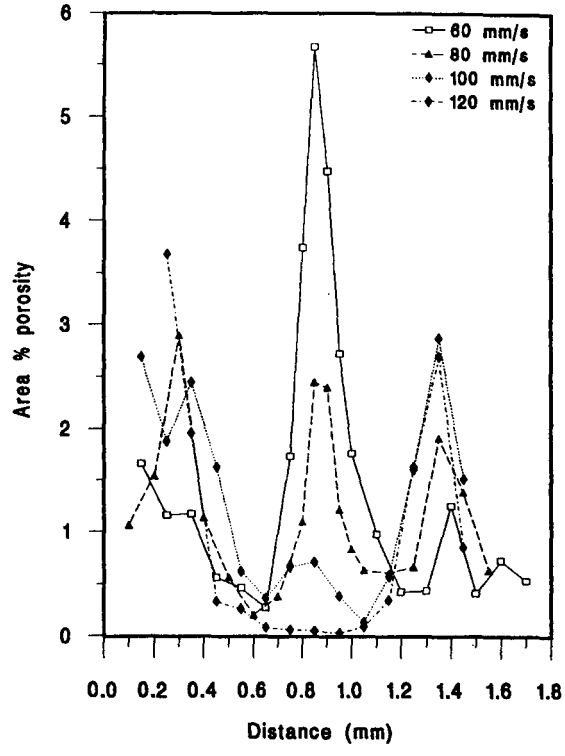

(b)

Figure 4.18. Graphs illustrating area percent porosity versus longitudinal plane position (arbitrary origin) for a laser beam power of 2 kW. (a) represents welding speeds of 60 and 100 mm/s on 4 mm thick sheet. (b) represents welding speeds of 60, 80, 100 an 120 mm/s on 4 mm thick sheet and (c) represents welding speeds of 80, 100, 120 and 140 mm/s on 3 mm thick sheet.

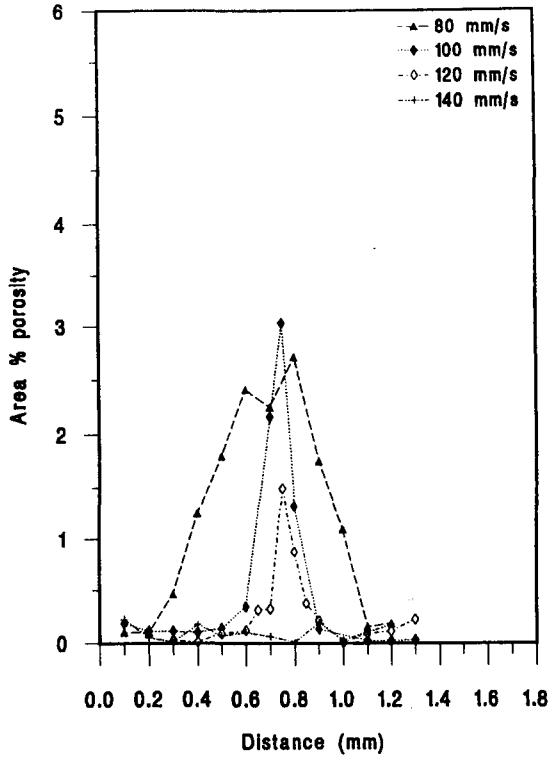

(c)

Figure 4.18. Graphs illustrating area percent porosity versus longitudinal plane position (arbitrary origin) for a laser beam power of 2 kW. (a) represents welding speeds of 60 and 100 mm/s on 4 mm thick sheet. (b) represents welding speeds of 60, 80, 100 an 120 mm/s on 4 mm thick sheet and (c) represents welding speeds of 80, 100, 120 and 140 mm/s on 3 mm thick sheet.

(a)

(b)

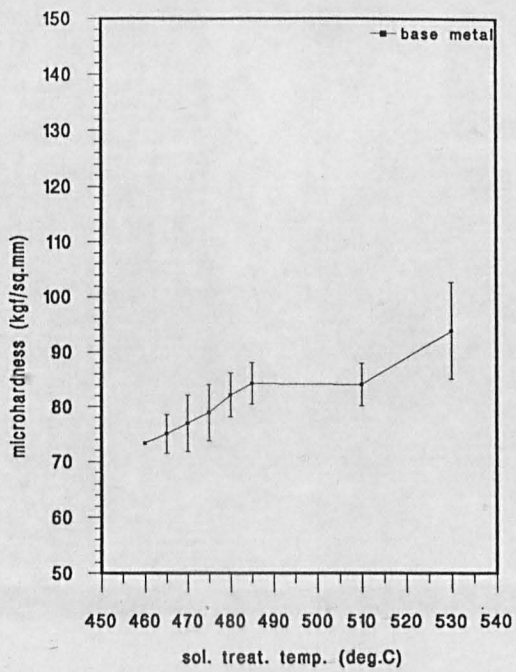

Figure 4.19. (a) Etched optical micrograph of 8090 base metal after solution treatment at 530°C. On this transverse section a region of Li depletion can be seen at the surface. (b) Plots of microhardness vs. solution treatment temperature of the 8090 base metal.

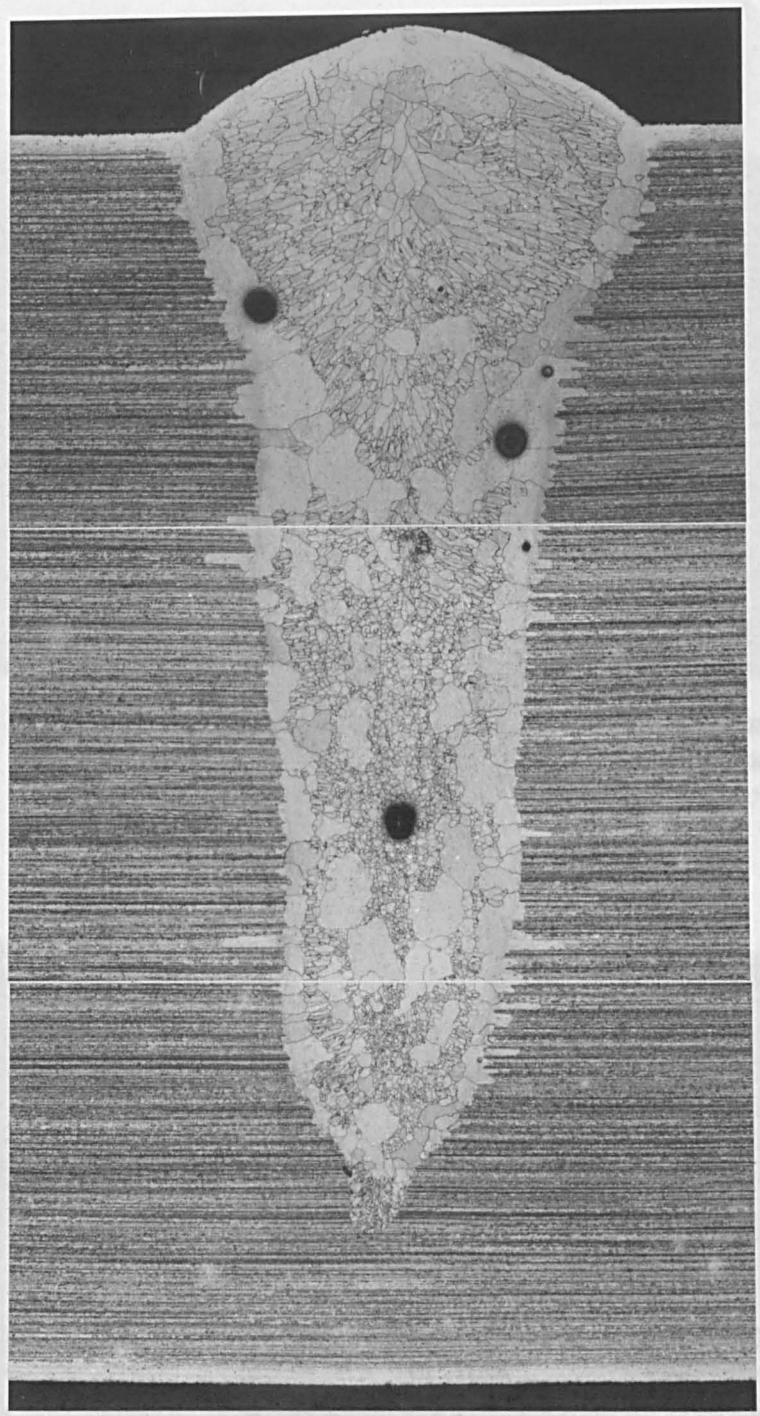

(a)

250μm

Figure 4.20. Optical micrographs of CO_2 8090 weld after solution treatment at 530°C without heating rate control. (a) shows the entire fusion zone and massive grains can be seen throughout. (b) is at a higher magnification showing the residual cast structure.

(b)

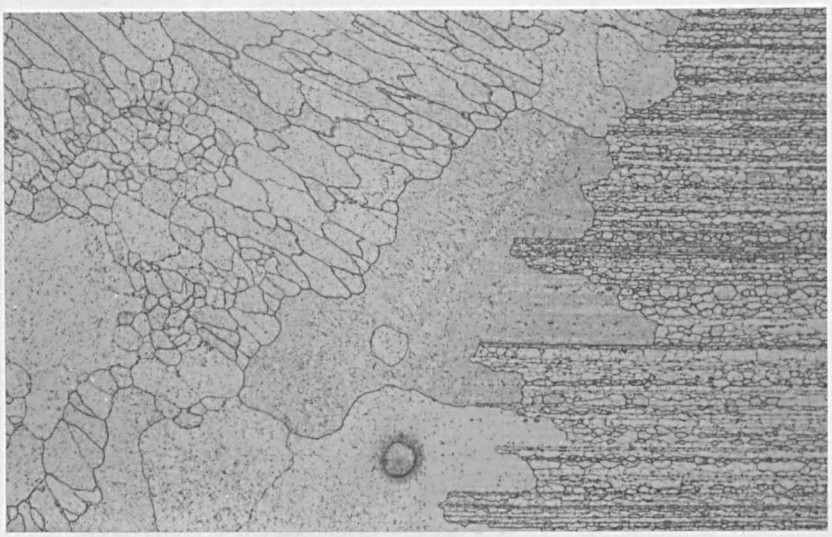

Figure 4.20. Optical micrographs of CO_2 8090 weld after solution treatment at 530°C without heating rate control. (a) shows the entire fusion zone and massive grains can be seen throughout. (b) is at a higher magnification showing the residual cast structure.

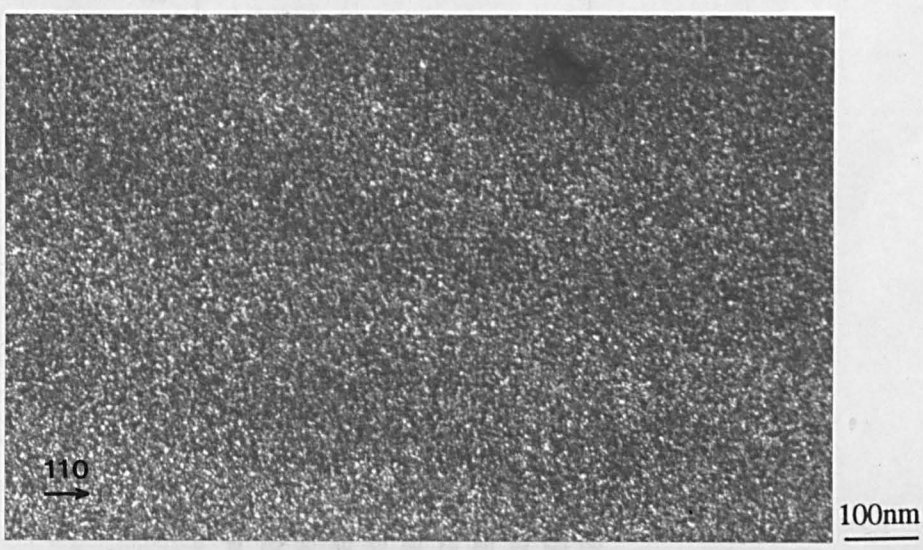

Figure 4.21. Centred dark field transmission electron micrograph of the solution treated 8090 CO_2 weld without heating rate control. Taken using a δ′ reciprocal lattice spot, a uni-modal precipitate distribution is observed. Z=[$\bar{1}$12]

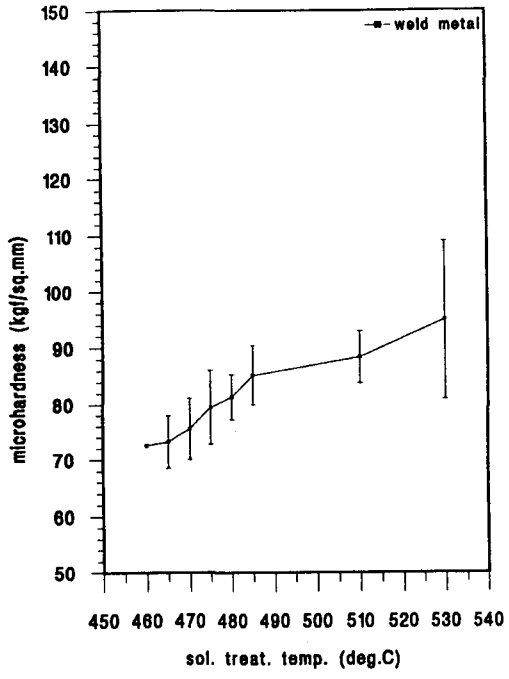

Figure 4.22. Plot showing the influence of 8090 CO_2 weld solution treatment temperature on fusion zone microhardness.

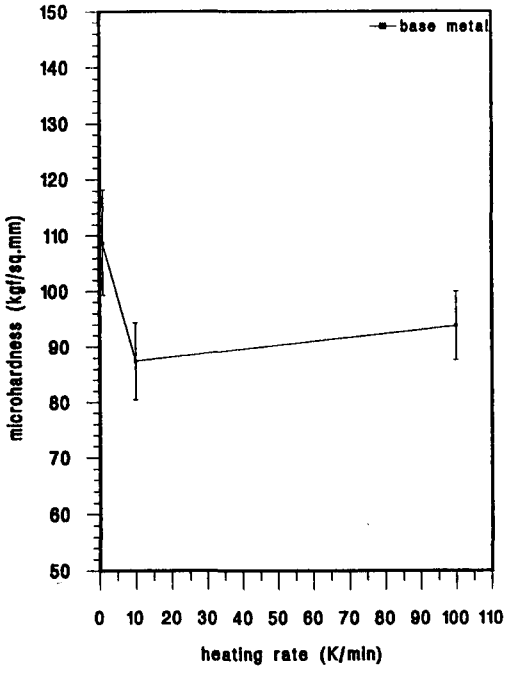

Figure 4.23. Plot showing the influence of heating rate to the solution treatment temperature (530°C) on the 8090 base metal microhardness.

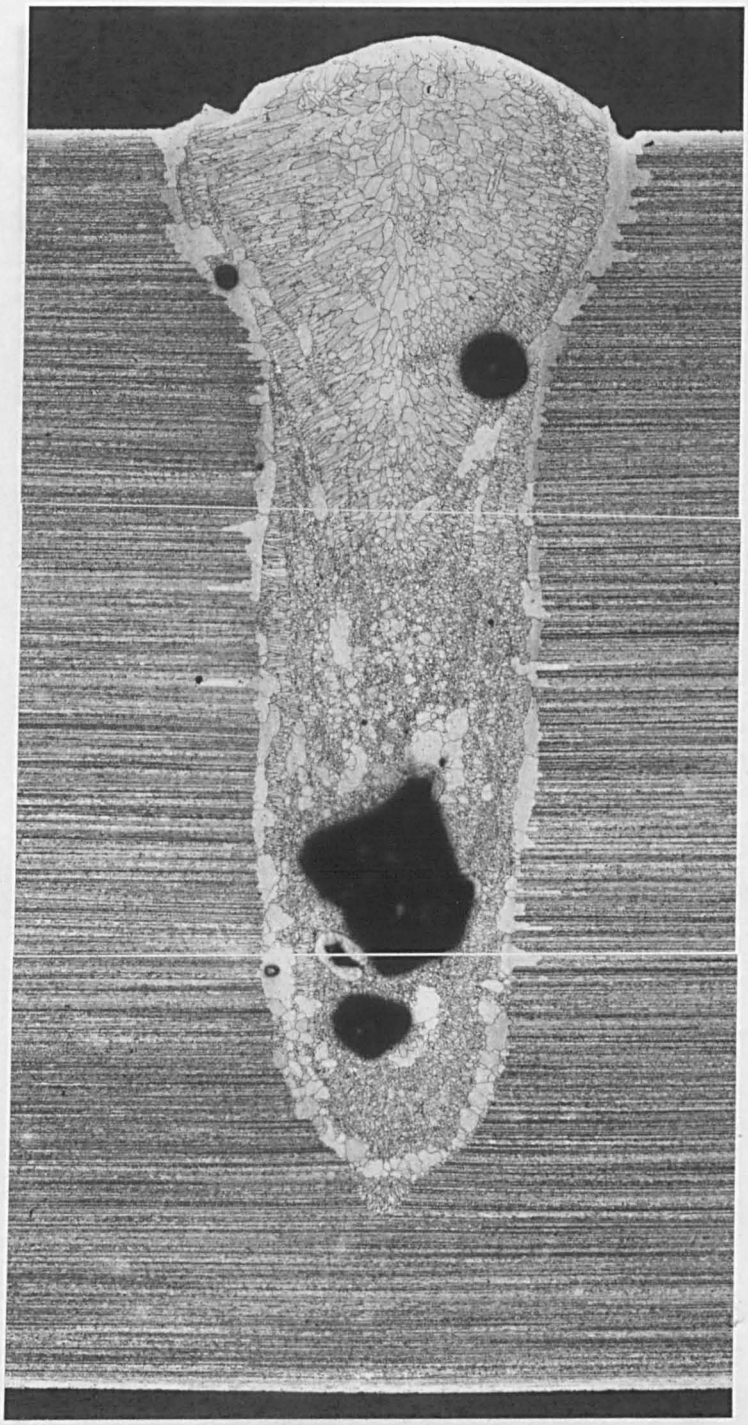

(a)

250μm

Figure 4.24. Optical micrographs of 8090 CO_2 welds with variations in the heating rate to the solution treatment temperature (530°C). (a) was made with a heating rate of 10 K/min whereas (b) was made with a 1 K/min heating rate. The grain size is most uniformly small in (b).

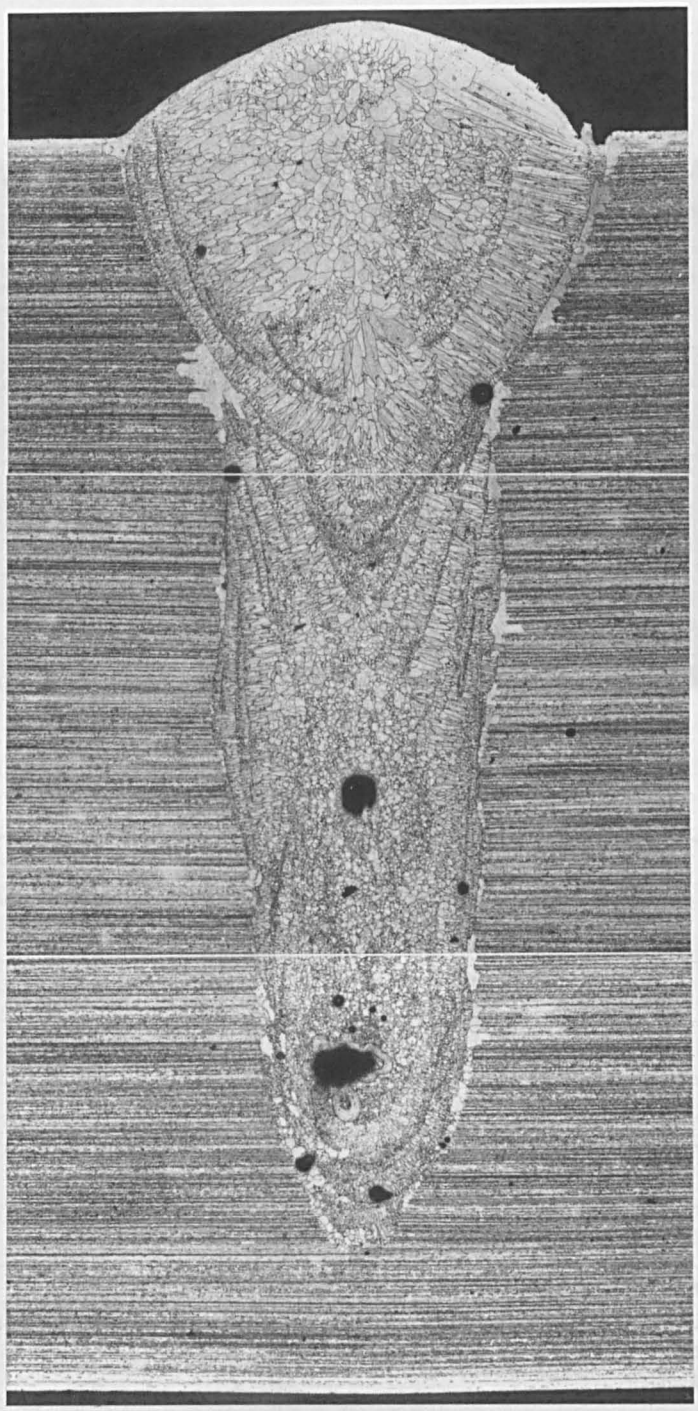

(b)

250μm

Figure 4.24. Optical micrographs of 8090 CO_2 welds with variations in the heating rate to the solution treatment temperature (530°C). (a) was made with a heating rate of 10 K/min whereas (b) was made with a 1 K/min heating rate. The grain size is most uniformly small in (b).

(a)

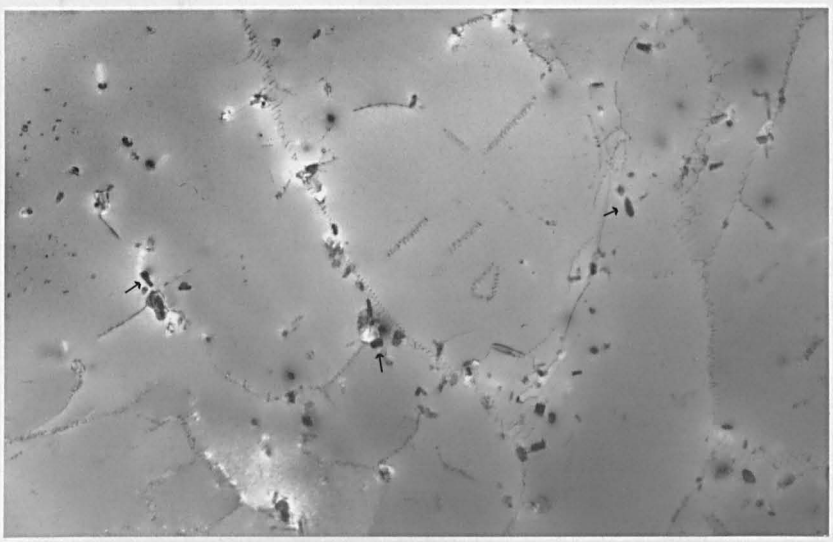

(b)

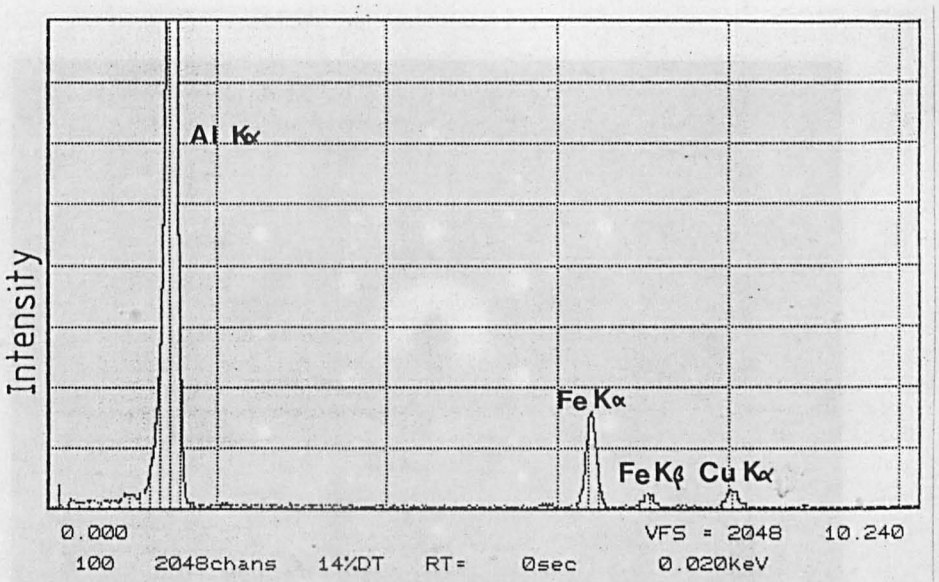

Figure 4.25. Transmission electron micrographs of the solution treated 8090 CO_2 weld without heating rate control. (a) shows the residual cast structure and (b) and (c) are EDX spectra from two rods. (d) shows a [111] zone axis SADP with Al_2O_3 reciprocal lattice spots arrowed.

(c)

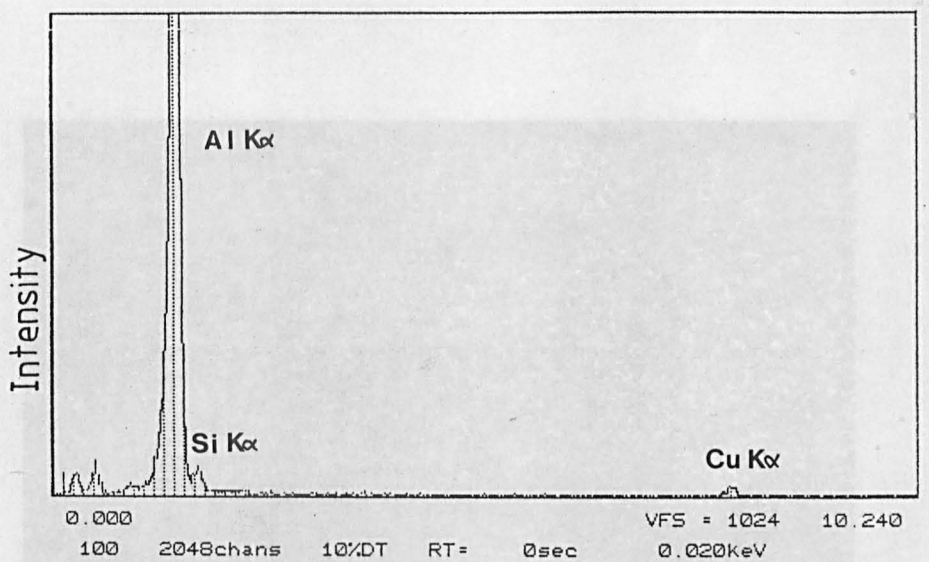

(d)

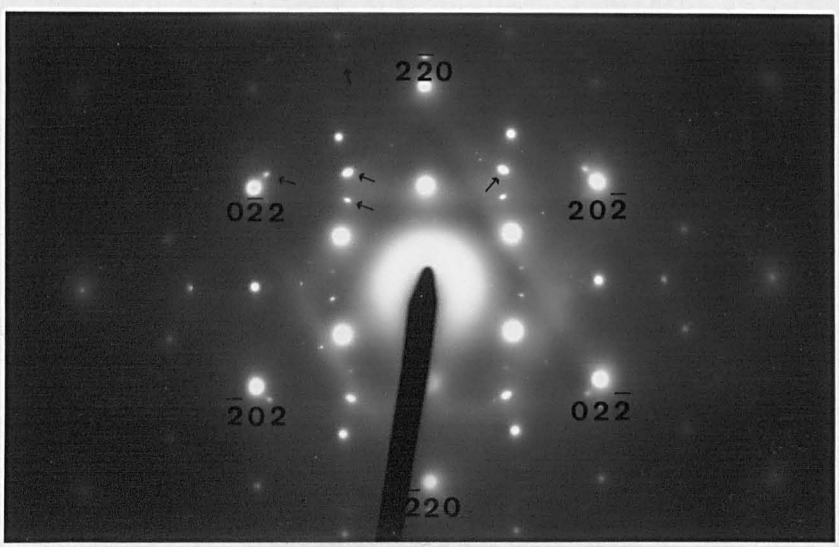

Figure 4.25. Transmission electron micrographs of the solution treated 8090 CO_2 weld without heating rate control. (a) shows the residual cast structure and (b) and (c) are EDX spectra from two rods. (d) shows a [111] zone axis SADP with Al_2O_3 reciprocal lattice spots arrowed.

(a)

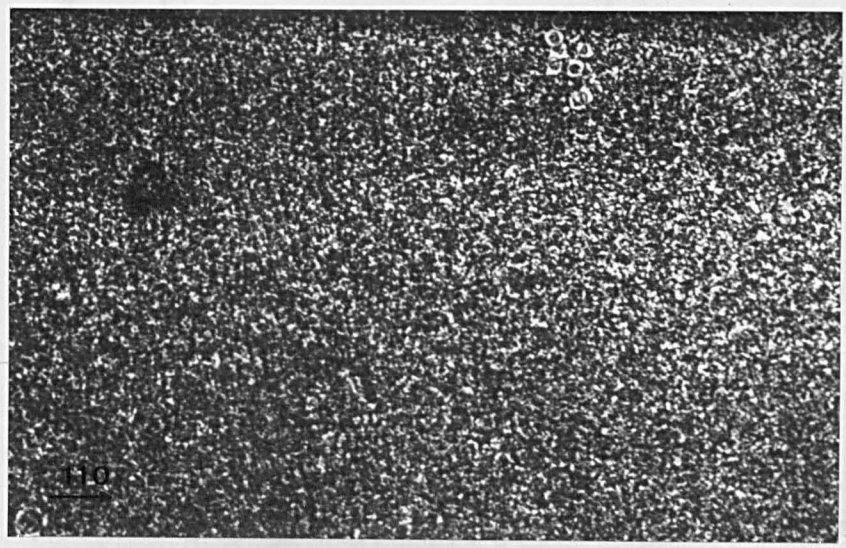

(b)

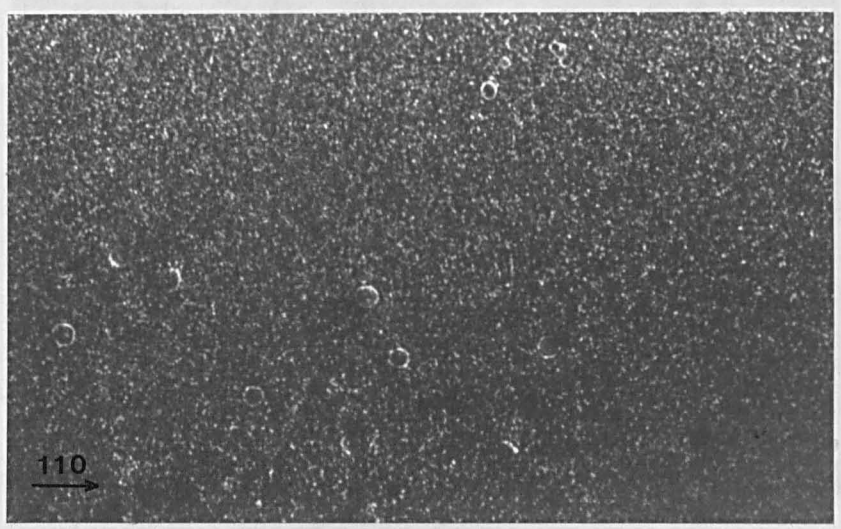

Figure 4.26. Centred dark field transmission electron micrograph from solution treated 8090 CO_2 welds with heating rates of (a) 10 and (b) 1 K/min. Taken using δ' reciprocal lattice spots, a bi-modal precipitate distribution is observed. Z=[$\bar{1}$12].

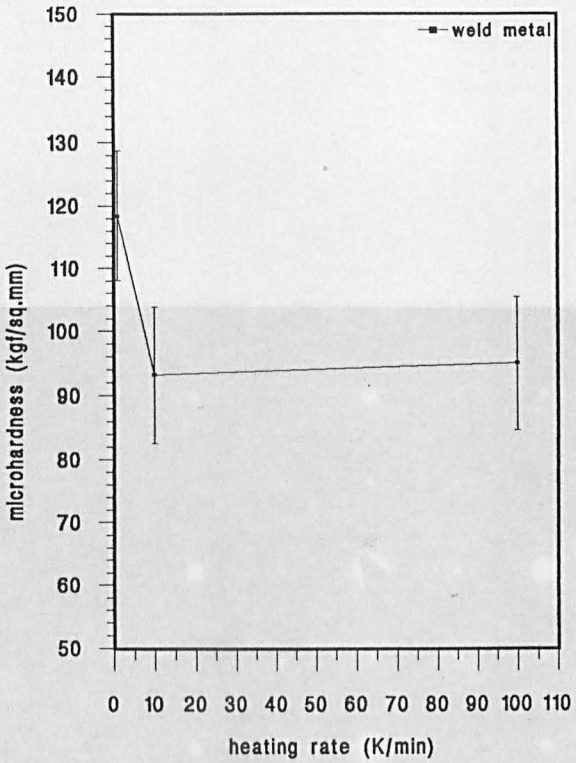

Figure 4.27. Plot showing the influence of heating rate to the solution treatment temperature (530°C) on the 8090 CO_2 weld microhardness.

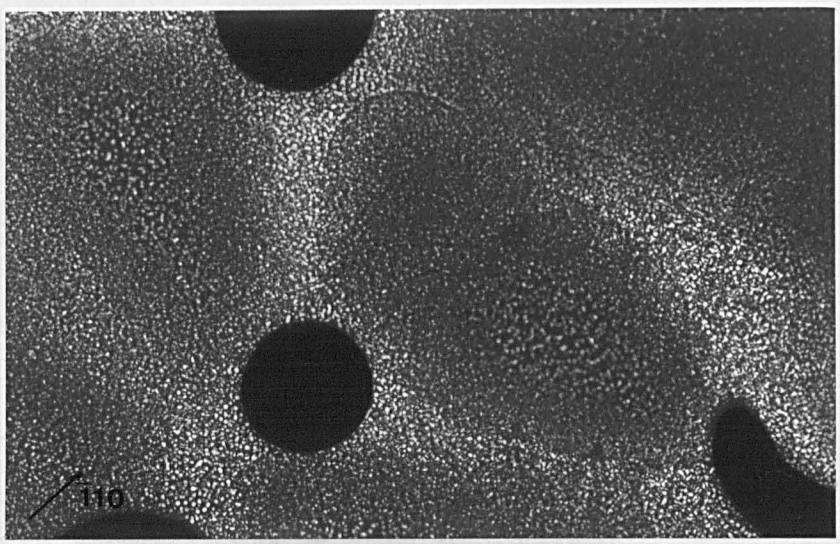

Figure 4.28. Transmission electron micrographs of the 8090 CO_2 weld in the aged condition. (a) is a centred dark field image of the uni-modal δ′ distribution taken using a δ′ reciprocal lattice spot, (b) is a SADP taken using a [001] zone axis which illustrates reciprocal lattice spots and streaks and (c) is a bright field image close to a cell boundary showing rods of S′ phase.

(b)

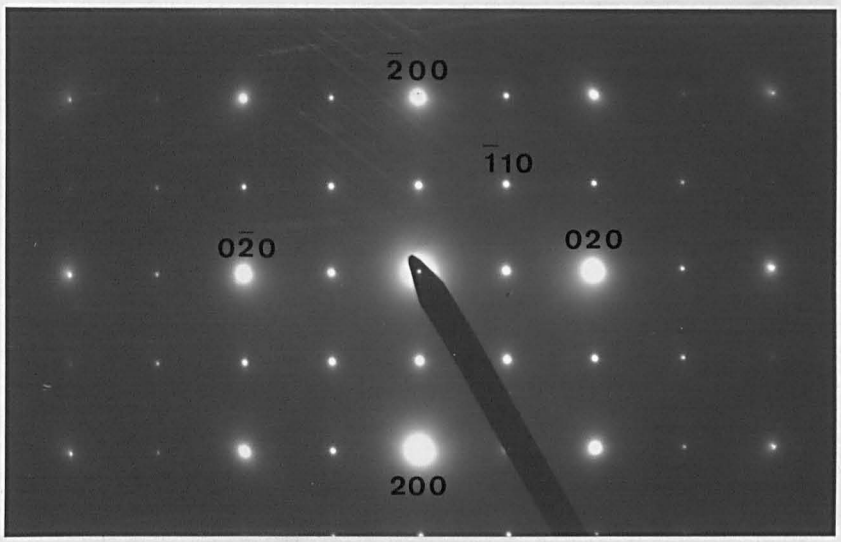

(c)

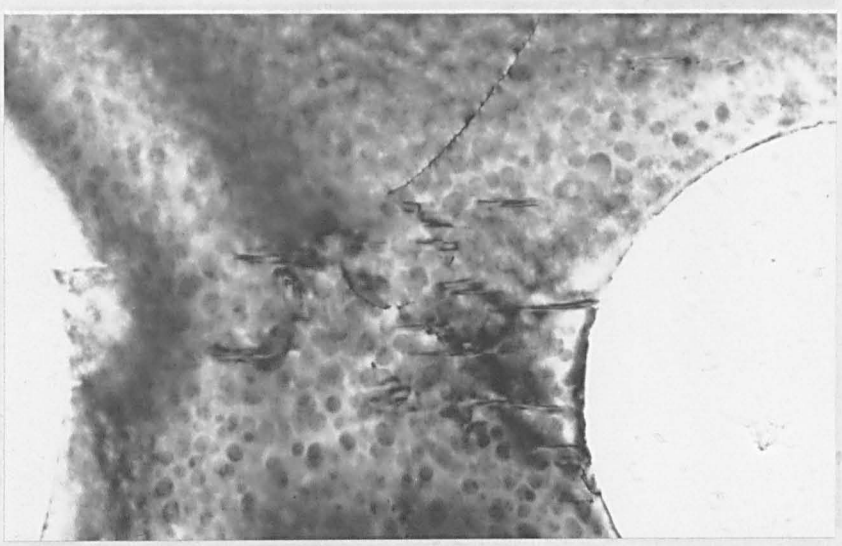

Figure 4.28. Transmission electron micrographs of the 8090 CO_2 weld in the aged condition. (a) is a centred dark field image of the uni-modal δ′ distribution taken using a δ′ reciprocal lattice spot, (b) is a SADP taken using a [001] zone axis which illustrates reciprocal lattice spots and streaks and (c) is a bright field image close to a cell boundary showing rods of S′ phase.

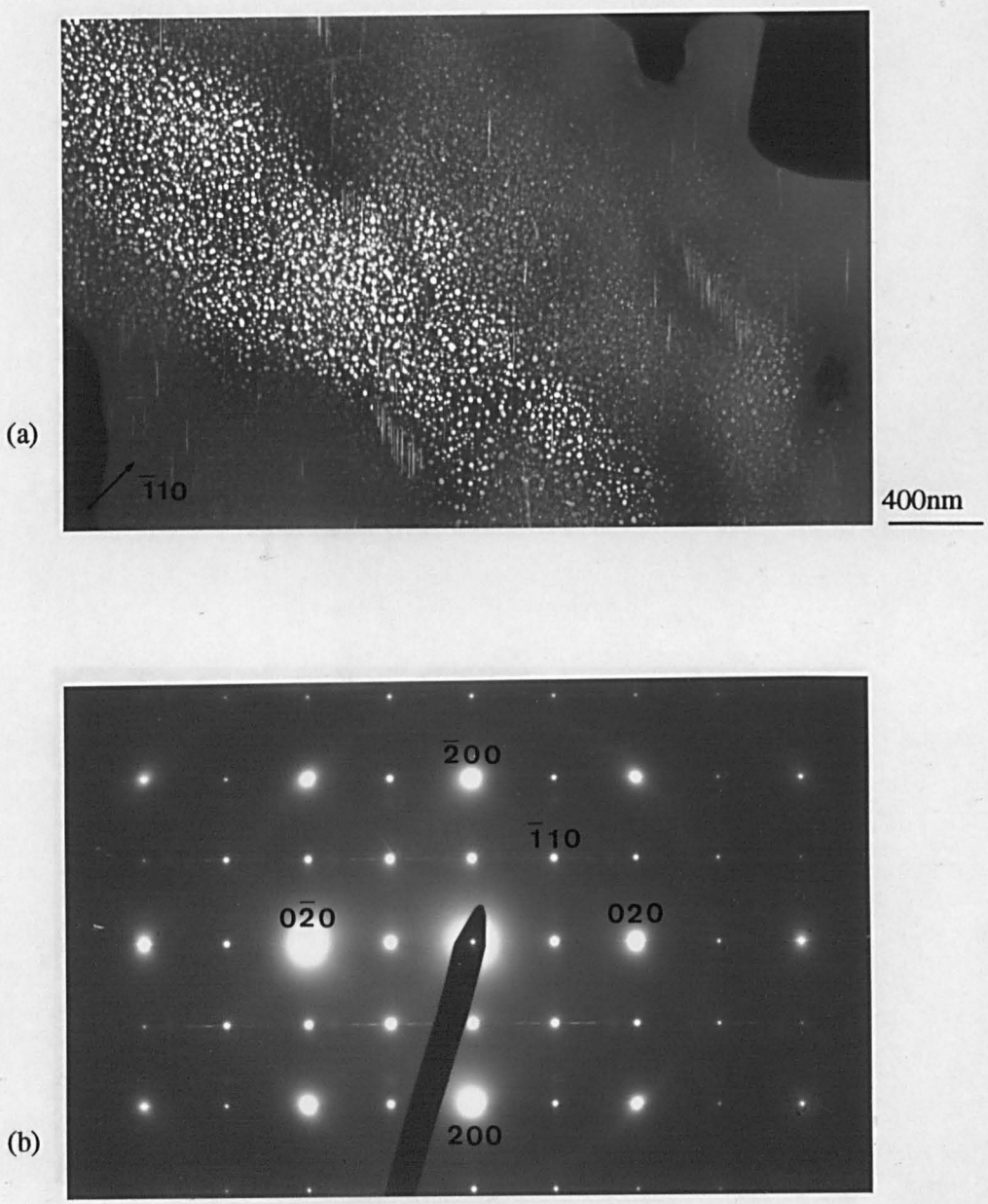

Figure 4.29. Transmission electron micrographs of the 8090 CO_2 weld after uncontrolled heating to the solution treatment temperature (530°C) followed by ageing. (a) is a centred dark field image of the uni-modal δ′ distribution taken using a δ′ reciprocal lattice spot (S′ rods can also be seen) and (b) is a SADP taken using a [001] zone axis which illustrates reciprocal lattice spots and streaks.

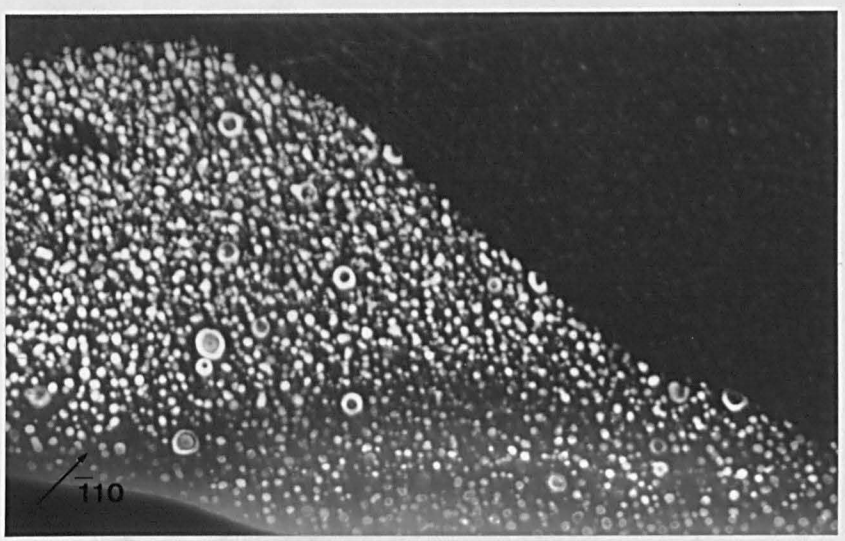

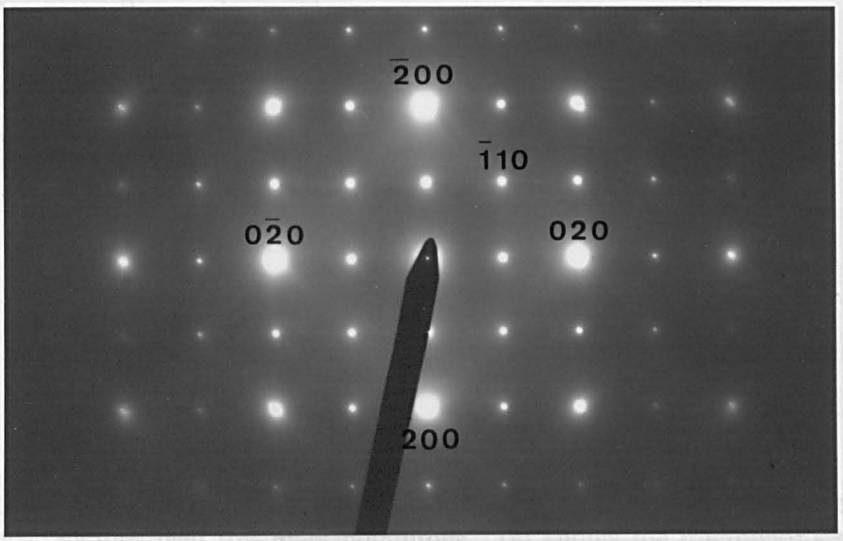

Figure 4.30. Transmission electron micrographs of the 8090 CO_2 weld after heating at 1 K/min to the solution treatment temperature (530°C) followed by ageing. (a) is a centred dark field image of the bi-modal δ′ distribution taken using a δ′ reciprocal lattice spot and (b) is a SADP taken using a [001] zone axis which illustrates reciprocal lattice spots and streaks.

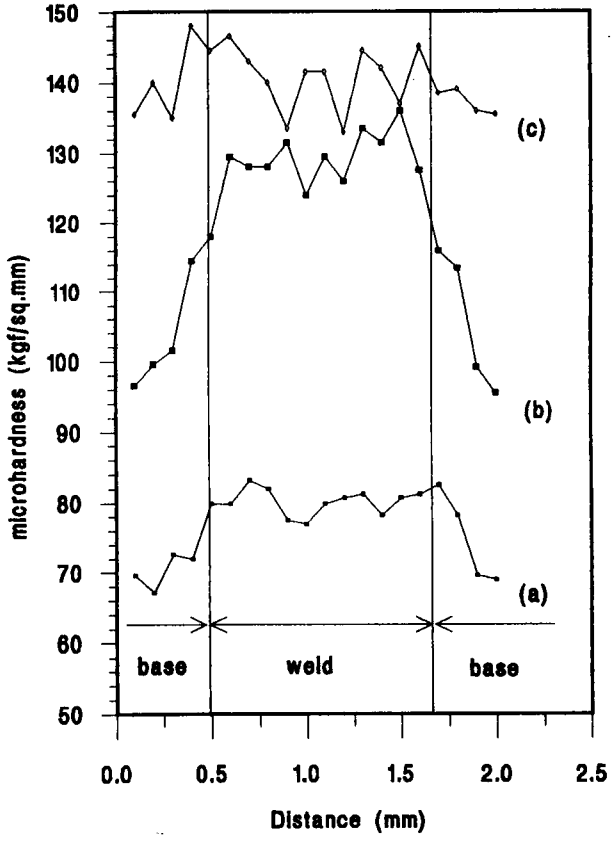

Figure 4.31. Plots of 8090 CO_2 weld microhardness profiles across transverse sections in various heat treatment conditions. (a) shows the microhardness in the as-received condition, (b) is for the aged condition and (c) is for the solution treated and aged condition.

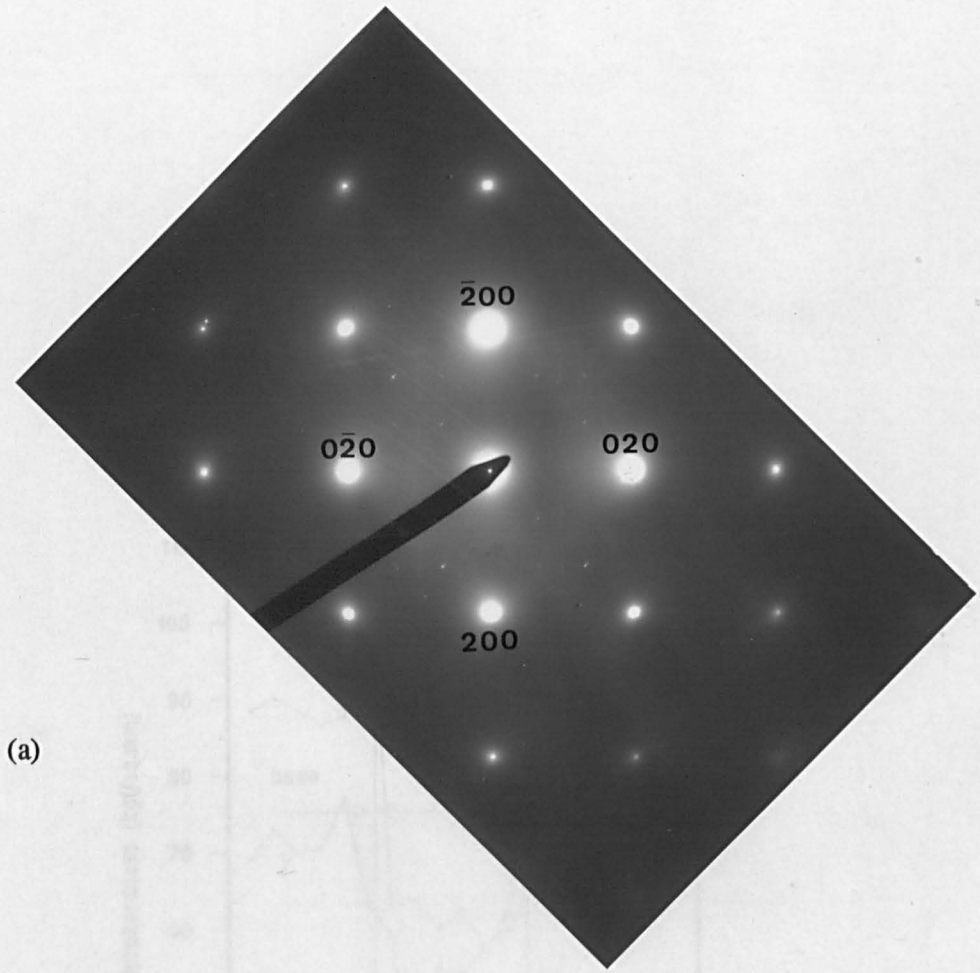

(a)

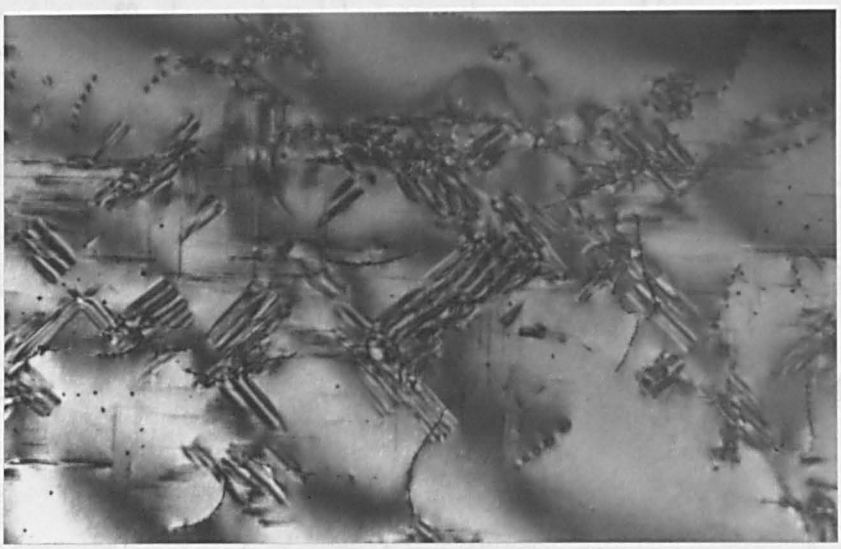

(b)

100nm

Figure 4.32. Transmission electron micrographs of the aged 8090 Nd:YAG weld. (a) is a SADP taken using a [001] zone axis which illustrates the absence of $L1_2$ reciprocal lattice spots but the presence of streaking due to S′ and T_1 phases and (b) is a bright field image taken near to a cell boundary showing rods of S′ phase and plates of T_1.

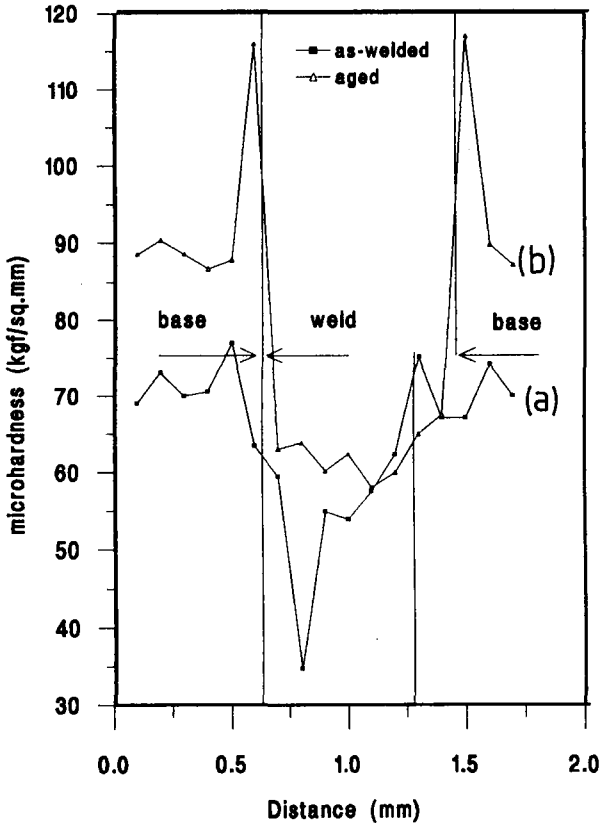

Figure 4.33. Plots of 8090 Nd:YAG weld microhardness taken across near surface sections in (a) the as-welded condition and (b) the aged condition.

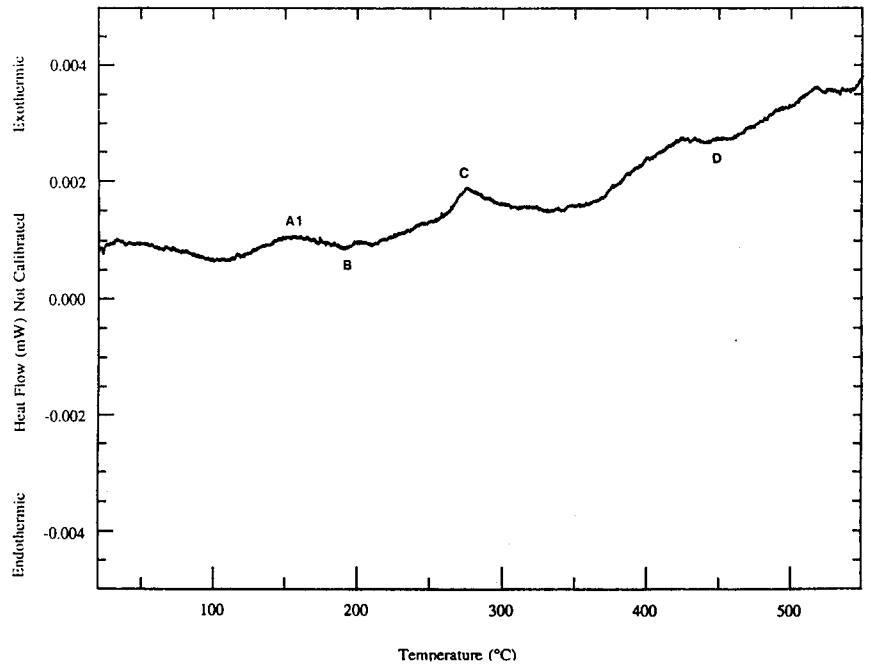

(a)

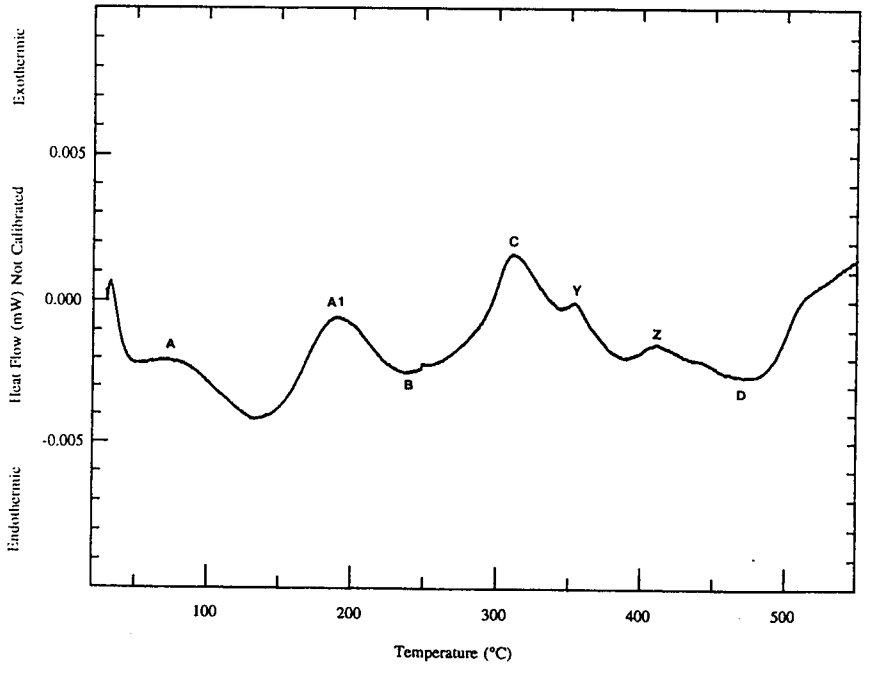

(b)

Figure 4.34. DTA traces for the 8090 weld heated at rates of (a) 1, (b) 10 and (c) 50 K/min. (d) is the trace obtained when the 10 K/min sample was reheated at the same heating rate up to the melting point.

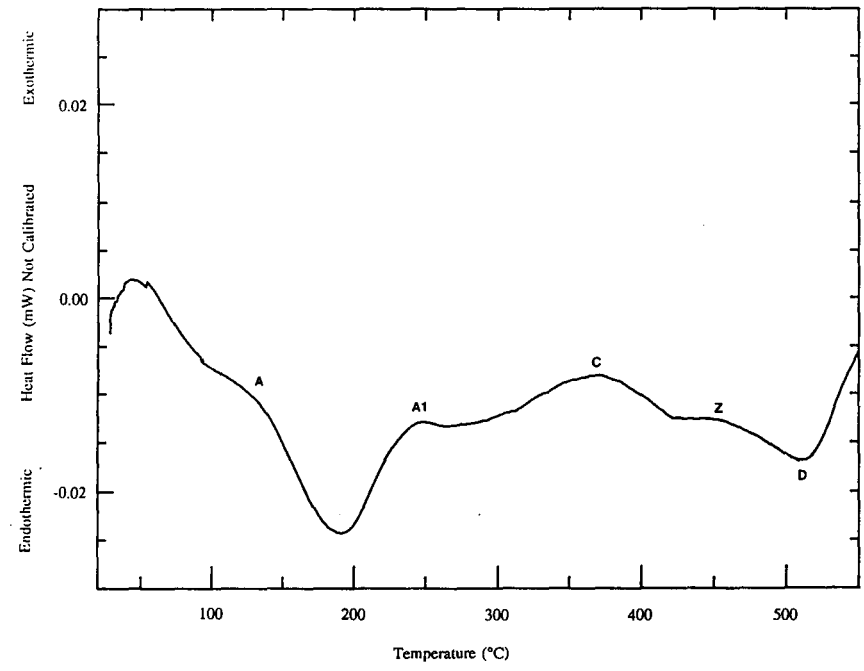

(c)

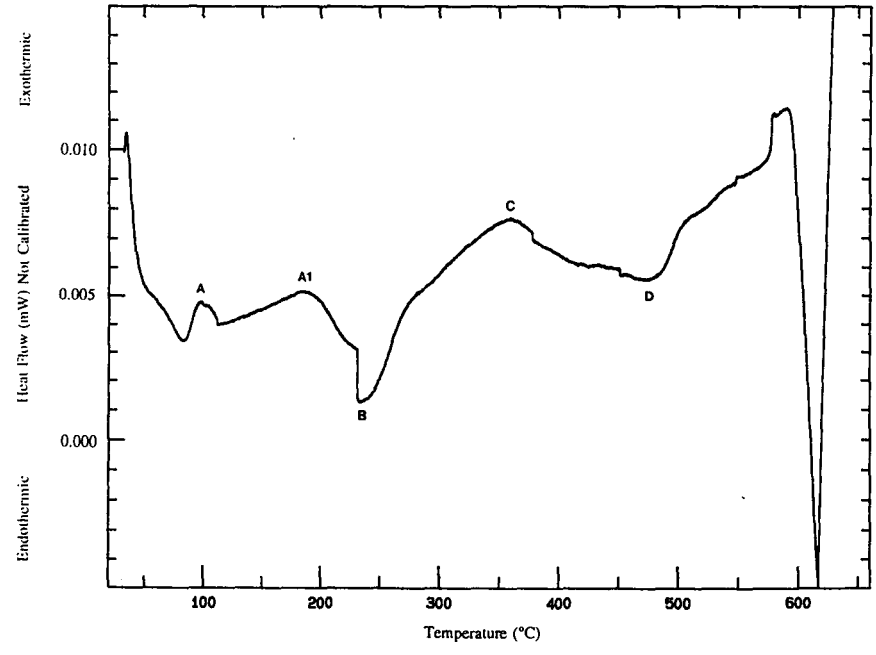

(d)

Figure 4.34. DTA traces for the 8090 weld heated at rates of (a) 1, (b) 10 and (c) 50 K/min. (d) is the trace obtained when the 10 K/min sample was reheated at the same heating rate up to the melting point.

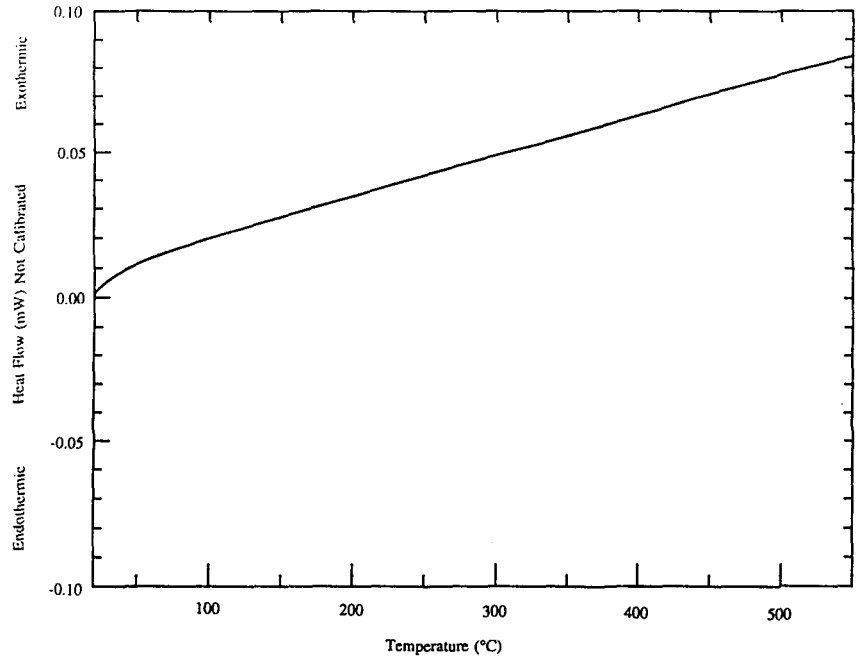

(a)

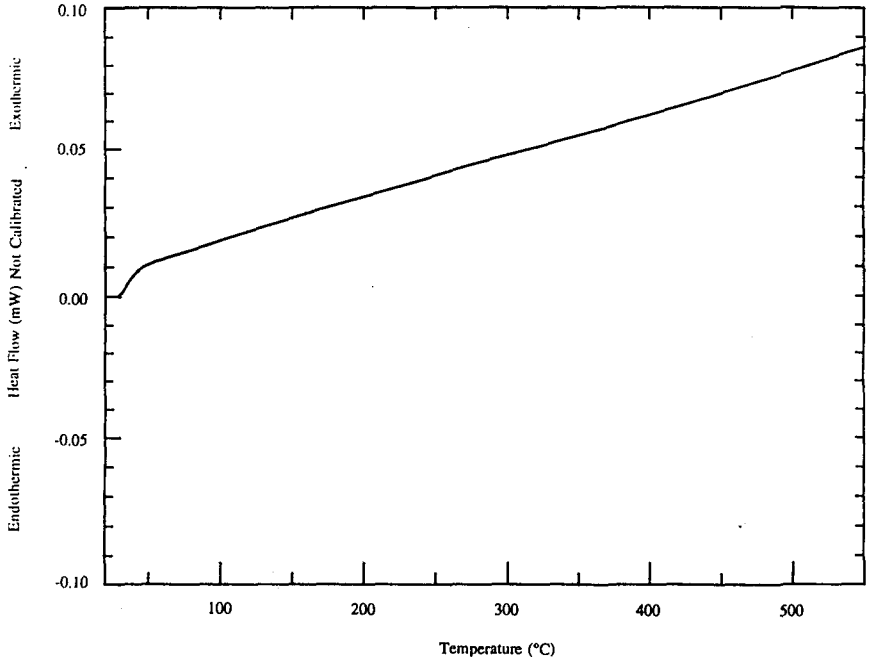

(b)

Figure 4.35. DTA traces for the super purity Al heated at rates of (a) 1, (b) 10 and (c) 50 K/min.

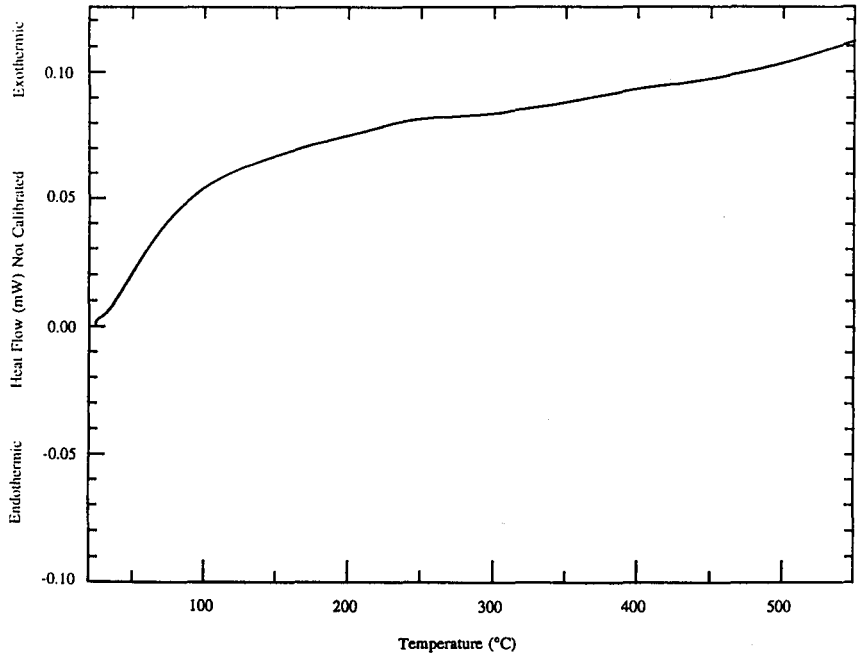

(c)

Figure 4.35. **DTA traces for the super purity Al heated at rates of (a) 1, (b) 10 and (c) 50 K/min.**

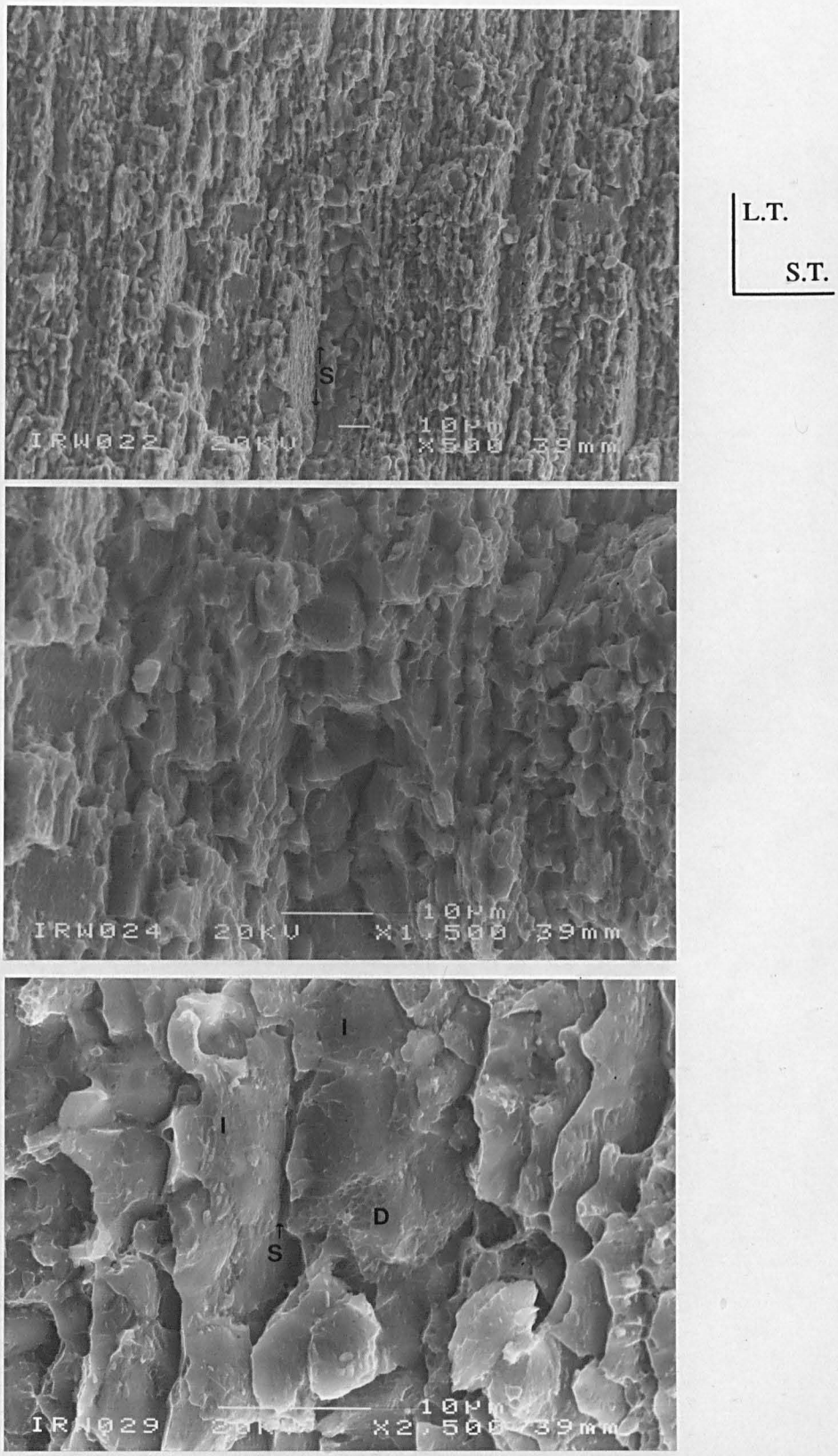

Figure 4.36. SEM micrographs from an unnotched 8090 base metal tensile test specimen. The specimen was tested after solution treating at 530°C for ~ 40 minutes and ageing at 190°C for 16 hours.

(a)

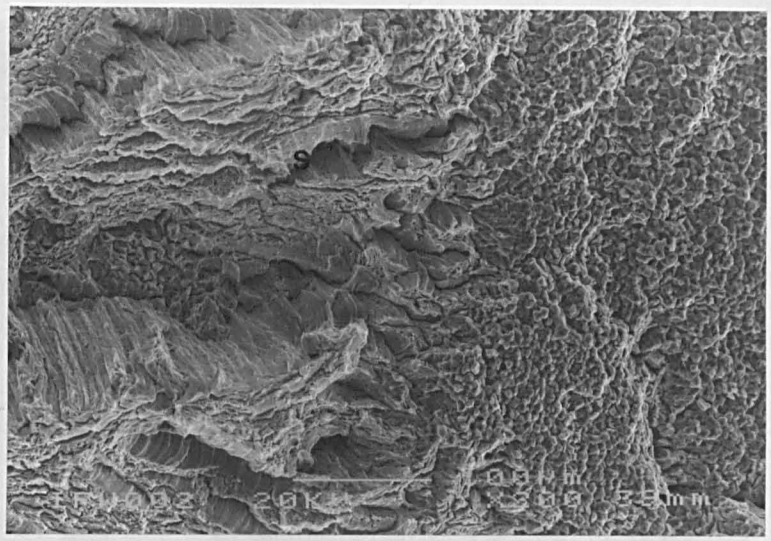

(b)

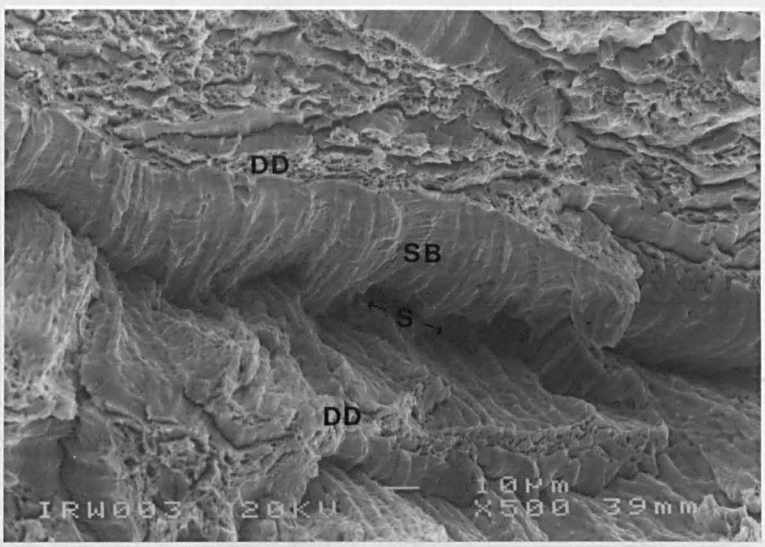

Figure 4.37. SEM micrographs from a notched 8090 weld in the as welded condition.

(c)

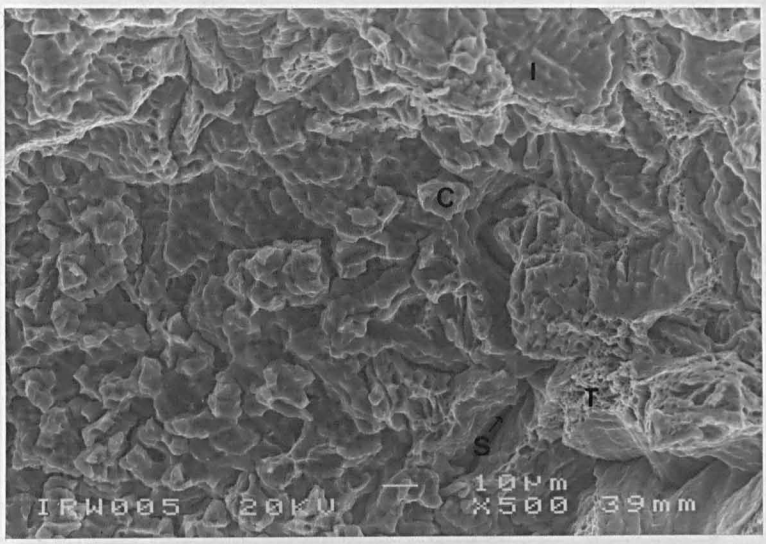

(d)

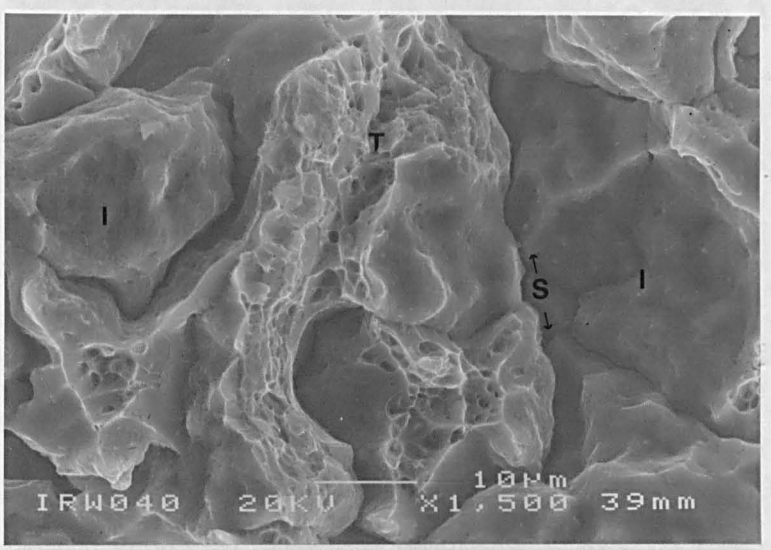

Figure 4.37. SEM micrographs from a notched 8090 weld in the as welded condition.

(a)

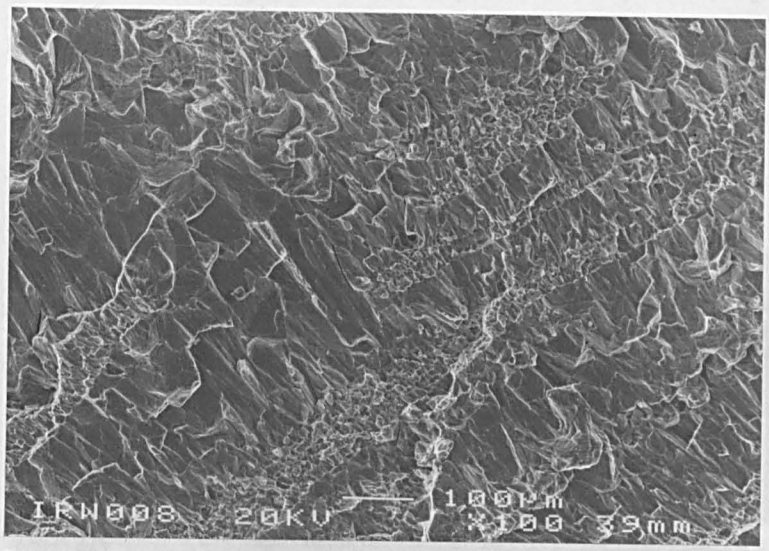

(b)

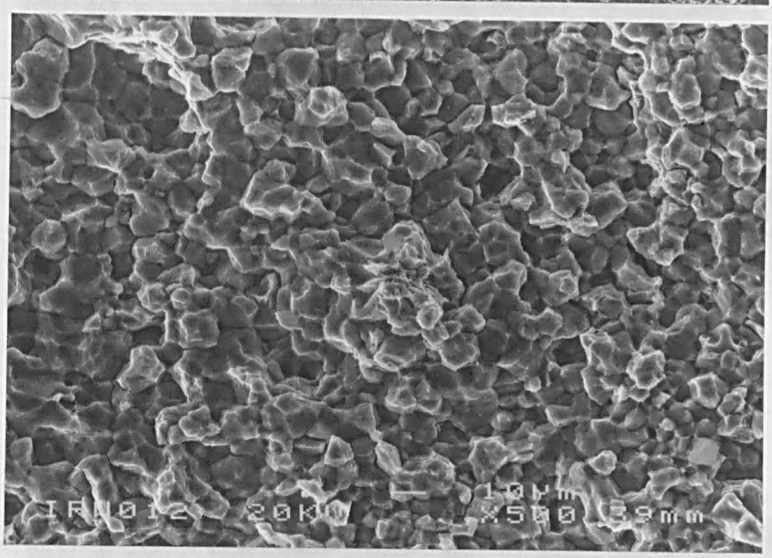

(c)

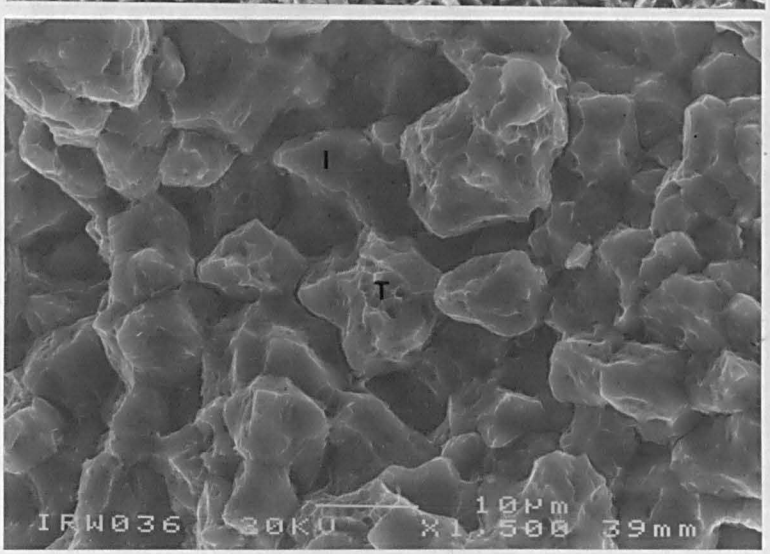

Figure 4.38. SEM micrographs from a notched 8090 weld solution treated at 530°C for ~ 40 minutes with a heating rate of 1 K/min.

(a)

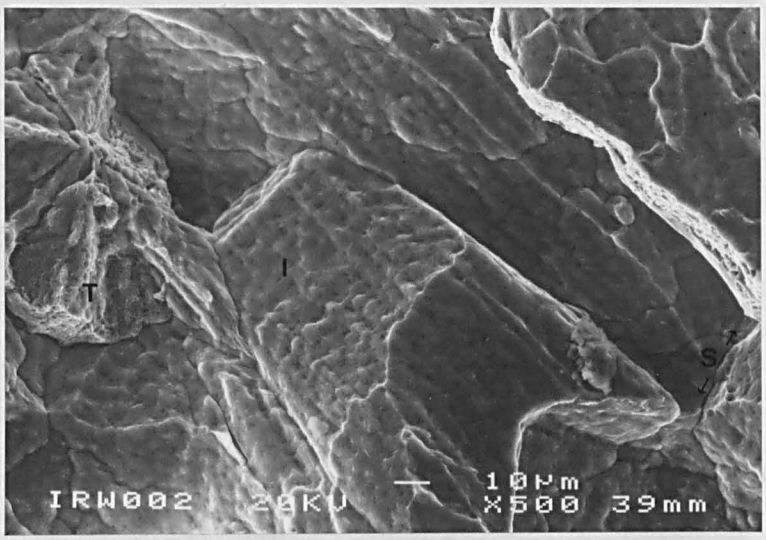

(b)

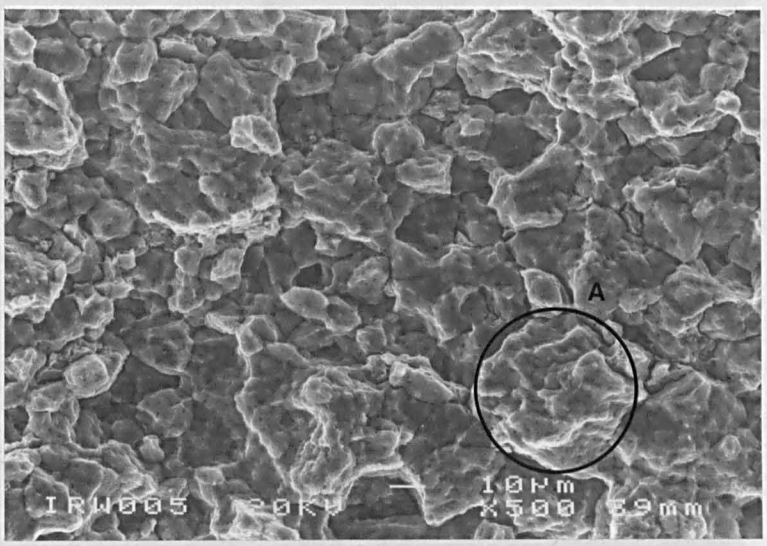

Figure 4.39. SEM micrographs from a notched 8090 weld solution treated at 530°C for ~ 40 minutes with a heating rate of 100 K/min.

(a)

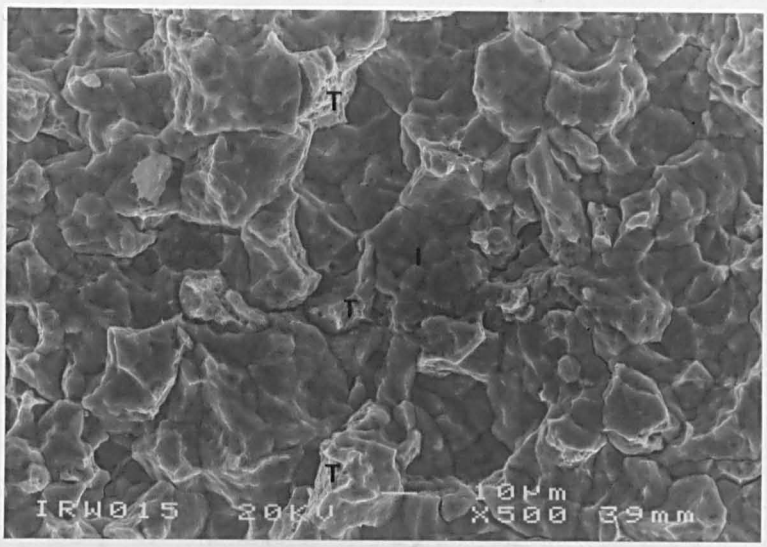

(b)

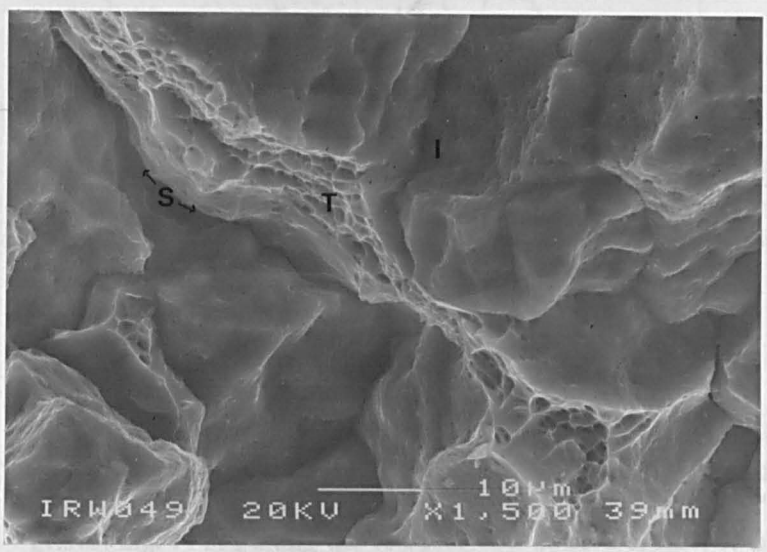

(c)

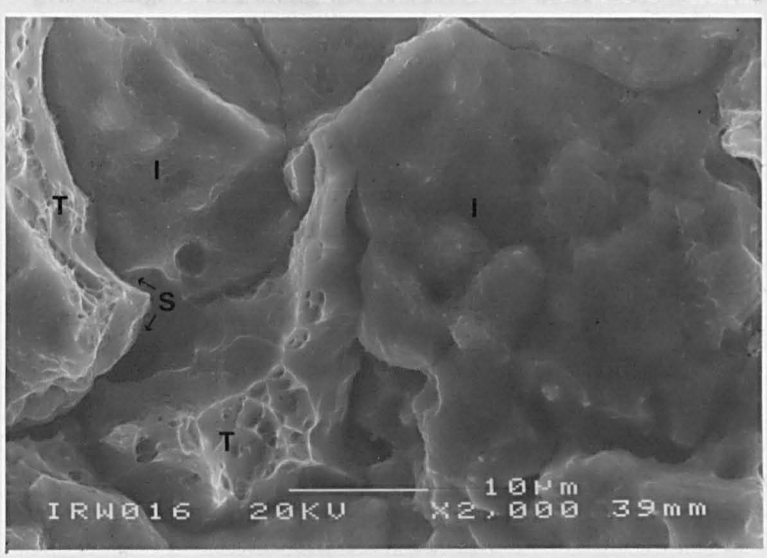

Figure 4.40. SEM micrographs from a notched 8090 weld solution treated at 530°C for ~ 40 minutes with a heating rate of 1 K/min and aged at 190°C for 16 hours.

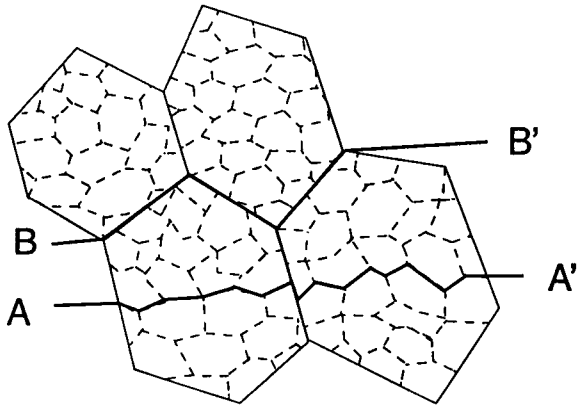

Figure 4.41. Schematic illustration of the mechanism of crack growth along intermetallic particles. Large grains can be seen with an internal distribution of undissolved intermetallic particles. A crack can propagate 'transgranularly' across the large grains, e.g. A-A', along the residual cast structure, instead of along the true grain boundaries, e.g. B-B'.

Chapter 5. Discussion of 8090 Results

This aims of this chapter are (i) to interpret and explain the results on 8090, (ii) to compare and contrast the main features of Nd:YAG and CO_2 welds and (iii) to examine the results in the context of previous studies. The discussion is split into five sections because of the diverse nature of the results. These sections are as follows:

1. Weld metal macrostructure, section 5.1,
2. Formation of porosity, section 5.2,
3. Base metal and as-welded, fusion zone microstructures, section 5.3,
4. Microstructures following heat treatment, section 5.4 and
5. Mechanical properties, section 5.5.

5.1 Weld Metal Macrostructure

This section introduces the influence of the welding parameters such as laser power, radiation wavelength, welding speed and laser beam focus on the resultant weld bead shape. Thus the weld pool shapes from the CO_2 and Nd:YAG lasers can be compared.

Regarding the CO_2 laser welded 8090 it has been shown that the shape of the solidified weld pool is characterised essentially by the depth of penetration, d, and the top bead width, w. Furthermore, the shape is sensitive to variations in the laser beam power, W, the welding speed, v, and the focal position of the beam. In this work the weld bead width or depth has shown an inverse relationship with welding speed but is directly proportional to the laser beam power. In addition, focus positions on and above the surface using a 2.25 kW laser beam created very similar, fully penetrating weld pool shapes. It is interesting to note, though, that the weld bead shapes made at the slightly lower power of 2 kW were invariant with respect to the laser focus, and these shapes showed similar profiles to those of the sub-surface focus welds made at 2.25 kW.

If we consider the specific heat capacity of the material at constant pressure, C_p, thermodynamic relationships state that[129]

$$C_p = \frac{dH}{dT} \qquad 5.1$$

where dH is the change in internal energy, or heat content, of the material for a change in temperature dT. The weld pool volume generated per unit time is in simple terms given by the product of the depth, width and speed[34];

$$\textit{weld pool volume} = (d.w.v) \quad \textit{per unit time} \qquad 5.2$$

Thus the energy supplied to melt the volume of material per second is the power, W, which is given by

$$W = C_p.\rho.(d.w.v).(T_m - T_o) + L.(d.w.v) \qquad 5.3$$

where ρ is the density of the material, T_m is the melting temperature, T_o is the initial temperature and L is the latent heat of fusion per unit volume. From these basic relationships it is clear that at constant speed

$$W \propto d.w \qquad 5.4$$

and at constant power

$$\frac{1}{v} \propto d.w \qquad 5.5$$

which agrees with the results. Variations in shape with the power and speed are consistent with the findings of other workers for laser welds[16][28] and indeed with the theory.

The concept of welding efficiency was introduced in section 2.1.6 where it was stated that there was a theoretical maximum of 0.48[29]. Sonti and Amateau[130] have calculated the welding efficiency for CO_2 laser welds in 2219, 5456 and 6061 aluminium alloys. Values between 0.02 and 0.31 are given for powers in excess of 5 kW. In this study, the equation for efficiency, η, below

$$\eta = \frac{Av(C\Delta T + L)}{W} \qquad 5.6$$

where A is the weld area, ~ w.d m^2

ΔT is the temperature range, ~ (933-298) K

L is the latent heat of fusion, ~ 1.0×10^9 J/m^3

C is the volumetric heat capacity, ~ 3.4×10^6 $J/m^3/K$

(W = incident power in W and v is the welding speed in m/s)

(values taken from Wills et al.[131])

yields an efficiency of 0.47 for a welding speed of 100 mm/s and an incident laser beam power of 3000 W. This calculation suggests that the alloy 8090 is more weldable with a CO_2 laser than conventional aluminium alloys and achieves a higher efficiency, approaching that of the theoretical maximum, due to the lower powers required for melting large volumes.

However, such simple relationships cannot readily be derived for the influence of focus position on weld bead shape. Ideally, it might be expected that as the laser focus is moved away from the surface, the power density striking the surface of the material will be reduced. Ultimately this will result in a reduction in penetration and an increase in top bead width owing to the effective larger heat source. This was found by Willgoss[16] for CO_2 laser welding of stainless steels. It can be shown that the distance over which the focal spot size changes by ± 5%, the depth of focus, is a function of the laser optics and radiation wavelength[15]. The depth of focus, z_f, is given by[15]

$$z_f = \pm 1.48 F^2 \lambda \qquad 5.7$$

where F is the focal length divided by the unfocussed beam diameter and λ is the radiation wavelength. For the optical conditions of the CO_2 laser used, F is 125/20 and λ is 10.6 μm which gives a depth of focus of ± 0.4 mm, i.e. the intensity of the beam will be reduced by more than 5% at ±0.4mm from the focus position. If the on-focus beam is taken as a reference then the intensity at 1mm increments along the beam axis will be markedly decreased. Thus the 1mm variations in focus position

used in the experiments can be expected, on the basis of this calculation, to reduce the intensity of the beam on the surface quite considerably. The power densities at off-focus positions can be calculated as follows. The highest power density occurs when the beam is narrowest say with a radius of 0.1mm. This value is approaching the minimum, diffraction limited spot size, which is given by $r_{min}=1.22F\lambda$[15] for a circular, Gaussian laser beam. For laser optics of F=125/20 (F=focal length divided by unfocussed beam diameter) simple linear scaling can be used to obtain the radius at distances along the beam axis. For a 2 kW beam contained in an area of radius 0.1 mm, the power density is ~ 6.4 x 10^{10} W/m^2. If the focus is moved 1 mm above or below, then the beam has a calculated radius of 0.18 mm, giving a power density of 2 x 10^{10} W/m^2 i.e. 30% of the maximum power density. Similarly, for a focus position 2 mm above or below the surface, the calculated beam radius is 0.27 mm giving a power density of 8.7 x 10^9 W/m^2 i.e. ~ 14% of the maximum power density. These calculations confirm that the power density incident on the surface can reduce considerably for off-focus positions. Swift-Hook and Gick[29] developed an analytical analysis for predicting the penetration in laser welds. Fig. 2.3 shows their theoretical curve for predicting penetration. The Swift-Hook and Gick[29] analysis was introduced in section 2.1.6, and equation 2.2 can be rearranged as follows:

$$\frac{W}{\pi w^2} \sim \frac{k_c T d}{\pi} \cdot \left(\frac{v}{\alpha}\right)^2 \qquad 5.8$$

It is apparent that the weld penetration, d, is directly proportional to the power density, W/πr^2, (assuming the weld bead width, w is a linear function of the incident spot size, r) and would, therefore, be expected to decrease at off-focus positions. From the earlier calculation for welding efficiency it is apparent that in this case the welding is taking place in the linear region of the curve of Fig. 2.3. Thus for a welding speed of 100 mm/s, a weld bead width of 1.5 mm and a laser beam power of 3000 W, the equations from Swift-Hook and Gick[29] (equation 2.2) give a normalized weld width, Y, of

$$\frac{vw}{\alpha} = \frac{vwC}{k_c} = \frac{100x10^{-3}.1.5x10^{-3}.3.4x10^6}{181} = 2.82 \qquad 5.9$$

where α is the thermal diffusivity =k_c/C

C is the volumetric specific heat = 3.4×10^6 J/m^3/K

k_c is the thermal conductivity = 181 W/m/K[131]

When substituted into equation 2.2 at a temperature of 1000 K, this gives a value for the penetration, d, of approximately 2 mm. This is comparable to the experimentally observed penetration of 3 mm, as is evident from Fig. 4.1 (a). If, however, the same information is substituted into equation 2.4 from Banas[34] for a beam radius of 0.2 mm (which was experimentally determined in this study), the depth of penetration is 2.9 mm. This is very close to the experimental value. Thus, it is clear that these analyses can be readily applied to predict, to a reasonable accuracy, the maximum depth of penetration during CO_2 laser welding of 8090.

It is also clear form the above analysis, that decreasing the power density reduces the weld penetration. A possible explanation why the weld pool shape might not vary much with variations in the focus position lies with the plasma effects. The precise role which the plasma plays during laser welding is not well understood but at low electron densities it is thought to actively couple the laser beam into the surface of the material[132]. Added to this observation, Ducharme et al.[133] have shown that at high temperatures (and high electron densities) the plasma plume above the keyhole can cause the focal radius of the laser beam to increase which decreases the energy supply to the keyhole. Thus it can be concluded that, without more detailed analysis of the temperature and existence of the plasma plume above the keyhole, especially at different off-focus positions it is very difficult to quantify the effect of focus positions on weld pool shapes.

Comparing the CO_2 weld pool shapes in Fig. 4.1 (c) to those from the Nd:YAG weld pool shapes in Fig. 4.4 it is clear that Nd:YAG welds in 8090 are more difficult to create, even though the peak power supplied can be as high as 8 kW. However, the transverse sections of the Nd:YAG welds certainly do not demonstrate large molten volumes and the pool shapes appear to be described by a conduction mode rather than keyhole mode of heating[15][27]. To summarise the major differences between the CO_2 and Nd:YAG laser processes, the Nd:YAG laser is pulsed with a beam diameter of 0.8 mm (peak power density ~ 2×10^{10} W/m^2) and an output radiation of 1.06 μm,

whereas the CO_2 laser is continuous with a beam diameter of 0.4 mm (power density at 2.5 kW ~ 2 x 10^{10} W/m^2) and an output radiation of 10.6 μm. In theory, the metal absorptivity is increased at lower radiation wavelengths[15] so in this respect it should be more advantageous to use the Nd:YAG laser for welding. It is also known that plasma above the keyhole can aid beam coupling into the material[34][132] at low electron densities. Herziger[35], however, has shown that the power density required to create a plasma with a Nd:YAG laser is nearly two orders of magnitude greater than that with a CO_2 laser. The following equation shows the relationship between the plasma absorption coefficient and the frequency of the electromagnetic radiation[35];

$$\textit{plasma absorption coefficient} = \textit{const.}\ \frac{n_e . n_m . I}{\omega^2} \qquad 5.10$$

where n_e is the electron density of the plasma, n_m is the vapour density in the plasma, I is the power density required for plasma formation and ω is the laser frequency. Thus higher power densities are required at shorter wavelengths to maintain constant conditions of absorptivity, electron and vapour densities. It is possible, therefore, that there has been insufficient formation of plasma above the Nd:YAG weld, due to short interaction times and low power densities, and thus plasma aided coupling of the laser beam into the material has not occurred. In effect the Nd:YAG laser would need a power density of ≥ 10^{12} W/m^2 in order to form a plasma and presumably a keyhole.

The majority of the welds, both CO_2 and Nd:YAG, contained solidification cracks. In the CO_2 weld these ran across the weld bead width, perpendicular to the welding direction. In the Nd:YAG weld the cracks were perpendicular the weld pool solid/liquid interface. In both cases these are most likely as a result of the thermal stresses generated by sheets being clamped during welding. In the CO_2 welds cracking has occurred in the upper, wine-glass region of the weld pool and the cracks were intergranular. Later analysis will show that this region was probably the last to solidify, hence thermal stresses would have been concentrated here during solidification. 8090 has a solidification range in excess of 100 K due to its high alloy content and during solidification low melting point segregates can persist as grain boundary liquid films to temperatures well below that of the equilibrium solidus

temperature under non-equilibrium cooling conditions. Thus the true solid-solid grain boundary contact will be substantially reduced, the thermal stresses will be acting over reduced surface areas and the ductility of the solidifying system will be exceeded. Al-Li based alloys have previously been demonstrated to be very susceptible to solidification cracking[6][8][96] and Lippold[5] has in fact shown that the alloys 2090 and 8090 are more susceptible to solidification cracking than other aluminium alloys such as 2219, 5083 and 6061. However, the ability of a system to withstand solidification cracking is therefore possibly enhanced by a small grain size[38].

To summarize, the laser characteristics and welding parameters play an important role in determining the weld pool shape. Furthermore, the weld pool shapes made using the Nd:YAG laser are quite different from those made using the CO_2 laser. This was suggested to be in part due to plasma effects combined with the pulsed mode of Nd:YAG operation.

5.2 Formation of Porosity

In this section the mechanisms underlying the formation of weld porosity in CO_2 laser welds will be examined with particular reference to the differences between type I and type II porosity. Type I porosity is defined as being due to essentially spherical pores as shown for example in Fig. 4.16 (a). On the other hand type II porosity is defined as the irregular type of pore shown in Fig. 4.16 (c). The spatial distribution of porosity is summarized in Figs. 4.17 and 4.18.

With regard to type I pores, their spherical nature and the observation of a dendritic structure on their internal surface (Fig. 4.16 (b)) strongly suggests that they formed through gas evolution, most probably H_2 gas. A possible model for their formation is as follows. H_2 gas can readily be absorbed into the melt from surface contaminants such H_2O. The chemical reaction

$$3H_2O + 2Al \rightarrow Al_2O_3 + 3H_2 \qquad 5.11$$

evolves H_2 which then dissolves in the melt. As shown by the Al-H phase diagram[134] in Fig. 5.1, pure Al has a high solubility for H_2 gas which increases

with increasing temperature. Similar behaviour is expected for 8090, and at the melt pool temperatures well in excess of 1000 K expected in laser welding, significant H_2 pick up seems likely. When the melt pool begins to cool it becomes supersaturated with hydrogen since gas bubbles do not nucleate readily[135]. Furthermore, when solidification begins hydrogen is rejected into the melt since it is much less soluble in solid aluminium. For pure aluminium the solubility ratio is 29[136] although it is reported to be only 3 for Al-Li alloys[136]. Nevertheless there will be a significant supersaturation of hydrogen in the melt and hence driving force for gas bubble nucleation. A large spherical, type I pore can be expected to develop if a gas bubble nucleates in the melt, very close to the solidification front, and then grows by diffusion of gas towards it. At the high laser welding speeds employed there is clearly insufficient time for such a bubble to float to the surface. It is instead trapped by the solidifying dendrites.

Such a spherical type of porosity is a common occurrence in conventional welding of Al alloys as discussed in the review by Devletian et al.[137]. Moreover, Sonti[123] also found numerous spherical pores in his laser welded 2XXX and 5XXX alloys. In summary then, aluminium alloys are very susceptible to H_2 gas porosity which can give rise to large spherical pores as in the present work. It may be possible to reduce the level of porosity in the weld metal by removing a surface layer prior to welding, as found by other workers on Al-Li based alloys[6][10][13][99]. Better gas shielding might also reduce the chance of water inclusion from the atmosphere.

Turning now to the irregular, type II pores, it is very important to note that they occur in partial penetration welds but not full penetration welds. This together with their cold-shut type structure suggests that their formation is related to the keyhole dynamics of partial penetration welds[15]. The precise mechanism is unclear and probably complex. However, the observations by Arata[33], using in-process optical and X-ray analysis during laser welding of soda-lime glass and mild steel, can be used to propose a mechanism for their formation. The pattern he reported is very similar to that seen in Fig. 4.17. Furthermore, similar spiking effects have been observed in electron beam welding[138][139][140]. Schauer and Giedt[139] have examined the

balance between surface tension and vapour pressure forces within the keyhole and predicted that instabilities will form at the depth where the surface tension force added to the hydrostatic force just exceeds that due to the vapour pressure. Along the sides of the keyhole shown in Fig. 2.2, the vapour pressure at a depth x must exceed the surface tension force and hydrostatic force so that

$$p_v(x) > \frac{\gamma}{r} + \rho g x \qquad 5.12$$

if the keyhole is to be stable. However, both the vapour pressure and surface tension are temperature dependent properties and, as has been shown recently by Metzbower[141], further calculations would require a detailed knowledge of the keyhole temperature profile. From Appendix A2 it is clear that the vapour pressure of 8090 is high due to the presence of Li and Mg which are volatile elements. But Mg[142] and Li[52] decrease the surface tension, whereas Cu[143] increases the surface tension, of pure aluminium. So, on balance, it is possible that in 8090 the high vapour pressure might be able to support a keyhole which is surrounded by a very fluid molten pool. If this is the case, then stability should not be a problem. It is likely, then, that the hydrostatic force could play a role due to the fluidity of the melt. This force is usually taken to be negligible due to the ideal cylindrical shape of the keyhole. However, as can be seen by the schematic diagrams in Figs. 5.2 (a) and (b), there is likely to be a large, unstable volume of molten metal which can flow into the keyhole[138]. This downward flow could cause the folded structure in Fig. 4.16 (c), as a vapour explosion created a lateral expansion at the base of the keyhole[33][140], thus leaving a 'rolling' cavity which freezes in place. In full penetration welds, then, a vapour explosion is not expected to cause a lateral expansion of the keyhole. Instead, the explosion would be lost out of the base of the keyhole and the keyhole dynamics appear to be more stable. The molten head still causes an uneven bottom weld bead as it flows down the trailing edge of the keyhole. This could explain the observation of type II pores in the partial penetration welds but not in the full penetration welds. The influence of welding speed on volume fraction of porosity (in partial penetration welds) could therefore, in part, be due to its effect on both melt pool temperatures and trailing melt pool size which, as described above, can influence

keyhole stability.

5.3 Base Metal and Weld Metal Microstructure

This section describes the as-received base metal microstructure which needs to be assessed, together with likely production routes, before any attempt can be made to produce a similar microstructure in the weld metal. The microstructure of the CO_2 weld metal is then described and compared to that of the Nd:YAG weld metal, and an attempt is made to explain any observed differences in terms of welding conditions.

The microstructure of the as-received base metal in a superplastically formable condition was found to contain coarse intermetallic particles together with a fine subgrain size of 1-2 μm. The microstructure also contained a bi-modal δ′ distribution; fine homogeneous precipitates together with heterogeneous precipitates on a core of β′. Equilibrium tetragonal β was also identified but neither S′ nor T_1 were observed.

The precise thermomechanical processing route for developing, in 8090, the fine grain microstructure for superplasticity remains a proprietary process[144][145][146]. However, several authors have outlined the important stages[147][146]. These are solutionize at 530°C for 30 minutes, cold water quench and age at 400°C for 16 hours, air cool and isothermal roll at 300°C to 90% reduction. This process, or at least a version of it, would have resulted in the microstructure shown in Figs. 4.5 and 4.6 and described above. The δ′ precipitates presumably formed during air cooling after warm working and it would appear that there is evidence for the formation of a δ′ precipitate free zone around the larger cored δ′ particles. This is in contrast to the findings of Gregson and Flower[64], however, who showed that in aged Al-Li-Cu-Mg-Zr alloys the larger, cored precipitates did not form as a result of preferential coarsening.

The bright field micrograph of the base metal in Fig. 4.8 clearly displays these latter features but also contains precipitates which were analyzed to be tetragonal equilibrium β. Srinivasen et al.[148] has shown that metastable cubic β′ exists up to ~ 570-580°C whereupon it transforms to tetragonal β, but several authors have observed the equilibrium β phase after ageing at lower temperatures such as

500°C[59][149] and 450°C[150] in Al-Zr alloys. Therefore it is possible that the equilibrium tetragonal β observed in Fig. 4.8 formed during thermomechanical processing where the temperatures were around 400°C.

The intermetallic precipitates were qualitatively identified by EDX analysis and the compositions are similar to those reported by Pandey et al.[151] who examined intermetallic particles in an Al-Li based superplastic alloy of similar composition. It is likely that the intermetallic particles formed during warm working after the short solutionizing treatment.

The first point to note from the work on the CO_2 weld metal is that the chemical analyses from the weld and base metal compare quite favourably suggesting that elements which have a high rate of evaporation e.g. Li and Mg (see Appendix A2) have not been lost from the melt pool during welding. Added to this TEM on (a) as-welded, (b) aged and (c) solution treated and aged weld metal showed that δ′ precipitation can occur. Also, Mg was identified to have segregated to the intercellular phase during solidification and the Mg bearing phase S′ (Al_2CuMg) was present in the solution treated and aged heat treatment condition. It is inevitable that these elements will have contributed to the formation of the keyhole owing to their high vapour pressures, but the mechanism which prevents their total evaporation from the weld pool is not certain. It is possibly a consequence of the low pressure compared to that of the atmosphere around it. Giedt[32] has estimated the vapour pressure in a 1100 Al alloy during electron beam welding and within the keyhole the vapour pressure had a maximum of 26000 μHg, the log of which is 4.4. In these units, the log of atmospheric pressure is 5.9. Thus the vapour pressure in the keyhole is probably an order of magnitude less than atmospheric pressure and it is reasonable to assume that most of the vapour in the keyhole will be contained and must condense on the cooler parts of the keyhole. Near the top of the weld pool some vapour will escape which contributes to forming the laser induced plasma[133].

Therefore, if evaporation does take place from the weld metal it must occur at the top (and bottom) surface of the weld pool where the temperature is much reduced in

comparison with the centre of the keyhole. Block-Bolten and Eagar[152] confirmed that evaporation from the weld pool surface occurs on arc welds made in Al alloys and that when high vapour pressure elements are present these can reduce the temperature of the weld pool below that of the boiling point of the pure metal. The elemental loss due to vaporization is difficult to predict, but Collur et al.[153] and Mundra et al.[154] have successfully shown that the overall vaporization rates from the surfaces are controlled by the presence of the plasma in CO_2 laser welds. It was found that when a plasma is present the vaporization rate was lowered significantly compared to that predicted from theory (Appendix A2) by an order of magnitude.

The composition of the weld pool is an important issue since the presence of Li in particular is essential for the of precipitation of δ' . In summary, it has been shown that the CO_2 welds made in 8090 contain the alloying elements required for the production of mechanical properties

The grain structure of the CO_2 weld solidified fusion zone was quite different from that of the base metal and varied considerably from one part of the weld cross-section to another as shown in Fig. 4.2. The molten pool profile has been identified by the banded structure in Fig. 4.2 (c), where periodic instabilities in the solidification sequence have caused grain growth to stop and start. The possible profile is sketched in Fig. 5.2 (a). This shows that there is a shallow, drawn back pool in the upper part, perhaps due to conduction mode heating from the plasma[34], together with a rapid increase in penetration with the formation of the keyhole. At the interface with the base metal, columnar grains were seen to form which grew into the weld pool with what appeared to be epitaxial growth on pre-existing solid grains at the fusion boundary. In the lower part of the weld, associated with the near parallel sided keyhole, columnar growth was rapidly terminated and a fully equiaxed grain structure developed giving a relatively fine equiaxed grain size. The microstructure at the edge of the weld pool was also coarser than that at the weld centre with cell sizes of 5 and 2 μm respectively. In the upper, wine-glass portion of the weld, columnar growth predominated and columnar grains continually changed their orientation whilst presumably attempting to follow the maximum thermal gradient. However, towards

the weld centre-line the structure did become more equiaxed with much larger equiaxed grains than in the lower part of the keyhole. Clearly, without detailed numerical calculations it is only possible to consider, in a qualitative manner, the differences in grain structure within the weld. The columnar to equiaxed transition is known to be promoted by a number of factors including a low temperature gradient in the melt, a high solidification front velocity, fluid flow in the melt and the presence of heterogeneous nucleating particles[155]. The number density of nucleating particles is unlikely to vary from one part of the weld pool to another and it is most probably changes in fluid and heat flow conditions which are responsible for the different grain structures, with the pronounced columnar structures in the upper part of the weld perhaps indicating that melt temperature gradients were significantly higher there, or that the solidification front velocity was lower.

The observed grain structure development is generally consistent with that reported by several workers[10][13][44][100]. The temperature gradient is highest at the edge of the weld pool where the growth rate is a minimum[47], consistent with the preferred conditions for columnar growth, and at the weld pool centre-line the temperature gradient is shallow due to the proximity of the keyhole to the molten metal and the growth rate is a maximum. Thus constitutional supercooling is most prominent at the weld pool centre and equiaxed structures can freely form. This analysis applies to the lower, keyhole region of the weld. However, the grains in the upper region of the weld, as shown in Fig. 4.2 (c), have a significant upward growth direction. Judging by the orientation of these columnar grains, it is probable that they actually nucleated on grains in the lower region of the weld pool which had already solidified. This can be explained by the shape of the molten weld pool. The lower keyhole part of the weld, due to its lower melt volume, solidifies quickly and can provide a substrate for the molten upper part to freeze on. That the grains are coarse and columnar in the upper region is probably due to a low solidification front velocity. This can be explained as follows. Referring to Fig. 2.8, the maximum growth rate occurs when a grain is growing in the same direction as the welding direction. However, the columnar grains in Fig. 4.2 (c) are steeply inclined to the welding direction. Thus the growth rate of the large columnar grains could be a small fraction of the maximum.

If this is the case, G.R would be low resulting in a higher local solidification time and consequently coarser microstructure, with limited constitutional supercooling.

The observed difference in cell spacing between the centre and edge of the weld pool implies that the local solidification time at the pool edge is high compared to the pool centre. This is probably due to the variation in temperature gradient and growth rate conditions which can exist across the weld pool as discussed in section 2.2.1. The values are similar to those reported by Sonti and Amateau[130] on laser welded non-lithium containing alloys of otherwise similar composition. From the relationship between secondary dendrite arm spacing and local solidification time it seems likely that the local solidification time was less than 1s. Since the non-equilibrium freezing range for 8090 is in excess of 100 K, these figures would indicate a cooling rate through the semi-solid state of greater than 100 K/s. Von Bradsky et al.[156] have produced micrographs with similar segregation patterns in gas atomized powders of equivalent composition and the cell spacing was ~ 1 μm. The cooling rate for gas atomized processes is in the range of 10^3 -10^4 K/s[104] so in this respect the above estimate for the 8090 laser weld solidification is not unrealistic.

The microstructure close to the fusion boundary is particularly interesting in that it consists of a band of globular grains of α-Al whose sizes are around 1-5 μm as shown in Figs. 4.9 (a) and (b). The HAZ which is illustrated in Fig. 4.9 (b) is of the order of ~ 100 μm wide and is characterized by star-shaped intermetallic particles which presumably exist at α-Al sub-grain boundaries and triple points. Similar fusion boundary microstructures have been observed by other workers in GTA welds[8][99], electron beam welds[6] and laser welds[9][10][22] in Al-Li based alloys containing Zr. Yunjia[8] explains that these fine equiaxed grains could stem from heterogeneous nucleation of α-Al on small unmelted Al_3Zr particles which exist in the liquid after the base metal has melted. At the fusion boundary it is suggested that the temperature of the liquid is slightly higher than the liquidus of the alloy. As shown by the Al-Zr binary phase diagram[134] in Fig. 5.3 Al_3Zr melts at 1580°C and is therefore solid below this temperature even though the aluminium is molten. Thus Al_3Zr particles can provide heterogeneous nucleation sites for the molten alloy to begin solidification.

This is in contrast to the usual, epitaxial mode of weld pool solidification[38][41][46] which has also been stated to take place in welds in Al-Li based alloys with[14][100], and without[96], Zr additions. In fact, studies on solution treated welds, which will be described in section 5.4, showed significant grain growth within this fine grained region. An alternative explanation can be proposed as follows. In order to understand the presence of these globular grains it is necessary to identify the influence of the molten weld metal on the HAZ. Due to the high solute content of the intermetallic particles identified in the base metal microstructure, the melting point of these particles will be much lower than that of the α-Al. Hence close to the edge of the weld pool it is likely that these intermetallic particles will melt to differing degrees according to their proximity to the molten metal. Fig. 4.9 (b) shows that the intermetallic particle morphology gradually changes as the HAZ is traversed. Away from the fusion boundary the star-shape is barely noticeable and the particles are basically unaffected, but closer to the weld pool edge, sub-grain boundaries and triple points are clearly defined due to incipient melting. It is reasonable to suggest, then, that as the HAZ consists of melted intermetallic material, that the globular grains at the fusion boundary also consist of grains of unmelted α-Al, surrounded by once liquified intermetallic material. This liquid would have been able to wet the sub-grain boundaries if the interfacial energy between the solid sub-grains is greater than twice that of the solid-liquid interface[157]. Otherwise, the liquid would prefer to exist with near-spherical morphologies as it does at triple points in the HAZ. Such a mechanism would account for the spatial scale of the globular α-Al (since 1-2 μm sized sub-grains are present in the base metal) and has, in fact, been observed to occur in stir-cast Al alloys[158].

Therefore, the scale of the solidified microstructure generally suggests that it is approaching the limits required for superplastic forming. This is especially so in the keyhole region of the weld. In addition, there has been minimum distortion of the base metal due to the small size of the HAZ. Coupled with the previous observations on composition it would appear that post-weld ageing might be able to produce similar base and CO_2 weld metal microstructures.

The features of the CO_2 weld described above, such as (a) fusion boundary microstructure and (b) HAZ structure were also observed in the Nd:YAG weld. However, in the Nd:YAG fusion zone, hardness and TEM observations from (a) as-welded and (b) as-welded plus aged samples showed that δ' was absent from the weld metal. Similarly, Mg was also absent from the intercellular phase. The observed Nd:YAG weld secondary dendrite arm spacing at the weld centre was ~ 0.5 μm whereas at a similar location in the CO_2 weld the secondary dendrite arm spacing was ~ 2 μm. It has already been suggested that the Nd:YAG welds were made by a conduction mode of heating, and here the ratio of surface area to weld pool volume is high. Thus, since there was no keyhole formation and consequently no plasma, two reasons can be identified for elemental loss: (a) surface tension driven fluid flow in the Nd:YAG weld pool and (b) no plasma aided suppression of the vaporization rate. That conduction mode laser weld pools can show severe turbulent fluid flow has been demonstrated by Paul and Debroy[159] in stainless steels. Following their analyses of (a) weld pool temperatures, (b) vapour formation and (c) secondary dendrite arm spacings a reasonable estimate of the secondary dendrite arm spacing in the Nd:YAG weld pool can be made. It will be assumed that the peak weld pool temperature at the centre of the weld pool is the boiling point of aluminium, 2720 K[188]. For a weld pool with a radius of 0.5 mm there could then be a temperature gradient of ~ 2720/0.5 K/mm. The cooling rate at the weld pool centre is given by the product of the temperature gradient with the welding speed, 5 mm/s, i.e. G.R ~ 27200 K/s. This is an order of magnitude lower than that suggested by Milewski et al.[27], 1×10^5 K/s, for Nd:YAG welds on a 2024 (Al-4wt.%Cu) alloy although they measured a secondary dendrite arm spacing of ~ 1 μm. Assuming a non-equilibrium freezing range of 100K, the following equation for Al-4.5 wt.% Cu[130]

$$\lambda_2 = 7.5 (t_f)^{0.39} \qquad 5.13$$

yields a secondary dendrite arm spacing of 0.8 μm. This is comparable to the observed spacing of ~ 0.5 μm. However, if the cooling rate from Milewski et al.[27] is substituted into equation 5.13, a secondary dendrite arm spacing of 0.5 μm is obtained. Zacharia et al.[160] studied the heat transfer during Nd:YAG welding on stainless steels and similar values of cooling rate and secondary dendrite arm spacing

were reported. Clearly, then the cooling rate of the Nd:YAG welds is typically of the order of 10^4-10^5 K/s. Furthermore, comparison of measured and predicted values in the present work suggests that the composition of the Nd:YAG weld pool could essentially be that of an Al-Cu alloy which would confirm the TEM and hardness observations described above. To substantiate this observation, for increased alloy additions, for example when Mg and Li are present, both the non-equilibrium freezing range and the constant of proportionality increase[48]. Thus if both the freezing range and constant are double in 8090 compared to Al-4.5 wt.% Cu, the calculated λ_2 is ~ 2 μm for an identical cooling rate. This is very qualitative but it does demonstrate that the secondary dendrite arm spacing is sensitive to the composition.

It can also be shown that there is ample opportunity for the volatile elements to evaporate from the whole of the weld pool volume. Even though the effect of plasma on vaporization is difficult to determine, either qualitatively or quantitatively, the turbulence within the molten metal alone can lead to elemental losses. Together with the temperature gradient there will also be a surface tension gradient (assuming that surface tension is inversely proportional to temperature) with the maximum surface tension occurring at the weld pool edge. Paul and Debroy[159] solved the equations of change and showed that the radial velocity along the surface of the weld pool was of the order of 1 m/s which is several orders of magnitude higher than the welding speed. Assuming that the weld pool will begin to solidify at 993 K with a cooling rate of 27200 K/s from 2720 K, then the time taken to solidify is ~ 0.063 seconds. Thus, at a surface velocity of 1 m/s an element on the surface could travel 0.063 m before the weld pool solidifies. For a weld pool radius of 0.5 mm this presents the possibility of the surface being regenerated ~ 0.063/0.0005 times, i.e. 126 times. This, then, constitutes vigorous circulation of the molten metal and presents the possibility of total evaporative loss of Li and Mg.

In summary, then, it seems likely that the loss of Li and Mg during Nd:YAG welding, together with the small molten volume, has resulted in the formation of a microstructure which is 1 to 2 orders of magnitude finer in scale when compared to that of the CO_2 weld.

The major differences between the microstructures of the CO_2 and Nd:YAG welds can be summarized as follows: (a) the Nd:YAG weld contains substantially reduced amounts Li and Mg, unlike the CO_2 weld as shown by the absence of δ' precipitation and the composition of the interdendritic material, (b) the Nd:YAG weld is made by a conduction mode mechanism whereas the CO_2 weld is made by a keyhole mode mechanism and (c) the Nd:YAG weld has a finer microstructure than the CO_2 weld. This suggests that quite different welding mechanisms are operative in each case.

Apart from the reduced radiation wavelength between the CO_2 and Nd:YAG lasers, the major operating difference was that the Nd:YAG laser was pulsed whereas the CO_2 laser was continuous. The effect of pulsing on the weld microstructure will be discussed as follows. The banded structure which is obvious in Figs. 4.13 (a) and (b) delineates the weld bead at successive laser pulses. On Fig. 4.13 (a) the average band separation is ~ 63 μm and the bands themselves have a more pronounced solidification pattern. Furthermore, the weld was made at 5 mm/s with a pulse frequency of 86 Hz. Thus the time between bands measured on the weld surface is ~ 13 ms, and the time between successive laser pulses is ~ 12 ms. It is clear that these figures are very close in magnitude so the banding probably stems from the laser pulsing. The bands are also visible on Fig. 4.13 (a) which is a transverse section. This shows that several laser pulses have, in some parts of the weld volume, overlapped. The illustration in Fig. 5.4 perhaps demonstrates more clearly that on a transverse section only the outside edge of the weld pool, i.e. a layer close to the fusion boundary undergoes one thermal cycle. Towards the top of the weld pool on a transverse section successively more and more thermal cycles have affected the weld volume. Of course, the number of times which the laser pulse affects a particular cross section of weld depends on the laser pulse frequency and the welding speed. This phenomenon possibly explains why the microstructure of the Nd:YAG weld is difficult to characterize and appears to consist of an almost random distribution of intermetallic particles. After the formation of fine equiaxed and columnar grains at the edge of the weld pool, as in the CO_2 weld, the solidification process is interrupted by another thermal cycle. Solidification is rapid and the direction of the maximum thermal gradient in the weld pool will be complex and far from constant. Thus there could be little consistency in

the direction of the solidifying structure. It is also possible that the grains in the newly reheated volume can nucleate epitaxially on the solidifying grains from the previous pulsed volume. This would explain the continuity of grain boundaries across the bands in Figs. 4.13 (a) and (b). Added to this, it is quite likely that coarsening of the solidification structure can occur in previously solidified pulsed volumes. As the welding process advances, the influence of the newly melted pool on a previous semi-solid region decreases with distance, but the overlapping temperature gradient may be sufficient to cause localized heating and coarsening of the rapidly solidified structure.

In summary, the processing differences between the CO_2 and Nd:YAG laser welding can qualitatively account for the observed variations in microstructure and composition.

5.4 Microstructures following Heat Treatment

It has been demonstrated, both by TEM analysis and hardness measurements in the welded plus aged condition, that the CO_2 weld is susceptible to age hardening heat treatment whereas the Nd:YAG weld is not. This is due to the lack of hardening phases in the Nd:YAG weld. The mechanisms of Li and Mg loss from the Nd:YAG weld pool have been outlined. Furthermore, that these elements have not evaporated during CO_2 laser welding suggests that there is a fundamental processing difference between the two techniques in this case. However, even though the CO_2 weld still contained essentially all the elements required for the manufacture of desirable properties, the distribution of elements was inhomogeneous after welding and therefore the welded structure had to be solution treated. This section then, aims to examine the results of the effect of post-weld heat treatment on the CO_2 weld fusion zone microstructure.

It was shown that at higher solution treatment temperatures homogenization of the cast structure became more complete, but the fusion zone grain size gradually increased until at the superplastic forming temperature of 530°C several massive grains were present. The average grain size was appreciably larger than that of the base metal and the as-welded cell size. The heating rate to 530°C influenced the average weld metal

grain size and the massive grains were absent after adopting a slow heating rate of 1 K/min to 530°C. It is interesting to note that the majority of the massive grains were situated around the fusion boundary. Furthermore, some of these had spread part way into the HAZ. Within the large grains the residual cast structure was still present as shown in Fig. 4.20 (b), and dislocation networks and misfit dislocations had formed at the prior cell boundaries. However, DTA of the weld metal did not reveal any melting reactions at or below the solution treatment temperature.

It is appropriate at this point to identify the main microstructural differences between the as-welded metal and the base metal. The base metal is unrecrystallized with large intermetallic particles, a sub-grain size of 1-2 μm and sub-micron δ′, β′/δ′ and equilibrium β precipitates. The weld metal consists of crystallographically oriented cellular or equiaxed α-Al dendrites with fine δ′ precipitates. The secondary dendrite arm spacing is 2-5 μm and TEM showed that Mg, Cu, Fe and Li (Zr was not detected) were situated predominantly at cell boundaries. It is known that the base metal is expected to dynamically recrystallize during superplastic forming[144] with the conversion of low angle grain boundaries to high angle grain boundaries and the β′ dispersoids pin the grain boundaries to maintain a small recrystallized grain size[161][162][163][164]. The theory behind this is as follows. Normal grain growth is affected by the grain boundary surface energy and the presence of inclusions. In addition, the rate of grain boundary migration is inversely proportional to the radius of curvature of the boundary[165]. Furthermore, that particles can hinder grain boundary motion has been studied with reference to Zener drag by Nes et al.[166] who confirmed that maximum grain boundary pinning is effected by a large distribution of small diameter particles.

Within the cast structure of the weld fusion zone it might be expected that during homogenization solute would diffuse to regions of lower concentration thereby dissolving intermetallic particles. Thus prior cell boundaries would transform to grain boundaries. If this was the case in the 8090 CO_2 welds, a stable grain size of the order of 2-5 μm would be expected to result in a homogeneous distribution of solute elements. Clearly this was not the situation after the thermal cycle of heating,

solutionizing and cooling. Three mechanisms were identified as being possibly responsible for the massive grain growth. In the first case, welding stresses might increase the internal energy of the system which could be reduced by grain boundary migration. Secondly, liquation of the grain boundaries could present easy diffusion paths for migrating boundaries enabling the grains to grow to large sizes in relatively short times. Thirdly, grain boundary migration could occur freely over large distances due to (a) low misorientations between the cells in the solidified structure and (b) the absence of grain boundary pinning particles. The issue of residual welding stresses was thought unlikely, the reason being that stresses of any magnitude would probably have appeared as solidification cracks due to the large solidification range of the alloy. Grain boundary melting was examined as a possible cause by DTA and no melting reactions were observed at or below the solution treatment temperature. Added to this observation, Burke[165] has shown that grain growth is temporarily prevented by the occurrence of partial melting at the grain boundaries. The remaining theory, then, was one of normal grain growth in a matrix of similarly orientated cells which were devoid of appropriate grain boundary pinning particles. The fact that the majority of the massive grains were situated at the fusion boundary possibly substantiates this proposal. The columnar cells at the fusion boundary probably had very similar orientations due to the common $<100>_{Al}$ growth directions and the grains freely coalesced to form one large grain. This would account for the misfit dislocations and dislocation networks along prior cell boundaries in Fig. 4.25 (a) since the boundaries between neighbouring cells would be semi-coherent. In a similar manner, the grains were able to spread into the HAZ because the grains at the fusion boundary in the base metal provided epitaxial nucleation for the grains in the weld metal, thus their crystallographic orientations would have been nearly identical. However, there are still some enlarged grains in the body of the weld metal which cannot be wholly attributed to coalescence due to their uncertain orientation.

This analysis of the mechanism is supported by the TEM investigation on the weld metal microstructure. After heating to 530°C at a rate of 100 K/min, solutionizing and cooling, in both the solution treated and the solution treated and aged conditions, the characteristic bi-modal δ' precipitates were not observed. This indicated that the β'

dispersoids were either absent or too small to be resolved. (Although the area available for inspection in the TEM is small, it should be pointed out that the observed precipitate distribution ought to be representative of the whole weld since it is believed that substantial mixing of the weld pool occurred during welding). This would explain the optical observation of massive grain growth after this thermal cycle. β' has a low driving force for coarsening[150] and in the absence of, or at least reduction of, appropriate grain boundary pinning precipitates there would be a possibility of enhanced grain boundary migration. So a method was needed of giving the Zr atoms more time to diffuse through the α-Al lattice in order to encourage β' coarsening. From studies conducted by Watts et al.[167] and Thomas[168] it was decided that a reduction in heating rate to the superplastic forming temperature might encourage the growth of β' dispersoids.

An investigation was initiated into the effect of a reduced heating rate to the superplastic forming temperature on the weld metal microstructure. The results were very enlightening and optical microscopy successfully showed that as the heating rate was decreased to 10 and 1 K/min, the weld metal grain size became increasingly finer and more uniform, as was demonstrated by Figs. 4.24 (a) and (b). Subsequent analysis of the welds in the TEM showed that the characteristic δ' bi-modal distribution, indicative now of β' precipitation, was present to greater extents after heating at rates of 10 and 1 K/min. This indicated that the Zr atoms had diffused greater distances in the extra time available and appreciably increased the size of the β' dispersoids. This result can also be arrived at via simple calculations using the diffusivity of Zr in Al. From Zedalis et al.[150], the coefficient of diffusivity, D_0, for Zr in Al is 5400 mm^2/s and the activation energy for diffusion, Q, is 222 kJ/mole. The diffusivity, D, at various temperatures (in K) can be found by substitution into the following equation

$$D = D_0 \exp\left(\frac{-Q}{RT}\right) \qquad 5.14$$

where R = 8.3145 J/mole/K

A characteristic Zr diffusion distance, $\sqrt{(Dt)}$, can be estimated by considering heating

rates of 100, 10 and 1 K/min (where t is the diffusion time in seconds). It can be assumed that heating at 100 K/min is approximately equal to 1 minute durations at 300, 400, 500....etc. K. Similarly, heating at 10 K/min is approximately equal to 10 minute durations at 300, 400, 500....etc. K and heating at 1 K/min is approximately equal to 100 minute durations at 300, 400, 500....etc. K. Using the temperatures 300, 400, 500, 600, 700 and 800 K the total diffusion distances for heating rates of 100, 10 and 1 K/min heating rates are 35, 110 and 350 nm respectively. By way of comparison, calculations for Cu diffusion in Al[169] give values of 3, 10 and 33 μm for identical, hypothetical heating rates of 100, 10 and 1 K/min respectively. Thus the sluggish nature of the Zr diffusion is confirmed and consequently longer times are needed before any appreciable growth of β′ dispersoids occurs.

The weld sample which had been heated at 1 K/min to 530°C was subsequently aged for 16 hours at 190°C. This caused widespread δ′ precipitation and therefore highlighted the location of the β′ dispersoids. The TEM micrograph in Fig. 4.30 (a) clearly illustrated that β′ had coarsened substantially to a size approaching that of the dispersoid in the base metal as a direct result of the low heating rate. It is present within the grains but more importantly at the grain boundaries. Thus it seems likely that the β′ distribution is indeed controlling the weld metal grain size during solution treatment.

5.5 Mechanical Properties

The preceding sections of the discussion have been concerned with the microstructure and microhardness of CO_2 and Nd:YAG weld metal in both the as-welded condition and after a post-weld thermal treatment. In the results section it was shown that the CO_2 weld is more age-hardenable than the Nd:YAG weld and microhardness measurements on the heat treated CO_2 weld metal revealed that similar values of microhardness could be obtained between base and CO_2 weld metal after solution treating and ageing. However, the effect of grain size on the weld metal mechanical properties has not been discussed. Therefore it is the aim of this section to (a) compare the fracture mode of the CO_2 weld metal both in the as-welded and heat

treated conditions with that of the base metal and (b) comment on the mechanisms which control the fracture.

To summarize the main results from section 4.8 it was found that there was no observable difference in fracture strength between the weld samples which had been solution treated with heating rates of either 100 and 1 K/min to the solution treatment temperature of 530°C. This was despite the difference in weld metal grain size between the samples heated at different rates, which was described in sections 4.4.2 and 4.5.2. In both the as-welded and solution treated conditions, the weld metal had a lower fracture strength than the base metal. However, comparable strengths between base and weld metal were obtained after solution treating and ageing. Predominantly intergranular failure was observed in all samples. In the solution treated and aged base metal, secondary cracking occurred parallel to the tensile axis and perpendicular to the short-transverse direction along grain boundaries. Shallow grain boundary dimples in the base metal sample, together with transgranular ductile dimples in the weld metal samples confirmed the limited ductility of this alloy. It was shown qualitatively that microvoid formation in the weld metal was increased after solution treating and ageing compared to the as-welded and solution treated conditions.

There has been limited work on the fracture of Al-Li alloy welds. However, Edwards et al.[6] showed that TIG and electron beam welds in 8090 failed intergranularly but with enhanced grain boundary ductility after solution treatment and ageing, as observed in this work. Microvoids formed at grain boundary precipitates and the low ductility observed was associated with the grain boundary structure rather than the grain size. In TIG welds on 8090, Erjing et al.[99] observed intergranular failure in (a) as-welded and (b) solution treated and aged conditions. The grain surfaces were initially smooth and featureless but shallow ductile dimples formed after solution treating and ageing. Again, similar features were observed in the present study.

The fracture behaviour of Al-Li based alloys has been addressed generally by Miller et al.[49] and Quist et al.[1]. More specifically, several workers have studied the fracture of 8090 type alloys[170][171][172][173][174]. Indeed, Wert et al.[174] have

shown that in an Al-Li based alloy secondary cracks formed at those grain boundaries which were parallel to the tensile axis. The crack spacing was approximately equal to the spacing of the grain boundaries in the short-transverse direction. However, as well as the intergranular fracture, final failure occurred transgranularly across the delaminated grains. After ageing, parallel ridges were observed on the transgranular fracture surface which were possibly caused by slip bands. In an ingot-cast Al-Li based alloy Butler at al.[175] determined that fracture occurred by a mixture of intergranular and transgranular modes. However, in the solution treated condition the intergranular surface was faceted in appearance while in the over-aged condition ductile microvoiding had occurred. Thus void nucleation was made easier in aged material. Fe-Cu rich particles were associated with the microvoids. Indeed, dimples were observed in the solution treated and aged base metal in the present work, but no attempt was made at determining the mechanism of their formation.

In summary then, the observations described above by other workers agree quite favourably with the present study. As indicated in Fig. 4.41, it seems likely that it is the distribution of intermetallic precipitates in the solution treated welds, which exist at prior solidification cell boundaries, that are responsible for controlling the fracture behaviour. This satisfactorily explains why the fracture strength did not vary with fusion zone grain size. Though no attempt was made to identify the particles within the shallow intergranular microvoids, the intermetallic particles which exist at prior solidification cell boundaries were shown to be enriched in Fe and Cu as in Fig. 4.25 (a). Therefore, following the model suggested by Butler et al.[175] the sequence of events leading to fracture could be as follows. Planar slip in the grains containing δ' precipitates causes dislocation pile-ups at the large intermetallic particles be they inter or intragranular. The intermetallic particle is more brittle than the matrix and cracks under the imposed stress intensity. A void is nucleated where the particle has cracked which can grow under the applied tensile stress and the more ductile matrix eventually separates at the matrix-particle interface. Where several particles are grouped in stringers the voids can coalesce during decohesion resulting in a dimpled, intergranular fracture surface. That microvoid formation is enhanced after solution treating and ageing is probably due to the ease of coplanar slip across larger δ' precipitates. Since

the weld in this heat treatment condition contained only a small volume fraction of S′ phase and no T_1 phase, the conventional mechanisms for reducing coplanar slip[68][69][83] were not operative. However, the fracture strengths clearly show that, as with the microhardness values discussed previously, similar properties can be obtained between base and weld metal after appropriate post-weld heat treatment, despite the large difference in grain size which can occur in the solution treated weld fusion zone.

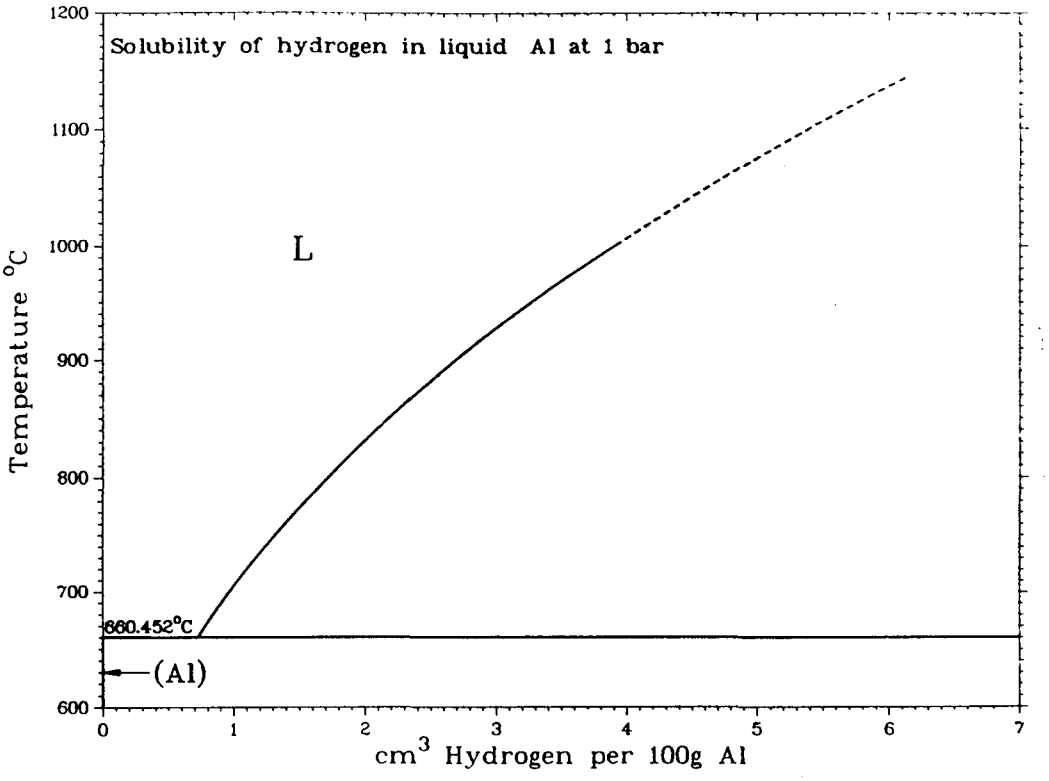

Figure 5.1. Al-H binary phase diagram[134].

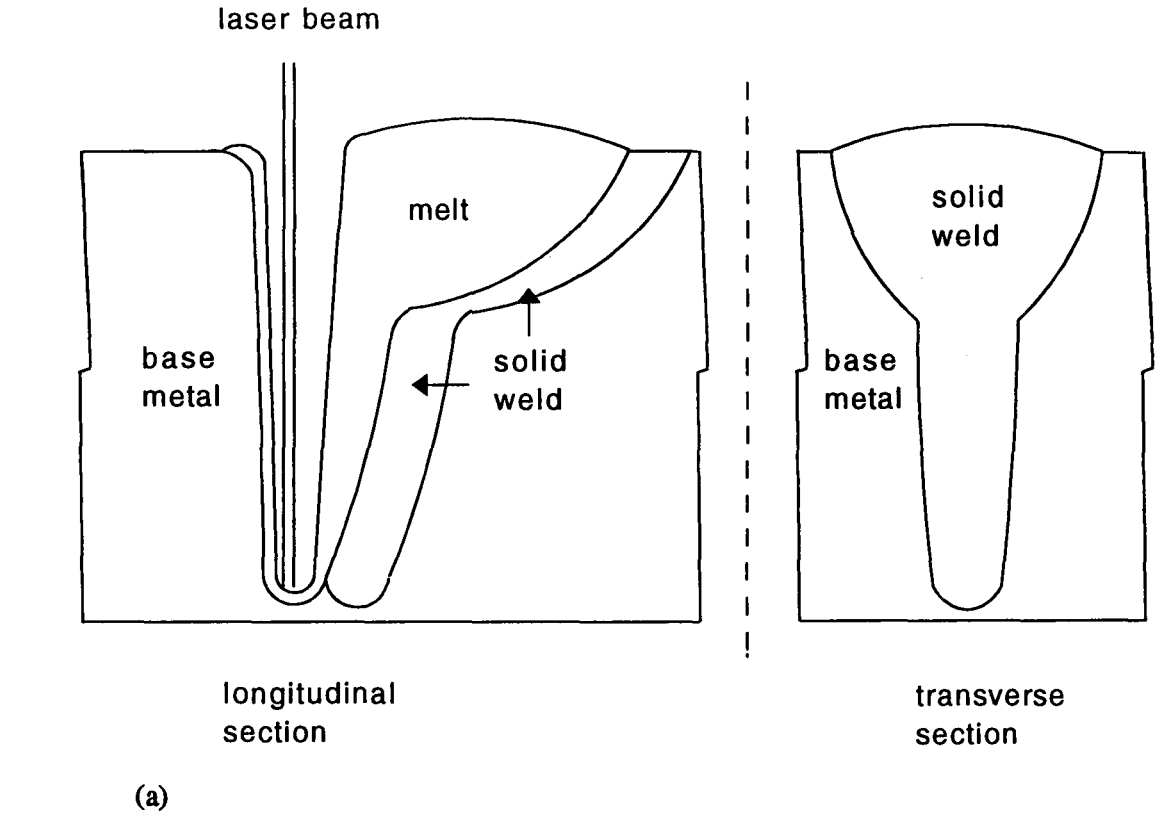

(a)

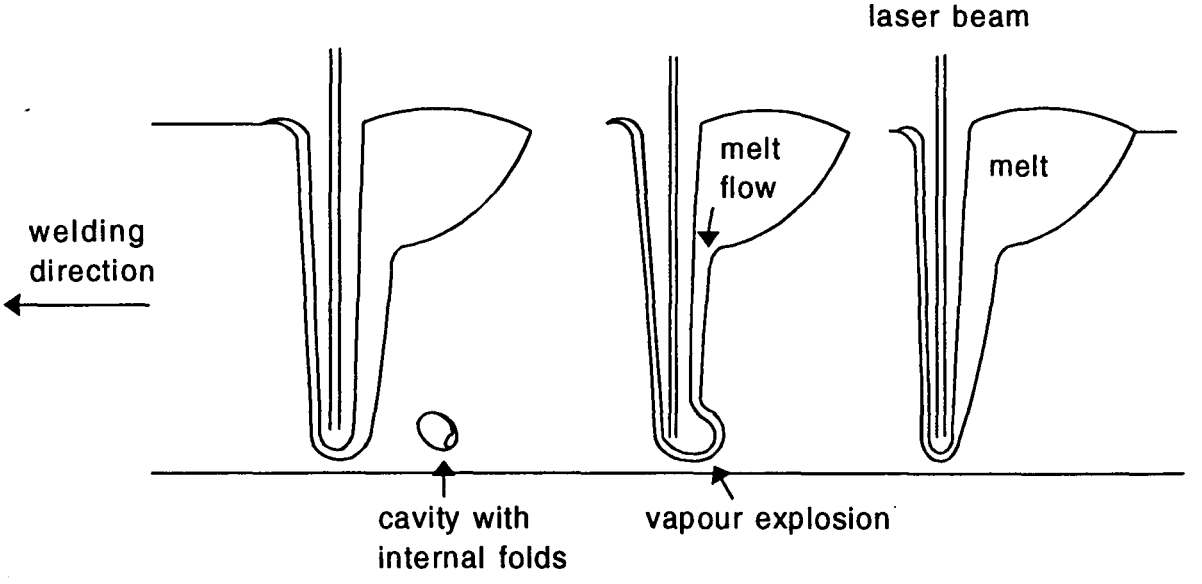

(b)

Figure 5.2. Schematic diagrams of the 8090, CO_2 laser generated molten weld pool. (a) illustrates the longitudinal and transverse sections and (b) shows how the molten head might lead to porosity formation.

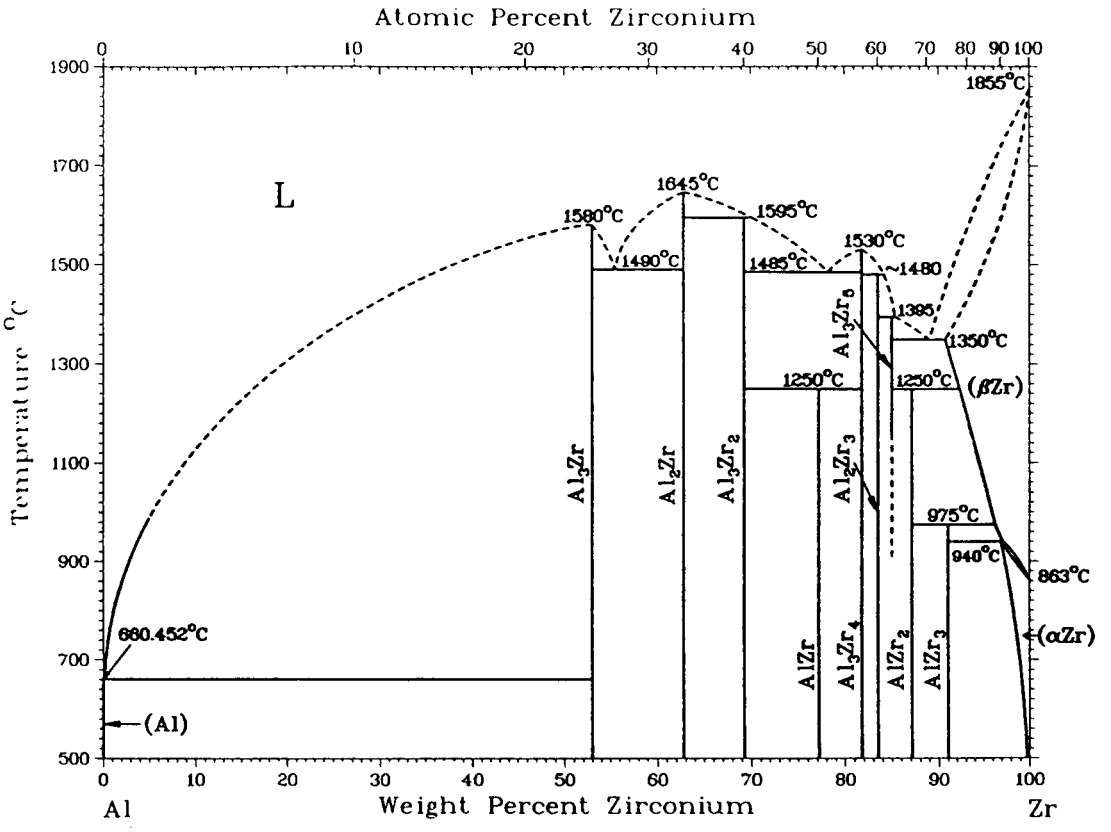

Figure 5.3. Al-Zr binary phase diagram[134].

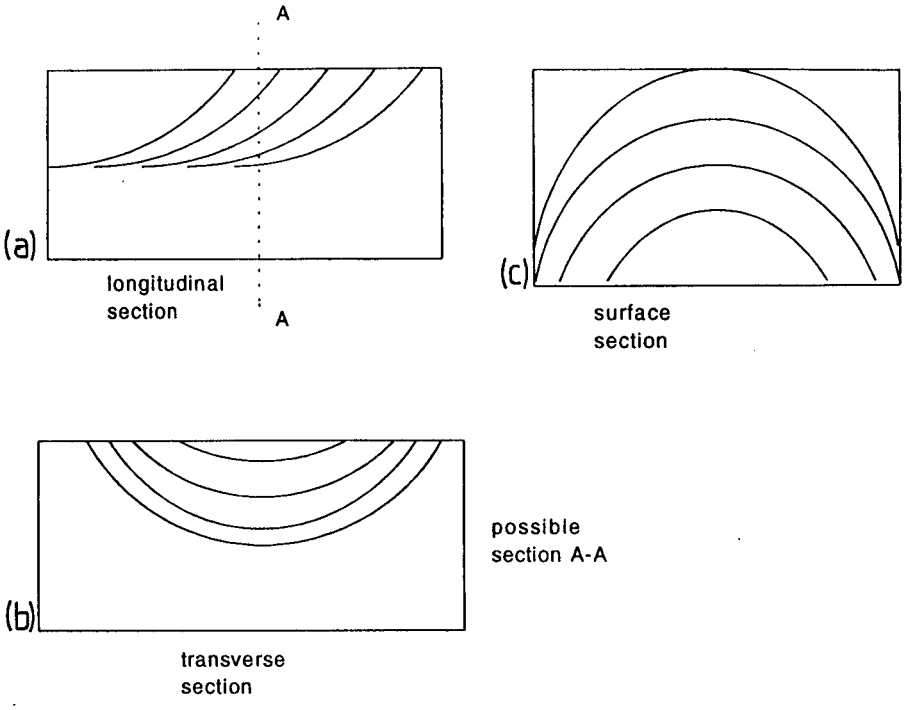

Figure 5.4. Schematic diagrams of (a) longitudinal, (b) transverse (through a section A-A) and (c) surface sections of the Nd:YAG laser generated weld pool. The overlapping weld pools can be clearly seen.

Chapter 6. 8009 and 6061 Results

6.1 8009 Results

6.1.1 Base Metal Microstructure

Optical microscopy of the base metal revealed a fine, sub-micron precipitate dispersion in an α-Al matrix. The overall composition of the base metal was determined by EDX analysis on the SEM using a Tracor Northern quantification routine. The alloy was found to contain 1.4 wt.% V, 1.6 wt.% Si, 8.4 wt.% Fe, 88.6 wt.% Al consistent with the nominal composition of 8009. Bright field TEM showed that the material's microstructure consisted of α-Al grains, about 500 nm in diameter, with a high volume fraction of near-spherical, inter- and intragranular precipitates; the precipitates, which ranged in size from 50 to 200 nm, can be seen in Fig. 6.1 (a).

EDX analysis of precipitates using a focused probe showed that they contained Al,Fe,V,Si. They were enriched in Fe,V,Si compared to the α-Al matrix as can be seen by comparing the EDX spectra shown in Figs. 6.1 (b) and (c). A selected area ring diffraction pattern from the base metal is shown in Fig. 6.2. The effective camera length, L, was back-calculated from the recognised Al rings (with Al lattice parameter = 0.40496 nm) to be 3.3697 m. The schematic diagram of the completed rings is marked every fifth ring and the diameters are those used for the lattice parameter calculations. The rings were identified as being due to either α-Al or a bcc phase with a lattice parameter of 1.247 nm and are listed in table 6.1 according to the schematic ring number. Reference should be made to Appendix A1 for details of the solution of ring patterns. Thus the precipitates have a crystallography consistent with that reported by Skinner[116] for the $Al_{12}(Fe,V)_3Si$ dispersoid phase. Although the EDX analysis was only qualitative it is also consistent with the composition of this phase reported in the literature.

6.1.2 Weld Metal Structure

(i) Weld Dimensions and Porosity

The dimensions of the autogenous bead-on-plate welds were found to vary with

welding parameters. Full penetration welds were achieved in 2 mm thick sheet with a nominal beam power of 3 kW over a range of speeds from 50 to 150 mm/s. However, at 2 kW beam power penetration changed from full to partial penetration as the welding speed increased from 50 to 80 mm/s. The width of the fusion zone was a function of the weld parameters and Fig. 6.3 shows the effect of welding speed on weld top bead width at a constant nominal power of 3 kW; the bead width decreases with increasing welding speed.

Macro and micro porosity were observed using X-ray radiography. Partial penetration welds contained severe linear porosity with large spherical pores measuring up to 0.8 mm in diameter. In the partial penetration welds the pores were situated predominantly near the weld fusion zone root, as shown by the micrograph of a longitudinal section in Fig. 6.4 (a). Fig. 6.4 (b) is a transverse section micrograph of a full penetration weld. Widespread spherical microporosity is evident and some pores can measure up to 0.2 - 0.3 mm in diameter. As the weld volume increases, i.e. as the welding speed decreases at fixed beam power, the volume fraction of porosity appeared to increase though the latter was only assessed qualitatively.

(ii) Weld Metal Microstructure

The thermal cycle imposed by the high intensity laser beam effectively destroys the microstructure of the RS/PM base metal in the fusion zone. The nature of the weld metal microstructure was characterized using optical microscopy, SEM and TEM and the micrographs in Fig. 6.5 (a) and (b) show that there is a widespread distribution of coarse, star-shaped intermetallic particles in the fusion zone which can measure up to ~ 10 μm across. The etched SEM micrograph of Fig. 6.5 (b) suggests that several intermetallic particle morphologies might exist. The particles appear to be hexagonal, trapezoidal or clusters of irregular, angular particles. Fine cellular-dendrites of α-Al surround the coarse particles and the cell spacing is of the order of 1 - 2 μm. Quantitative EDX analysis was performed on the star-shaped particles which indicated that they had the composition given in table 6.2. There was no obvious difference in composition between the different particle morphologies. The average composition of the weld was found to be 89.2 wt.% Al, 7.9 wt.% Fe, 1.2 wt.% V, 1.7 wt.% Si as

obtained for five small area analyses ~ 0.1 x 0.1 mm.

A microstructural study was undertaken in the TEM to further examine the various features observed in the SEM. A disc was cut from the near surface plane as illustrated in Fig. 3.3, as this was the only straightforward method of taking a 3 mm diameter disc out of a 2 mm thick sheet. The bright field TEM micrograph in Fig. 6.6 shows smaller sub-micron sized hexagonal and larger micron sized rectangular, intermetallic particles. The fine scale α-Al cellular structure is also revealed with cell boundary intermetallics observable. The large rectangular particle also contained branches perpendicular to its long edges which appear to be moulded into the body of the large particle. From a point near to the centre of the large particle a fan-like contrast is present.

A focused probe was used in the TEM to obtain qualitative analyses of the primary intermetallic particles, the intercellular phase and the α-Al cellular-dendrites. Spectra are given in Figs. 6.7 (a), (b), (c) and (d). For the different morphologies of the coarse particles all invariably contained Al,Fe,V,Si. However, the hexagonal particles were generally somewhat richer in V and Si than the rectangular particles, as can be seen by comparing Figs. 6.7 (a) and (b). This is in contrast, though, to the quantitative analyses obtained from the SEM discussed earlier. The intercellular phase was composed of Al,Fe,Si, Fig. 6.7 (c) and the α-Al was composed of Al with traces of Fe,Si,V, Fig. 6.7 (d).

Selected area diffraction patterns were taken from one of the large rectangular intermetallic particles. These showed that the particle was virtually a single crystal. Several crystal orientations were examined using the double tilt goniometer. Figs. 6.8 (a) and (b) are SADP's taken from the particle illustrated in Fig. 6.8 (c). Using the method of indexing described in Appendix A1 calculations based on Fig. 6.8 (a) give lattice parameters of a = 0.885 nm and c = 2.136 nm if it is assumed that the crystal is tetragonal with a $[1\bar{1}0]$ axis to the beam. This is also consistent with Fig. 6.8 (b) having a $[1\bar{1}1]$ zone axis in the tetragonal system. Similar SADP's were presented by Skjerpe[113] who describe the patterns according to the Al_mFe (m=4.0 to 4.4) phase with

lattice parameters of a = 0.884 nm and c = 2.16 nm. It is thus probable that the intermetallic has the tetragonal Al_mFe structure. Super reflections are just visible in the $<110>_{particle}$ directions as also noted in ref. (113). Extra spots are also observed which may possibly be due to a nearby crystal with a similar orientation which was in the region selected by the aperture.

In the partial penetration welds, regions of 'light' and 'dark' etching are observed toward the weld fusion zone root as in Fig. 6.4 (a). The dark etching region is that of coarse intermetallic particles with a fine α-Al cellular-dendritic structure just described previously. The light etching region is illustrated schematically in Fig. 6.9 (a) and a SEM micrograph taken from the spike is also shown in Fig. 6.9 (b). There is a transition from fine, predominantly cellular α-Al with very little primary intermetallic precipitation, to columnar and equiaxed dendrites as the distance upwards from the weld root increases. Columnar and equiaxed growth apparently develops from spherical precipitates, which were not characterised, with a secondary dendrite arm spacing of 250 - 350 nm. Where clusters of coarse intermetallic particles have formed the α-Al cellular-dendrites adjacent to the cluster are coarser when compared to those further away from the cluster.

The fusion boundary is delineated by an almost continuous line of coarse intermetallic particles, as shown in Fig. 6.10. The HAZ has been identified optically as an over-etched region which extends ~ 100 μm into the base metal and is illustrated in the transverse weld section of Fig. 6.4 (b). The microstructure of the HAZ is not significantly different from that of the base metal and, as shown by the SEM micrograph of Fig. 6.10, there is no evidence of grain boundary melting or significant dispersoid dissolution. There is, however, some evidence of dispersoid coarsening.

(iii) Hardness of Base and Weld Metal

Vicker's microhardness measurements showed that the base metal had a hardness of 139±9 kgf/mm^2. Microhardness measurements were also made throughout the weld fusion zone. Fig. 6.11 (a) is a microhardness profile from the longitudinal centre-line section of Fig. 6.4 (a), traversing up the section from the fusion boundary and into the

bulk weld metal as shown by the line AB on the micrograph. The weld was made at 2 kW with a power of 80 mm/s and was partially penetrating. There is considerable scatter of the results but the microhardness tends to increase with depth from the weld surface, until at the weld root the microhardness reaches a maximum. A microscopical study of the region revealed that the peak coincided with a 'light' etching region of the microstructure. In the centre of the weld the average hardness is ~ 115±34 kgf/mm^2 which is somewhat less than that of the base metal.

Another microhardness profile was taken across the weld root spike of Fig. 6.4 (a). This profile, Fig. 6.11 (b), shows a significant rise in microhardness within the spike up to ~ 300 kgf/mm^2 which is also a 'light' etching region.

There was no observed systematic variation in microhardness within the fusion zone when measurements were made on a transverse section of the fully penetrating weld of Fig. 6.4 (b). The microhardness profile shown in Fig. 6.11 (c) illustrates the lower hardness of the fusion zone when compared to the base metal. The full penetration weld with an average hardness of 86 ± 36 kgf/mm^2 also shows a lower hardness than the partial penetration weld described above. It is apparent that the hardness is affected by the weld pool volume and presumably the size and spatial distribution of the intermetallic particles.

6.2 6061 Results

6.2.1 Base Metal Microscopy

Optical microscopy of the unetched base metal and subsequent EDX analysis in the SEM showed that the microstructure consisted of an irregular Al-Cu-Mg-Si-Fe phase together with rounded, dark Mg-Si rich particles distributed throughout the α-Al matrix, as shown in Fig. 6.12. The Mg-Si rich particles were presumably globules of Mg_2Si. The grain size was measured from anodized sections which are illustrated in Fig. 6.13 for a 3 mm thick sheet. This shows that the grains are non-equiaxed, but are pancake shaped being elongated in the rolling direction and the longitudinal-transverse direction. On longitudinal-transverse sections grain sizes in 3 mm thick sheet were 49x30 μm whereas in 1.6 mm thick sheet the grains measured 81x28 μm.

6.2.2 Weld Metal Structure

(i) Weld Dimensions and Grain Structure

The depth of penetration and the weld top bead width both increased with decreasing welding speed at a constant, nominal laser beam power of 3 kW, as illustrated in the graph in Fig. 6.14. The shielding gas used was nitrogen and the focal length of the lens was 75 mm. At this power, the penetration was low and not suggestive of a keyhole weld, compared to welds in 8090, for example, described in chapter 4. The weld was then presumably more conduction mode with a low ratio of penetration to top weld bead width.

A typical weld transverse section from a weld made in 3 mm thick sheet at 3 kW and 15 mm/s is shown in Fig. 6.15 (a), together with surface and longitudinal centre-line sections in Figs. 6.15 (b) and (c) respectively. These three sections illustrate that the α-Al grains are predominantly columnar and have undergone considerable curvature during weld pool solidification. This would suggest that the weld pool is quite elliptical at the surface, if the columnar grains can be assumed to grow nearly perpendicular to the liquidus isotherm. On the transverse section, Fig. 6.15 (a), columnar grains are seen to grow epitaxially from grains in the base metal as illustrated in Fig. 6.15 (d). In this partial penetration weld columnar grains which nucleated at the weld root have a vertical growth component as demonstrated by the longitudinal centre-line section of Fig. 6.15 (c). Here the grains grow vertically upwards initially, then curve towards the welding direction until an almost constant slope carries the grains towards the surface. On closer inspection of these sections, particularly the surface and longitudinal centre-line sections of Fig. 6.15 (b) and (c) respectively, short black flakes can be seen throughout the weld metal. These short flakes appear to be oriented almost perpendicular to the grain growth direction.

(ii) Microstructural and Chemical Analysis of Weld Metal

The microstructure of the solidified weld metal is shown in Figs. 6.16 (a), (b) and (c). These micrographs were taken from the fusion boundary/HAZ region, Fig. 6.16 (a) and (b), and from the central region of the weld pool, Fig. 6.16 (c). Columnar-dendrites grow into the body of the weld from the fusion boundary, Fig. 6.16 (b). At

the weld centre, Fig. 6.16 (c), the cell spacing of the α-Al is ~ 1 - 2 μm and appears to be reduced when compared to that at the edge of the weld pool which is of the order of 4 - 5 μm, Fig. 6.16 (b). The HAZ has been identified as a narrow region adjacent to the base metal where some large Mg_2Si rich globules in the base metal have changed morphology. Near to the fusion boundary the globules have remelted and resolidified with a fine eutectic structure, which is shown in Fig. 6.17. The Mg_2Si rich globules appear to be unaffected at a distance of ~ 100 μm away from the fusion boundary as shown in the optical micrograph of Fig. 6.16 (a). Thus the HAZ is estimated to be ~ 100 μm wide. As described earlier, short flakes are present in all micrographs within the weld metal and EDX analysis was performed on the flakes using the SEM. This showed that the flakes were significantly enriched in nitrogen compared to the bulk weld metal as a whole. The spectrum from the flake in Fig. 6.18 (a) illustrates this when it is compared to that of the weld metal Fig. 6.18 (b). Welds were also made with a shielding gas of helium instead of nitrogen and these also contained flakes which were not analysed chemically.

EPMA was employed to study the loss of volatile elements from the fusion zone. Wavelength dispersive X-ray spectroscopy was performed on a polished section close to the weld surface over an area which was 50 x 50 μm. The Mg concentration for two profiles is shown plotted against distance in the graph of Fig. 6.19. This graph illustrates that the Mg concentration in the fusion zone was more uniform but perhaps slightly lower than that in the base metal. The average Mg concentration was calculated from ~ 20 readings in the base metal and ~ 20 readings in the fusion zone. These were found to be 0.85 ± 0.05 wt.% and 0.78 ± 0.02 wt.% respectively. When these values are compared to the nominal base metal composition given in the Experimental Techniques (0.88 wt.%) it would appear that some Mg has been lost during welding.

Microhardness measurements from the transverse section in Fig. 6.15 (a) have shown that the average hardness of the HAZ is 101 ± 4 kgf/mm^2, compared to the average weld metal and base metal values of 97 ± 11 and 97 ± 8 kgf/mm^2 respectively. Clearly, there is not a significant difference between any of these values.

Table 6.1 Ring identification of the unknown phase, X, according to the ring pattern in Fig. 6.2.

Ring number	Indices - X (bcc)	Indices - Al (fcc)
1	220	
2	310	
3	222	
4	321	
5	411, 330	
6	420	
7	332	
8	422	
9	510, 431	
10		111
11	520,432	
12	440	
13	530, 433	
14	600, 442	
15		200
16	620	
17	541	
18	533	
19	630, 542	
20	700	
21	720, 641	
22	722, 544	
23	810, 652	
24		
25		
26		220
27		
28		
29		
30		
31		311
32		420
33		422
34		511

Table 6.2 Average composition of the star-shaped intermetallic particles in the 8009 fusion zone.

Element	Al	Fe	V	Si
wt.%	69.8 ± 5.2	23.3 ± 5.4	1.8 ± 0.6	4.7 ± 2.3
at.%	81.7 ± 3.2	13.3 ± 3.6	2.9 ± 0.6	2.1 ± 1.4

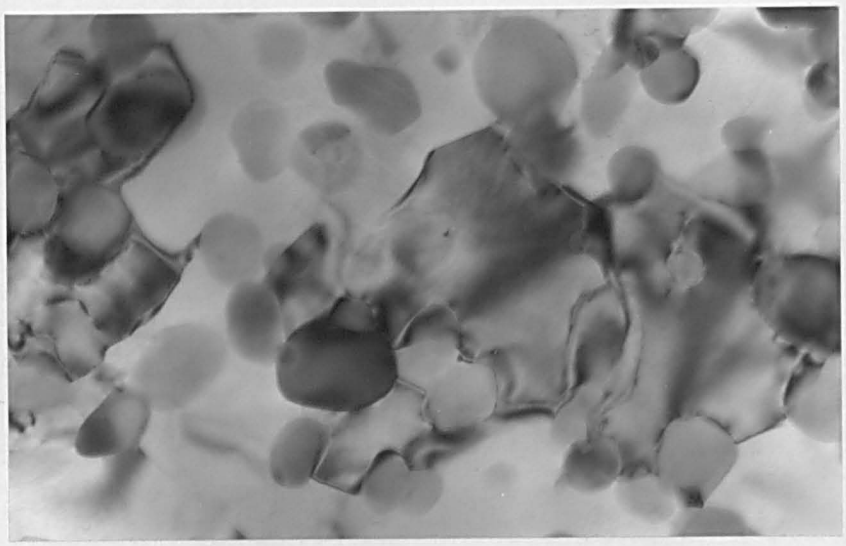

(a) 200nm

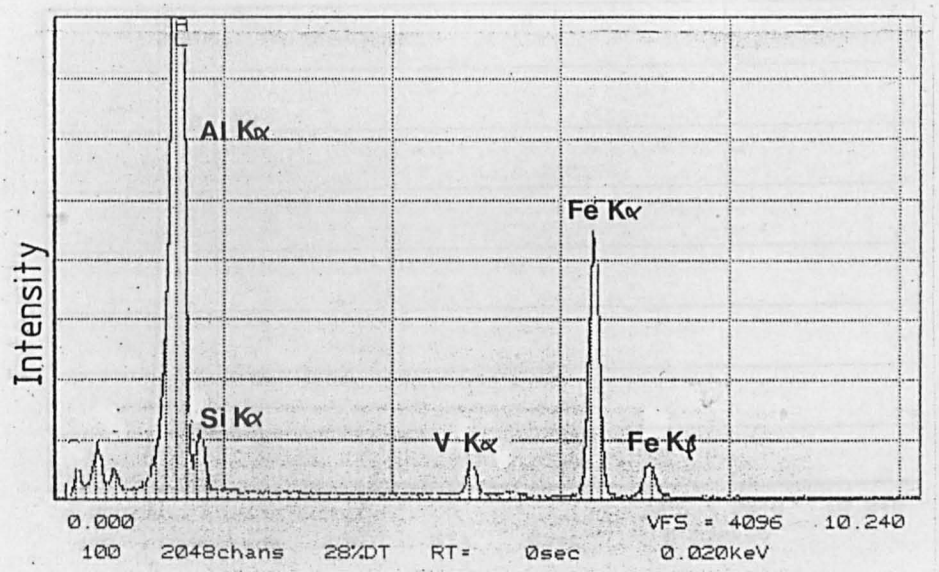

(b)

Figure 6.1. (a) Bright field transmission electron micrograph of the 8009 base metal showing spherical precipitates and small α-Al grains, (b) and (c) are EDX spectra from the precipitates and the α-Al matrix respectively.

(c)

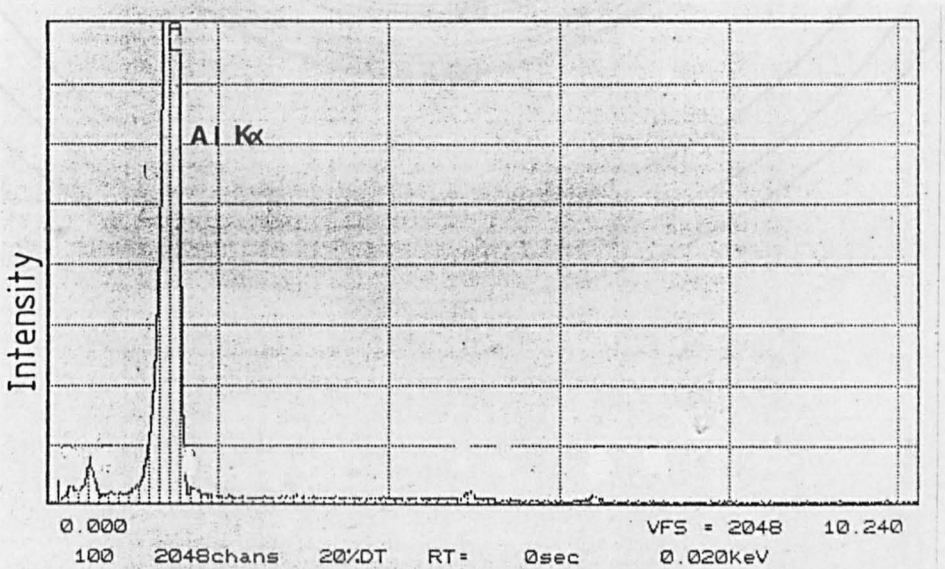

Figure 6.1. (a) Bright field transmission electron micrograph of the 8009 base metal showing spherical precipitates and small α-Al grains, (b) and (c) are EDX spectra from the precipitates and the α-Al matrix respectively.

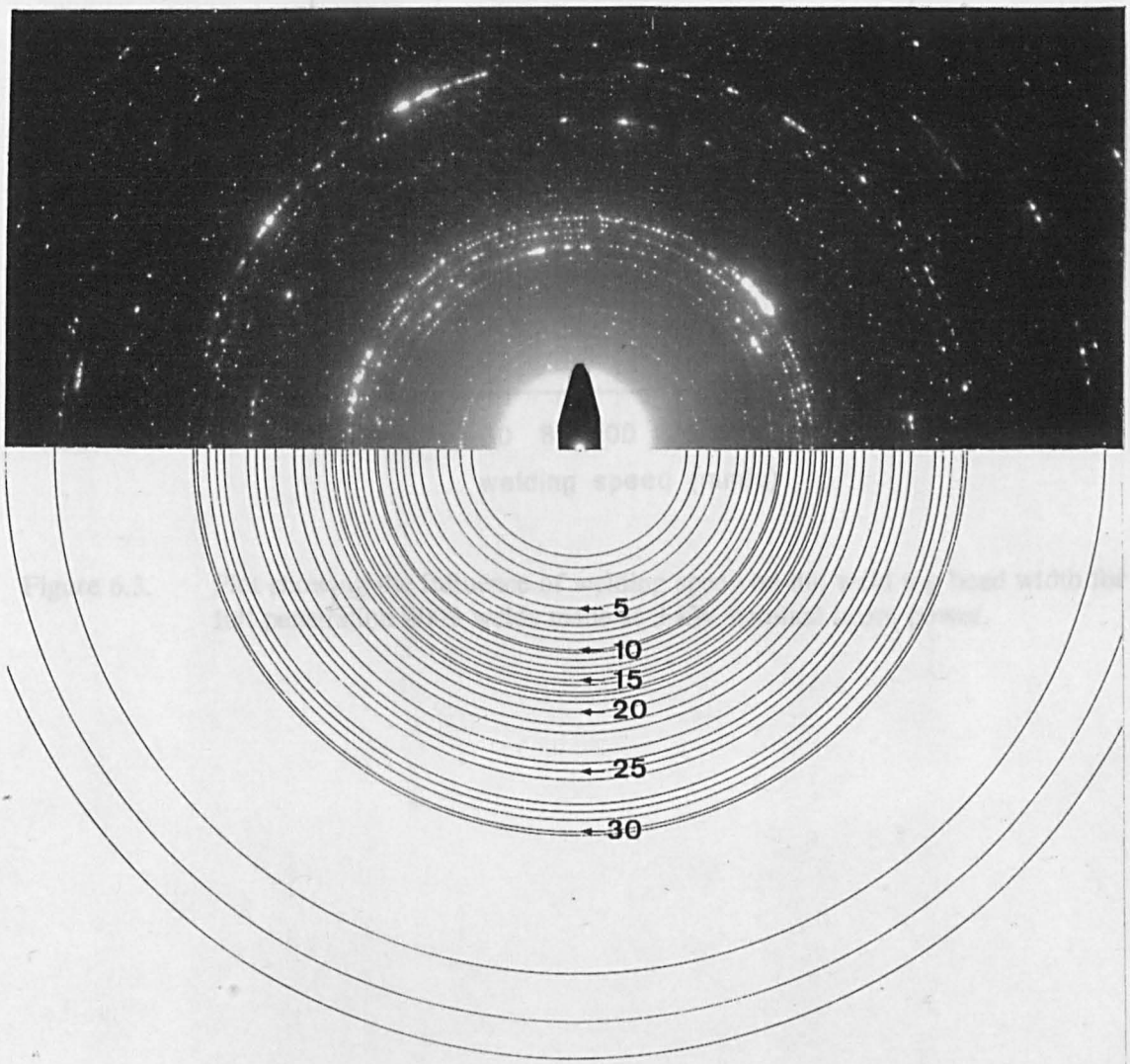

Figure 6.2. A selected area ring diffraction pattern of the 8009 base metal together with a schematic index of the rings.

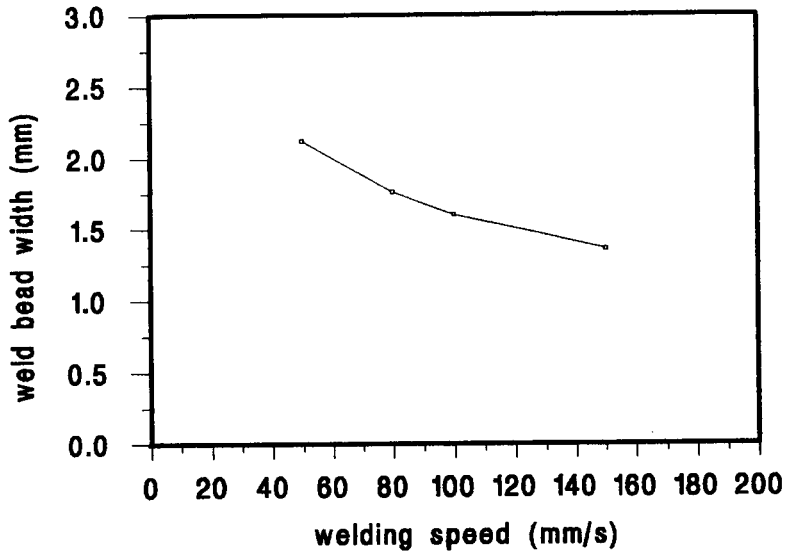

Figure 6.3. Plot showing the influence of welding speed on the weld top bead width for full penetration 8009 welds made at 3 kW nominal beam power.

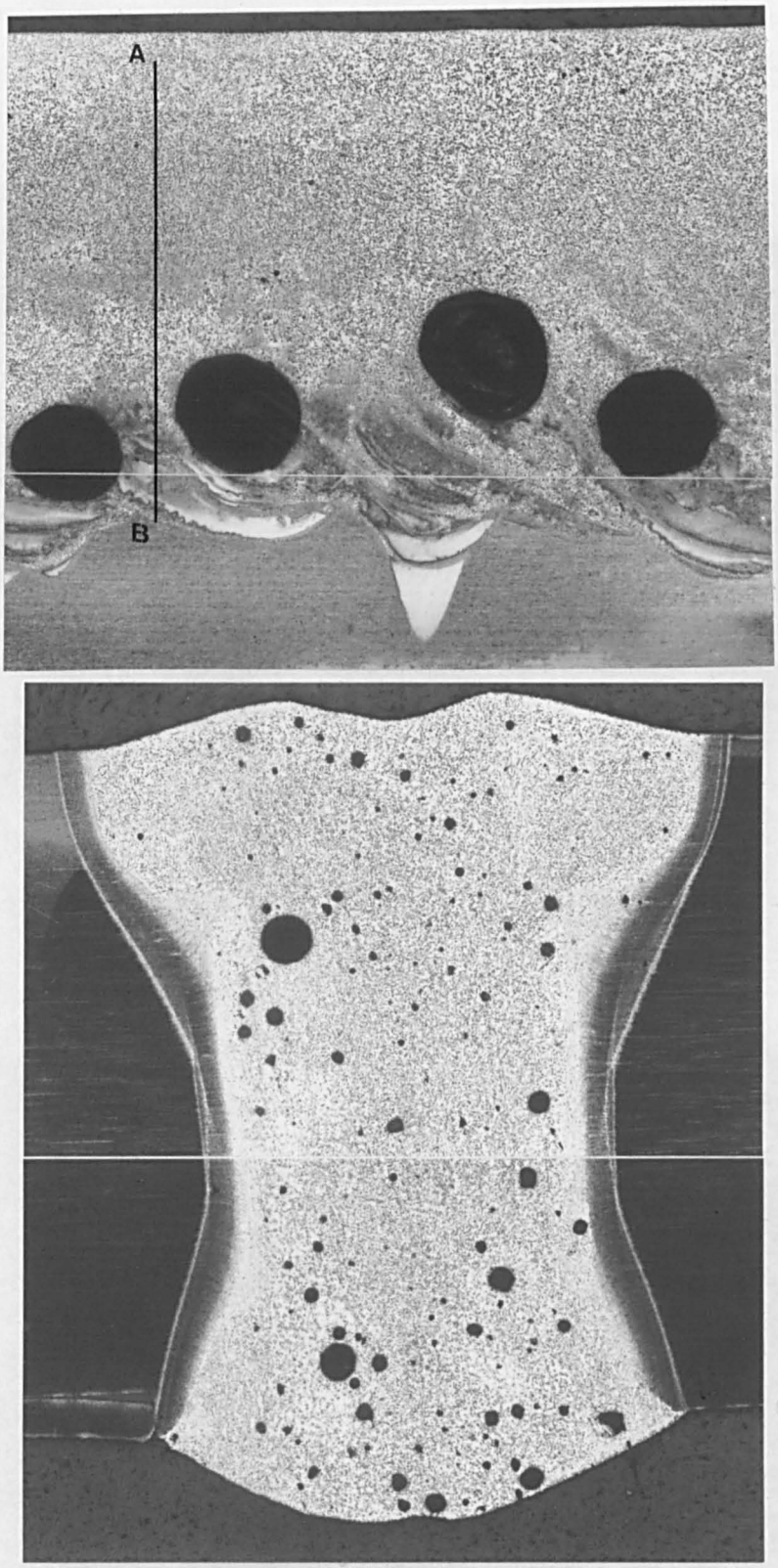

Figure 6.4. Optical micrographs of (a) partial and (b) full penetration welds in 8009 showing the nature of the porosity.

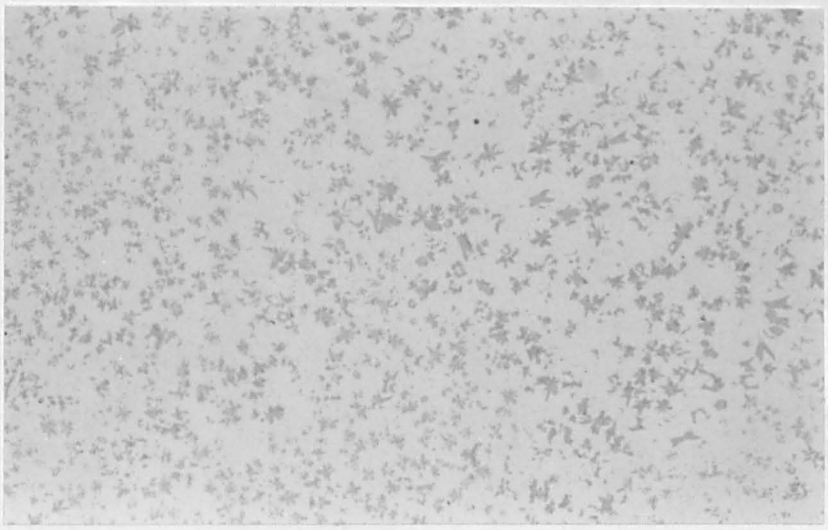

(a)

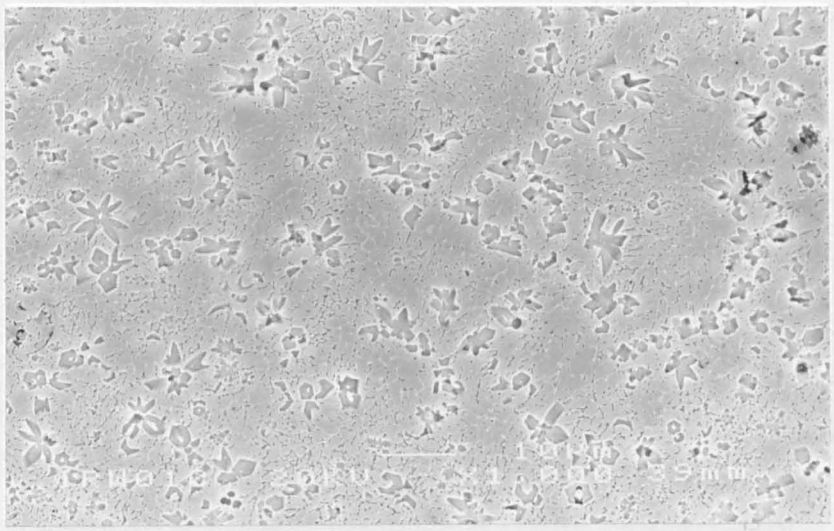

(b)

Figure 6.5. The microstructure of the 8009 weld is illustrated by optical microscopy in (a) and scanning electron microscopy in (b). Coarse star-shaped intermetallics are visible in both micrographs.

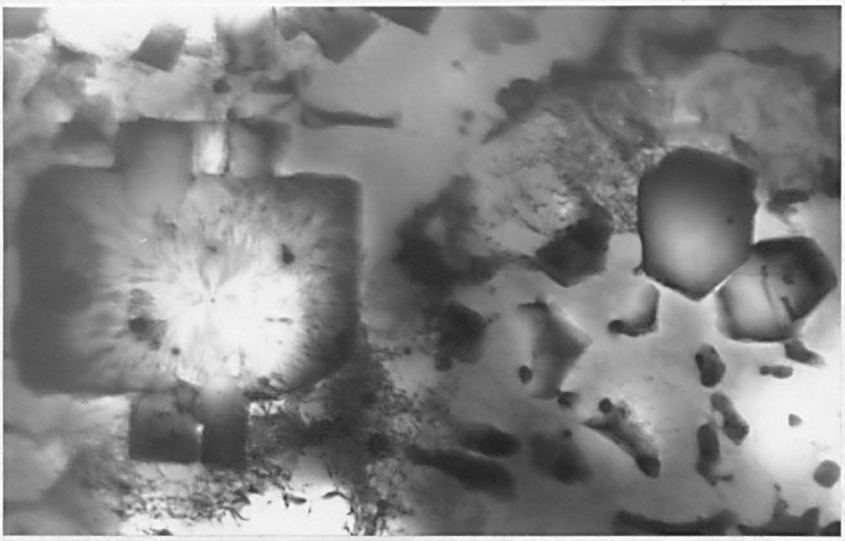

Figure 6.6. Bright field transmission electron micrograph of the 8009 weld microstructure showing large, branched rectangular and hexagonal particles together with intercellular phase.

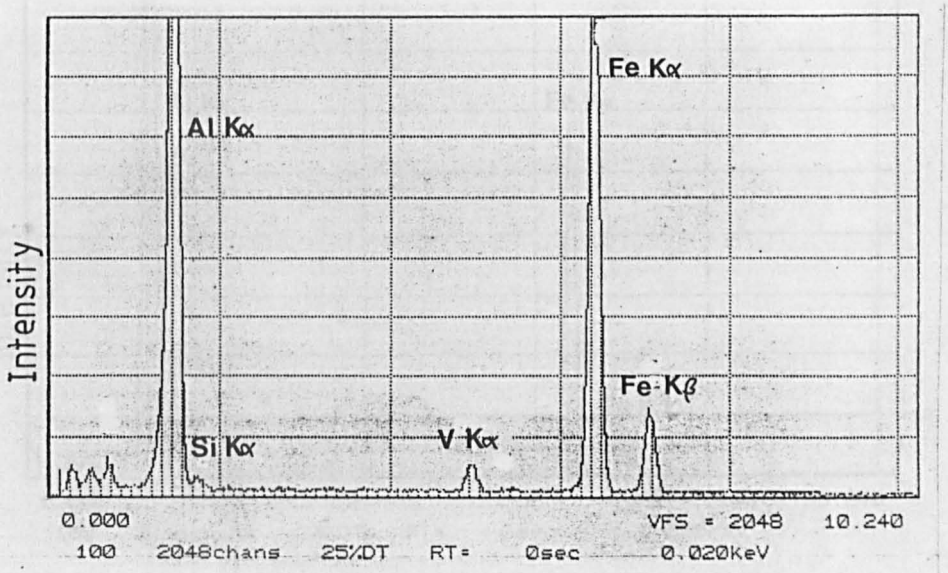

(a)

Figure 6.7. TEM EDX spectra taken from the 8009 weld microstructure. (b) is from a hexagonal particle, (a) is from a rectangular particle, (c) is from the intercellular phase and (d) is from the α-Al matrix.

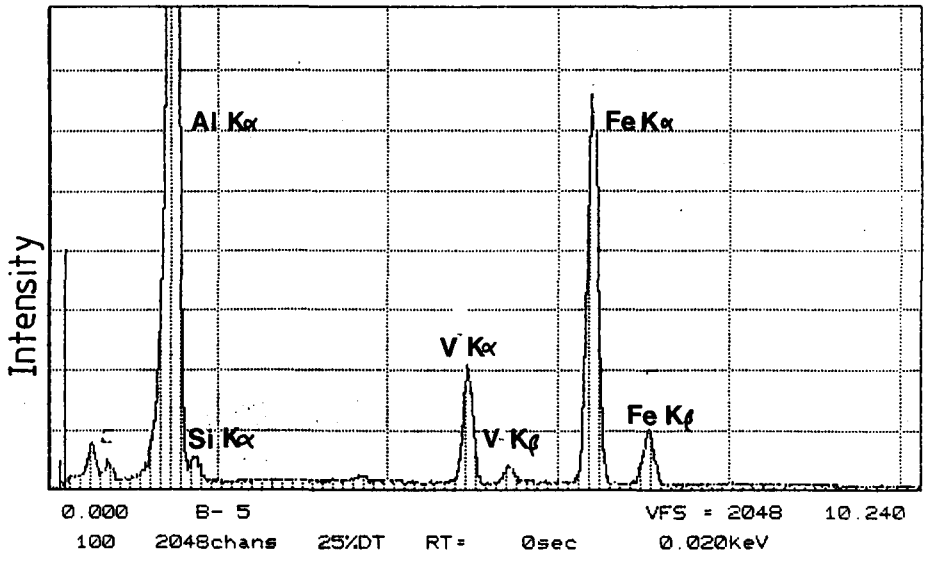

(b)

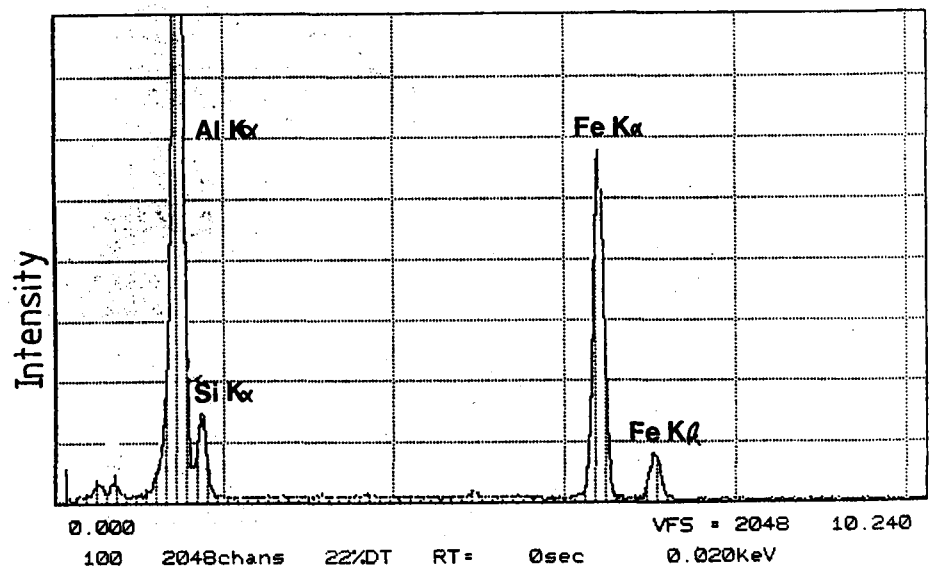

(c)

Figure 6.7. TEM EDX spectra taken from the 8009 weld microstructure. (a) is from a hexagonal particle, (b) is from a rectangular particle, (c) is from the intercellular phase and (d) is from the α-Al matrix.

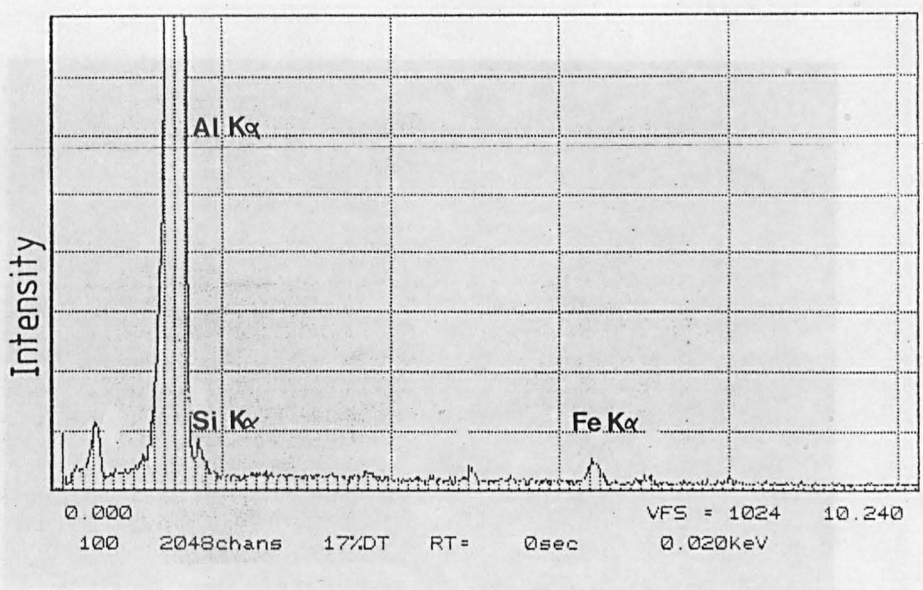

(d)

Figure 6.7. TEM EDX spectra taken from the 8009 weld microstructure. (a) is from a hexagonal particle, (b) is from a rectangular particle, (c) is from the intercellular phase and (d) is from the α-Al matrix.

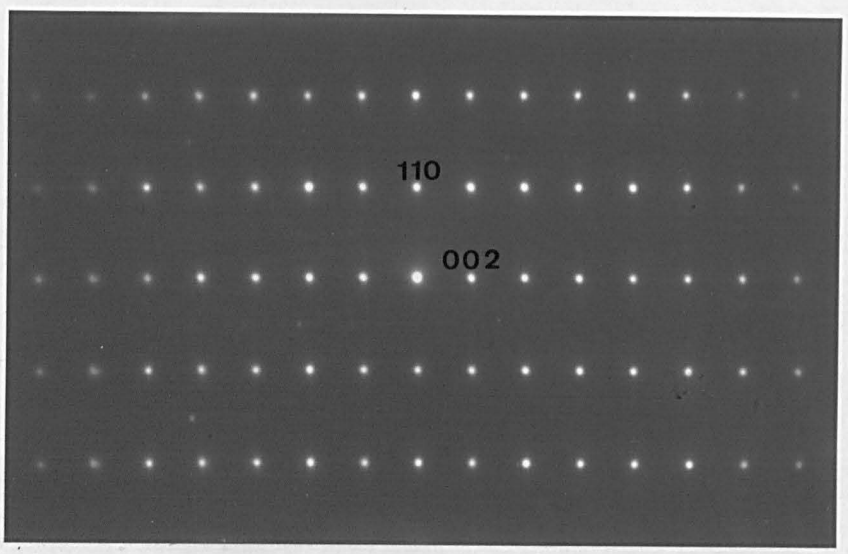

(a)

Figure 6.8. Transmission electron micrographs of the 8009 weld microstructure. (a) and (b) are selected area diffraction patterns with beam directions of Z=[1$\bar{1}$0] and [1$\bar{1}$1] respectively, taken from the particle in (c) which was rectangular with a branched structure.

(b)

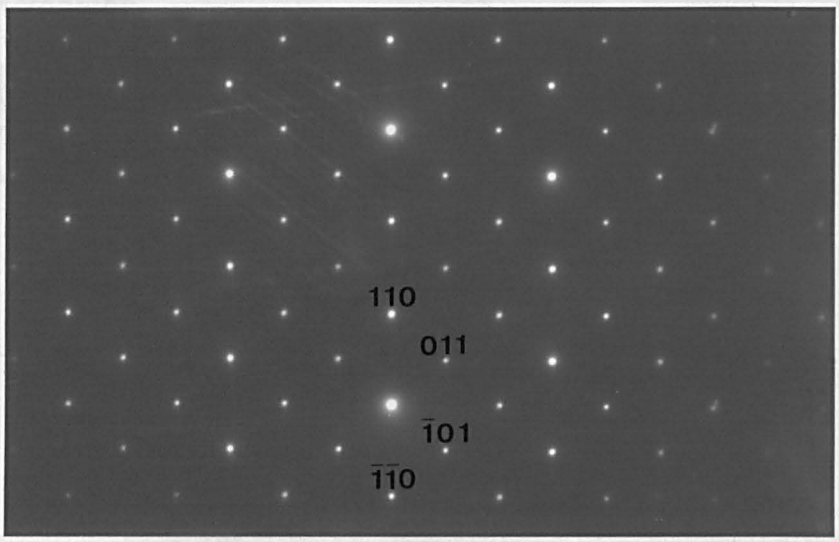

(c)

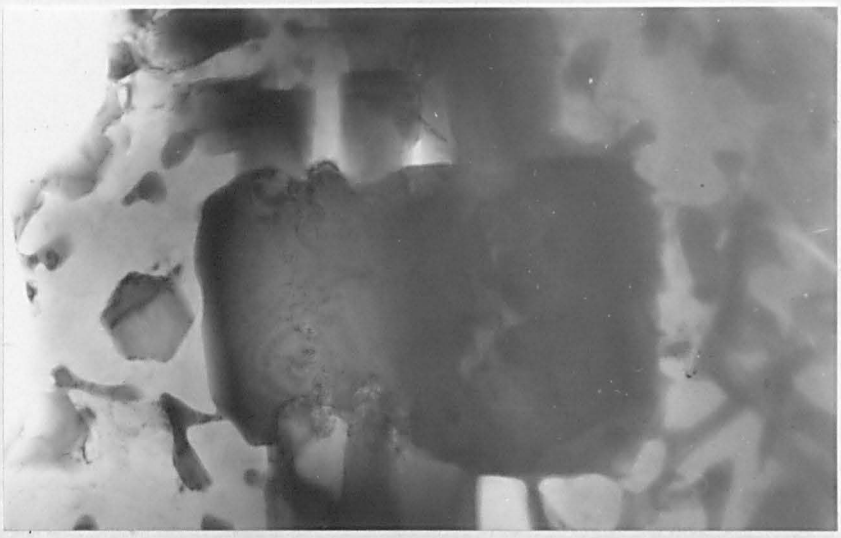

Figure 6.8. Transmission electron micrographs of the 8009 weld microstructure. (a) and (b) are selected area diffraction patterns with beam directions of Z=[1$\bar{1}$0] and [1$\bar{1}$1] respectively, taken from the particle in (c) which was rectangular with a branched structure.

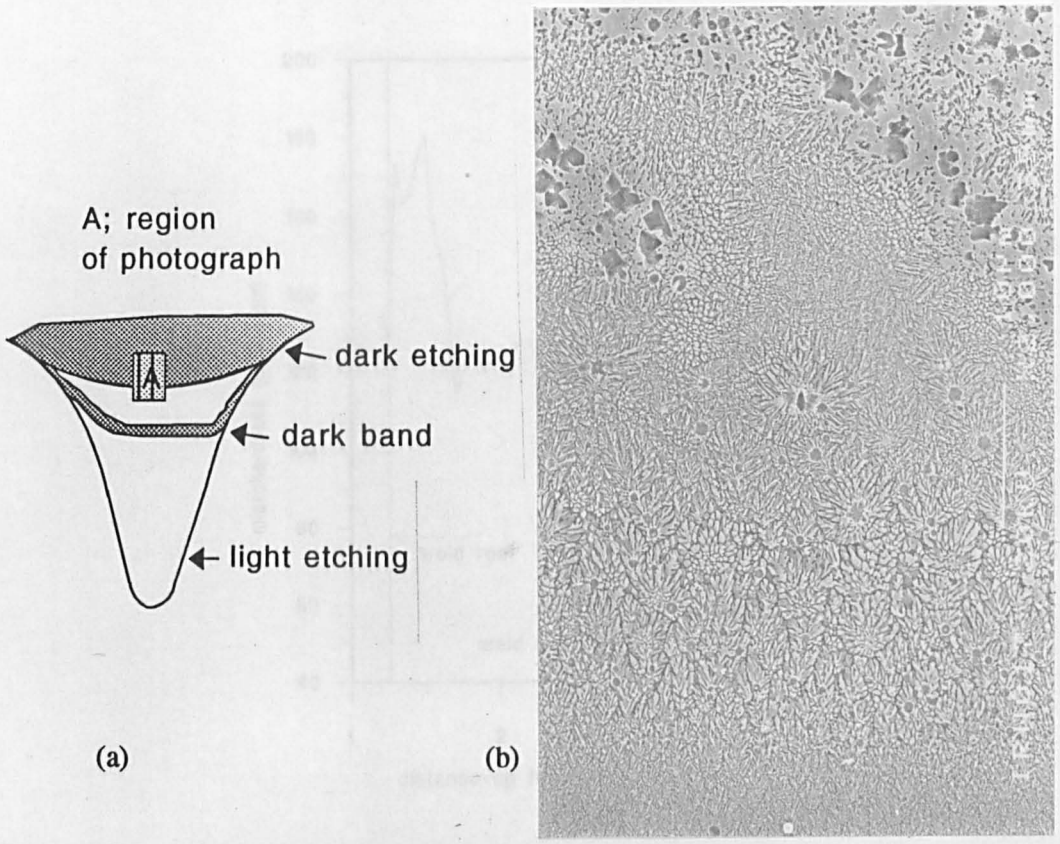

Figure 6.9. Scanning electron micrograph of the light etching spike illustrated in Fig. 6.4 (a) together with a schematic diagram illustrating the location of the micrograph. A transition is observed at the top of the spike from cellular to columnar and equiaxed dendrites.

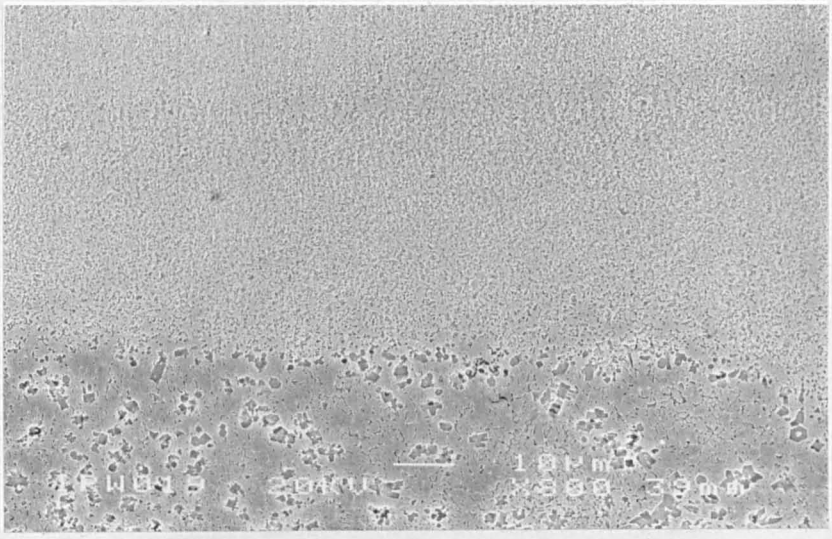

Figure 6.10. Scanning electron micrograph of the 8009 weld fusion boundary and HAZ.

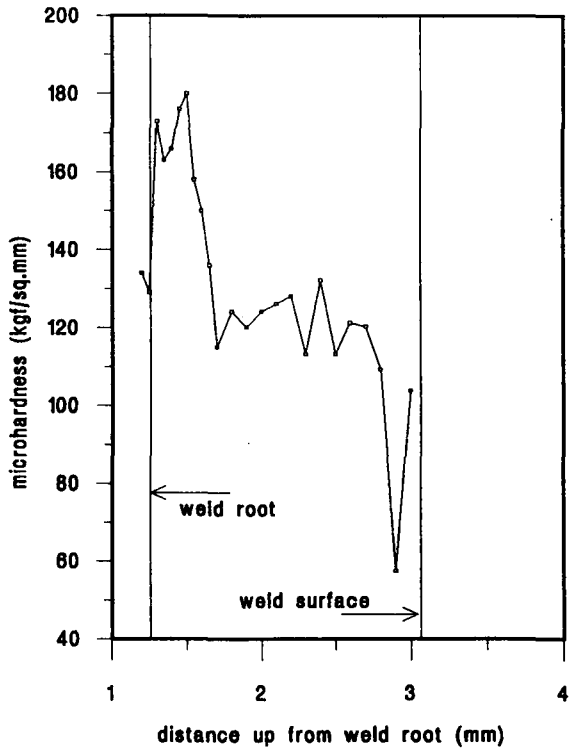

(a)

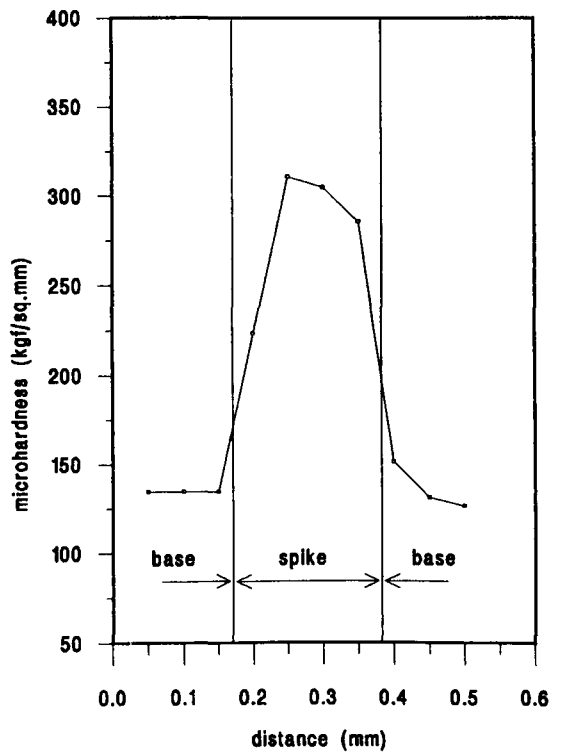

(b)

Figure 6.11. Plots of 8009 weld microhardness. (a) is a profile taken up the longitudinal weld section illustrated in Fig. 6.4 (a), (b) is a profile taken across the light etching spike and (c) shows two profiles taken across a transverse section.

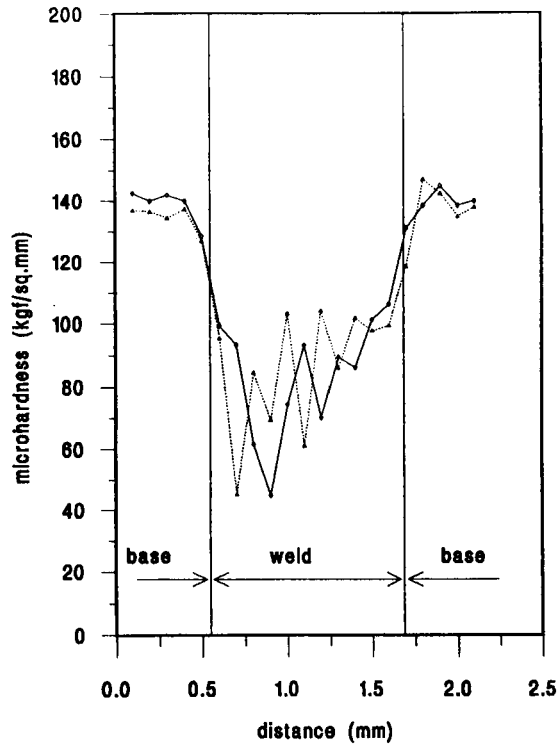

(c)

Figure 6.11. Plots of 8009 weld microhardness. (a) is a profile taken down the longitudinal weld section illustrated in Fig. 6.4 (a), (b) is a profile taken across the light etching spike and (c) shows two profiles taken across a transverse section.

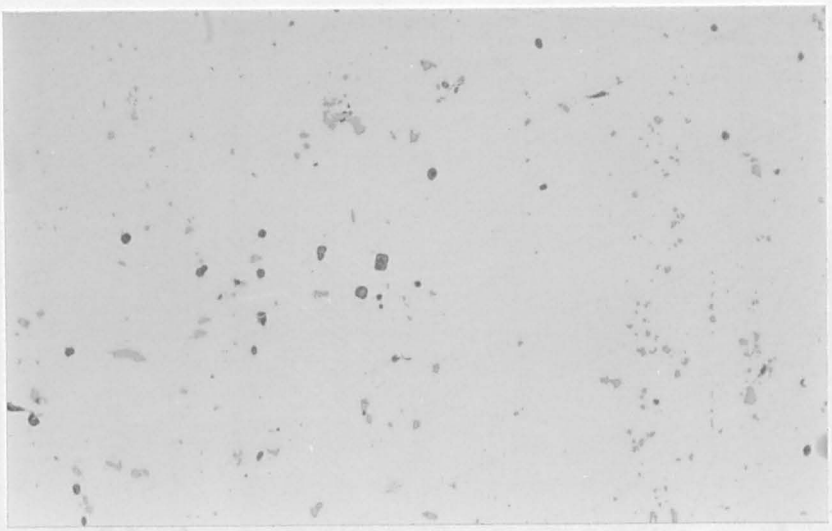

Figure 6.12. Optical micrograph of the unetched 6061 base metal.

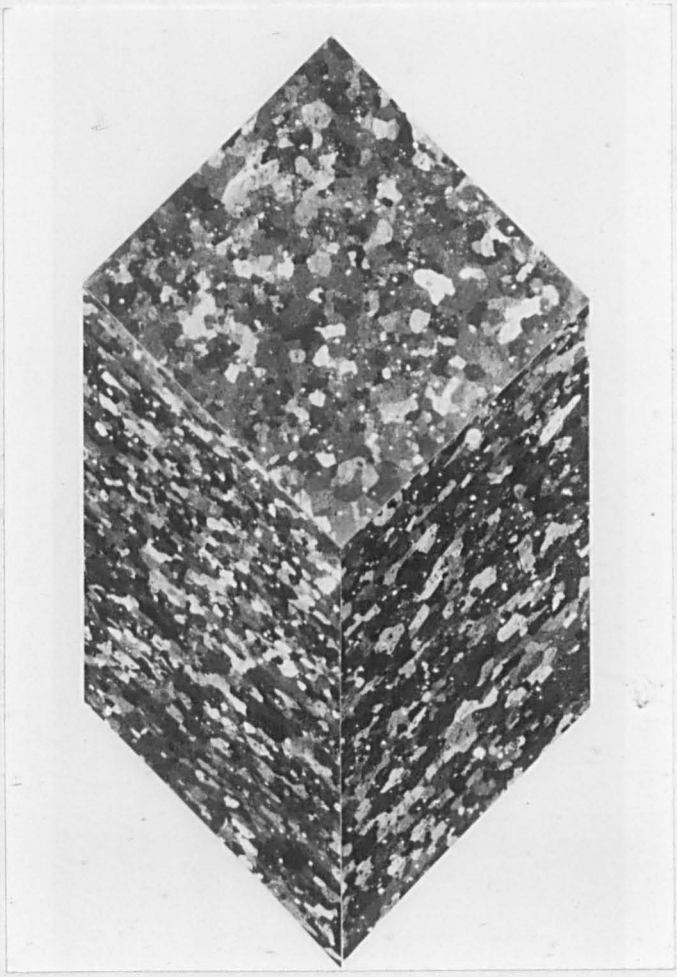

Figure 6.13. Optical micrographs of the anodized 6061 base metal perpendicular sections.

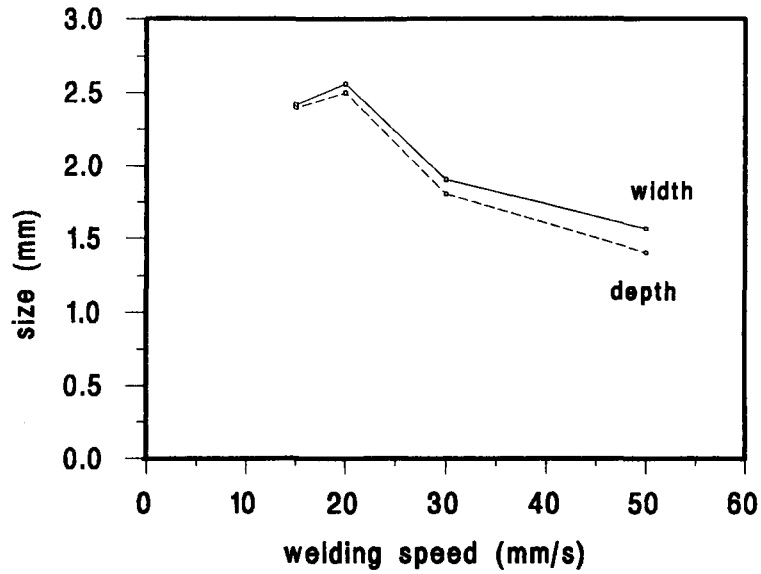

Figure 6.14. Graphs illustrating the influence of welding speed on weld penetration and top bead width for welds made at constant nominal beam power of 3 kW.

(a)

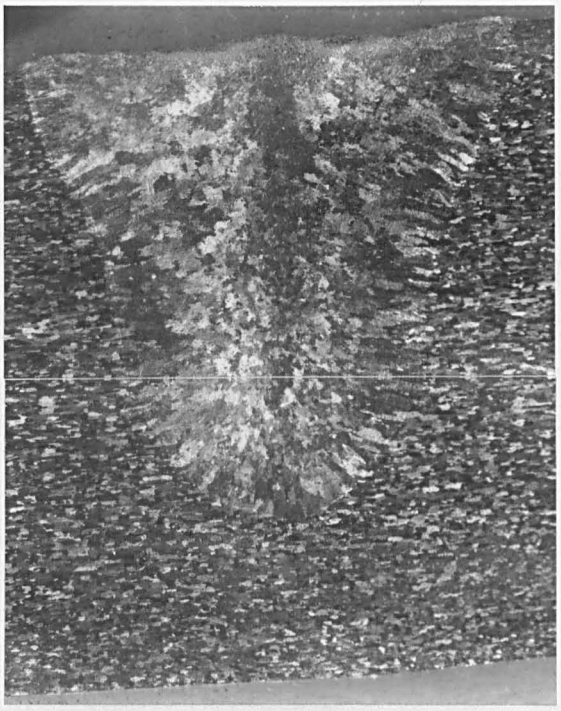

(b)

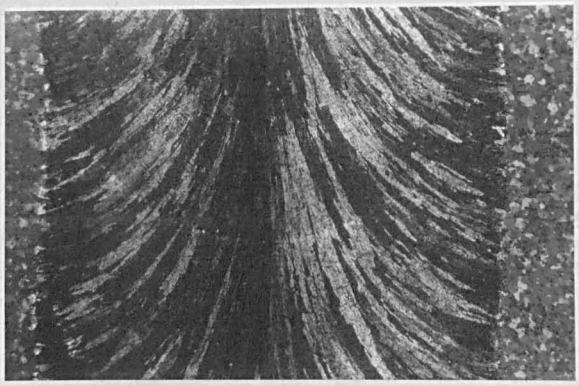

500μm

Figure 6.15. Optical micrographs of an anodized partial penetration 6061 weld. (a) is a transverse section, (b) and (c) are surface and longitudinal centre-line sections respectively. (d) illustrates epitaxial nucleation at the weld fusion boundary.

(c)

500μm

(d)

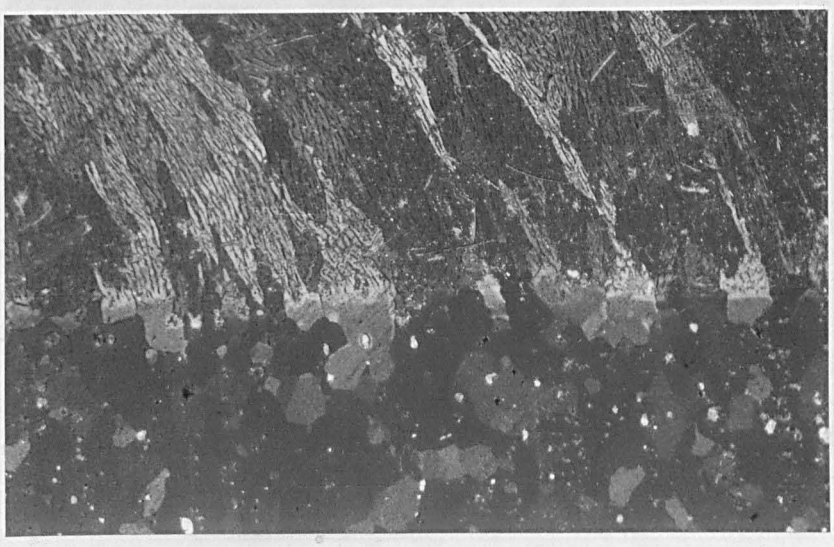

100μm

Figure 6.15. Optical micrographs of an anodized partial penetration 6061 weld. (a) is a transverse section, (b) and (c) are surface and longitudinal centre-line sections respectively. (d) illustrates epitaxial nucleation at the weld fusion boundary.

(a)

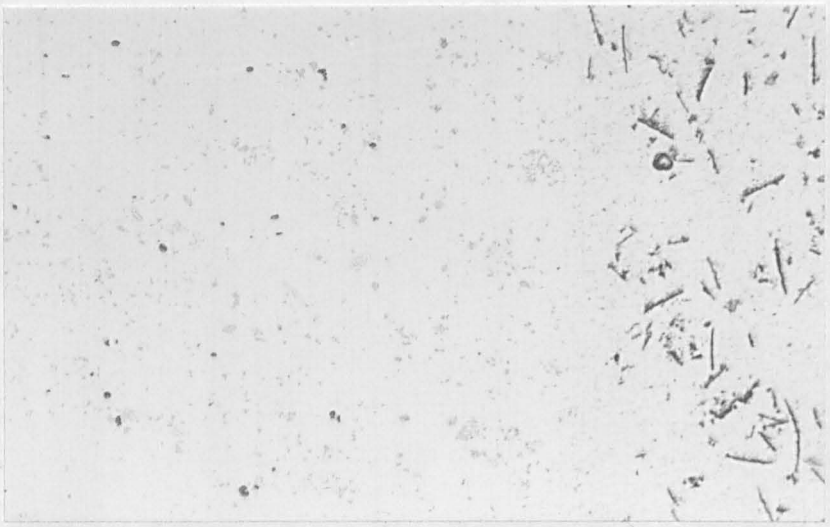

(b)

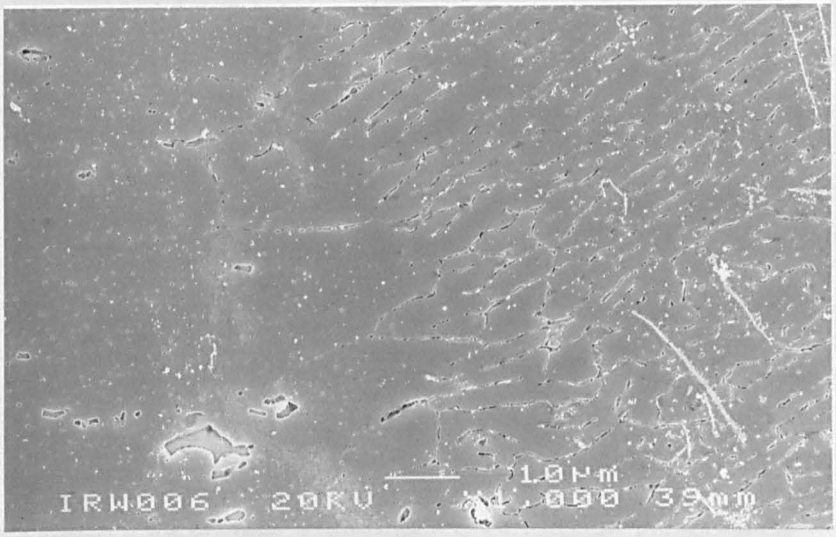

Figure 6.16. Micrographs of the microstructure of the 6061 weld HAZ/fusion boundary region is shown in (a) and (b) and the weld centre is shown in (c).

(c)

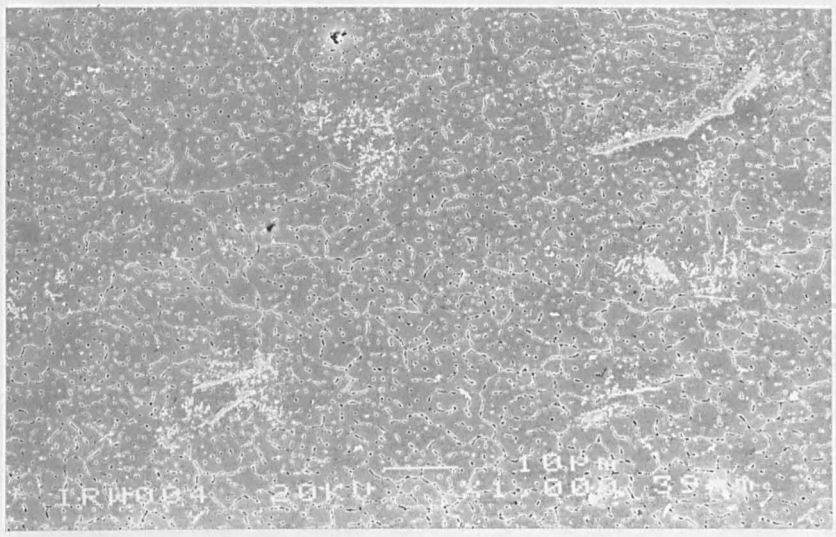

Figure 6.16. Micrographs of the microstructure of the 6061 weld HAZ/fusion boundary region is shown in (a) and (b) and the weld centre is shown in (c).

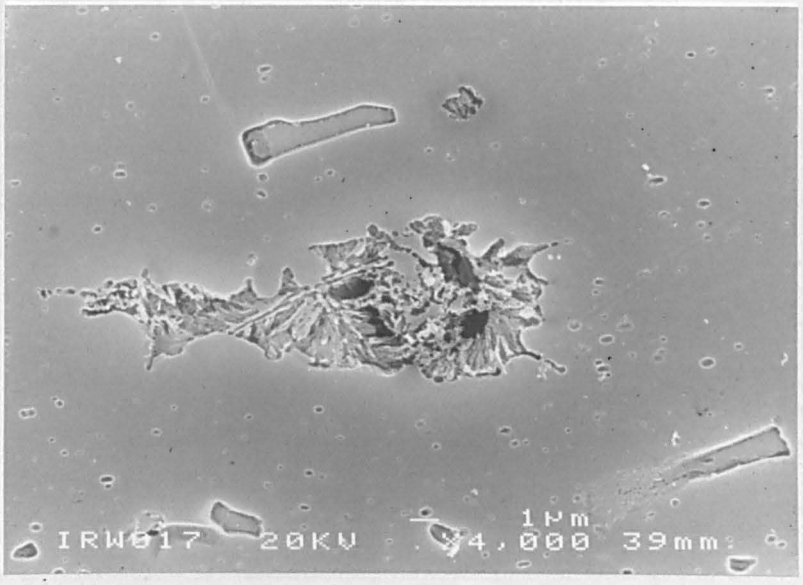

Figure 6.17. Scanning electron micrograph from the HAZ of the 6061 weld illustrating a remelted region with a fine eutectic structure.

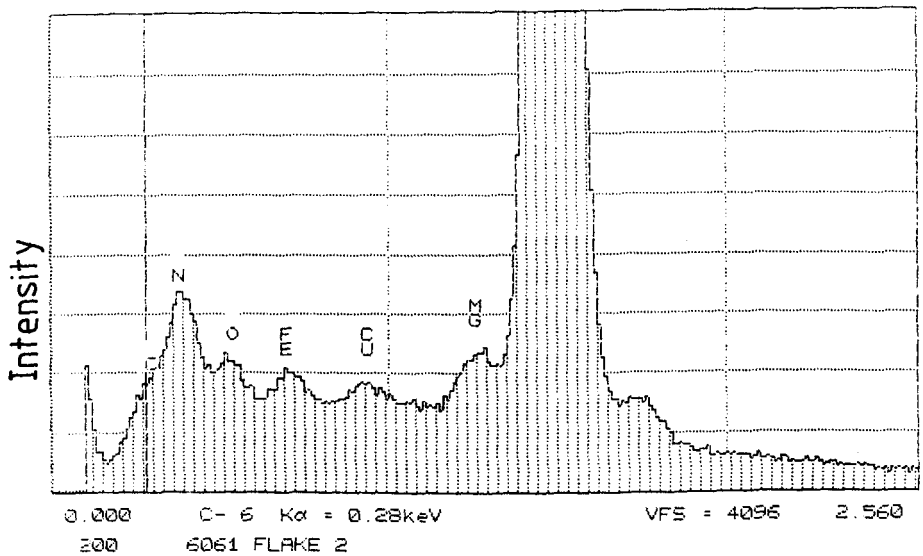

(a)

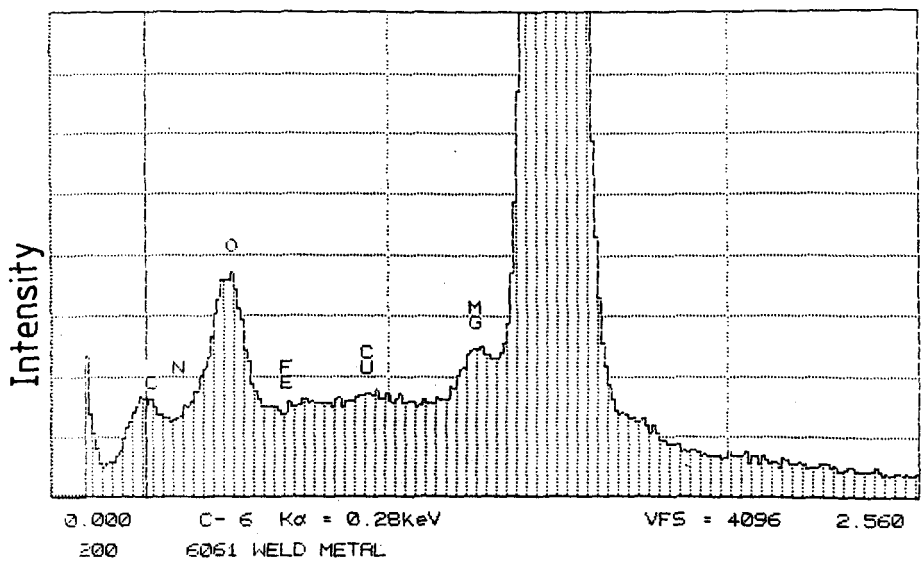

(b)

Figure 6.18. SEM EDX analyses from the flake in the 6061 weld and the bulk weld metal are shown in (a) and (b) respectively.

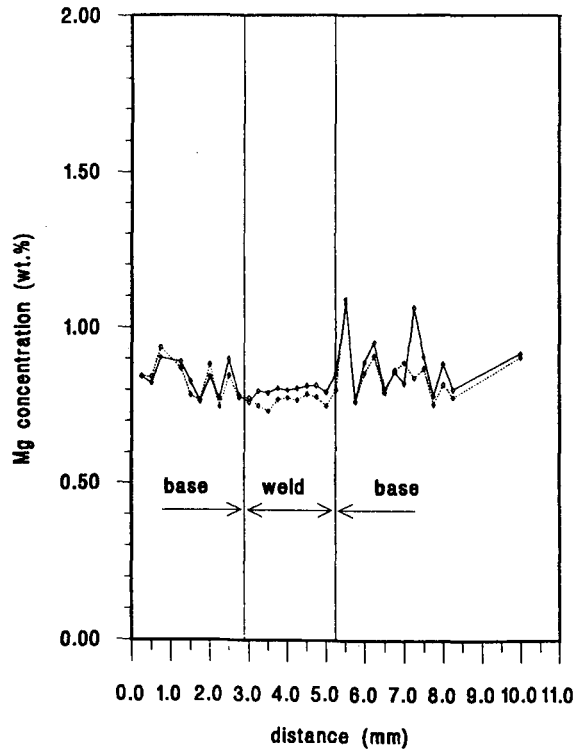

Figure 6.19. EPMA plots of Mg concentration vs. distance across a near surface section of a partial penetration 6061 weld.

Chapter 7. Discussion of 8009 and 6061 Results

The results obtained from the work on 8009 and 6061 serve to support the findings from the work on 8090 where estimates of cooling rate and evaporative losses are concerned. It is necessary, though, to discuss the results from each alloy separately, with reference to particular items in the 8090 work. In the first part then, this discussion aims to interpret the microstructural evolution and concomitant hardness of the solidified 8009 weld metal in terms of the cooling rate, growth rate and microstructure formation during solidification. In the second part, the microstructure and composition of the 6061 weld metal will be discussed and compared to that of the CO_2 laser welds in 8090.

7.1 Microstructure of 8009 weld metal

In chapter 6 the outstanding features of the 8009 weld metal microstructure were identified as (a) the formation of coarse primary intermetallic particles and (b) the observation of 'dark' and 'light' etching regions in partial penetration welds with each region having a different hardness. The intermetallic particles were micron-sized as shown in Fig. 6.5 and had morphologies such as hexagonal and trapezoidal or were clusters of irregular, angular particles. Quantitative chemical analysis in the SEM revealed that there was no measurable difference in composition between the different morphologies and it might, therefore, be assumed that the particles analysed were identical. One such particle was identified by electron diffraction analysis to have a tetragonal crystal structure equivalent to the phase Al_mFe (where m=4.0-4.4) reported by other workers[113]. However, it would appear that in the present work, V and Si are both incorporated into the structure with no apparent significant effect on the tetragonal lattice parameters. This might be explained as follows. If one considers the atomic radii for Al,Fe,Si and V which are respectively 0.2863, 0.2482, 0.2351 and 0.2622 nm[176] it is clear that Si is ~5% smaller in diameter than Fe whereas V is ~6% larger in diameter than Fe. As the tetragonal lattice is not close packed it is reasonable to suggest that the tetragonal lattice can accommodate the substitution of Si and V at Fe sites. That this in fact occurs is substantiated by the proposed stoichiometry of the particles which is $Al_{4.5}$(Fe,V,Si) obtained from table 6.2. This is

very close to that of $Al_{4.0\text{-}4.4}Fe$ given by Skjerpe[113]. Indeed, the selected area diffraction patterns shown in Figs. 6.8 (a) and (b) taken from the particle in Fig. 6.8 (c) are directly comparable to those given by Skjerpe[113], with similar streaking effects.

It is apparent from the literature that the solidification rate required for the formation of the metastable phase Al_mFe is dependent on the base metal composition. Miki et al[112] observed interdendritic Al_mFe phase in binary Al-Fe alloys with Fe contents in the range 0.03 to 0.11 wt.% and it formed with cooling rates between 10 and 700 K/s. Skjerpe[113] observed a 'eutectic type' Al_mFe phase in a chill cast Al-0.25wt.% Fe-0.13wt.% Si alloy and considerable amounts of Al_mFe had formed with a cooling rate of 6 K/s, with lesser amounts at a cooling rate of 1 K/s. More recently, Liang[106] observed primary Al_mFe phase formation in Al-9.5wt.% Fe and Al-8.5wt.% Fe-2.2wt.% Si alloys after chill casting with cooling rates greater than 150 K/s. In addition, Bridgmann solidification and TIG weld traversing caused Al_mFe formation for growth rates of greater than 10 mm/s for the binary alloy and 20 mm/s (G~8 K/mm and dT/dt~150 K/s) for the ternary alloy. However, at much more rapid laser surface melting rates cellular α-Al formed. From these studies it would appear that intermetallic phase formation is made more difficult by the addition of solute. Moreover, cooling rates in Al-Fe-Si in excess of 150 K/s are apparently required for Al_mFe formation. Therefore it would be expected that in the present alloy $Al_m(Fe,V,Si)$ would have formed at cooling rates well in excess of 150 K/s which is consistent with previous estimates of cooling rate for the 8090 alloy.

Given that the microstructure in the weld metal is not consistent with the equilibrium microstructure of the base metal, that is, the stable dispersoid $Al_{12\text{-}14}(Fe,V)_3Si_{0.9\text{-}1.28}$ was not identified in the weld metal, it is appropriate to reconsider the manufacturing route for the base metal 8009. Skinner[116] reported that the alloy was formed by melt spinning and subsequently consolidated via hot pressing and deformation processes. The effective cooling rate during melt spinning was 10^6 K/s and it was found that at cooling rates of 1-500 K/s the first intermetallic phase to form was Al_3Fe. Thus a high cooling rate greater than 500 K/s was needed to form the silicide phase.

Hariprasad et al.[177] attempted to produce an equivalent dispersion strengthened microstructure in an alloy of similar composition by an atomized melt deposition process. It was found that the stable dispersoid phase $Al_{13}(Fe,V)_3Si$ formed when the cooling rate of the atomized particles was between $8.5x10^3$ and $3x10^4$ K/s. At cooling rates below this the equilibrium phase $Al_3(Fe,V)Si$ formed. In relating this previous work to the present work an upper limit to the weld solidification rate can be proposed. The upper limit, then, from the work of Hariprasad et al.[177] is $8.5x10^3$ K/s since at higher cooling rates the stable silicide phase would be expected to form. Thus it can be concluded that the 8009 weld pool solidifies with rates of the order of 10^2-10^3 K/s which matches closely those suggested for the 8090 weld pool. This is similar to the work of Sampath et al.[178] who proposed a cooling rate of 10^3-10^4 K/s in electron beam welds in an RS/PM alloy of similar composition.

It has been shown that the Al_mFe particles can exhibit side arms, Figs. 6.6 and 6.8, and the arms are perpendicular to the particle {110} faces. From the diagram in Fig. 7.1 it is possible that particles can coalesce on {110} planes, and that particles can join together is evident from Fig. 6.6. Here, two hexagonal type particles appear to have joined together. Particle coalescence could account for the super reflections in $<110>_{particle}$ directions. Skjerpe[113] has suggested that super reflections are caused by faults on {110} planes.

The 'dark' and 'light' regions in partial penetration welds are also worthy of some consideration. Optical microscopy revealed that the 'dark' etching regions consisted of intermetallic particles (described above) within a matrix of α-Al. The 'light' etching region did not contain intermetallic particles when viewed using optical microscopy, and SEM showed a fine scale, cellular α-Al microstructure. The microhardness was also significantly higher in the 'light' etching regions when compared to the 'dark' etching regions. These findings suggest that both the temperature gradient and the solid growth rate were much higher in the 'light' etching region. The microhardness dependence on microstructure was also discussed by Krishnaswamy et al.[122], Baeslack[121] and Sampath et al.[178] It is likely that fluctuations in the CO_2 welding process have caused an uneven weld root in partial

penetration welds. This was also observed in the CO_2 welds made on 8090. The fluctuation is probably responsible for the observed variations in solidification rates resulting in 'light' and 'dark' etching regions.

Fig. 6.4 shows a transition in microstructure at the point where the 'light' etching region becomes a 'dark' etching region. The microstructure changes from a fine, cellular precipitate free structure, through a coarser, cellular dendritic structure with increased intermetallic precipitation, to an equiaxed dendritic structure which has nucleated on intermetallic particles. This sequence of events is consistent with a reduction in the growth rate and hence a change in the solidification mode[106].

In view of the work by Baeslack[121], Krishnaswamy et al.[122] and Sampath et al.[178] it is likely that the equiaxed α-Al dendrites have nucleated on the primary intermetallic particles which Liang[106] has proposed for Al_mFe grow at temperatures between 890 and 930°C. Since no analysis was made of the spherical-type intermetallic particles in Fig. 6.9(b), it will be assumed that they are either un-melted base metal dispersoids or the intermetallic phase Al_mFe. It can be shown that the lattice disregistry between these two types of particle and α-Al is less than 10% and it has been suggested[179] that under these conditions catalytic nucleation of α-Al can occur. Comparison of the following lattice parameters give evidence for this:

α-Al, a=0.40496nm
Al_mFe, a/2=0.4425nm
⇒misfit=9%

α-Al, a=0.40496nm
Al_mFe, c/5=0.4272nm
⇒misfit=5%

α-Al, a=0.40496nm
$Al_{12}(Fe,V)_3Si$, a/3=0.416nm
⇒misfit=3%

Overall, the 8009 microstructure results can be readily interpreted in terms of local

solidification conditions and it is proposed that the 8009 weld metal solidifies by many isolated nucleation events rather than the usual epitaxial mode of growth form the fusion boundary which was identified in 8090 welds, chapters 4 and 5.

Finally, the weldability of 8009, as defined in the introduction, was assessed by microhardness measurements. The graphs in Fig. 6.11(c) clearly illustrate that the average microhardness of the weld is reduced compared to the base metal. This is presumably due to the influence of the welding thermal cycle on the base metal microstructure. The base metal acquires its strength from a high volume fraction of small diameter dispersoids[116][118]. During welding the majority of the base metal dispersoids in the molten volume are dissolved and, as has been shown above, the weld metal microstructure contains quite coarse particles which offer only limited hardening. Thus, although 8009 sheets could be successfully joined, the match in microhardness (and presumably other mechanical properties) is poor. Therefore, in an engineering sense 8009 is not readily weldable.

7.2 Microstructure and composition of 6061 weld metal

In contrast to the 8009 weld metal described above, Fig. 6.15 showed that the 6061 weld metal solidified via epitaxial growth from partially melted grains in the base metal at the fusion boundary. Due to the partial penetration nature of the weld bead, solidification has proceeded with a distinct three dimensional heat flow and the grains which nucleated towards the weld root showed significant upward growth directions. It was also shown that α-Al cellular-dendrites at the weld centre were finer than those near the fusion boundary. Constituent flakes which were believed to be compounds of Al-N-O were a dominant feature of the weld metal microstructure and it is significant that these displayed a perpendicular orientation relationship with the grain growth direction. It was also demonstrated that there was a negligible change in microhardness across the fusion zone, through the HAZ and into the base metal. That there was very little reduction in the average Mg content of the weld metal when compared to the base metal is believed to be a significant result since it indicates little Mg loss during CO_2, keyhole mode laser welding.

The microstructure can be interpreted in terms of the temperature gradients and growth rates which exist within the molten weld pool during solidification. Near the edge of the weld pool, the temperature gradients are relatively high but the growth rate can be very low due to the steep inclination of the grains to the welding direction. Thus G.R can be low resulting in a coarse cellular-dendritic structure. Nearer the weld centre, the cellular-dendrites become finer as the growth rate increases, since the growth direction approaches the welding direction. That the scale of the α-Al cells at the weld centre is again of the order of 1-2μm suggests that this is characteristic of the CO_2 laser welding conditions employed throughout this work. Similarly, cooling rates of the order of 10^2-10^3 K/s can be implied.

The flakes which were analysed as being enriched in Al-N-O presumably have a high melting point (alumina alone has a melting temperature of 2050°C) and do not dissolve in the molten weld pool. Just where the flakes came from is open to question but Behler et al.[37] have suggested that nitrogen shielding gas (which was used in the present experiments) reacts with the molten weld at the rear of the keyhole. In this present study, however, similar flakes (which were not chemically analysed) were also observed with helium as the shielding gas. Thus, since there is an even distribution of flakes throughout the solidified structure, which presumably did not form via a solid state reaction, it seems likely that their existence is linked to the mixing in of surface contaminants. A possible explanation could be as follows. The trailing molten pool has been open to the atmosphere and reacted with the air. This might have resulted in the formation of an Al-N-O layer on the weld pool surface. Recirculation in the weld pool, driven by the variation of γ_{LV} with T, where γ_{LV} is the melt/air surface tension, could be responsible for the entrainment of the Al-N-O phase. The alignment of the flakes presumably arises from the fluid flow pattern. This will cause them to lie parallel to flow lines and perpendicular the solid/liquid interface.

To complement the results of the influence of CO_2 laser welding on 8090 it is apparent that there has been very little Mg loss due to vaporization from the molten, 6061 weld pool. This is in spite of the fact that Mg has a high vaporisation flux (see Appendix A2) at the typically high temperatures expected in CO_2 laser welding (≥

2000°C). It is interesting to note that the Mg loss levels recorded, in the region of ~8% for a welding speed of 20 mm/s, correlate very well to the work by Cieslak et al.[124], as can be seen from Fig. 2.19. Similar to the discussion for 8090 vaporization losses, it is proposed that the low vapour pressure of the keyhole relative to the outside atmospheric pressure hinders element loss. In addition, the presence of the laser induced plasma discussed in a previous section can also hinder element vaporization. Thus it may be concluded that even alloys which contain very volatile elements, which are necessary for precipitation hardening reactions, can be successfully welded using CO_2, keyhole techniques.

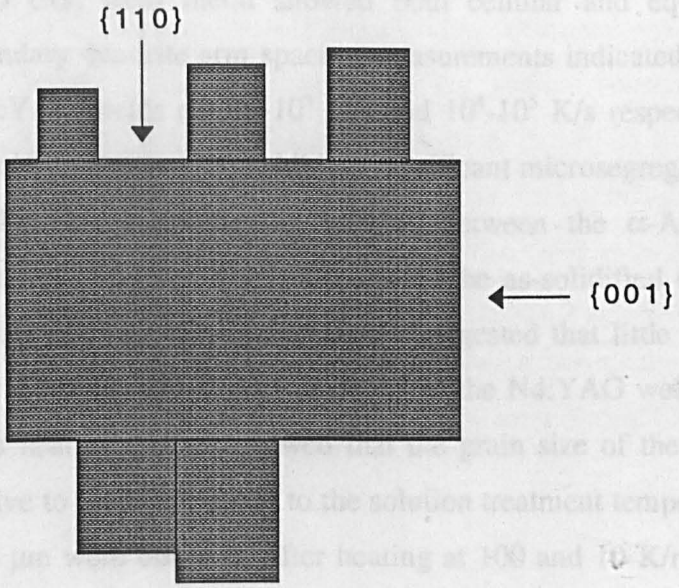

Figure 7.1 Schematic diagram of the particle shown in Fig. 6.8 (c) with the plane labelled according to the SADP in Fig. 6.8 (a).

Chapter 8. Conclusions

1. When welded with a CO_2 laser, alloys 8090, 8009 and 6061 showed a reduction in weld penetration and/or top weld bead width with decreasing laser beam power and increasing welding speed. Keyholing occurred more readily at lower incident beam power in 8090 than in either 6061 or 8009.

2. Pulsed Nd:YAG welding in 8090 did not result in successful deep penetration keyhole welds under the processing parameters investigated. The weld bead showed a low depth to width ratio (<1) indicative of conduction mode welding.

3. Two types of porosity were observed in 8090 CO_2 laser welds. Spherical pores due to the evolution of hydrogen gas formed throughout the weld metal. In addition, irregular shaped cavity closure type pores were found predominantly at the weld centre-line in partial penetration welds. The volume fraction of porosity decreased with increasing welding speed. Possible mechanisms for the formation of the latter type of pores have been proposed.

4. The 8090 CO_2 weld metal showed both cellular and equiaxed dendritic structures. Secondary dendrite arm spacing measurements indicated cooling rates in the CO_2 and Nd:YAG welds of 10^2-10^3 K/s and 10^4-10^5 K/s respectively. The as-solidified CO_2 weld microstructure exhibited significant microsegregation in the α-Al with Cu-Mg-Si-Fe rich intermetallics forming between the α-Al dendrites. δ' precipitates ~5 nm in diameter were observed in the as-solidified CO_2 weld metal. This, together with the bulk chemical analysis suggested that little Li loss occurred during CO_2 laser welding. No δ' was observed in the Nd:YAG weld metal.

5. Post-weld heat treatments showed that the grain size of the 8090 CO_2 weld metal was sensitive to the heating rate to the solution treatment temperature. Massive grains up to 200 μm were observed after heating at 100 and 10 K/min whereas at 1 K/min the grains were uniformly small with a size of ~10μm. TEM showed that the grain size was controlled by the grain boundary pinning dispersoid $\beta'(Al_3Zr)$. There was increased time for Zr diffusion at the slowest heating rate thus enabling a significant volume fraction of the dispersoid to form.

6. Microhardness measurements of the 8090 CO_2 and Nd:YAG weld metal showed that the CO_2 weld metal was age-hardenable whereas the Nd:YAG weld metal

was not. Notched specimen tensile tests on the CO_2 weld metal confirmed this observation. Thus post-weld heat treatments were able to produce a good match in mechanical properties between 8090 base metal and CO_2 weld metal. The 8090 CO_2 weld failed in a brittle, predominantly intergranular manner and the fracture strength did not depend on the weld metal grain size. This was due to the fracture path being determined by the residual cast structure i.e. the secondary dendrite arm spacing and not the grain size.

7. The microstructure of the 8009 CO_2 weld metal was found to be sensitive to the temperature gradient and growth rate during solidification with 'light' and 'dark' etching regions. Primary intermetallic particles, which were identified to be tetragonal (lattice parameters a=0.885 and c=2.136 nm) with a stoichiometry of $Al_{4.5}(Fe,V,Si)$, existed within a matrix of α-Al cellular dendrites with a secondary dendrite arm spacing of 1-2 μm. The α-Al presumably nucleated on these particles and the weld pool solidified via many independent nucleation events. The weld microhardness was significantly lower than that of the base metal.

8. The 6061 CO_2 weld metal solidified with columnar grains which grew epitaxially from grains in the base metal at the fusion boundary. The weld microstructure contained flakes of Al-N-O which were mixed in to the molten pool probably via surface oxidation. The secondary dendrite arm spacing in the CO_2 6061 weld metal decreased from 4-5 μm at the edge of the weld pool to 1-2 μm at the centre of the weld pool. A cooling rate of 10^2-10^3 K/s was estimated. Together with the measurements of microhardness and Mg concentration across the weldment it was suggested that the majority of the Mg is retained in the melt during CO_2 laser welding.

Further Work

1. Perform further welding experiments on 8090 to try and reduce the levels of porosity in partial penetration welds. This will involve changing the angle of the laser with respect to the workpiece and employing a more elaborate atmosphere control.

2. Attempt an analysis of the temperature profiles within the keyhole of especially 8090 using high speed infra-red photography. Peak weld pool temperatures could be measured together with the surface temperature. This information will enable a more precise model to be made of the nature of the forces between surface tension and vapour pressure. The effect of the weld pool shape on porosity could also be monitored in this way.

3. Make a series of 8090 test panels with different penetrations and post-weld heat treatments in order to perform superplastic forming trials. This would be valuable information in order to compare the laser welding process to conventional diffusion bonding techniques, prior to superplastic forming.

4. Change the processing conditions of the Nd:YAG laser in order to create deeper penetration welds in 8090 with minimal loss of alloying elements. This would involve adding pre and post pulses to alter the laser interaction time on the target material. The power density of the Nd:YAG laser could also be improved by adopting a lens system which decreased the focussed spot size of the incident beam.

5. Characterize more fully the microstructure of the 8009 and 6061 weld, especially precipitate formation. The primary particles in the 8009 weld microstructure indicate that the solidification conditions prevented the formation of the stable silicide phase. Studies could be attempted to determine the range of cooling rates for which the Al_mFe phase forms in 8009 type alloys and the CO_2 laser conditions such as power and spot size could be varied in order to increase the cooling rate in the molten volume.

6. Determine the fracture characteristics of both 8009 and 6061 weldments in both the as-welded and post-weld heat treatment conditions. For the 8009 alloy which in the as-received condition has useful mechanical properties up to 400°C, suitable welds could be examined for their elevated temperature properties. Alloy 6061 is age-

hardenable and the loss of Mg could be monitored, at different welding speeds and beam powers, for its influence on weld strength and volume fraction of Mg_2Si phase formation. The existence of the Al-N-O flakes in the 6061 weld metal should also be examined for their influence on mechanical properties and conditions such as surface oxide and shielding gas purity could be altered in order to produce flake free structures.

Publications

I.R. Whitaker, N. Calder, D.G. McCartney and W.M. Steen, *J. Mat. Sci.*, **28** (1993) 5469-5478.

N. Calder, I.R. Whitaker, D.G. McCartney and W.M. Steen, Proc. of ICALEO, Boston, USA, November 1992, in press.

I.R. Whitaker, N. Calder, D.G. McCartney and W.M. Steen, Proc. of EUROMAT'93, Paris, France, June 1993, in press.

I.R. Whitaker, N. Calder, D.G. McCartney and W.M. Steen, Proc. of EMAG'93, Liverpool, UK, August 1993, in press.

Appendix A1 Interpretation of TEM Results

A1.1 Analysis of TEM Diffraction Patterns

The interpretation of electron diffraction patterns has been well documented by Edington[180] and others[181][182] and the ring and spot patterns included in this thesis have been solved commensurate with these guidelines. A brief summary of the theory and methodology is included here together with relevant equations and explanations.

A1.1.1 Introduction

The wavelength of the electrons in electron microscopy is a function of the accelerating voltage and the wavelength is given by

$$\lambda = \frac{h}{\left\{2mV_c e\left(1+\frac{eV_c}{2m_e c^2}\right)\right\}^{\frac{1}{2}}} \qquad \text{A1.1}$$

where h is Planck's constant, m_e is the mass of the electron, e is its charge, V_c is the accelerating voltage and c is the velocity of light. Table A1.1 lists values of λ for typical accelerating voltages.

The electrons are transmitted through the specimen and on exit several diffracted beams are present in addition to the transmitted beam. The intensity of the diffracted beams from planes in the unit cell is governed significantly by the position of the atoms in the reflecting planes and the atomic species that are scattering. These factors are known as the structure factor [$F(\Theta)$] and the atomic scattering factor [$f(\Theta)$] respectively.

The scattering factor from a perpendicular (hkl) plane can be calculated by summing the values of $f(\Theta)$ for each of the n atoms in the unit cell, taking into account the phase difference between each scattering point and the origin. It can be shown that where x_n, y_n and z_n are the atomic coordinates of the nth atom and the exponential

$$F(\theta) = \Sigma_n f_n(\theta)\exp[-2\pi i(hx_n + ky_n + lz_n)] \qquad \text{A1.2}$$

term represents the phase difference.

The intensity of the diffracted beam is proportional to $|F(\Theta)|^2$. Thus for different crystal structures different intensities will arise from the same (hkl) plane and when $F(\Theta)=0$ the scattered intensity will be zero.

Table A1.2 lists some of the allowed (non-zero intensity) reflections for simple cubic, bcc and fcc crystal structures, together with the values for $(h^2+k^2+l^2)$. Generally, simple cubic structures have no systematic absences, bcc structures only reflect if $(h^2+k^2+l^2)$ is even and fcc structures only reflect if (h,k,l) are all odd or all even.

A1.1.2 Solution of Patterns

In order to solve the electron diffraction patterns in this work the following relationships for the cubic interplanar spacings were considered:

$$d = \frac{\lambda L}{OX} \quad , \quad \frac{1}{d^2} = \frac{h^2+k^2+l^2}{a^2} \qquad \text{A1.3}$$

where d is the interplanar spacing for plane (hkl), λ is the electron wavelength, OX is the ring diameter or the distance from the transmitted beam to a diffracted beam, L is the camera length and a is the cubic lattice parameter.

Rearranging these two relationships the ratio

$$\frac{OX^2}{OY^2} = \frac{h_1^2+k_1^2+l_1^2}{h_2^2+k_2^2+l_2^2} \qquad \text{A1.4}$$

where OY is the diameter of an outer ring or the distance from the transmitted beam to another diffracted spot which is positioned clockwise from OX.

Thus, to solve ring patterns, the following procedure was adopted:

(1) Measure the ring diameters.

(2) Determine the ratios of the squares of the diameters of the outer rings to that of the first visible ring.

(3) Compare the ratios to those for the allowed reflections in the simple cubic, bcc or fcc systems.

(4) Index the rings and calculate the lattice parameter.

To solve the spot patterns the following procedure was adopted:

(1) Determine the rotational symmetry and measure the angles between the rows of spots. If the symmetry is simple, compare the pattern to standard, documented patterns.

(2) Measure the interplanar spacings from the average of several spots and compare with a list of d spacings of possible materials.

(3) Arbitrarily assign one spot the indices $(h_1k_1l_1)$ and consider two other spots so that when added vectorially they give $(h_1k_1l_1)$.

(4) Check the angle between these planes with those measured from the spot pattern using the formula

$$\cos\theta = \frac{h_1h_2+k_1k_2+l_1l_2}{(h_1^2+k_1^2+l_1^2)^{1/2}(h_2^2+k_2^2+l_2^2)^{1/2}} \qquad \text{A1.5}$$

(5) Determine the zone axis [uvw]=Z=B, the beam direction, using the relationships

$$u=k_1l_2-k_2l_1$$
$$v=l_1h_2-l_2h_1$$
$$w=h_1k_2-h_2k_1$$

where spot $(h_1k_1l_1)$ is positioned anticlockwise around the centre spot relative to spot $(h_2k_2l_2)$. Thus B is defined as the upward drawn normal of the diffraction pattern printed emulsion side up and is antiparallel to the incident electron beam.

Extension to Non-Cubic Systems

For crystal structures where the lattice parameters are not identical eg tetragonal $a=b\neq c$

and orthorhombic a≠b≠c, the interplanar spacing becomes

$$\frac{1}{d^2} = \frac{h^2}{a^2} + \frac{k^2}{b^2} + \frac{l^2}{c^2} \qquad \text{A1.6}$$

and the angle between the planes is

$$\cos\theta = \frac{\frac{h_1h_2}{a^2} + \frac{k_1k_2}{b^2} + \frac{l_1l_2}{c^2}}{\left(\frac{h_1^2}{a^2} + \frac{k_1^2}{b^2} + \frac{l_1^2}{c^2}\right)^{1/2}\left(\frac{h_2^2}{a^2} + \frac{k_2^2}{b^2} + \frac{l_2^2}{c^2}\right)^{1/2}} \qquad \text{A1.7}$$

otherwise the solution of these types of diffraction pattern follows the procedure outlined earlier.

A1.1.3 Other Features of the Electron Diffraction Pattern

Selected area diffraction patterns can contain extra reflections depending on the types of precipitate eg structure, morphology and composition. For example, 8090 shows extra reflections which arise from the precipitates δ′ (Al_3Li)[53], β′ (Al_3Zr)[59], β (Al_3Zr)[59], S′ (Al_2CuMg)[126] and T_1(Al_2CuLi)[67].

δ′ and β′ are isostructural with the α-Al and are ordered solid solutions, or superlattice with the stoichiometry A_3B and Strukturbericht symbol $L1_2$. The unit cell is shown in Fig. A1.1 and is a prototype of four interpenetrating simple cubic sub-lattices, each occupied by atoms of only one kind. This means that all planes can reflect which gives rise to the extra spots (termed superlattice spots) observed on the diffraction patterns.

Streaking of spots is observed when S′ and T_1 are present. Streaks are observed on the diffraction pattern because S′ and T_1 are rod/lath and plate like precipitates, which are thin in one direction relative to the others. In reciprocal space, lattice points become extended by an amount which is inversely proportional to the thickness of the crystal, thus thin crystal plates exhibit reciprocal lattice spikes normal to the plane of the plate. Hence, in a diffraction pattern, streaking is observed in a direction parallel

to the thin direction of the crystal when the spikes are perpendicular to the electron beam.

A1.2 Accuracy of Selected Area Diffraction

Diffraction patterns can be obtained in the TEM by inserting a selected area aperture into the first image plane of the objective lens, illustrated schematically in Fig A1.2. In the JEOL 2000 FX2 the diameter of the selected area apertures are 20, 100 and 300 μm which enables small or large regions of interest to be inspected. As the image plane is conjugate with the object plane, an aperture thus placed in the first image plane of the objective lens is equivalent to an aperture placed physically upon the specimen. The image will be magnified by an amount M, and inverted, so the selected area aperture of diameter d defines a region d/M on the object.

In an ideal world, then, it might be expected that for M=50X and d=20μm the region on the object would be 0.4μm in diameter. However there is an inaccuracy due to spherical aberration[183][184][185]. This occurs since the outer zones of the lens have a greater strength and bring beams to focus slightly before the geometrical focus of the lens, Fig A1.3. The axial change in focus for beams close to the axis, but inclined at an angle 'a' turns out to be

$$dv = C_s a^2 \qquad \text{A1.8}$$

where C_s is termed the spherical aberration coefficient. Hence in the true image plane there is a fuzziness dr_s

$$dr_s = C_s a^2 \tan(a) \qquad \text{A1.9}$$

If 'a' is sufficiently small then

$$dr_s = C_s a^3 \qquad \text{A1.10}$$

For the JEOL 2000 FX2 operating at 200kV, C_s is of the order of 2mm and 'a' might be ≈0.02 rad. Thus substituting these values, dr_s=16nm.

Reconsidering the ideal selected specimen area of 0.4μm, the diameter could be extended 32nm due to spherical aberration. Thus there is an 8% error in the diameter of the area selected.

A1.3 Determination of 'Interaction Volume' During X-ray Analysis

During EDX analysis with a finite probe diameter one ought to consider how far into the specimen the electron beam can penetrate and also from which regions X-rays can escape[183][184][186]. Fig. A1.4 shows systematically the shape of the 'interaction volume' in solid and thin specimens. Read[186] has shown that the spatial resolution, ie the approximate diameter of the interaction volume, is given by

$$d = \frac{0.077(E_0^{1.5} - E_c^{1.5})}{\rho} \quad (\mu m) \qquad \text{A1.11}$$

where E_0 is the incident electron energy in keV, E_c is the critical excitation energy and ρ is the density in g/cm^3.

However, for a thin specimen, penetration is of little concern, but the extent of beam broadening during transmission through the sample needs to be estimated. The calculated broadening (in nm) of a 100kV electron beam is shown in the table A1.3 for specimens of increasing thickness[183].

Table A1.1 Wavelength of electrons at different accelerating voltages.

Accelerating Voltage (kV)	Wavelength (m)
100	3.701×10^{-12}
120	3.349×10^{-12}
200	2.511×10^{-12}

Table A1.2 Table of reflecting planes for simple cubic, bcc and fcc crystals.

Simple Cubic	bcc	fcc	$h^2 + k^2 + l^2$
100			1
110	110		2
111		111	3
200	200	200	4
210			5
211	211		6
		220	7
220	220		8
300; 221			9
310	310		10
311		311	11
222	222	222	12
320			13
321	321		14
			15
400	400	400	16
410; 322			17
411; 330	411; 330		18
331		331	19
420	420	420	20

Table A1.3 Electron beam broadening (nm) in thin foils for 100 keV electrons[183].

	Film thickness (nm)				
Element	**10**	**50**	**100**	**300**	**500**
Carbon	0.22	1.9	4.1	16	33
Aluminium	0.41	3.0	7.6	30	66.4
Copper	0.78	5.8	17.5	97	244
Gold	1.71	15.0	52.2	599	1725

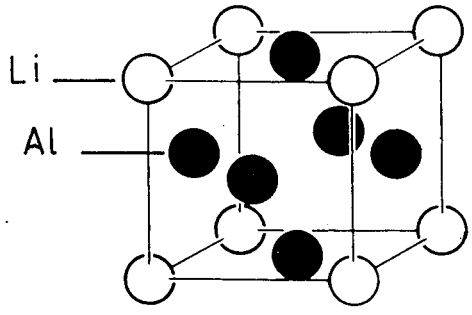

Figure A1.1. Schematic diagram of the $L1_2$ crystal structure.

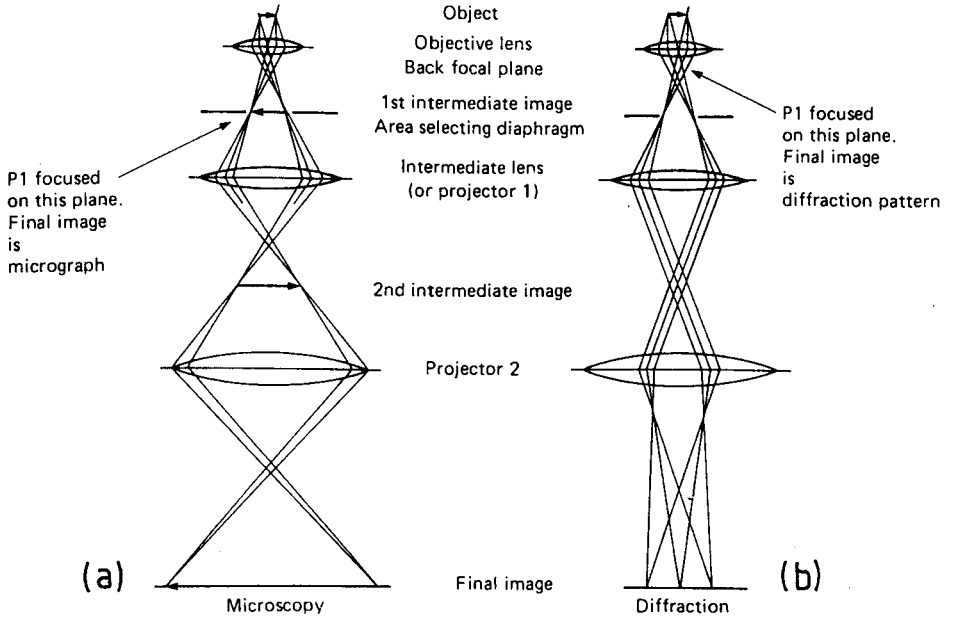

Figure A1.2. Ray diagram showing the formation of a bright field image in (a) and a SADP in (b). The first intermediate image plane is conjugate with the object plane and the projector lens can be strengthened or weakened to focus on the first intermediate image or the back focal plane of the objective plane lens respectively[183].

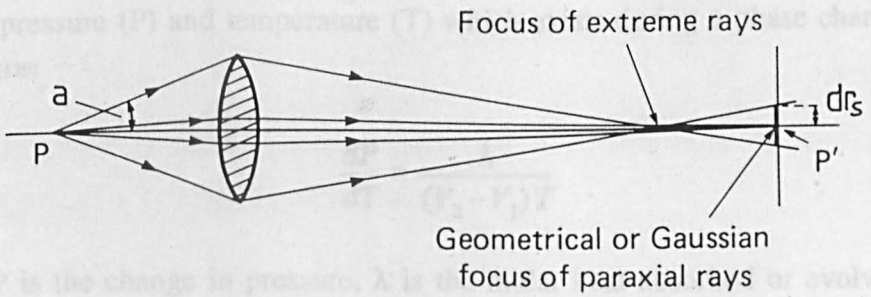

Figure A1.3. Ray diagram illustrating the formation of spherical aberration[183].

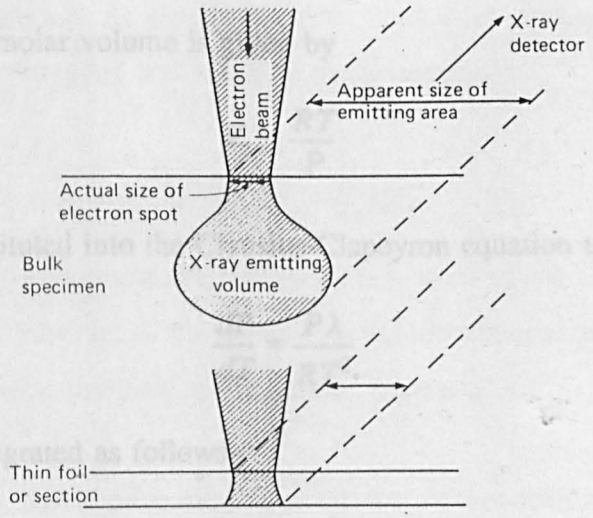

Figure A1.4. Schematic diagram illustrating the interaction between the electron beam and the target material. X-rays are emitted from a much larger volume than a simple cylinder except when the target is thin compared to the electron penetration depth[183].

Appendix A2 Equilibrium Vapour Pressure Data

It is the purpose of this appendix to set out the basic thermodynamic relationships which need to be utilized in order to assess the volatility of constituent elements within alloy solutions. The Clausius-Clapeyron equation provides the relationship between pressure (P) and temperature (T) which exists during a phase change and is given by[129],

$$\frac{dP}{dT} = \frac{\lambda}{(V_2 - V_1)T} \qquad \text{A2.1}$$

where dP is the change in pressure, λ is the molar heat absorbed or evolved (latent heat) associated with a change in molar volume (V_2 - V_1) at the absolute temperature, T. Since the molar volume of the vapour phase is much greater than that of the liquid phase V_1 becomes negligible and

$$(V_2 - V_1) \sim V_2 \qquad \text{A2.2}$$

For an ideal gas the molar volume is given by

$$V_2 = \frac{RT}{P} \qquad \text{A2.3}$$

and this can be substituted into the Clausius-Clapeyron equation to give

$$\frac{dP}{dT} = \frac{P\lambda}{RT^2} \qquad \text{A2.4}$$

This can then be integrated as follows

$$\ln P = -\frac{\lambda}{RT} \qquad \text{A2.5}$$

In the range of vapour pressures below about 1 mmHg it has been observed that for most pure metals, the vapour pressure can be represented as a function of T by the relation[187]

$$\log P = A - \frac{B}{T} \qquad \text{A2.6}$$

where A and B are constants. However, when we consider the vapour pressure of alloys, it must be noted that the vapour pressure of the element in solution, P_2, is lower than that of the pure element, P_1[129]. The ratio P_2/P_1 is called the activity, a, of the metal in solution;

$$a = \frac{P_2}{P_1} \qquad \text{A2.7}$$

For an ideal solution there is a linear variation of P_2 with composition, hence for a solution made of a fraction X of the metal

$$P_2 = XP_1 \qquad \text{A2.8}$$

Comparison of these equations shows that for an ideal solution

$$a = X \qquad \text{A2.9}$$

This relationship is known as Raoult's law and states that the activity of a solvent in an ideal solution is equal to its atomic fraction. The mole fractions of the elements in a solution can be calculated according to the relationship

$$X_a = \frac{q_a/M_a}{q_a/M_a + q_b/M_b} \qquad \text{A2.10}$$

where q is the weight percent of the component, a or b, which has an atomic mass, M. Hence the vapour pressure of the element in solution is deduced from the product of the mole fraction with the pure metal vapour pressure.

It can be shown that the relationship between the vapour pressure and the rate of evaporation in a vacuum is given by[188]

$$W = P\left(\frac{M}{2\pi RT}\right)^{0.5} \qquad \text{A2.11}$$

where W is the evaporative flux in g/cm^2s, M is the atomic mass of the evaporating

species in g, and P is the vapour pressure of the element. This equation can then give

$$\log W = \log P + \frac{1}{2}\log\frac{M}{2\pi R} - \frac{1}{2}\log T \qquad \text{A2.12}$$

These equations have been used to determine the vapour pressures and vaporization rates for the more volatile elements in the alloys 8090 and 6061. The exact equations are given at the end of this appendix and the graphs of vapour pressure (in Pa) and vaporization rate (in g/cm^2.s) versus absolute temperature are shown in Figs. A2.1 and A2.2. The graph in Fig. A2.1 (a) is a plot of vapour pressure versus absolute temperature for the pure elements Mg, Li and Al, and Fig. A2.1 (b) is a plot of the vapour pressure of the same elements in solution in 8090. Compared to Al, Mg and Li are much more volatile. The same trend is also observed for the rates of evaporation as illustrated in Fig. A2.1 (c). It is also apparent from the graphs in Fig. A2.2 (a) and (b) that for alloy 6061 Mg has a higher vapour pressure and evaporation rate than Al.

The boiling points for Mg, Li and Al are respectively 1377 K, 1604 K and 2720 K[187]. and the actual equations which were used to calculate the vapour pressures and evaporation rates of the elements are given below where pressure is in units of μHg and temperature is absolute. Pressure is then converted to Pascals by multiplying the pressure in Hg by a factor of 0.13333.

For Mg,

$$\log P = 11.64 - \frac{7650}{T} \qquad \text{A2.13}$$

$$\log W = -3.5411 + \log P - 0.5\log T \qquad \text{A2.14}$$

For Li,

$$\log W = -3.8133 + \log P - 0.5\log T \qquad \text{A2.16}$$

$$\log P = 10.99 - \frac{8070}{T} \qquad \text{A2.15}$$

For Al,

$$\log P = 11.79 - \frac{15940}{T} \qquad \text{A2.17}$$

$$\log W = -3.5185 + \log P - 0.5 \log T \qquad \text{A2.18}$$

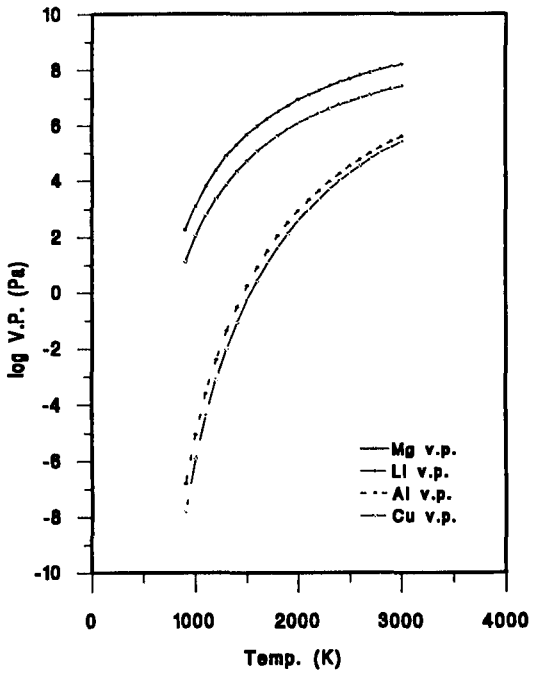

Figure A2.1 (a). A plot of theoretical vapour pressure for the pure elements.

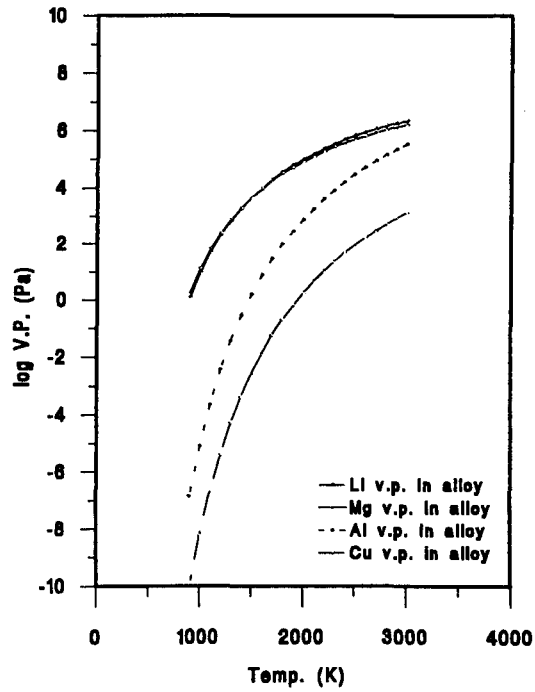

Figure A2.1 (b). A plot of theoretical vapour pressure for the elements in solution in 8090.

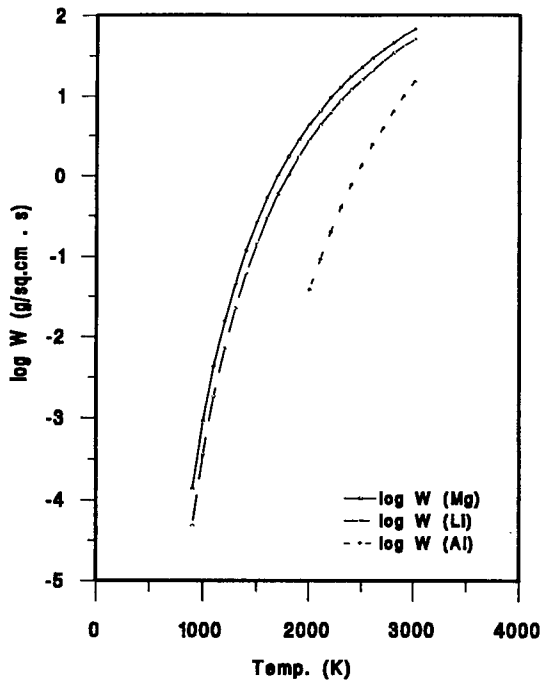

Figure A2.1 (c). Vaporization flux of elements in solution in 8090.

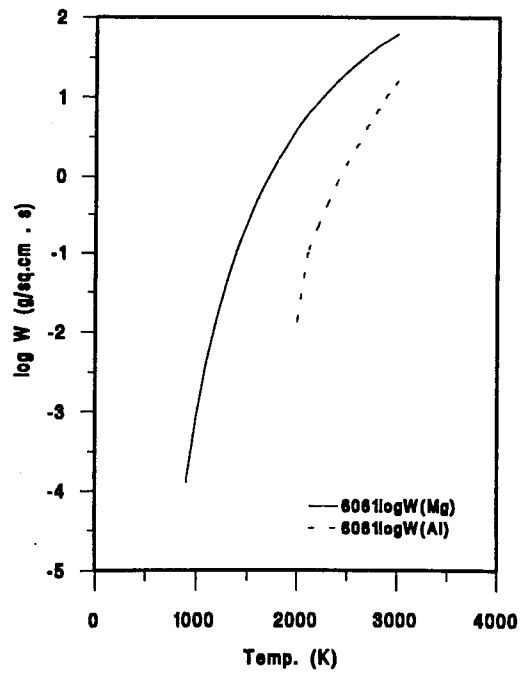

Figure A2.2. Vaporization flux of elements in solution in 6061.

References

[1] W.E. Quist and G.H. Narayanan, Treatise on Materials Science and Technology, vol. 31, Academic Press, Inc., 1989, pp. 219-254, ISBN 0-12-341831-3.

[2] K.K. Sankaran and N.J. Grant, *Mat. Sci. and Eng.*, **44** (1980) 213-227.

[3] J.R. Pickens, *J. Mat. Sci.*, **20** (1985) 4247.

[4] J.R. Pickens, *J. Mat. Sci.*, **25** (1990) 3035.

[5] C.J. Lippold, Proc. of the Fifth Int. Conf. on Al-Li Alloys, Williamsburg, Virginia 1989, Ed. by T.H. Sanders Jr. and E.A. Starke, p. 1365.

[6] M.R. Edwards and V.E. Stoneham, *Journal de Physique*, Coloque. 3, **48** (1987) C3-293.

[7] J.R. Pickens, T.J. Langen and E. Bharta, Proceedings of the 3rd International Al-Li Alloys Conference, Ed. by C. Baker, P.J. Gregson, S.J. Harris and C.J. Peel, Institute of Metals, London, 1986, pp. 137-147.

[8] H.E. Yunjia, G. Dalu and S. Zhixiong, Proc. of the Sixth Int. Conf. on Al-Li Alloys, Garmisch-Partenkirchen, Germany 1991, p.1215.

[9] C.S. Lin, *Aerospace Engineering*, **Dec.** (1988) 23.

[10] P.A. Molian and T.S. Srivatsan, *J. Mat. Sci.*, **25** (1990) 3347.

[11] M.F. Gittos, Welding Institute Members Report, 425/1990.

[12] B. Biermann, R. Dierken, R. Kupfer, A. Lang and H.W. Bergmann, Proc. of the Sixth Int. Al-Li Alloys Conf., Garmisch-Partenkirchen, Germany, October 1991, p.1159.

[13] D.S. Gnanamuthu and R.J. Moores, Proc. of Int. Conf. on Power Beam Processing, San Diego, California, 1988, pp.181-183.

[14] T. Zacharia, S.A. David, J.M. Vitek and R.P. Martukanitz, Proc. of the Fifth Int. Conf. on Al-Li Alloys, Williamsburg, Virginia 1989, Ed. by E.A. Starke Jr. and T.H. Sanders, pp. 1387-1396.

[15] W.M. Steen, in 'Laser Material Processing', Springer-Verlag, London Ltd., 1991, ISBN 3 540 19670 6.

[16] R.A. Willgoss, J.H.P.C. Megaw and J.N. Clark, *Welding and Metal Fabrication*, **March** (1979) 117.

[17] J. Mazumder and W.M. Steen, *Met. Trans. A*, **13A** (1982) 865.

[18] P.E. Denney and E.A Metzbower, *Welding Journal*, **68** (1989) 342-s.

[19] G. Ricciardi, M. Cantello and F.G. Micheletti, *Advanced Manufacturing Processes*, **1** (1986) 223.

[20] I. Jones, S. Riches, J.W. Yoon and E.R. Wallach, Proc. of LAMP, Nagaoka, June, 1992, pp.523-528. Ed. A. Matsunawa and S. Katayama, ISSN 0918-2993.

[21] D.W. Moon and E.A. Metzbower, *Welding Journal*, **62** (1983) 53-s.

[22] T.A. Marsico and R. Kossowsky, LIA vol. 69, Proc. of ICALEO, 1989, pp.61-71

[23] H.C. Peebles and R.L. Williamson, Proc. of LAMP, Osaka 1987, pp. 19-24.

[24] N. Nakajima, Y. Shimokusu, S. Shono and T. Ishide, *Welding In The World*, no. 5/6, **27** (1989) 43.

[25] T. Watanabe, Y. Yoshida and T. Arai, Proc. of LAMP, Nagaoka, June 1992, pp.505-510, Ed. A. Matsunawa and S. Katayama, ISSN 0918-2993.

[26] H. Simidzu, F. Yoshino, S. Katayama and A. Matsunawa, *ibid*, pp.511-516.

[27] J.O. Milewski, G.K. Lewis and J.E. Wittig, *Welding Journal*, **72** (1993) 341-s.

[28] S.L Engel, *Laser Focus*, **Feb.** (1976) 44.

[29] D.T. Swift-Hook and A.E.F. Gick, *Welding Journal*, **52** (1973) 492-s.

[30] P.S. Wei and L.R. Chiou, *J. Heat Transfer*, Trans. ASME, **110** (1988) 918.

[31] J.F. Lancaster, in 'The Physics of Welding', Pergamon Press, 1986, ISBN 0-080-34076 8

[32] W.H. Giedt, in 'Trends in Welding Research in the U.S.', Ed. S.A. David, 1981, ASM, Metals Park, Ohio 44073, pp.109-131.

[33] Y. Arata, Proceedings of the Conference of Laser Advanced Material Processing LAMP '87, Osaka, May 1987, published by the High Temperature Society of Japan, pp. 3-11.

[34] C. Banas, in 'Industrial Laser Handbook - Annual Review of Laser Processing', 1985, pp.69-86.

[35] G. Herziger, in 'Industrial Laser Handbook - Annual Review of Laser Processing', 1986, pp. 108-115.

[36] A. Bharti, *Bull. Mater. Sci.*, **11** (1988) 191.

[37] K. Behler, E. Beyer and R. Schäfer, Proc. of ICALEO, 1988, p.249.

[38] G.J. Davies and J.G. Garland, *Int. Metallurgical Reviews*, **20** (1975) 83.

[39] W.F. Savage, C.D. Lundin and A.H. Aronson, *Welding Journal*, **44** (1965) 175-s.

[40] W.F. Savage and A.H. Aronson, *Welding Journal*, **45** (1966) 85-s.

[41] R.S. Bray, L.J. Lozano and R.E. Willett, *Welding Journal*, **48** (1969) 181-s.

[42] W.A. Tiller and J.W. Rutter, *Can. J. of Physics*, **34** (1956) 96.

[43] 'Phase Transformations in Metals and Alloys', by D.A. Porter and K.E. Eaterling, Van Nostrand Reinhold, 1988, ISBN 0-442-40439-0, pp.208-221.

[44] F.A.C. Calvo, K.P. Bentley and R.G. Baker, *Acta metall.*, **8** (1960) 898.

[45] A. Hellawell and P.M. Herbert, *Proc. Roy. Soc. A*, **269** (1962) 560.

[46] W.F. Savage, C.D. Lundin and R.J. Hrubec, *Welding Journal*, **47** (1968) 420-s.

[47] T. Senda, F. Matsuda, M. Kato and H. Nakagawa, *Japan Welding Journal*, **39** (1970) 44.

[48] W. Kurz and D.J. Fisher, in 'Fundamentals of Solidification', Trans Tech Publications Ltd., 1989, ISBN 0-878-49522-3.

[49] W.S. Miller, J. White and D.J. Lloyd, in 'Aluminium Alloys - Their Physical and Mechanical Properties', International Conference at the University of Virginia, Charlottesville, Virginia, 15-20 June 1986.

[50] H.M. Flower and P.J. Gregson, *Mat. Sci. and Tech.*, **3** (1987) 81.

[51] E.J. Lavernia and N.J. Grant, *J. Mat. Sci.*, **22** (1987) 1521.

[52] L.F. Mondolfo, 'Aluminium Alloys: Structure and Properties', Butterworth and Co. Ltd., 1976, ISBN 0 408 706805.

[53] B. Noble and G.E. Thompson, *Metal Science*, **5** (1971) 114.

[54] D.B. Williams and J.W. Edington, *Metal Science*, **9** (1975) 529.

[55] R. Nozato and G. Nakai, *Trans. Japan Inst. of Metals*, **18** (1977) 679.

[56] G. Schmitz and P. Haasen, *Acta metall. mater.*, **40** (1992) 2209.

[57] J.M. Silcock, *J. Inst. Metals*, **88** (1959-60) 357.

[58] B. Noble, S.J. Harris and K. Dinsdale, *Metal Science*, **16** (1982) 425.

[59] N. Ryum, *Acta metall.*, **17** (1969) 269.

[60] S. Rystad and N. Ryum, *Aluminium*, 53 Jahrg. 1977-3, p.193.

[61] W.L. Fink and L.A. Willey, *Trans. Am. Inst. Min. Engrs.*, **133** (1939) 69.

[62] K.S. Vecchio and D.B. Williams, *Acta metall.*, **35** (1987) 2959.

[63] F.W. Gayle and J.B. VanderSande, *Scripta Met.*, **18** (1984) 473.

[64] P.G. Gregson and H.M. Flower, *J. Mat. Sci. Lett.*, **3** (1984) 829.

[65] B.P. Gu, G.L. Liedl, T.H. Sanders, Jr. and K. Welpmann, *Mat. Sci. and Eng.*, **76** (1985) 147.

[66] H.K. Hardy and J.M. Silcock, *J. Inst. Metals*, **84** (1955-56) 423.

[67] J.C. Huang and A.J. Ardell, *Mat. Sci. and Tech.*, **3** (1987) 176.

[68] W.A. Cassada, G.J. Shiflet and E.A. Starke, Jr., *Met. Trans. A*, **22A** (1991) 287.

[69] W.A. Cassada, G.J. Shiflet and E.A. Starke, Jr., *ibid*, p.297.

[70] M.H. Tosten, A.K. Vasudevan and P.R. Howell, *Met. Trans. A*, **19A** (1988) 51.

[71] M. Audier, P. Sainfort and B. Dubost, *Phil. Mag. B*, **54** (1986) L105.

[72] M.A. Marcus and V. Elser, *ibid*, p.L101.

[73] C. Bartges, M.H. Tosten, P.R. Howell and E.R. Ryba, *J. Mat. Sci.*, **22** (1987) 1663.

[74] M.D. Ball and D.J. Lloyd, *Scripta Met.*, **19** (1985) 1065.

[75] D. Levine and P.J. Steinhardt, *Phys. Rev. B*, **34** (1986) 596.

[76] J.E.S. Socolar and P.J. Steinhardt, *ibid*, p.617.

[77] R.E. Crookes and E.A. Starke, Jr., *Met. Trans. A*, **15A** (1984) 1367.

[78] D.H. Kim, B. Cantor and H.I. Lee, *J. Mat. Sci.*, **23** (1988) 1695.

[79] H. Perlitz and A. Westgren, *Arkiv. for Kemi, Mineralogi och Geologi*, Band 16B, N:o 13, 1943.

[80] J.M. Silcock, *J. Inst. Metals*, **89** (1960-61) 203.

[81] J. Yan, *J. Mat. Sci. Lett.*, **10** (1991) 591.

[82] R.N. Wilson and P.G. Partridge, *Acta metall.*, **13** (1965) 1321.

[83] P.J. Gregson and H.M. Flower, *Acta metall.*, **33** (1985) 527.

[84] J.M. Papazian, C. Sigli and J.M. Sanchez, *Scripta Met.*, **20** (1986) 201.

[85] E.S. Balmuth, *Scripta Met.*, **18** (1984) 301.

[86] J.M. Howe, in 'Aluminium Alloys - Their Physical and Mechanical Properties', International Conference at University of Virginia, Charlottesville, Virginia, 15-20 June 1986, pp.603-619.

[87] A.K. Jena, A.K. Gupta and M.C. Chaturvedi, *Acta metall.*, **37** (1989) 885.

[88] A.K. Mukhopadhyay, C.N.J. Tite, H.M. Flower, P.J. Gregson and F. Sale, *Journal de Physique, Colloqe. C3*, **48** (1987) C3-439.

[89] S. Abis, E. Evangelista, P. Mengucci and G. Riontino, *ibid*, p.447.

[90] P.J. Gregson, K. Dinsdale, S.J. Harris and B. Noble, *Mat. Sci. and Tech.*, **3** (1987) 7.

[91] M.C.S. deMacedo, I.G. Solorzano and R.R. deAvillez, Proc. of the Sixth Int. Conf. on Al-Li Alloys, Garmisch-Partenkirchen, Germany, October 1991, p.1227.

[92] P. Gomiero, F. Livet, J.P. Simon and O. Lyon, *ibid.*, p.69.

[93] Y.L. Wu, J. Qiang, S.C. Wang and B.C. Liu, *Mat. Sci. and Tech.*, **9** (1993) 114.

[94] A. Luo, D.J. Lloyd, A. Gupta and W.V. Youdelis, *Acta metall. mater.*, **41** (1993) 769.

[95] A. Trowsdale, Ph.D. Thesis, Nottingham University, U.K., 1993.

[96] C.E. Cross, D. Olson, G.R. Edwards and J.F. Capes, Proc. of the Second Int. Conf. on Al-Li Alloys, Monterey, California, April 1983, p.675.

[97] A. Ravindra and E.S. Dwarakadasa, *J. Mat. Sci. Lett.*, **11** (1992) 1543.

[98] P. LePoac, A.M. Nomine and D. Miannay, *Journal de Physique*, Colloque. 3, **48** (1987) C3-301.

[99] Y. Erjing, L. Ganhong and W. Zhaoqing, Proc. of the Sixth Int. Conf. on Al-Li Alloys, Garmisch-Partenkirchen, Germany, October 1991, p.1191.

[100] A.J. Sunwoo and J.W. Morris, Jr., *Welding Journal*, **68** (1989) 262-s.

[101] A.J. Sunwoo and J.W. Morris, Jr., *Met. Trans. A*, **22A** (1991) 903.

[102] P.A. Molian and T.S. Srivatsan, *J. Mat. Sci. Lett.*, **9** (1990) 245.

[103] P.A. Molian and T.S. Srivatsan, Proc. of the Fifth Int. Conf. on Al-Li Alloys, Williamsburg, Virginia, 1989.

[104] E.J. Lavernia, J.D. Ayers and T.S. Srivatsan, *Int. Materials Reviews*, **37** (1992) 1.

[105] R. Mehrabian, *Int. Metals Reviews*, **27** (1982) 185.

[106] D. Liang, Ph.D. Thesis, University of Sheffield, U.K., 1993.

[107] C.McL. Adam and L.M. Hogan, *J. Australian Inst. Met.*, **17** (1972) 81.

[108] C.McL. Adam and L.M. Hogan, *Acta metall.*, **23** (1975) 345.

[109] E.H. Hollingsworth, G.R. Frank and R.E. Willett, *Trans. AIME*, **224** (1962) 188.

[110] I.R. Hughes and H. Jones, *J. Mat. Sci.*, **11** (1976) 1781.

[111] R.M.K. Young and T.W. Clyne, *Scripta Met.*, **15** (1981) 1211.

[112] I. Miki, H. Kosuge and K. Nagahama, *J. Japan Inst. of Light Metals*, *25 (1975) 1.*

[113] P. Skjerpe, *Acta Cryst.*, **B44** (1988) 480.

[114] C.J. Simensen and R. Vellasamy, Z *Metallkunde*, **68** (1977) 428.

[115] D.J. Skinner, R.L. Bye, D. Raybould amd A.M. Brown, *Scripta Met.*, **20** (1986) 867.

[116] D.J. Skinner, in 'Dispersion Strengthened Aluminium Alloys', Ed. Y.W. Kim and W.M. Griffith, The Minerals, Metals and Materials Society, 1988.

[117] M. Cooper, *Acta Cryst.*, **23** (1967) 1106.

[118] M.E. Fine, *Met. Trans. A*, **6A** (1975) 625.

[119] M.E. Fine, in 'Dispersion Strengthened Aluminium Alloys', Ed. Y.W. Kim and W.M. Griffith, The Minerals, Metals and Materials Society, 1988, p.103.

[120] D.Y. Lee and D.E. Zupon, *ibid*, p. 265.

[121] W.A. Baeslack (III), *Metallography*, **18** (1985) 73.

[122] S. Krishnaswamy and W.A. Baeslack (III), *Materials Characterization*, **24** (1990) 331.

[123] N. Sonti, Ph.D. Thesis, Penn. State University, Pa. 16802, 1988.

[124] M.J. Cieslak and P.W. Fuerschbach, *Met. Trans. B*, **19B** (1988) 319.

[125] G.C. Lim and W.M. Steen, Proc. of the 1st Int. Conf. on Lasers in Manufacturing, Ed. by M.F. Kimmitt, Brighton, U.K., November 1983, pp.161-167.

[126] P.J. Gregson, Ph.D. Thesis, University of London, U.K., 1983.

[127] J.M. Papazian, R.L. Schulte and P.N. Adler, *Met. Trans. A*, **17A** (1986) 635.

[128] J.J. Blandin, *Mat. Sci. and Eng.*, **A122** (1989) 215.

[129] 'Alloy Phase Equilibria', by A. Prince, Elsevier Publishing, 1966.

[130] N. Sonti and M.F. Amateau, *Numerical Heat Transfer, Part A*, **16** (1989) 351.

[131] V.A. Wills and D.G. McCartney, *Mat. Sci. and Technol.*, **8** (1992) 114.

[132] R.R. Lober, T.J. Rockstroh and J. Mazumder, Modeling of Casting and Welding Processes IV, Ed. by A.F. Giamei and G.J. Abbaschian, The Minerals, Metals and Materials Society, 1988, page 213.

[133] R. Ducharme and P. Kapadia, Proc. of ICALEO, (1992) 187.

[134] 'Binary Alloy Phase Diagrams', Ed. T.B. Massalski, ASM, Metals Park, OHIO 44073, ISBN 0-87170-261-4.

[135] 'Castings' by J. Campbell, Butterworth-Heinemann, London, 1991, ISBN 0750610727.

[136] D.E.J. Talbot in 'Solidification Processing 1987', Ed. J. Beech and H. Jones, Inst. of Metals, London, 1988, pp. 29-32.

[137] J.H. Devletian and W.E. Wood, Welding Research Council Bulletin 290 (1983) pp. 1-18.

[138] H. Tong and W.H. Giedt, *Welding Journal*, **49** (1970) 259-s.

[139] D.A. Schauer and W.H. Giedt, *Welding Journal*, **57** (1978) 189-s.

[140] Y. Arata, E. Abe and M. Fujisawa, *Trans. JWRI*, **5** (1976) 1.

[141] E.A. Metzbower, *Met. Trans. B.*, **24B** (1993) 875.

[142] C. Garcia-Cordovilla, E. Louis and A. Pamies, *J. Mat. Sci.*, **21** (1986) 2787.

[143] D.R. Poirier and R. Speiser, *Met. Trans. A*, **18A** (1987) 1156.

[144] W.S. Miller and J. White, 'Superplasticity in Aerospace', Ed. by H.C. Heikkenen and T.R. McNulley, 1988, pp.211-228.

[145] D.H. Shin, Y.H. Shin and Y.W. Chang, *Scripta Met.*, **26** (1992) 117.

[146] J. Wadsworth, A.R. Pelton and R.E. Lewis, *Met. Trans. A*, **16A** (1985) 2319.

[147] J. Pilling and N. Ridley, 'Superplasticity in Crystalline Solids', The Institute of Metals, London, 1989, p. 20.

[148] S. Srinivasen, P.B. Desch and R.B. Schwarz, *Scripta Met.*, **25** (1991) 2513.

[149] O. Izumi and D. Oelschlägel, *Scripta Met.*, **3** (1969) 619.

[150] M.S. Zedalis and M.E. Fine, *Met. Trans. A*, **17A** (1986) 2187.

[151] M.C. Pandey, J. Wadsworth and A.K. Mukherjee, *J. Mat. Sci.*, **23** (1988) 3509.

[152] A. Block-Bolten and T.W. Eagar, Trends in Welding Research in the U.S., Ed. S.A. David, American Society for Metals, Metals Park, OHIO 44073, 1981, pp. 53-71.

[153] M.M. Collur, A. Paul and T. Debroy, *Met. Trans. B*, **18B** (1987) 733.

[154] K. Mundra and T. Debroy, *Met. Trans. B*, **24B** (1993) 145.

[155] S.C. Flood and J.D. Hunt in 'Metals Handbook', 9th Edition, vol. 15, ASM Int., Ohio, 1988, pp. 130-135.

[156] G. Von Bradsky and R.A. Ricks, *J. Mat. Sci.*, **22** (1987) 1469.

[157] C. S. Smith, *Trans. Amer. Inst. Metall. Engnrs.*, **175** (1948) 15.

[158] R.D. Doherty, *Mat. Sci. and Eng.*, **65** (1984) 181.

[159] A. Paul and T. Debroy, *Met. Trans. B*, **19B** (1988) 851.

[160] T. Zacharia, S.A. David, J.M. Vitek and T. Debroy, *Met. Trans. A*, **20A** (1989) 957.

[161] B.M. Watts, M.J. Stowell, B.L. Baikie and D.G.E. Owen, *Metal Science*, **10** (1976) 198.

[162] H. Aiko and N. Furushiro, 'Superplasticity in Advanced Materials', Ed. S. Hori, M. Tokizane and N. Furushiro, The Japan Society for Research on Superplasticity, 1991. p. 423.

[163] H. Pu, S. Yen, J. Huang and P. Kao, *ibid*, p. 429.

[164] S. Matsuda, Y. Okubo and H. Yoshida, *ibid*, p. 441.

[165] J.E. Burke, *Trans. Amer. Inst. Min. Metall. Engnrs.*, **180** (1949) 73.

[166] E. Nes, N. Ryum and O. Hunderi, *Acta metall.*, **33** (1985) 11.

[167] B.M. Watts, M.J. Stowell, B.L. Baikie and D.G.E. Owen, *Metal Science*, **10** (1976) 189.

[168] A.T. Thomas, Proceedings of the 6th International Conference on Light Metals, Aluminium-Verlag, GMBH, 1975, p. 58.

[169] 'Smithells Metals Reference Book', 7th Edition, Butterworth-Heinemann Ltd., 1992, page 13-72, ISBN 0-7506-1020-4.

[170] T.S. Srivatsan and T. Alan Place, *J. Mat. Sci.*, **24** (1989) 1543-1551.

[171] S.P. Lynch, *Mat. Sci and Eng.*, **A136** (1991) 25-43.

[172] S.P. Lynch, *ibid*, pp. 45-57.

[173] I.M. Robertson, *Materials Forum*, **15** (1991) 102-111.

[174] J.A. Wert and J.B. Lumsden, *Scripta Met.*, **19** (1985) 205.

[175] E.P. Butler, N.J. Owen and D.J. Field, *Mat. Sci and Tech.*, **1** (1985) 531.

[176] 'Structure of Metals' by C.S. Barret and T.B. Massalski, Third Revised Edition, Pergamon International Library: International Series on Materials Science and Technology; vol. 35, ISBN 0-08-026172-8.

[177] S. Hariprasad, S.M.L. Sastry, K.L. Jerina and R.J. Lederich, *Met. Trans. A*, **24A** (1993) 865.

[178] K. Sampath and W.A. Baeslack III, *Welding Journal*, **72** (1993) 416.

[179] J.H. Perpezko and S.E. LeBeau in 'Aluminium Transformation Technology and Applications - 1981', Ed. by C.A. Pampillo, H. Biloni, L.F. Mondolfo and F. Sacchi, ASM, Materials Park, OHIO 44073, pp. 309-346.

[180] J.W. Edington, 'Practical Electron Microscopy in Materials Science', Monographs 1-3, Macmillan Press Ltd., 1974, ISBN 333 181 336.

[181] M.H. Loretto, 'Electron Beam Analysis of Materials', Chapman and Hall Ltd., 1984, ISBN 0412 234009.

[182] G. Thomas, 'Transmission Electron Microscopy of Metals', J. Wiley, 1962.

[183] I.M. Watt, 'The Principles and Practice of Electron Microscopy', Cambridge University Press, 1985, ISBN 0 52125557 0.

[184] 'Short Course in Electron Microscopy of Materials' held at the University of Liverpool, U.K., 15-19 July 1991.

[185] 'Practical Methods in Electron Microscopy', Volumes 1 and 2, Ed. A.M. Glauert, North-Holland Publishing Company, 1974, ISBN 0 7204 42508.

[186] S.J.B. Read, 'Electron Microprobe Analysis', second edition, Cambridge University Press, 1993, ISBN 0 521 41956 5.

[187] 'Scientific Foundations of Vacuum Technique', 2nd. ed., S. Dushman and J.M. Lafferty, Eds., John Wiley, New York, 1962, Chapter 10.

[188] I. Langmuir, *The Physical Review*, 2nd Series, **2** (1913) 329.